GEOMETRIC AND NUMERICAL OPTIMISATION OF SINGLE- AND TWO-PHASE CONVECTIVE HEAT TRANSFER IN MICROCHANNEL HEAT SINKS

David Olugbenga Ariyo

Thesis Presented for the Degree of

DOCTOR OF PHILOSOPHY

in the Department of Mechanical Engineering

Faculty of Engineering and the Built Environment

UNIVERSITY OF CAPE TOWN

September 2020

Supervisor: Professor Tunde Bello-Ochende

PLAGIARISM DECLARATION

Plagiarism is totally unacceptable; therefore, I declare that the work in this thesis is my own and it is an original contribution to knowledge. Studies from other authors have been duly acknowledged. I confirm that concerns emanating from the Turnitin have been resolved with my supervisor. No quotation or information derived from this work should be published without full acknowledgement of the source. The thesis is to be used for private study or non-commercial research purposes only.

Signature: Signed by candidate

Date: 10.09.2020

ABSTRACT

Innovative and efficient cooling systems are required for the present and future high heat flux applications because natural and forced air convection and many other cooling methods employing liquid coolants cannot meet up with the challenges. More transistors are added to the surfaces of electronic chips to increase the capacity of integrated circuits and more heat is generated; hence a better cooling method is highly desirable. A cooling system should be designed in such a way that pressure drop is minimised while maximising thermal performance at low thermal resistance and temperature. To satisfy high heat flux demand and compact size for the present and future applications, single-phase and two-phase convective heat transfer mechanisms in circular, equilateral triangular, rectangular and square microchannels (micro passages for liquid flow in the heat sinks) were studied to enable electronic chip manufacturers to produce more powerful and durable integrated circuits at temperatures well below the recommended highest operating temperature. There is the need to optimise different microchannel configurations for low, medium and high heat fluxes at moderately low velocities and pressure drops with the aim of having optimal microchannel heat sinks that perform well in two-phase and single-phase flow and at low pumping power. Also, the problem of instability has to be solved by having optimal and stable microchannel heat sinks. In operation, microchannel heat sinks could be used beyond their optimal limits, hence specification of maximum permissible heat fluxes (critical heat fluxes) is necessary. Deionised water was used as the working fluid because of its thermal advantage (high thermal conductivity, high specific heat), availability and environmental friendliness compared to other fluids like refrigerants. Aluminium was used as the heat sink material because of its light weight, low cost, ease of fabrication and relatively high thermal conductivity. Copper was used as the heat sink material for high heat flux study (800 to 1200 W/cm^2) in rectangular microchannel heat sinks solely because of its high thermal conductivity. Simulation and optimisation studies of two-phase and single-phase convective heat transfer in microchannels are limited considering the way they have been done presently. Goal driven optimisation was used and the volumes of microchannels and heat sinks were fixed over a wide range of heat fluxes and velocities.

Geometric optimisation and flow parameters modelling were studied for subcooled flow boiling (two-phase flow) in horizontal circular, equilateral triangular, rectangular and square microchannels to solve the problem of high heat flux dissipation in microelectronic devices and other similar applications. The four microchannel heat sink configurations presented for

simulations and optimisations were considered to be good designs after being tried in single-phase and two-phase flow simulations. The objective was to minimise the thermal resistance of microchannel heat sink at each velocity range and fixed heat flux subject to fixed volume constraints of the heat sink and microchannel. Manufacturing constraints were also applied to ensure reliability in practical applications. Geometric and numerical optimisation was carried out to determine the optimal shapes of microchannel heat sinks and the optimal numerical values of flow parameters. The geometric and flow parameters were allowed to morph to obtain their optimal values. Highly subcooled deionised water at inlet temperature of 25 ^{o}C (degree of subcooling being 75 ^{o}C) was used as the cooling fluid and aluminium as the heat sink material for heat fluxes up to 700 W/cm^2. For high heat flux study (800 to 1200 W/cm^2), deionised water at inlet temperature of 10 ^{o}C (degree of subcooling, 90 ^{o}C) was used and copper was the heat sink material. Velocities from 0.1-0.5 to 6.5-7.0 m/s and heat fluxes between 100 and 1200 W/cm^2 (1x10^6 W/m^2 and 1.2x10^7 W/m^2) were considered in the modelling and optimisation procedures. Computational fluid dynamics (CFD) code, ANSYS (heat flux partitioning model and goal driven optimisation tool) was used for the simulations and optimisations of the microchannel heat sink configurations. The numerical code used for the simulations in two-phase flow was validated by the available experimental data in the literature and the agreement showed the capability of CFD (ANSYS) to predict accurately, subcooled flow boiling (two-phase flow) in the microchannels for cooling of microelectronic devices. Single-phase flow validation was also done with the available experimental data in the open literature and the agreement was good. Grid refinements were done for the initial designs of microchannel heat sink configurations presented for simulations and optimisations to achieve grid independent results.

In two-phase flow, optimal results were obtained for rectangular microchannel heat sinks for all the heat fluxes considered while for the remaining microchannel heat sinks, results could only be obtained up to the maximum of 500 W/cm^2 for equilateral triangular microchannel heat sinks and 400 W/cm^2 each for circular and square configurations. Two-stacked and v-grooved rectangular microchannel heat sinks were used to achieve the maximum heat flux of 1200 W/cm^2. In single-phase flow, optimal results were obtained up to 200 W/cm^2 for circular and rectangular microchannel heat sinks while for equilateral triangular and square configurations, results were obtained at 100 W/cm^2 only, due to high base (bottom) temperatures. Comparisons were made between two-phase and single-phase flow by using their optimal geometric and

flow parameters, and the results clearly demonstrated the superiority of two-phase flow regime in all the microchannels, for removal of high heat fluxes at low Reynolds numbers. The pumping power requirements for optimal microchannels were compared and considered useful in practical applications such as in the cooling of electronic devices. Contours are provided to show wall temperature distribution for the heat sinks, water and water vapour in the microchannels. Using non-equilibrium subcooled boiling model which is an extension of heat flux partitioning model, critical heat fluxes for optimal microchannel heat sinks at velocities in the range 2.0-2.5 to 3.5-4.0 m/s and 100 W/cm^2 were computed, to demonstrate that optimal microchannel heat sinks could be operated beyond the heat fluxes for which they had been optimised.

Multichannels of optimal microchannel heat sink configurations were compared over a width of 1 cm which is common in electronic packaging and rectangular microchannel heat sinks had the best thermal performance while circular configuration had the least performance in subcooled flow boiling. For the four microchannel configurations considered, an array of optimal microchannel heat sinks that performed well in two-phase and single-phase flow, one-stacked and two-stacked in parallel flow and counterflow arrangements, has been achieved at high heat fluxes not reported in open literature for similar geometries, for cooling of electronic devices and in other applications. Stability of optimal results was ensured in the simulations and optimisations, and in the critical heat flux computations.

Keywords: Optimisation, Microchannel heat sink, CFD, Thermal resistance, Critical heat flux, Deionised water, Two-phase flow, Single-phase flow

ACKNOWLEDGEMENTS

Glory be to God in the highest for the successful completion of this work. I am grateful to my supervisor, Professor Tunde Bello-Ochende for his support and trust in this research. His encouragement, patience, advice and outstanding research ability have helped in stretching me to the limit to achieve the objectives and goals of this work. I am grateful to Federal Polytechnic Offa and TETFund for the release and financial support for the research. The financial support received from University of Cape Town is appreciated.

I express my sincere appreciation to my friends, Dr Steeve Bassi, Yusuf, Aminu, Dr Idowu Atilola, Dr Kayode Akintoye and Dr F.I. Sodiq who were part of my coming to University of Cape Town for the research, and the encouragement I received from them throughout. I appreciate my friend Dr Deepti Charitar, who has always been there to provide useful advice and encouragement. I am grateful to Mukaila and Abayomi for their love and encouragement. My colleagues in our research group; Nahum, Raymond, Tanimu and Samson are appreciated for providing the atmosphere of peace and robust knowledge-based friendship culminating in the desired research outputs. My sincere appreciation to loved ones in my family.

TABLE OF CONTENTS

LIST OF FIGURES

LIST OF TABLES

NOMENCLATURE

Symbol	Definition	Unit
A	Area	m^2
A_{int}	Interfacial area between liquid and vapour phases	m^2
AR	Aspect ratio, $AR = H_{ch}/W_{ch}$	-
Be	Bejan number based on a unit volume, $Be = \Delta pV^{2/3}/\alpha\mu$	-
C_p	Specific heat at constant pressure	J/kgK
CFD	Computational fluid dynamics	-
CHF	Critical heat flux	W/m^2
D_h	Microchannel hydraulic diameter	m
DNB	Departure from nucleate boiling	-
F	Force	N
g	Acceleration due to gravity	m/s^2
h	Specific enthalpy	J/kg
h_c	Convective heat transfer coefficient	W/m^2K
H_b	Thickness of base of microchannel heat sink	m
H_{ch}	Height of microchannel	m
H_{cp}	Height of cover plate of microchannel heat sink	m
H_s	Height of microchannel heat sink	m
k	Thermal conductivity	W/mK
L	Axial length of microchannel	m
MCHS	Microchannel heat sink	-
n	Normal	-
Nu	Nusselt number, $Nu = \frac{h_c D_h}{k}$	-
ONB	Onset of nucleate boiling	-
p	Pressure	N/m^2
PP	Pumping power	W
q	Heat flux	W/m^2
Q	Total heat transfer	W
R_{th}	Thermal resistance	K/W
Re	Reynolds number, $Re = \rho u_{in} D_h/\mu$	-

RPI	Rensselaer polytechnic institute	-
T	Temperature	K
T [-]	Dimensionless temperature	-
U [-]	Dimensionless velocity	-
u, v, w	Velocities in x, y, z directions	m/s
V	Volume	m^3
W	Multichannel heat sink width	m
W_{ch}	Channel width	m
W_s	Width of unit cell (computational domain)	m
W_w	Width of microchannel side wall (fin thickness)	m
Y [-]	Dimensionless length in y-direction	-
x, y, z	Cartesian coordinates	

Greek symbols

Symbol	**Definition**	**Unit**
α	Thermal diffusivity	m^2/s
α_i	Volume fraction	-
Δ	Difference	-
μ	Dynamic viscosity	Pa.s
μm	Micrometre	
ρ	Density	kg/m^3
σ	Surface tension	N/m
ϕ	Mass velocity (mass flux)	kg/m^2s

Subscripts

Symbol	**Definition**
b	Base (bottom)
ch	Channel
cp	Cover plate
f	Fluid
h	Hydraulic
in	Inlet

int	Interfacial
max	Maximum
min	Minimum
opt	Optimum
out	Outlet
s	Sink
sat	Saturation
sub	Substrate
th	Thermal
w	Wall

LIST OF PUBLICATIONS

Journal papers

[1] D.O. Ariyo, T. Bello-Ochende, Constructal design of subcooled microchannel heat exchangers, International Journal of Heat and Mass Transfer 146 (2020) 118835 https://doi.org/10.1016/j.ijheatmasstransfer.2019.118835.

[2] D.O. Ariyo, T. Bello-Ochende, Critical heat fluxes for subcooled flow boiling in optimised microchannels, International Journal of Hydromechatronics 3(2) (2020) 140-154. DOI: 10.1504/IJHM.2020.107786.

[3] D.O. Ariyo, T. Bello-Ochende, Optimal design of triangular microchannels for high performance cooling of electronic devices, Under review in International Journal of Heat and Mass Transfer.

Conference papers

[1] D.O. Ariyo, T. Bello-Ochende, Optimization of geometric and flow parameters of horizontal rectangular microchannels in subcooled two-phase flow, Heat Transfer, Fluid Mechanics and Thermodynamics (HEFAT) Conference, Wicklow, Ireland, 22-24 July 2019 (Presented).

[2] D.O. Ariyo, T. Bello-Ochende, Optimal design of subcooled microchannel heat sinks with variable heat inputs, Journal of Physics: Conference Series (2020), KEYNOTE PRESENTATION.

CHAPTER 1
INTRODUCTION

1.1. Background

Computing power has increased and this has resulted in decrease in size and increase in power density. The demand for high performance (small and faster) electronic devices and continued miniaturisation have led to increase in heat generation and operating temperature. As a result, conventional air-cooling methods cannot cope with this trend. The flow of electric current through a resistive element generates heat and this process is irreversible, hence a heat flow path must be created to get rid of the heat generated for effective operation of an electronic device. Heat has to be removed at a rate equal to or greater than its generation by electronic devices to ensure their good performance and longevity. It has been reported that more than 50% of all integrated circuit failures are related to thermal issues [1]-[4]. As a result of improvement in power density, heat dissipation per unit area has increased, hence effective cooling methods are required to cope with the pace of advancement in electronics. The temperature of an electronic device increases above the ambient temperature because of heat dissipation as a result of its operation.

Modern electronic chips can withstand maximum chip temperatures (junction temperatures) in the range of 85-90 °C [5]-[7]. These devices need to be cooled to ensure their operational reliability, capability and lifespan. The need for new and effective cooling techniques due to increase in heat dissipation of microelectronic devices is highly desirable and has led researchers to look for viable options. It is an established fact that whenever electrical current flows through a resistive element, heat is generated and an increase in the current or resistance will produce an increase in the amount of heat which is generated in the element. As long as current flows, heat will continue to be generated. An electronic device can be maintained in its operating range if a heat path is created to remove the heat flux being generated. The concept of microchannel heat sink for electronic cooling applications was initiated by Tuckerman and Pease [8] to predict single-phase forced convective cooling in rectangular microchannels to cool integrated circuits. Deionised water was used as the coolant and the microchannels were fabricated on the back of a silicon substrate (The silicon wafer orientation was 110). Heat flux of about 790 W/cm^2 for a pressure drop of approximately 213737 N/m^2 in rectangular microchannels of width 50 μm and height 302 μm each and velocity of flow of approximately

5.7 m/s was reported. The inlet temperature of water was 23 °C, thermal resistance was 0.09 °C/W, substrate to coolant temperature rise was 71 °C (above inlet water temperature) and pumping power was 1.838 W. However, the pressure drop and pumping power are quite large for plain microchannels [9]. Approaches of cooling solutions in microchannels have been developed since the initiation of Tuckerman and Pease [8]. Heat transfer managements in many applications have employed single-phase flow for many years. For high heat flux transfer and effectiveness, there is the need for microminiaturisation of channels and two-phase flow in them for cooling of microelectronics and other power electronic devices. Small diameter channels are desirable for high heat flux applications for the following reasons:

1. High heat transfer coefficient can be achieved

2. High heat transfer surface per unit flow volume can be achieved

Various attempts have been made to maximise heat transfer rates in microchannel heat sinks. Microchannel heat sinks are directly embedded on the back of the heat source to enhance uniform heat flux removal. A microchannel heat sink made of silicon is common, and the component is electrically insulated with a silicon oxide layer. A microchannel heat sink is composed of a base substrate which is usually made from silicon, copper and aluminium, and a cover plate. For a rectangular microchannel heat sink, a series of parallel micro slots are cut into the top surface of the base substrate and the cover plate is attached at the top to form rectangular microchannels. Microchannel heat sinks have become increasingly popular and interesting to researchers due to potential high heat transfer coefficients and low to moderate pressure drops when compared to conventional air and liquid cooling systems [9]-[11].

The trend of miniaturisation has significantly aggravated the problem associated with overheating of integrated circuits hence new thermal control methods have become necessary. A relatively small area of microelectromechanical system requires huge heat flux to be dissipated; therefore, effective thermal design is required [12]. Examples of applications of microchannel heat sinks include high performance computers, power electronics, laser diode arrays, X-ray medical devices, power electronics in hybrid vehicles and refrigeration and air conditioning. Numerical modelling of single-phase and two-phase flow through microchannels is desirable because available experimental data can be used for validation. Heat transfer coefficient is high in micro and mini channels; also, ratio of surface area of the microchannel to volume of fluid flowing is high which translates to high heat transfer rates. Many

configurations of microchannels have been studied in the literature. Examples include: circular [13]-[18], square [19]-[23], triangular [24]-[27], trapezoidal [28]-[30] while rectangular microchannels have been used in more studies.

The first working transistor and integrated circuit were invented in 1947 and 1958 respectively and since then, there has been a focus in the electronics industry to reduce the size of transistor which will lead to improved performance of electronic devices. A trend was identified by Moore [31] which is known as Moore's law and states that the number of transistors on integrated circuits doubles every two years. It was predicted by The International Technology Roadmap of Semiconductors (ITRS 2011) that the power dissipation from a microprocessor chip will exceed 800 W by 2026 whereas the predicted value was 270 W in 2015. In 2011, a value of 240 W was reached for ORACLE SPARC T4 processor which was produced by Oracle Corporation for high performance computers. The average heat flux could reach values of 200 W/cm^2 in high performance computers and 450 W/cm^2 (die size is smaller) in desktop computers by 2026. The chip performance decreases as its temperature increases, hence thermal solution for high heat flux dissipation is inevitable [7].

1.2. Conventional cooling methods for electronic devices

High increase in power density particularly for high performance chips is as a result of advances in semiconductor and other mini and micro scale electronic technologies. The maximum power dissipation and heat flux from high performance microprocessor chips were projected to reach about 360 W/cm^2 by 2020 [2]. However, an earlier study by Agostini et al. [32] indicated that many electronic industries were facing a difficult challenge of removing high heat flux of 300 W/cm^2 while maintaining the temperature of the devices below 85 °C. The speed of operation and density of transistors increase, consequently heat dissipation from electronic chips increases. There is the need for effective cooling methods for these microelectronic devices. For all cooling methods, an important parameter characterising cooling is the thermal resistance defined as:

$$R_{th} = \frac{\Delta \mathrm{T}}{Q} \tag{1.1}$$

where R_{th} is the thermal resistance in K/W or °C/W, ΔT is the temperature difference between the highest heat sink base temperature and fluid temperature at the inlet in K or °C and Q is the heat removed from the cooled device in W. It is evident from Equation (1.1) that, if the thermal

resistance is low and the same temperature difference is maintained, more heat can be removed. Based on coolants used, cooling methods can be classified generally as follows:

- Air cooling
- Liquid cooling
- Refrigeration cooling

Some of the cooling methods based on the process adopted are discussed below.

1.2.1. Air cooling

Passive (or natural convective) cooling of electronic devices is based on natural convection which is as a result of density differences between the hot air at the electronic device and the surrounding air. The flow rate and thermal conductivity of air are low and the convective heat transfer associated with this method of cooling is low. By increasing air flow speed with a fan, active or forced convective air cooling is achieved. The combination of fan and heat sink is widely used in cooling of electronics. Despite improvements with air cooling, such as the optimised design of the heat sink and thermal consideration in the integrated circuit layout, this cooling technique approaches its limit with central processing unit (CPU) heat dissipation flux of 100 W/cm^2 [33]-[36]. The general concept of air cooling is shown in Figure 1.1 [37].

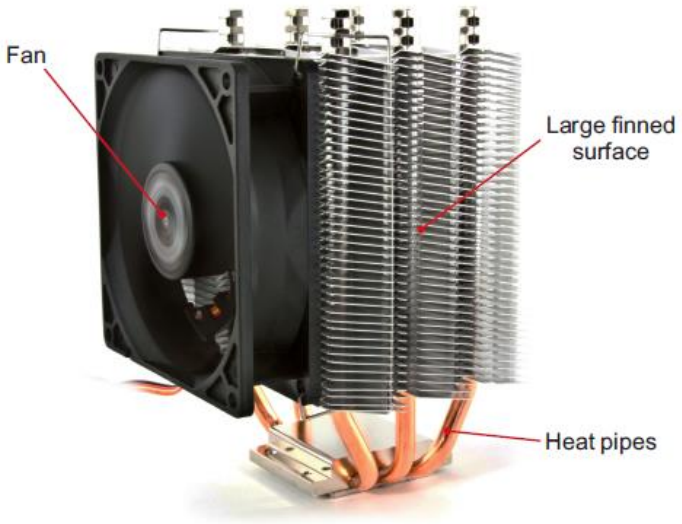

Figure 1.1. Active air cooling [37].

1.2.2. Liquid cooling

Most liquids are better conductors of heat than air. In direct liquid cooling schemes, the coolant is in direct contact with the back of the chip. Spray cooling with a fluorocarbon liquid (FC72) is capable of removing heat fluxes between 50 and 60 W/cm^2 while maintaining the junction temperature at 85 °C [38]-[40]. The arrangement is shown in Figure 1.2 [38].

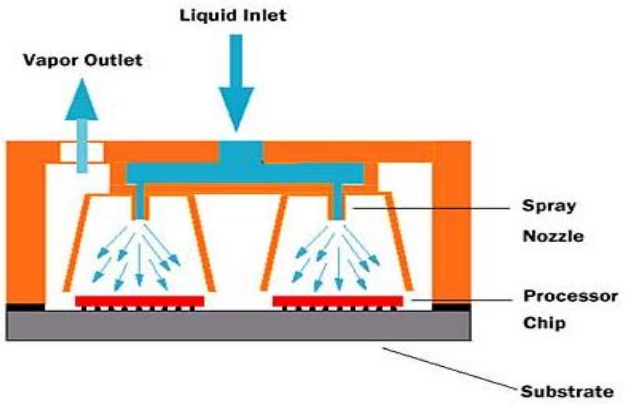

Figure 1.2. Direct liquid cooling [38].

Lasance and Simons [41] reported that heat flux up to 100 W/cm^2 could be achieved with immersion cooling. Figure 1.3 [42] demonstrates this method of cooling for electronic devices. The entire electronic device is immersed in the liquid and pool boiling occurs at local high heat fluxes. Enhanced cooling occurs at high heat generation locations which ensures overall uniform temperature. Vapour generated either condenses on the sides of the container or in a condenser.

Figure 1.3. Immersion cooling and pool boiling [42].

1.2.3. Heat pipes

Heat pipe, whose working principle is based on phase change of the working fluid is an effective passive device for transmitting heat at high rates over considerable distances. It is widely used as a two-phase electronic cooling device [43]. Figure 1.4 [2] shows the working principle of a conventional heat pipe used to cool electronic components. It operates by evaporating liquid from a capillary wick structure at one end of the device and condensing vapour back into the wick structure at the other end of the device. Capillary force drives the liquid through the wick structure resulting in a vapour flow at the centre of the device. Working fluids such as methanol, water, acetone, ammonia and sodium can be used based on the required operating temperature. Heat flux of 150 W/cm^2 at operating temperatures of 60 to 95 °C, using water as the cooling medium has been reported [44].

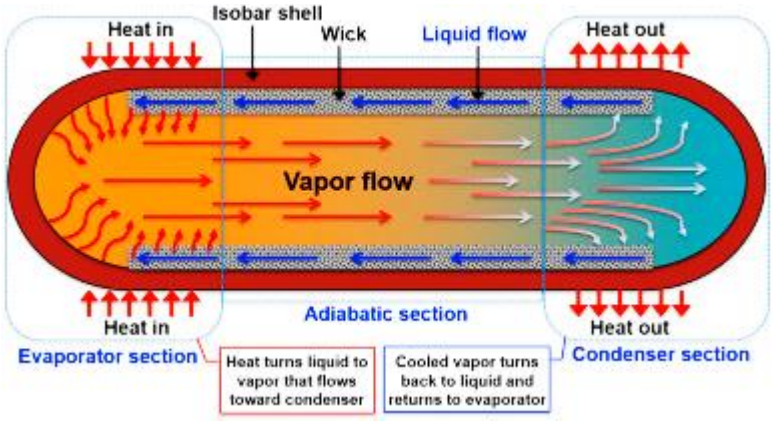

Figure 1.4. Working principle of a conventional heat pipe [2].

1.2.4. Thermoelectric cooling

A thermoelectric cooler uses Peltier effect to create heat flux between the junctions of two different types of semiconductors. Thermoelectric coolers are compact and can be integrated into electronic packages for cooling [45], [46]. Thermoelectric cooling consists of p-type and n-type semiconductor pellets which are connected electrically in series. When direct current passes through the circuit, there is a temperature difference between the sides and as a result, there exists a cold side and a hot side [47]. The arrangement for this cooling method is shown in Figure 1.5 [2]. Thermoelectric cooling could be used to remove heat flux of 20 W/cm^2, but with high thermal conductivity substrates, higher values are possible [48], [49].

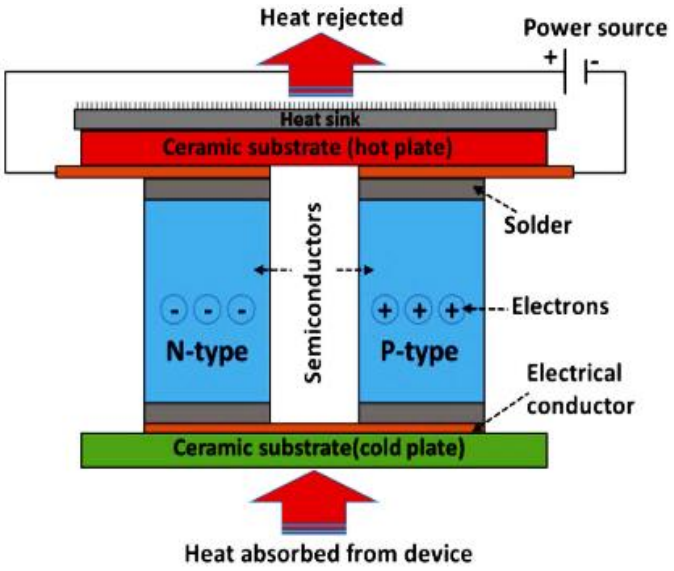

Figure 1.5. Thermoelectric cooling method [2].

1.3. Microchannel cooling

Microchannel based forced convective liquid cooling is employed in high heat generating electronic devices because the heat transfer performance is better than other cooling methods for electronic devices. Circuit density and operating speed of microprocessors have increased, hence more heat is generated. It is anticipated that some of the next-generation microprocessors and electronic components may dissipate over 1000 W/cm^2 [50]. A large amount of heat generated by a microelectronic device is carried away by a relatively small quantity of coolant inside the microchannel which results in its temperature rise, hence microchannel cooling technology is adaptable to on-chip integration because of its small size [51], [52]. Water is normally used in the deionised form in microchannel applications. Figure 1.6 [53] shows the liquid cooling concept of a microchannel heat sink.

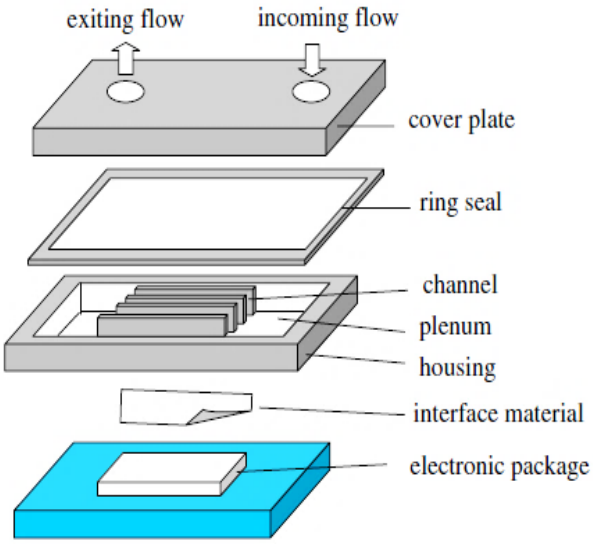

Figure 1.6. Microchannel liquid cooling concept for electronic packages [53]

Cooling with or without enhancement by employing single-phase flow in microchannel for removing high heat flux from electronic devices has been reported in the literature [54]-[57]. However, improvement in electronic devices has led to increase in heat generation which may stretch single-phase cooling to its limits in the future generation of electronics. A disadvantage of single-phase cooling is the relatively high and non-uniform temperature distribution along the microchannel compared to two-phase flow boiling [58]. Two-phase flow boiling in microchannel has the advantage of maintaining temperature uniformity together with better heat transfer characteristics. Phase change processes produce high heat transfer rates, therefore for high heat flux applications such as in modern electronics, flow boiling mechanism (two-phase flow) is highly desirable. Two-phase boiling can be found in many applications including cooling of electronic devices [9],[59],[60]. A microchannel heat sink can be used as a micro cold plate which can be attached directly to the back of a chip. It can also be fabricated directly on the backside of the chip.

The non-dimensional Nusselt number (Nu) is constant for fully developed laminar flow in the microchannel, hence heat transfer coefficient (h_c) is inversely proportional to hydraulic diameter (D_h) as shown in Equation (1.2) and Equation (1.3):

$$Nu = \frac{h_c D_h}{k} = constant \tag{1.2}$$

$$h_c = \frac{Nu.k}{D_h} = \frac{Constant}{D_h} \tag{1.3}$$

$$h_c \propto \frac{1}{D_h} \quad (thermal\ conductivity, k\ is\ assumed\ to\ be\ constant)$$

This shows that as the hydraulic diameter decreases, heat transfer coefficient increases, which is one of the advantages of cooling with microchannels. An enhanced microchannel has additional features like pin fins to increase heat transfer, whereas a plain microchannel is without enhancement.

1.3.1. Microchannel heat sink materials and coolants

Different coolants have been employed to dissipate heat generated by electronic devices. Liquid coolants such as methanol, water, refrigerants, nanofluids and gaseous coolants (for example air, helium, nitrogen, argon and ammonia) have been used to dissipate heat from electronic devices [61]. The properties of microchannel heat sink materials and deionised water are shown in Table 1.1 and Table 1.2 [62], [63], [64].

Table 1.1. Properties of materials for construction of microchannel heat sinks [62], [63].

Material	Density ρ (kg/m^3)	Specific heat capacity C_p (J/kgK)	Thermal conductivity k (W/mK)
Aluminium	2719	871	202.4
Copper	8978	381	387.6
Silicon	2330	700	149

Table 1.2. Properties of water at 25 °C and 101325 N/m^2 [62], [63], [64].

Material	Density ρ (kg/m^3)	Specific heat capacity C_p (J/kgK)	Thermal conductivity k (W/mK)
Water	997.1	4183	0.5948

1.4. Problem statement

Increase in chip power and high packaging densities are as a result of miniaturisation of electronics being motivated by new application areas and modern fabrication techniques. Integrated circuits temperatures have to be controlled, therefore effective and reliable methods of cooling to remove excess heat are required. Addition of more transistors to increase chip performance results in excessive heat generation that cannot be controlled by present day conventional cooling methods.

Simulation and optimisation of subcooled flow boiling in different configurations (circular, equilateral triangular, rectangular and square) of microchannels were studied over a wide range of heat fluxes and velocities to solve the problem of high heat flux dissipation in modern electronic devices.

1.5. Scope of study

The scope of the present study includes:

1. Numerical simulation and optimisation studies for single-phase and two-phase (subcooled flow boiling) convective heat transfer in selected configurations of horizontal microchannels (circular, equilateral triangular, rectangular and square) over a wide range of heat fluxes and velocities (100 to 1200 W/cm^2 and 0.1-0.5 to 6.5-7.0 m/s; 100 W/cm^2 intervals for heat flux, 0.5 m/s intervals for velocity except 0.1-0.5 m/s range).

2. Comparison of different configurations of optimal microchannel heat sinks in two-phase and single-phase flow to establish the order of performance.

3. Comparison of optimal two-phase and single-phase microchannel heat sinks for all the configurations.

4. Investigation of the effects of geometric and flow parameters on thermal resistance, pumping power, base temperature, Bejan number and Reynolds number.

5. Computation of critical heat fluxes for selected optimal microchannels for all the configurations.

6. Stacking of the best performing microchannel heat sink configuration at high heat fluxes in parallel flow and counterflow arrangements to enhance heat transfer.

7. Consideration of v-grooved rectangular microchannel heat sink for high heat flux applications.

1.6. Objectives and aims of the research

Objectives

1. Presentation of good designs of microchannel heat sink configurations for simulation and optimisation.
2. Validation of CFD code used with available experimental data in the open literature.
3. Simulation and optimisation in two-phase and single-phase flow.
4. Critical heat flux study of optimal microchannel heat sinks.
5. High heat flux study with the best performing microchannel heat sink configuration.

Aims

1. To achieve optimal configurations of microchannel heat sinks for single-phase and two-phase flow (operating below CHF) through optimisation.
2. To achieve low coolant flow rates for optimal performance at low pumping power.
3. To achieve microchannel heat sink exit base temperatures lower than the highest operating temperature between 85 °C and 90 °C for modern electronic devices.
4. To attain heat flux removal of 1200 W/cm^2 in subcooled flow boiling (two-phase flow) through optimisation.

1.7. Motivation for study

New cooling systems are required for the present and future high heat flux applications because natural and forced air convection and other cooling methods employing liquid cannot meet up with the challenges. More transistors are added to the surfaces of chips to increase the capacity of integrated circuits and more heat is generated; hence a better cooling method is highly desirable. Simulation and optimisation studies for single-phase and two-phase convective heat transfer in plain horizontal microchannels over a wide range of heat fluxes and velocities have not been considered the way they were in this study.

This study was motivated by the need for an efficient heat transfer mechanism that involves sensible heat and latent heat removal to ensure temperature uniformity across the device being cooled. With low coolant flow rates to remove huge amounts of heat, low pressure drops were

maintained in the microchannels, hence low pumping power requirements. Computational fluid dynamic (CFD) approach was used and the code was validated by reliable experimental data in the open literature. Water was used because of its high thermal conductivity, high specific heat, environmental friendliness and availability. Optimisation of different configurations of horizontal microchannels without enhancement, in two-phase flow (subcooled flow boiling) up to a high heat flux of 1200 W/cm^2 and in single-phase flow up to 200 W/cm^2 at low pumping power requirements for practical applications, is the original contribution of this research.

1.8. Thesis outline

The thesis is structured as follows:

Chapter 1 Introduction

This chapter contains general background information on cooling methods for electronic devices. Cooling methods are compared and also direction for high heat flux removal is provided. The purpose, scope, objectives and aims of the study are also provided.

Chapter 2 Literature review

The chapter is on literature review of previous studies in single-phase and two-phase flow. Different methods employed are reviewed and comparisons with similar studies are made. Thereafter, the research gaps are identified and aligned with the objectives of the research.

Chapter 3 Mathematical models and numerical methods

The governing equations, viz., continuity, momentum and energy equations together with other models are presented in this chapter. Approach used in discretisation, and finite volume method (FVM) are explained. Mesh types, solver settings are also explained. Optimisation methods used previously in single-phase flow and the dearth of same in two-phase flow are explained. Simulation and optimisation schemes used are also explained.

Chapter 4 Subcooled boiling models and correlations

This chapter features subcooled flow boiling model and correlations. Wall heat flux partitioning model for boiling of liquid at the wall of the microchannel and non-equilibrium subcooled boiling model, an extension of wall heat flux partitioning model for simulating

departure from nucleate boiling (critical heat flux) together with other supporting models are presented.

Chapter 5 Simulation and optimisation in subcooled flow boiling

Simulation and optimisation in subcooled flow boiling are presented in this chapter. The models used and steps in computational fluid dynamics are explained. The grid refinements for the designs of different configurations (circular, equilateral triangular, rectangular and square) presented for simulation and optimisation are explained. The validation of each numerical results with experimental data in single-phase and two-phase flow to show that the CFD code used is reliable is carried out. Optimisation procedure and method used for critical heat flux simulation are presented.

Chapter 6 Results and discussion

This chapter features results and discussion. This comprises discussion of results generated for various configurations of microchannel heat sinks. Comparisons of microchannel heat sinks in two-phase and single-phase flow are made. The effects of geometric and flow parameters on thermal resistance, operating temperature and pumping power are discussed. Comparisons of multichannel heat sinks of different configurations in two-phase and single-phase flow are made to assess the order of performance in terms of thermal resistance, base temperature and pumping power. High heat flux study in optimal rectangular microchannel heat sinks, two-stacked (multi-layered) and v-grooved is presented. Critical heat flux study involving all the microchannel configurations is also presented.

Chapter 7 Contributions of the study, conclusions and recommendations

Highlights of contributions of the study are detailed. Conclusions from the study and direction for further studies are given.

CHAPTER 2
LITERATURE REVIEW

2.1. Single-phase convective heat transfer in microchannels

2.1.1. Introduction

Single-phase heat transfer occurs in the microchannel if the velocity of flow is high enough to prevent change of phase. Numerical and experimental investigations had been carried out on single-phase flow by many researchers. Numerical modelling had been used to arrive at flow parameters and configurations that provided optimal heat transfer rates. However, optimisation procedure in this research provides a wide range of optimal plain microchannels that can be used for moderately high heat flux and high heat flux applications. Microchannel concept was first introduced by Tuckerman and Pease [8] and deionised water was used in single-phase. The major disadvantage of single-phase liquid cooling is that it requires either high liquid flow rates or small hydraulic diameters of the microchannels and this can lead to large pressure drops.

Water cooling is better than air cooling in microchannel heat sinks because of its high thermal properties. The simplest internal flow problem in microtube heat sink can be treated as incompressible, fully developed, steady state for a Newtonian fluid. For practical applications of microchannel heat sinks in single-phase flow, friction factor and heat transfer coefficient could also be of interest. Research works described by some researchers were on the two parameters and their possible deviations from classical theory and reasons for the deviations. Research has not shown clearly the dependence of these parameters on the channel diameter [65]-[68].

Toh et al. [69] investigated single-phase three-dimensional heat transfer phenomena inside heated microchannels. The steady laminar flow and heat transfer equations were solved using finite volume method and the numerical procedure was validated by comparing the thermal resistances from the numerical computations with the experiments of Tuckerman and Pease [8] and were found to be in close agreement. Other authors [70]-[73] had validated finite volume method approach in ANSYS Fluent for solving single-phase flow in microchannels.

Numerical study was carried out by Vinodhan and Rajan [74] for the influence of microchannel width and aspect ratio on thermal performance by considering coolant (water) velocity of 0.25-

2 m/s, aspect ratio of 2-10 and range of microchannel width between 100 and 200 μm. Appropriate microchannel width and aspect ratio were found to be 200 μm and 6 respectively as evidenced from lowest total thermal resistance and lowest non uniformity of substrate temperature at comparable power consumption among different microchannel widths and aspect ratios considered. Correlations were developed for prediction of dimensionless pumping power, Nusselt number and dimensionless total thermal resistance.

Shkarah et al. [75] described numerical simulations carried out on rectangular microchannels of different depths and widths, using silicon, aluminium and graphene as substrate materials. Water was the cooling fluid and three different heat fluxes and volumetric flow rates were considered. They presented a result that showed that graphene gave the lowest thermal resistance.

2.1.2. Heat transfer and pressure drop

Based on the continuum assumption for a Newtonian liquid flowing in a smooth circular pipe, the fluid element with length dx (Figure 2.1) can be imagined to be in equilibrium such that the force due to the pressure difference dp is balanced by the frictional force due to shear stress τ_w at the wall and can be expressed as [76]:

$$\frac{\pi}{4}.(D_h)^2.dp = (\pi.D_h.dx).\tau_w \tag{2.1}$$

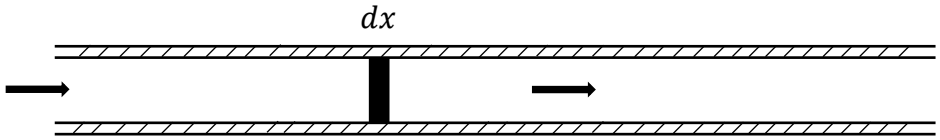

Figure 2.1. Fluid flow in a smooth circular pipe.

From Equation (2.1) the pressure gradient and wall shear stress are related as:

$$\frac{dp}{dx} = \frac{4\tau_w}{D_h} \tag{2.2}$$

The wall shear stress τ_w for Newtonian fluids, can be expressed in terms of the velocity gradient at the wall as:

$$\tau_w = \mu \frac{du}{dy}\Big|_w \tag{2.3}$$

The friction factor f is given by the following equation:

$$f = \frac{\tau_w}{(1/2)\rho u_m^2} \tag{2.4}$$

where u_m is the mean velocity of flow in the microchannel. The frictional pressure drop Δp over a length L can be obtained from Equation (2.2) and Equation (2.4) as:

$$\Delta p = \frac{2 f \rho u_m^2 L}{D_h} \tag{2.5}$$

For non-circular microchannels, hydraulic diameter D_h is defined as:

$$D_h = \frac{4 A_{ch}}{P} \tag{2.6}$$

where P is the wetted perimeter.

For a rectangular microchannel of sides a and b, D_h is given by:

$$D_h = \frac{4ab}{2(a+b)} \tag{2.7}$$

The friction factor f depends on the flow conditions and for laminar flow, it is theoretically given as:

$$f = \frac{64}{Re} \tag{2.8}$$

where the constant 64 is determined by the geometry of the microchannel cross-section. Table 2.1 shows the list of values of the constants (Poiseuille numbers) for different geometries.

Table 2.1. Characteristic values of laminar flow in circular and non-circular microchannels [76].

Microchannel cross-section	Microchannel geometry	Hydraulic diameter	Constant
Circular	diameter d	D_h	64
Rectangular	$a, b, {}^{a}/_{b} = 0.1$	$2ab/(a+b)$	85.76
Rectangular	$a, b, {}^{a}/_{b} = 0.2$	$2ab/(a+b)$	76.8
Rectangular	$a, b, {}^{a}/_{b} = 0.4$	$2ab/(a+b)$	65.28
Rectangular	$a, b, {}^{a}/_{b} = 0.6$	$2ab/(a+b)$	60.16
Rectangular	$a, b, {}^{a}/_{b} = 0.8$	$2ab/(a+b)$	57.6
Square	$Side\ a$	a	56.96

Different types of friction factor correlations are available in the literature for turbulent flow, which are generally defined by Blasius equation for smooth pipes:

$$f = 0.3164Re^{-1/4} \quad (2.9)$$

Heat transfer through a microchannel heat sink in single-phase flow can be calculated from the following equation [52]:

$$Q = \frac{Nu.k.\Delta T.A}{D_h} \quad (2.10)$$

where Nu is the Nusselt number which represents the nondimensional temperature gradient at the wall of the microchannel and it is also a measure of convective heat transfer, k is the thermal conductivity of the coolant, ΔT is the mean temperature difference between the substrate and the coolant, A is the cross-sectional area of the microchannel, D_h is the hydraulic diameter of the microchannel.

Vinodhan and Rajan [77] carried out simulations for flow and heat transfer in four quadrant microchannel heat sink configurations of overall width and length of 6.2 and 18 mm respectively, while other parameters were 400 μm and below. The designs consisted of four compartments with separate coolant inlet and outlet plenums for each compartment. The aim was to compare their performances with the modified microchannel heat sink of [78]. They reported higher Nusselt number, higher heat transfer rates and lower thermal resistances in the new designs compared to the modified channel. Despite their report of improved performance, they suggested optimisation of the new designs for better performances. Numerical simulations were carried out by Sahar et al. [73] to investigate single-phase flow pressure and heat transfer in single and multiple copper rectangular microchannels. Their study showed that multichannel configuration with an inlet manifold consisting of gradual decrease in cross sectional area achieved better uniform flow distribution among the microchannels which could provide uniform heat transfer rates across the base of the microchannel heat sink.

Modelling approaches for the analysis of convective heat transfer in microchannels were provided by Liu and Garimella [79]. A detailed computational fluid dynamics model was first used to obtain baseline results against which five approximate analytical approaches were compared. The approaches were: 1-D resistance model, a fin approach, two fin-liquid coupled models and a porous medium approach. A modified thermal boundary condition was proposed to correctly characterise the heat flux distribution. Results presented showed that models developed were accurate for practical designs while noting that optimisation should take into account inlet/outlet headers and that a prescribed pumping power may be used as the design constraint instead of pressure head. Upadhye and Kandlikar [80] presented results for direct

cooling of an electronic chip of 25 mm x 25 mm in size as a function of channel geometry for single-phase flow of water through small hydraulic diameters. They considered laminar flow with both constant wall temperature and constant channel wall heat flux boundary conditions. Their results indicated improvement in heat transfer performance for a given pressure drop constraint if the channel is narrow and deep. Bejan and Lorente [81] and Bejan [82] presented exhaustive constructal design (applying the constructal design method to several heat transfer systems) of heat transfer systems based on the structure and shape generation in freely morphing convective systems. Elemental passage geometries were considered in their designs and the best passage size and configuration for a fixed volume under convection cooling were determined. Knight et al. [83] developed equations governing fluid dynamics and combined conduction/convection heat transfer in a heat sink in dimensionless form for both laminar and turbulent flow. When compared to previous investigators, using the same microchannel heat sinks, their results indicated that when pressure drop through the channels was small, laminar solutions yielded lower thermal resistance than turbulent solutions whereas when the pressure drop was large, the optimal thermal resistance was discovered in the turbulent region. Their results showed improvement of design thermal resistance from 10 to 35%. Lee et al. [84] carried out experimental investigation to explore the validity of classical correlations based on conventional size channels for predicting the thermal behaviour in single-phase flow through rectangular microchannels. The width of the microchannels considered ranged between 194 and 534 μm with the channel depth being nominally five times the width in each case. Numerical predictions agreed with experimental results with an average of 5% deviation. Forced convective heat transfer in microchannel heat sinks for electronic system cooling was analysed by Chen [85]. Systematic study on the effects of major parameters on the flow and heat transfer characteristics of forced convection in microchannel heat sink was performed with the outcome that fluid inertia force altered noticeably the dimensionless velocity distribution and the fluid temperature distribution while the solid temperature distribution was almost insensitive to the fluid inertia. Pressure drop and volumetric discharge affect pumping power requirements in microchannels. Information on volumetric discharge for selected single-phase flow was presented by Laser and Santiago [86].

Friction factors in laminar flow could be lower while turbulent flow heat transfer coefficients could be higher than expected for larger diameter channels. Friction coefficient could be dependent on Reynolds number. Some authors believed that transition from laminar to

transition and turbulent flow starts at Reynolds number than expected for larger hydraulic diameters and that the critical Reynolds number decreases with decreasing hydraulic diameter [87], [88].

2.2. Two-phase convective heat transfer in microchannels

2.2.1. Introduction

Subcooled flow boiling occurs in the microchannel when the temperature of the bulk fluid remains below the saturation temperature and the inner wall temperature of the microchannel is above saturation for nucleation of bubbles. In saturated flow boiling, the temperature of the bulk fluid reaches saturation temperature. Pool boiling occurs over a heated surface under natural convection while flow boiling occurs over a heated surface with the aid of a pump. Two-phase flow can be adiabatic when no heat is added, for example the flow of air and water in the microchannel without heat transfer. It can be diabatic when heat is added to the flow; for example, the flow of water in the microchannel which involves phase change (water to water vapour).

Miniaturisation of microelectronic devices has led to rapid escalation in heat dissipation, it is therefore necessary to design a thermal solution that will meet this need. For a heat flux applied to the bottom of the microchannel heat sink and relatively high coolant flow rate, the coolant can maintain its single-phase state throughout in the microchannel which leads to a single-phase microchannel heat sink. Boiling point may be reached when coolant flow rate is relatively low, while still flowing in the microchannel and flow boiling occurs which results in a two-phase microchannel heat sink [89]. Bubble formation is initiated when the temperature of the heated surface exceeds the saturation temperature of the liquid.

Two-phase cooling involves vaporisation of liquid at the heated wall of the microchannel and condensation of vapour in another section (bulk fluid) of the microchannel, leading to high heat flux removal from the microstructure (electronic device) being cooled. As a result of the need to remove high heat fluxes from these microstructures, there is a growing interest to replace single-phase thermal solutions with two-phase cooling in microchannel heat sinks. Such applications that require phase change cooling with microchannel heat sinks include: computer electronics and data centres, medical X-ray equipment, fusion reactor blankets, hybrid vehicle power electronics and heat exchangers for hydrogen storage in automobiles, particle accelerator targets, magneto hydrodynamic generator electrode walls, defence radars, rocket

engine nozzles and both laser and microwave directed energy weapons [90], [91]. Experimental and computational methods have been applied successfully to two phase flow in microchannel heat sinks, but not without the problem of instability, critical heat flux (CHF) and dryout.

There are limitations to empirical correlations and theoretical models, hence interest in the use of computational fluid dynamics (CFD) simulations to predict phase change processes has developed [92]. Computational fluid dynamics technique possesses the ability to predict fluid flow and heat transfer together with spatial and temporal distributions of phase velocities and temperatures, and void fractions in detail. It could also help to better interpret the available experimental data and also explain the underlying physics [73], [93].

An embedded novel two-phase thermal management method that incorporates perforated walls was proposed and analysed by Warrier et al. [94] as a potential use for high heat flux semiconductor devices. Studies had also been conducted on fractal tree-like microchannels for improved performance over straight microchannels [95]-[99].

Correlations developed for conventional sized channels can be used for single-phase flow in microchannels, however microchannel flow boiling is significantly affected by the confinement of bubbles [100]-[102]. Over a wide range of operating parameters, existing heat transfer correlations cannot accurately predict the flow boiling heat transfer coefficient in small channels [103]-[105]. Berstch et al. [106] developed a composite correlation for saturated flow boiling in small channels with mean absolute error of less than 30% from fourteen experimental studies in the literature, covering wetting and non-wetting fluids. They reported that the model included nucleate boiling and convective heat transfer terms while accounting for the effect of bubble confinement in small channels.

2.2.2. Subcooled flow boiling

In subcooled flow boiling, nucleation of bubbles takes place on the heated microchannel wall surface while the surrounding liquid is at a subcooled condition (lower than the saturation temperature of the liquid). Cooling of liquid with microchannel heat sinks can be found in many applications such as electronic chip cooling. The important thermal advantage of microchannel cooling is the ability to dissipate fairly high heat fluxes while maintaining relatively low device temperatures. Cooling of electronic and power devices can be achieved by supplying the coolants to the microchannels in subcooled condition. Compared to single-

phase cooling, the latent heat absorbed by the coolant during the evaporation process increases heat transfer coefficients for higher heat fluxes and more uniform temperatures. A high heat flux can be removed with a relatively low wall superheat during subcooled flow boiling [21], [90], [107]-[109].

Nucleate heat transfer (subcooled boiling) can occur at the wall of the microchannel when it is in contact with fluid whose temperature is below its saturation temperature. High heat transfer rates and low wall temperatures are achievable under highly subcooled conditions. Subcooled boiling comprises the formation of bubbles, their interaction with each other and the surrounding fluid and their detachment from the wall. Vapour bubbles are generated when the degree of superheat required for nucleation is satisfied at the wall of the microchannel [110]. Some of these vapour bubbles condense in the bulk liquid whose temperature is below saturation. Heat transfer mechanism for subcooled boiling is different from that of saturated boiling because of large differences in void fraction. Phase change in subcooled boiling occurs mostly by bubble formation at the wall of microchannel while in saturated boiling, bubble nucleation is gradually replaced by evaporation of a residual liquid film at the heated wall [111], [112]. When flow boiling occurs inside the microchannel, bubble formation takes place if the inner wall temperature of the channel is above the local saturation temperature of the liquid. Flow pattern transition could be caused by the rate of bubble formation [113], [114]. Numerical and experimental studies were performed by Mukherjee et al. [115] to analyse wall heat transfer mechanisms during growth of a vapour bubble inside a 200 μm square microchannel with the conclusion that the bubble growth rate and shapes showed good agreement between the numerical and experimental results while Sadaghiani and Kosar [116] showed the effects of diameter and heated length on high mass and heat fluxes in subcooled flow boiling in horizontal microtubes. Numerical and experimental studies were carried out and the coolant was deionised water while the heat sink material was stainless steel. Eulerian multiphase model in ANSYS was used for the numerical simulations. Geometric parameters were inner diameters, 600 and 900 μm; outer diameters, 900 and 1100 μm and heated lengths, 6 and 12 cm respectively. Their results showed improvement in boiling heat transfer as the mass flux increased which implied convective heat transfer effects on flow boiling along with nucleate boiling. The numerical and experimental results showed good agreement.

Fukuda et al. [117] carried out numerical simulation of subcooled nucleate boiling in a duct by employing wall heat flux partitioning (RPI) model and other models to study the mean and

fluctuating velocity components over the heated section of the channel. Wall heat flux partitioning (RPI) model and its extension had been employed by various authors [118]-[120] in their studies.

2.2.3. Flow boiling instabilities

Different types of instabilities may occur during two-phase flow in microchannels. Kakac and Bon [121] and Boure et al. [122] identified two types of instabilities as static and dynamic. When the existing state of equilibrium tends to a new different state after disturbance, it is called static instability. The following static instabilities were identified: Ledinegg instability, boiling crisis, flow pattern transition instability, bumping, geysering and chugging. Ledinegg instability occurs when channel demand pressure drop versus flow rate curve (internal characteristics curve) has a negative slope and it is steeper than the slope of liquid supply system curve (external characteristics curve) with multiple intersections of internal and external curves; it is also a manifestation of sudden drop in flow rate [121]. When heat supplied to the system cannot be absorbed by two-phase flow in the microchannel, boiling crisis occurs. Flow pattern transition instability is connected with oscillations between bubbly and annular flow regimes. Bumping, geysering and chugging are associated with the process of violent liquid evaporation. When the disturbed flow cannot reach a new equilibrium point because of complex mechanism of multiple feedbacks occurring in the system (for example, from multiple feedbacks between flow rate, pressure drop and change in density as a result of the rate of vapour generation) this signifies the occurrence of dynamic instabilities. There are four distinguishable dynamic instabilities:

- Density wave oscillations
- Pressure drop oscillations
- Acoustic oscillations
- Thermal oscillations

Density wave oscillations have low frequency and large amplitudes and are as a result of multiple feedbacks between mass flow rate, vapour generation and pressure drop in the channel. Pressure drop oscillations are connected with the existence of compressible volume in the system which amplifies the interaction between microchannel and liquid supply system. Formation of acoustic oscillations is related to the speed of pressure waves in the system which

causes high frequency oscillations. Thermal oscillations of heating surface temperature are connected with transitions between different boiling regimes [121], [123].

Instabilities may occur when two fluids are in contact through an interface due to inertia, shear and capillary. In two phase flow and heat transfer, instabilities occur under flow conditions. Concerns about flow boiling in mini and micro channels relating to increased effects of surface tension forces, reverse flow arising from nucleation followed by rapid bubble growth and deterioration in heat transfer and critical heat flux due to flow instabilities were raised by Kandlikar [9]. A two-phase flow is stable if for any applied disturbance, the new operating conditions tend to the initial conditions and unstable if for any disturbance, a jump from one state to another is observed [124]. Kuo and Peles [125] studied the effects of pressure on flow boiling instabilities such as excursive and parallel channel instability, compressible volume/pressure drop instability, rapid bubble growth and critical heat flux (CHF) conditions in five parallel microchannels experimentally by employing water as coolant. They varied pressure from 50 to 205 kPa and observed that pressure significantly affected flow instabilities. It was observed that at a high pressure, boiling instabilities were significantly delayed with CHF being extended to high mass qualities, and local temperature measurements also revealed lower magnitudes and higher frequencies of oscillations at high system pressures. Hetsroni et al [126], [127] investigated different flow patterns and instabilities in parallel triangular microchannels in connection with flow and heat flux. Bubble nucleation, bubble size and the velocity of bubble motion were also investigated.

2.2.4. Flow boiling heat transfer and pressure drop

Frictional and heat transfer characteristics for microchannel heat sinks are not quite the same as those for conventional channels under specific flow conditions and flow regimes. A methodology for optimising the design of a two-phase microchannel heat sink was proposed by [89], [102], [128]. They grouped the heat sink parameters into geometrical and operating and thermal/fluid parameters. The objective of the proposed methodology was to optimise microchannel dimensions in pursuit of acceptable values for the thermal/fluid parameters corresponding to a given heat flux, coolant and overall dimensions of the heat generating device to which the heat sink was attached. It was assumed that boiling could take place at the exit of the channel. Kelkar et al. [129] presented a computational method for the analysis of conjugate heat transfer and two-phase flow in a heat sink containing multiple microchannels with prescribed flow rates. It involved coupled analysis of conduction within the solid and

simultaneous two-phase flow and heat transfer in the microchannels. The flow and thermal behaviour in each microchannel were determined by solving one-dimensional momentum and energy conservation equations. Coupling between heat transfer within the solid region and the two-phase flow in the microchannels was handled through iterations involving transfer of heat flux distribution on the channel boundary surfaces.

A heat transfer model for elongated bubbles in a microchannel was developed by Jacobi and Thome [130]. It was assumed that thin film evaporation into elongated bubbles was the dominant heat transfer mechanism of flow in microchannels and effective nucleation superheat and initial film thickness were required by the model. Heat transfer coefficient dependence on heat flux was found to be low at small heat fluxes but large at high heat fluxes. Heat transfer coefficient was predicted to be insensitive to mass flux by the model.

Mukherjee and Kandlikar [93] studied numerically using SIMPLER (semi-implicit method for pressure-linked equations revised), the growth of vapour bubble during flow boiling of water in a square microchannel to obtain the flow and thermal fields around a growing vapour bubble inside the microchannel. The behaviour of liquid-vapour interface and its interaction with the constraining wall were studied and the effects of inlet liquid superheat, Reynolds number and gravity on bubble growth rate were determined. Peng et al. [131] analysed the thermodynamic aspects of phase transformations of liquids in microchannels to further understand the boiling characteristics and to determine the conditions under which a portion of such liquids was likely to undergo phase change. They derived theoretically, a non-dimensional parameter and related criteria that determine the phase transition in microchannels. They noted that the size of the microchannels resulted in dramatically high heat fluxes and superheats for liquid nucleation when the microchannel was sufficiently small and the fluid thermal properties were also expected to have significant influence on the active cavity and bubble sizes. It was also found that high heat fluxes were required to initiate nucleation for water in microchannels.

Bowers and Mudawar [132]-[134] presented a comprehensive thermal design methodology for two-phase microchannel heat sinks which employed refrigerant coolants. A pressure drop model incorporating homogeneous equilibrium model to describe the two-phase region was constructed. The predictions of the models were in good agreement with experimental results for R-113 in both minichannel and microchannel heat sinks considered. Challenges in predicting the performance of such heat sinks were compressibility, flashing and choking.

These effects could be as a result of large axial property variations brought about by the relatively large microchannel pressure drop. Bergles and Dormer [135] studied flow boiling in small tubes (minichannels) with less than 3 mm diameter. Pressure drops associated with flow boiling of water in horizontal tubes of length to diameter ratio of 24 to 195 and 1.57 to 5.03 mm diameters were investigated. They varied the liquid velocity, inlet temperature and wall heat fluxes to: 1.51 to 18.2 m/s, 10 to 62.7 °C and 0 to 1733.6 W/cm^2 respectively. They reported that for a given inlet velocity and temperature, pressure drop increased rapidly once boiling was well established. Circular channels of diameter 0.51 mm and 2.54 mm were studied with R113 as coolant. Qu and Mudawar [128] reported that two types of dynamic instabilities were identified in their study of two-phase transport phenomena. These were: severe pressure drop oscillation and mild parallel channel instability and a simple method was recommended to completely suppress the severe pressure drop. They recommended further study on boiling behaviour and new predictive tools specifically tailored to microchannel heat sinks. From the review of literature carried out by Harirchian and Garimella [136], it was discovered that only a few studies had put effort into the modelling of flow boiling based on the existing flow regimes and taking into account the interfacial structure between the liquid and vapour phases.

Kelkar et al. [129] and Sarangi et al. [137] derived homogeneous flow model from momentum equation. Attributes of homogeneous flow model include the assumption that both liquid and vapour are a single mixture of fluid. The velocity and density of the mixture are considered to be constant across the channel.

Lee and Mudawar [138] developed a multi-phase model for the flow of R134a in a microchannel heat sink that served as an evaporator and it was shown to be in agreement with R134a data as well as previous microchannel data for water. Galvis and Culham [139] had shown that slug flow was the most observed pattern to occur in the two-phase flow region.

2.2.5. Critical heat flux (CHF)

Critical heat flux (burnout, dryout, departure from nucleate boiling and boiling crisis) represents the upper thermal limit for the safe operation of any boiling device [17], [140], [141]. The safe limit of operation of minichannels and microchannels can be determined by CHF (departure from nucleate boiling) in subcooled flow boiling. Disappearance of liquid from the surface of the microchannel can create departure from nucleate boiling and this leads to deterioration of heat flux removal and rapid increase in microchannel wall surface temperature.

The most important parameters that could affect CHF are: fluid properties, velocity or mass velocity, inlet subcooling and channel to diameter ratio. Critical heat flux is an important design parameter for flow boiling in microchannel heat sinks. Its determination is crucial in electronics cooling for the safe operation of high-performance microprocessors. Exceeding CHF indicates that the heated microchannel wall is completely covered by vapour and this is associated with rapid and sharp increase in the wall surface temperature which can lead to the destruction of the heat sink and the device being cooled. In subcooled flow boiling, this disappearance of liquid from the surface of the microchannel creates departure from nucleate boiling. The surface heat transfer coefficient drops drastically because the thermal conductivity of water vapour is lower than that of water. The drop in heat transfer coefficient results in sudden increase in microchannel surface temperature and thermal failure of the device being cooled. Critical heat flux occurs where the last stable temperature is obtained before large increases in temperature [7], [108], [140]-[142]. In subcooled flow boiling, substantial wall heat fluxes can be absorbed while at the same time the bulk liquid temperature remains below saturation. The vapour bubbles grow and detach rapidly and then condense after moving from the superheated near wall region (thermal boundary layer) to the cold bulk liquid [143]-[145]. Bubbly flow can persist over a substantial part of the microchannel length in a highly subcooled flow boiling and when bubbles near the wall coalesce into a localised vapour blanket, a sharp reduction in the local heat transfer coefficient occurs leading to CHF situation (subcooled flow boiling). The CHF in this case is known as departure from nucleate boiling (DNB) and occurs with high inlet subcoolings, high mass velocities and small length to diameter ratios. The surface temperature rise could be high [108], [146]. Flow regimes succession could be initiated because of large increases in void fraction in saturated flow boiling and the flow eventually culminates in high void fraction annular flow pattern where cooling is sustained by evaporation of a thin liquid along the surface of the microchannel. CHF can be classified as subcooled CHF or saturated CHF depending on whether the bulk fluid at microchannel outlet is subcooled or saturated. It can occur as a result of dryout of the liquid film (saturated flow boiling) because the surface is exposed directly to the vapour. Dryout occurs with low inlet subcoolings, low mass velocities and large length to diameter ratios [108], [146]. Figure 2.2 (a) and Figure 2.2(b) show the mechanisms for the two types of critical heat flux situations in a uniformly heated microchannel heat sink.

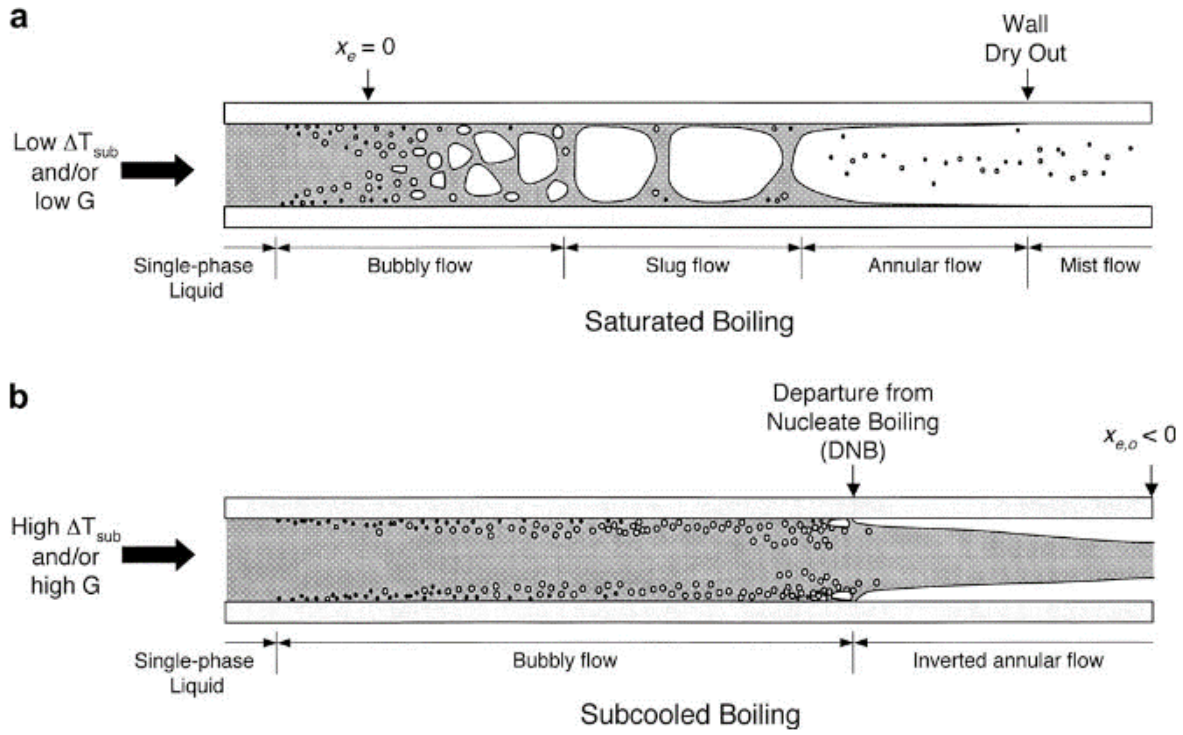

Figure 2.2. CHF mechanisms for flow boiling in a uniformly heated channel [108].
(a) dryout in saturated flow boiling (b) DNB in subcooled flow boiling

Bergles and Kandlikar [142] presented a study on the nature of critical heat flux in microchannels and concluded that CHF would be higher if the flow was stabilised by an orifice at the entrance of each channel. Correlations for the prediction of CHF in microchannels were developed by [128], [147] using their experimental data. The respective experimental observations and correlations were in good agreement; however, when the correlations were applied to other experimental data, deviations were observed. Critical heat flux is a limiting factor in flow boiling systems because it imposes an upper limit on the heat flux applied to the microchannel surface. Kosar [148] developed a model to predict saturated critical heat flux conditions in minichannels and microchannels. The model was compared to 151 experimental data points obtained from CHF studies on minichannels and microchannels encompassing various working fluids such as water, R123, R113, R134a, and R245fa over a broad range of mass velocities (ϕ) of 50-1600kg/m^{2}s and pressures of 101-888 kPa. A strong correlation was observed between the model and experimental data with an overall mean absolute error between 21.3 and 25.8%.

2.3. Classification of microchannels

Based on dimensional criterion, Mehendale et al. [149] used hydraulic diameter to classify microchannel heat sinks as follows:

Micro heat exchanger	$1\ \mu m \leq D_h \leq 100\ \mu m$
Meso heat exchanger	$100\ \mu m \leq D_h \leq 1\ mm$
Compact heat exchanger	$1\ mm \leq D_h \leq 6\ mm$
Conventional heat exchanger	$D_h > 6\ mm$

Kandlikar [150] and Kandlikar and Grande [151] proposed a microchannel classification for single-phase as well as two-phase flow applications based on dimensional criterion as follows:

Conventional channels	$D_h > 3\ mm$
Minichannels	$3\ mm \geq D_h > 200\ \mu m$
Microchannels	$200\ \mu m \geq D_h > 10\ \mu m$
Transitional microchannels	$10\ \mu m \geq D_h > 1\ \mu m$
Transitional Nanochannels	$1\ \mu m \geq D_h > 0.1\ \mu m$
Nanochannels	$D_h \leq 0.1 \mu m$

Based on confinement number (Co) approach, Kew and Cornwell [152] suggested bubble confinement criterion for macro to micro scale transition as

$$Co = \left[\frac{\sigma}{g(\rho_l - \rho_g)D_h^2}\right]^{1/2} \tag{2.11}$$

Subscripts l and g denote liquid and gas respectively. The heat transfer and flow characteristics of microchannel flow boiling were found to be significantly different from those of macrochannel for $Co > 0.5$.

The influence of surface tension is more than that of gravity in the microscale because stratified flow does not exist if the hydraulic diameter is sufficiently small. The bond number (Bo) is the ratio of buoyancy force to surface tension force and it is expressed as

$$Bo = \frac{g(\rho_l - \rho_g)D_h^2}{\sigma} \tag{2.12}$$

Based on the experimental studies of [152], macro to microscale threshold diameter occurs at $Bo = 4$. Values below 4 are in the microscale region.

Kawaji and Chung [153] came up with a criterion for two-phase microchannel flow which is based on a set of six dimensionless numbers namely: Bond number (Bo), superficial liquid (sl) and vapour or gas (sg) Reynolds numbers (Re), superficial liquid and vapour Weber numbers (We) and Capillary number (Ca). The numbers are as follows:

$$Bo = \frac{g(\rho_l - \rho_g)D_h^2}{\sigma} \ll 4 \quad (2.13)$$

$$Re_{sl} = \frac{\rho_l U_l D_h}{\mu_l} < 2000 \quad (2.14)$$

$$Re_{sg} = \frac{\rho_g U_g D_h}{\mu_g} < 2000 \quad (2.15)$$

$$We_{sl} = \frac{\rho_l U_l^2 D_h}{\sigma} \ll 1 \quad (2.16)$$

$$We_{sg} = \frac{\rho_g U_g^2 D_h}{\sigma} \ll 1 \quad (2.17)$$

$$Ca_l = \frac{\mu_l U_l}{\sigma} \ll 1 \quad (2.18)$$

The liquid and gas velocities are defined as:

$$U_l = \frac{\dot{V}_l}{A} \quad (2.19)$$

$$U_g = \frac{\dot{V}_g}{A} \quad (2.20)$$

Equation (2.13) which is based on [152] is applied after which the other five criteria are applied to further refine the microscale threshold analysis.

At present, there is no general agreement among researchers on the classification of microchannels. For example, in the experiment of Qu and Mudawar [154], the hydraulic diameter of the microchannel used was 348.95 μm. Other examples include Liu and Garimella [155], hydraulic diameters of 383.97 and 587.58 μm, and Agostini et al. [32], hydraulic diameter of 335.86 μm. In this study hydraulic diameters of microchannels were generally below 400 μm.

2.4. Research gaps

The review of available literature revealed the following gaps:

- Geometric and numerical optimisation for two-phase (subcooled flow boiling) and single-phase flow in plain wall microchannel heat sinks are not robust to give a wide range of optimal microchannel heat sinks applicable over a wide range of high heat fluxes and velocities

- Keeping thermal resistances, pressure drops, microchannel heat sinks maximum outlet base temperatures to acceptable levels while enhancing high heat flux dissipation
- Analyses with different configurations of microchannels (circular, equilateral triangular, rectangular and square) in two-phase and single-phase flow
- Multi-stacking of optimal microchannel heat sinks especially in two-phase flow (parallel flow and counterflow arrangements)
- Computation of critical heat fluxes for the optimal microchannel heat sinks at optimal velocities
- Heat fluxes up to 1200 W/cm^2 were not studied before in comparable geometries at relatively low velocities and pressure drops
- Relatively low micropump capacities over a wide range of thermal resistances for two-phase and single-phase flow in optimal microchannel heat sinks

In this study, Eulerian multiphase model in conjunction with wall heat flux partitioning (RPI) model in ANSYS code was used for the simulations of subcooled flow boiling heat transfer in circular, equilateral triangular, rectangular and square microchannel heat sinks and the code was validated by the available experimental data in the literature. The geometric and flow parameters were optimised using response surface optimisation, which is a goal driven optimisation, in ANSYS 18.1 design exploration and analysis [156].

In the optimisation procedure, a fixed volume constraint was applied to each of the microchannel heat sinks to obtain global optima with respect to microchannel hydraulic diameter, axial flow length and Bejan number for single-phase and subcooled (two-phase) regimes.

Critical heat fluxes for the optimal microchannel heat sinks at selected optimal velocities were computed using a non-equilibrium boiling model of wall heat flux partitioning (RPI) model in ANSYS 18.1 code [62], [63]. The aim was to demonstrate that the optimal microchannel heat sinks can be used beyond their optimal heat fluxes before the onset of their critical heat fluxes.

CHAPTER 3
MATHEMATICAL MODELS AND NUMERICAL METHODS

3.1. Introduction

The equations that govern fluid flow and heat transfer in microchannels are called governing equations. The continuity equation expresses the conservation of mass. The conservation of momentum equation is derived from Newton's second law of motion; the momentum of a system is conserved when the net force acting on it is zero and this is the conservation of momentum principle. The law of conservation of energy is expressed as the energy equation. It is derived from the first law of thermodynamics which states that the rate of change of energy of a fluid particle is equal to the rate of heat addition to the fluid particle plus the rate of work done on the particle. In order to compute the geometric and flow parameters accurately, a three-dimensional numerical analysis was used.

Heat is supplied to the aluminium substrate from a heating area located at the bottom of the heat sink. The heat is then removed by the fluid flowing through a number of microchannels as shown in the example in Figure 3.1(a). Using the advantage of symmetry, a unit cell consisting of a microchannel and the surrounding solid can be chosen for the analysis. The computational domain for a microchannel heat sink is shown in Figure 3.1(b).

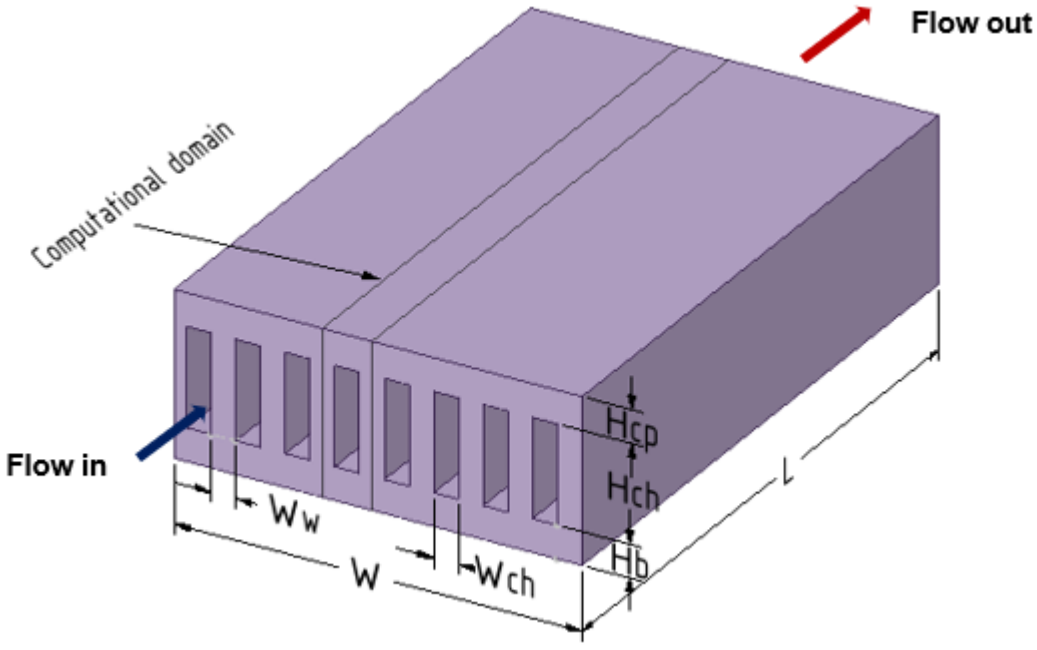

(a) Microchannel heat sink

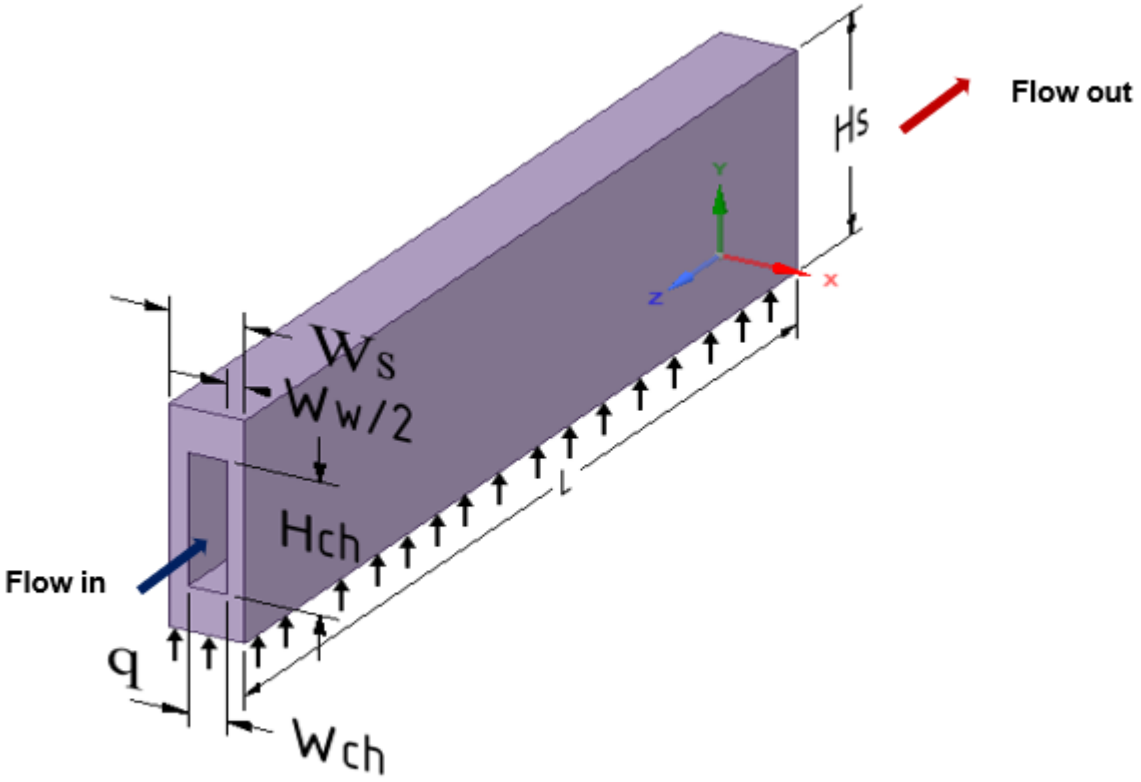

(b) Unit cell microchannel heat sink

Figure 3.1. Microchannel heat sink and a unit cell computational domain.

3.2. Mathematical models

3.2.1. Conservative equations

3.2.1.1. Single-phase flow

The fluid enters the microchannel in single-phase and exits at a relatively high temperature without change of phase. The flow is assumed to be fully developed with Reynolds number below 2000. Steady state conditions for the flow and heat transfer are assumed. Ignoring gravitational force, compressibility of the fluid and viscous dissipation heat, the continuity, momentum and energy equations for single-phase fluid flow in the microchannel can be expressed as:

Continuity equation

$$\frac{\partial u}{\partial x}+\frac{\partial v}{dy}+\frac{\partial w}{dz}=0 \tag{3.1}$$

Momentum equations

$$\rho\left(u\frac{\partial u}{\partial x}+v\frac{\partial u}{\partial y}+w\frac{\partial u}{\partial z}\right)=-\frac{\partial p}{\partial x}+\mu\nabla^2 u \quad (3.2)$$

$$\rho\left(u\frac{\partial v}{\partial x}+v\frac{\partial v}{\partial y}+w\frac{\partial v}{\partial z}\right)=-\frac{\partial p}{\partial y}+\mu\nabla^2 v \quad (3.3)$$

$$\rho\left(u\frac{\partial w}{\partial x}+v\frac{\partial w}{\partial y}+w\frac{\partial w}{\partial z}\right)=-\frac{\partial p}{\partial z}+\mu\nabla^2 w \quad (3.4)$$

Energy equation

$$\rho C_p\left(u\frac{\partial T}{\partial x}+v\frac{\partial T}{\partial y}+w\frac{\partial T}{\partial z}\right)=k\nabla^2 T \quad (3.5)$$

The energy equation for the solid regions can be written as:

$$k_s\nabla^2 T=0 \quad (3.6)$$

$$\nabla^2=\frac{\partial^2}{\partial x^2}+\frac{\partial^2}{\partial y^2}+\frac{\partial^2}{\partial z^2} \quad (3.7)$$

The origin of the Cartesian frame (x, y, z) is located as shown in Figure 3.1(b).

3.2.1.2. Two-phase flow

Many flow situations encountered in engineering and technology are a mixture of phases. These flow situations may be classified as [62], [63]:

1. Gas-liquid or liquid-liquid (bubbly flow, droplet flow, slug flow, stratified/free surface flow)

2. Gas-solid (particle-laden flow, pneumatic transport, fluidised bed)

3. Liquid-solid (slurry flow, Hydro transport, sedimentation)

4. Three-phase (this is a combination of any of other flow regimes above)

Two-phase flow in this work falls under category 1. The coolant enters the microchannel as liquid and bubble formation commences at the onset of nucleate boiling. The nucleation of bubbles, detachment from the wall of the microchannel and condensation in the bulk fluid flow continue until the coolant exits the microchannel. The different phases (liquid and vapour) are treated mathematically as interpenetrating continua (volume occupied by each phase is given by the volume fraction). Three different Euler-Euler multiphase models are available in ANSYS Fluent: Eulerian, volume of fluid (VOF) and mixture multiphase models. The Eulerian multiphase model is the most complex among the three models because it solves a set of N continuity, momentum and energy equations for each phase and coupling is achieved through pressure and interphase exchange coefficients whereas for other models, a single set of each

governing equation is solved for the fluids. The VOF model is used where the position of the interface between the fluids is of interest. It is a surface tracking technique which can be applied to a fixed Eulerian mesh. A single set of momentum equation is shared by the fluids (single-fluid approach) and their volume fractions in each of the computational cell is tracked throughout the domain. For heat and mass transfer studies, the heat transfer correlations and the source terms of the conservation equations are normally added through user defined functions (UDF). The mixture model is designed for two or more phases just like Eulerian model, but it uses single-fluid approach. Using separate sets of equations for the phases could lead to more accurate results. Owing to the nature of this study, Eulerian multiphase model was chosen and it is also recommended by ANSYS for bubbly flow. Accuracy was deemed more important than the computational time; also, the dispersed phase (vapour bubbles) was concentrated just in portions of the flow domain (microchannel wall) before detaching and condensing in the bulk liquid. Subcooled boiling is mostly in the bubbly flow regime. The bubble formation was concentrated at the bottom wall of the microchannel where heat was applied. There are many sub-models in Eulerian multiphase model and the initial task was to combine the right models to be able to achieve the desired results. This was achieved after several trials.

The Eulerian multiphase flow model in conjunction with wall heat flux partitioning (RPI) model was used to simulate the subcooled flow. It allows for the modelling of multiple separate, yet interacting phases (liquids, gases and solids) in nearly any combinations. A single pressure is shared by all phases and continuity, momentum and energy equations are solved for each phase. The conservation equations of mass, momentum and energy for each phase are [62],[63]:

Continuity equation

The general form of continuity equation for phase i is

$$\frac{\partial}{\partial t}(\alpha_i \rho_i) + \nabla.(\alpha_i \rho_i \vec{v}_i) = \sum_{j=1}^{n}(\dot{m}_{ji} - \dot{m}_{ij}) + S_i \quad (3.8)$$

The mass conservation equation can be expressed for liquid water (l) and water vapour (v) as follows:

Liquid

$$\frac{\partial}{\partial t}(\alpha_l \rho_l) + \nabla.(\alpha_l \rho_l \vec{v}_l) = (\dot{m}_{vl} - \dot{m}_{lv}) + S_l \tag{3.9}$$

Vapour

$$\frac{\partial}{\partial t}(\alpha_v \rho_v) + \nabla.(\alpha_v \rho_v \vec{v}_v) = (\dot{m}_{lv} - \dot{m}_{vl}) + S_v \tag{3.10}$$

$$\alpha_l + \alpha_v = 1 \tag{3.11}$$

where $\vec{v}_l$ represents the velocity of the liquid phase and $\vec{v}_v$ is the velocity of the vapour phase; $\dot{m}_{lv}$ characterises the mass transfer from the liquid to vapour phase while $\dot{m}_{vl}$ represents the mass transfer from vapour phase to liquid phase. S_l is the source term for liquid phase and S_v is the source term for vapour phase. The liquid water is the primary phase (continuous phase) while water vapour is the secondary phase (dispersed phase).

Momentum equation

The momentum balance for phase i can be written as

$$\frac{\partial}{\partial t}(\alpha_i \rho_i \vec{v}_i) + \nabla.(\alpha_i \rho_i \vec{v}_i \vec{v}_i) = -\alpha_i \nabla p + \nabla.\bar{\bar{\tau}}_i + \alpha_i \rho_i \vec{g} + \sum_{i=1}^{n}(\vec{R}_{ji} + \dot{m}_{ji}\vec{v}_{ji} - \dot{m}_{ij}\vec{v}_{ij}) + \vec{F}_i + \vec{F}_{lift,i} + \vec{F}_{wl,i} + \vec{F}_{vm,i} + \vec{F}_{td,i} + \vec{F}_{d,i} \tag{3.12}$$

where volume fraction, density, velocity, pressure and stress-strain tensor for phase i are denoted by α_i, $\rho_i, \vec{v}_i$, p_i, $\bar{\bar{\tau}}_i$, respectively. $\vec{F}_i$, $\vec{F}_{lift,i}, \vec{F}_{wl,i}, \vec{F}_{vm,i}, \vec{F}_{td,i}$, $and\ \vec{F}_{d,i}$ are: external body force, lift force, wall lubrication force, virtual mass force, turbulence dispersion force and drag force respectively. The stress-strain tensor $\bar{\bar{\tau}}_i$ for the i^{th} phase can be written as

$$\bar{\bar{\tau}}_i = \alpha_i \mu_i (\nabla \vec{v}_i + \nabla \vec{v}_i^T) + \alpha_i \left(\lambda_i - \frac{2}{3}\mu_i\right) \nabla.\vec{v}_i \bar{\bar{I}} \tag{3.13}$$

where μ_i and λ_i are the shear and bulk viscosities of phase i, $\bar{\bar{I}}$ is a unit tensor.

Pressure p is shared by the two phases (liquid water and water vapour) and $\vec{R}_{ji}$ is an interaction force between the phases. $\vec{R}_{ji}$ depends on pressure, friction, cohesion and other effects such that

$$\vec{R}_{ij} = -\vec{R}_{ji} \tag{3.14}$$

and

$$\vec{R}_{ii} = \vec{R}_{jj} = 0 \tag{3.15}$$

The interaction force, $\vec{R}_{ji}$ can be defined as

$$\vec{R}_{ji} = K_{ji}(\vec{v}_j - \vec{v}_i) \tag{3.16}$$

where $K_{ij} = K_{ji}$ denotes interphase momentum exchange coefficient, $\vec{v}_i$ and $\vec{v}_j$ are the phase velocities.

Substituting for $\vec{R}_{ji}$ in Equation (3.12), the **momentum equations** can be written as

Liquid

$$\frac{\partial}{\partial t}(\alpha_l \rho_l \vec{v}_l) + \nabla.(\alpha_l \rho_l \vec{v}_l \vec{v}_l) = -\alpha_l \nabla p + \nabla.\bar{\bar{\tau}}_l + \alpha_l \rho_l \vec{g} + K_{vl}(\vec{v}_v - \vec{v}_l) + \dot{m}_{vl}\vec{v}_{vl} - \dot{m}_{lv}\vec{v}_{lv}$$
$$+\vec{F}_l + \vec{F}_{lift,l} + \vec{F}_{wl,l} + \vec{F}_{vm,l} + \vec{F}_{td,l} + \vec{F}_{d,l} \tag{3.17}$$

Vapour

$$\frac{\partial}{\partial t}(\alpha_v \rho_v \vec{v}_v) + \nabla.(\alpha_v \rho_v \vec{v}_v \vec{v}_v) = -\alpha_v \nabla p + \nabla.\bar{\bar{\tau}}_v + \alpha_v \rho_v \vec{g} + K_{vl}(\vec{v}_l - \vec{v}_v) + \dot{m}_{lv}\vec{v}_{lv} - \dot{m}_{vl}\vec{v}_{vl}$$
$$+\vec{F}_v + \vec{F}_{lift,v} + \vec{F}_{wl,v} + \vec{F}_{vm,v} + \vec{F}_{td,v} + \vec{F}_{d,v} \tag{3.18}$$

The orientation of the microchannel heat sinks is horizontal and the effect of gravity on the flow is assumed to be negligible.

The predominant fluid is liquid (primary phase) and vapour is the secondary phase. The interface exchange coefficient can be written as

$$K_{vl} = \frac{\rho_v f}{6\tau_v} d_{bv} A_{int} \tag{3.19}$$

where f is the drag function, A_{int} is the interfacial area and τ_v is the particulate relaxation time which is defined as

$$\tau_v = \frac{\rho_v d_{bv}^2}{18\mu_v} \tag{3.20}$$

where the diameter of bubble of the vapour phase is d_{bv}.

If the velocity of liquid phase is the same as the velocity of vapour phase, i.e. $\vec{v}_l = \vec{v}_v$, then

$$K_{vl}(\vec{v}_v - \vec{v}_l) = K_{vl}(\vec{v}_l - \vec{v}_v) = 0 \tag{3.21}$$

$$A_{int} = \frac{6\alpha_v}{d_{bv}} \tag{3.22}$$

The drag modification term is introduced by defining

$$K'_{vl} = \eta K_{vl} \tag{3.23}$$

The Brucato et al correlation [157] defines η as

$$\eta = (1 + \gamma) \tag{3.24}$$

where

$$\gamma = K\left(\frac{d_{bv}}{\lambda}\right)^3 \tag{3.25}$$

and $K = 6.5\text{x}10^{-6}$, d_{bv} is the bubble diameter, λ is the Kolmogorov length scale given by

$$\lambda = \left(\frac{\nu_l^3}{\varepsilon}\right)^{1/4} \tag{3.26}$$

where ε is the average liquid phase turbulent eddy dissipation and ν_l represents the specific molecular viscosity of the liquid phase.

The interface velocity is v_{lv} . If $\dot{m}_{lv} > 0$ (mass is being transferred from the liquid phase to vapour phase),

$$v_{lv} = v_l \tag{3.27}$$

if $\dot{m}_{lv} < 0$ (mass is being transferred from the vapour phase to the liquid phase),

$$v_{lv} = v_v \tag{3.28}$$

Energy equation

Liquid

$$\frac{\partial}{\partial t}(\alpha_l \rho_l h_l) + \nabla.(\alpha_l \rho_l \vec{v}_l h_l) = \alpha_l \frac{\partial p_l}{\partial t} + \bar{\bar{\tau}}_l : \nabla \vec{v}_l - \nabla.\vec{q}_l + S_l + Q_{vl} + \dot{m}_{vl} h_{vl} - \dot{m}_{lv} h_{lv} \tag{3.29}$$

Vapour

$$\frac{\partial}{\partial t}(\alpha_v \rho_v h_v) + \nabla.(\alpha_v \rho_v \vec{v}_v h_v) = \alpha_v \frac{\partial p_v}{\partial t} + \bar{\bar{\tau}}_v : \nabla \vec{v}_v - \nabla.\vec{q}_v + S_v + Q_{lv} + \dot{m}_{lv} h_{lv} - \dot{m}_{vl} h_{vl} \tag{3.30}$$

where h_l and h_v represent the specific enthalpies of the liquid and vapour phases, $\vec{q}_l$ and $\vec{q}_v$ are the heat fluxes for the phases. Q_{lv} and Q_{vl} are the heat exchange intensities between the phases while h_{lv} and h_{vl} are the interface specific enthalpies. The following conditions must be satisfied by the heat exchange between the phases:

$$Q_{vl} = -Q_{lv} \tag{3.31}$$

$$Q_{ll} = Q_{vv} = 0 \tag{3.32}$$

3.3. Boundary conditions

The following assumptions were made to model the conjugate heat transfer (conduction in the solid and convection in the fluid) and fluid flow in the microchannels by employing the governing equations:

The cooling medium was water and the continuum regime can be applied; hence Navier-Stokes equations were used to describe the transport processes. The fluid was Newtonian, and the flow was laminar (Re < 2000) and assumed to be incompressible. The flow and heat transfer were three dimensional; steady states for fluid flow and heat transfer were assumed and heat transfer due to radiation and natural convection was negligible. No slip occurred on the inner walls of the microchannels. Viscous (heating) dissipation was negligible. The properties of the solid substrate were assumed to be constant while those of the fluid (coolant) were assumed to vary with temperature because of high heat flux consideration in this work, and appropriate functional relations were applied in the computations [69], [158].

Pressure, $p = p_{in}$, Temperature, $T_{f,in}(T_{f,min}) = 25\ °C$ at the inlet while $p_{out} = p_{atm}$ at the outlet. The thermal boundary condition consists of uniform heat flux which is applied at the bottom (base) of the heat sink as

$$q = k_s \frac{\partial T}{\partial y} \tag{3.33}$$

The top of the computational domain is adiabatic and symmetry condition applies at the right and left of the domains such that

$$\frac{\partial T}{\partial x} = 0 \tag{3.34}$$

The heat flux between the solid walls and the fluid is coupled; hence the continuity of the temperature and heat flux at the interface of the solid and fluid surfaces requires that:

$$k_s \frac{\partial T}{\partial n}|_{\text{wall}} = k_l \frac{\partial T}{\partial n}|_{\text{wall}} \tag{3.35}$$

where n is the direction normal to the walls. A no-slip boundary condition is specified at the walls, hence

$$u = v = w = 0 \tag{3.36}$$

Mass velocity is expressed as

$$\emptyset = \rho u_{in} \tag{3.37}$$

where ρ is the density of liquid and u_{in} is the inlet velocity.

Thermal resistance which is a measure of thermal performance of microchannel heat sink is computed as

$$R_{th} = \frac{T_{b,max} - T_{f,min}}{Q} \quad (3.38)$$

$$Q = q \times A_{b,s} \quad (3.39)$$

where $A_{b,s}$ is the heat sink base surface area (where the electronic device is attached).

The pumping power (PP) which drives the fluid through the microchannel for the elemental volume can be computed as

$$PP = u_{in}.A_{ch}.\Delta p \quad (3.40)$$

Bejan number Be is computed as

$$Be = \Delta P V^{2/3}/\alpha\mu \quad (3.41)$$

$$\alpha = k/\rho C_p \quad (3.42)$$

The summary of the models used for the simulations, and solver settings are given below:

Two-phase flow

Multiphase model	Eulerian (no of phases = 2)
Boiling model	RPI (wall heat flux partitioning)
Volume fraction	Implicit
Viscous model	k-ε (2 equations)
k-ε	Realizable
Near wall treatment	Menter-Lechner
Turbulence multiphase model	Mixture

Model constants are defined as follows:

C_2-Epsilon	1.9
Turbulence kinetic energy, TKE Prandtl number (σ_k)	1
Turbulent dissipation rate, TDR Prandtl number (σ_ε)	1.2
Dispersion Prandtl number	0.75

Energy Prandtl number	0.75

Phases

Primary phase	Deionised water
Secondary phase	Water vapour

Interfacial area concentration:

Vapour diameter	Sauter-Mean (it is the diameter of a vapour bubble whose ratio of its volume to surface area is similar to other bubbles in the computation)
Surface tension	0.0728
Coalescence kernel	Hibiki-Ishii
Breakage kernel	Hibiki-Ishii
Nucleation rate	Yao-Morel
Dissipation function	Fluent k-ε
Minimum diameter specified	$1x10^{-10}$ m
Maximum diameter specified	$1x10^{-2}$ m

Phase interactions

Virtual mass: vapour-water	0.5
Drag modification	Ishii
Drag factor	Brucato
Lift coefficient: vapour-water	Tomiyama
Wall lubrication: vapor-water	Antal et al.
Turbulent dispersion: vapour-water	Lopez-de-Bertodano
Turbulence interaction: vapor-water	Troshko-Hassan
Heat transfer coefficient: vapour-water	Ranz-Marshall

Mass transfer mechanism is through boiling

Liquid interface transfer coefficient	1
Saturation temperature	373.15K
Outlet pressure	101325 N/m^2 absolute (0 gauge)

Boiling model parameters

Bubble departure diameter	Tolubinski-Kostanchuk
Frequency of bubble departure	Cole
Nucleation site density	Lemmert-Chawla
Area influence coefficient	Devalle-Kenning
Bubble waiting time coefficient	1
Correction model	Fixed Yplus
Minimum reference temperature	288.16
Yplus value	250

Solution method

Pressure-velocity coupling	Coupled (pseudo transient option)
Spatial discretisation (Gradient)	Least square based
Momentum	Second order upwind
Volume fraction	First order upwind
Turbulent kinetic energy	First order upwind
Turbulent dissipation rate	First order upwind
Energy	Second order upwind
Interfacial area concentration	First order upwind

Solution controls

Pseudo transient explicit relaxation factors	
Pressure	0.5
Momentum	0.5

Density	1
Body forces	1
Volume fraction	0.5
Vaporisation mass	1
Turbulent kinetic energy	0.75
Turbulent dissipation rate	0.75
Turbulent viscosity	1
Energy	0.75
Interfacial area concentration	0.75

Residuals

Continuity equation	$1x10^{-5}$
Momentum	$1x10^{-7}$
Energy	$1x10^{-7}$
Convergence conditions	All the conditions above were met
Initialisation	Standard (Hybrid can also be used)
Pseudo transient options	The option used depended on the stability of the solution (user defined or automatic option)

Non-equilibrium boiling model with implicit volume fraction formulation was used to model subcooled flow boiling up to departure from nucleate boiling (DNB).

Single phase flow

Viscous model	Laminar
Fluid	Deionised water

Solution method

Pressure-velocity coupling scheme	Semi Implicit Method for Pressure Linked Equations (SIMPLE)

Spatial discretisation (gradient)	Least square cell based
Pressure	Second order upwind
Momentum	Second order upwind
Energy	Second order upwind

Solution controls	
Pressure	0.3
Density	1
Body forces	1
Momentum	0.7
Energy	1

Residuals	
Continuity equation	$1x10^{-5}$
Momentum	$1x10^{-7}$
Energy	$1x10^{-7}$
Initialisation	Hybrid

For single-phase and two-phase flow, results were obtained after convergence criteria were fully met. The output parameters were defined in the report definitions and post processing was done in the CFD post.

3.4. Finite volume discretisation

The grid or mesh is a discrete representation of the geometry of the flow and heat transfer problem. The grids are the cells or elements in which the flow and heat transfer problem is solved, hence high-quality grids are crucial to the successful implementation of computational fluid dynamics (CFD) analyses. The impact of grid on convergence, solution accuracy and CPU time required is significant; proper attention should be given to its quality. The problem to be analysed involves the shapes of the geometries (microchannel heat sinks and microchannel configurations). Different grid types are available (triangle, tetrahedron, pyramid, polyhedron, quadrilateral, hexahedron, wedge and hybrid) depending on the nature of the problem and solver capabilities. The grids can be arranged in regular (structured), irregular (unstructured) and hybrid (combination of cell types) fashions.

ANSYS uses finite volume method probably because of its robustness and efficiency in solving heat and mass transfer problems, ease of programming and accuracy. Other popular discretisation techniques include finite element and finite difference methods.

Unit cell heat sinks with circular, equilateral triangular, rectangular and square microchannels were chosen for the computational analyses to save computational time since the microchannels were of the same volume and arranged symmetrically in each multichannel heat sink. Also, it was assumed that the flow rates in the microchannels of each multichannel heat sink configuration were the same and heat flux was uniform. The meshes used for the computations are shown in Figure 3.2- Figure 3.5.

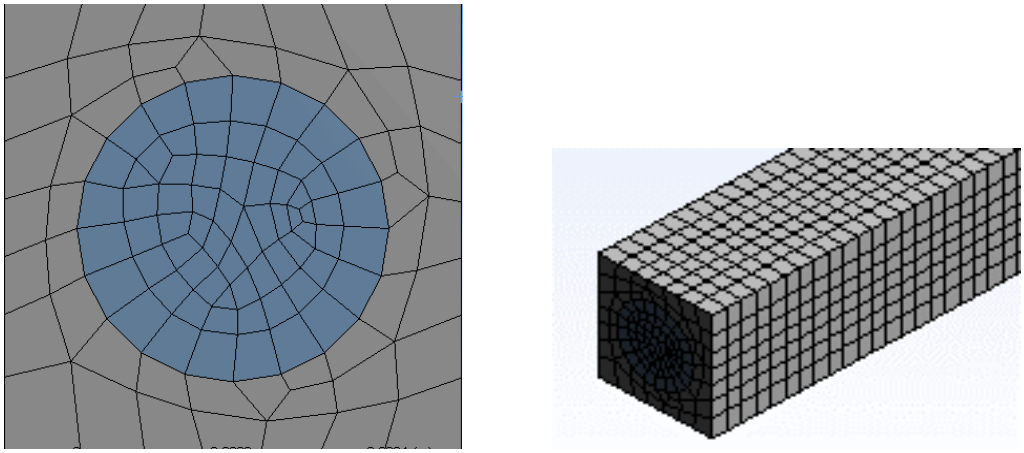

(a) unstructured mesh (b) Hexahedral mesh

Figure 3.2. Circular microchannel heat sink.

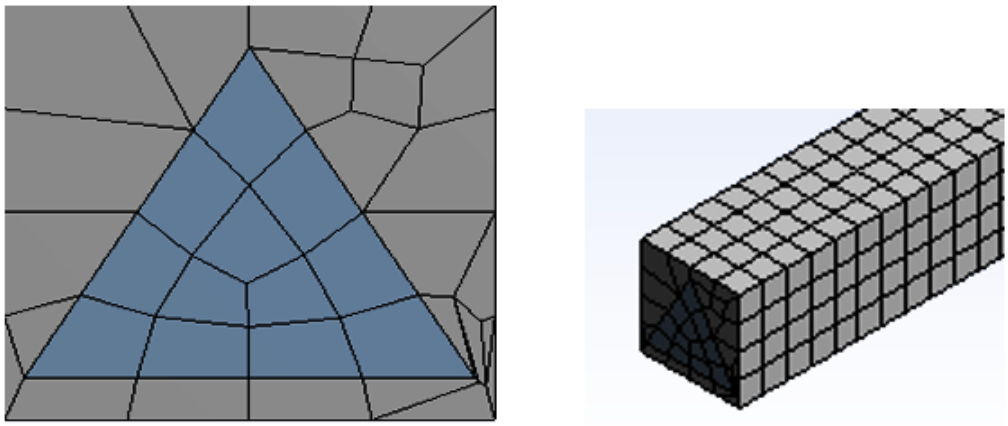

(a) Unstructured mesh (b) Hexahedral mesh

Figure 3.3. Equilateral triangular microchannel heat sink.

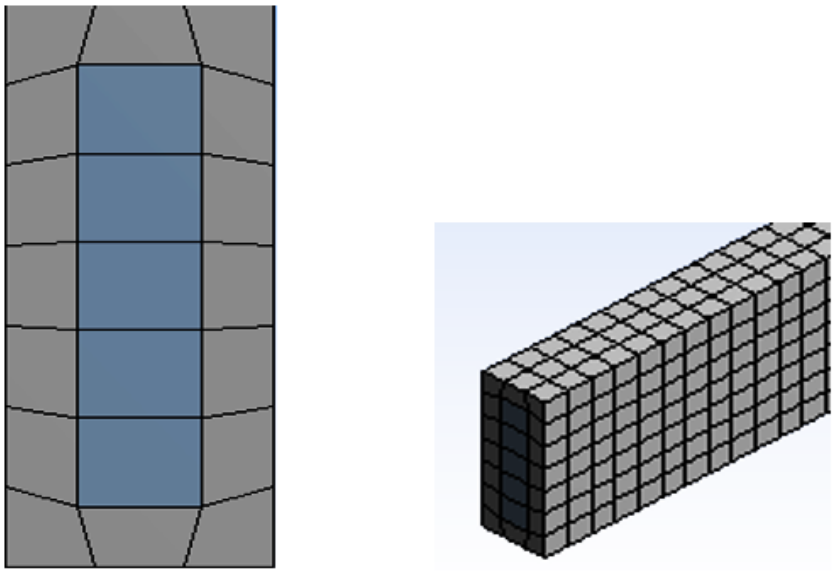

(a) Hexahedral/structured mesh (b) Hexahedral mesh

Figure 3.4. Rectangular microchannel heat sink.

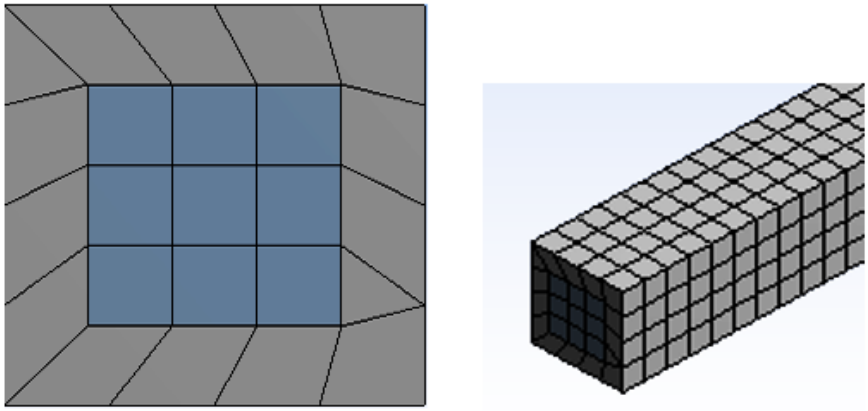

(a) Hexahedral/structured mesh (b) Hexahedral mesh.

Figure 3.5. Square microchannel heat sink.

The numerical analyses were carried out in three-dimension. The velocity ranged between (0.1-0.5m/s) and (6.5-7.0 m/s) and heat flux from 100 to 1200 W/cm^2. The simulation and optimisation processes were carried out on a Proline® computer of 64-bit Windows operating system, x64-based processor, Intel ® core ™ i5-4590 CPU at 3.30 GHz with installed memory of 16.0 GB. For example, the CPU time for simulation and optimisation in the velocity range of (1.0-1.5 m/s) for heat flux of 100 W/cm^2 was approximately seven hours for circular microchannel heat sink.

The governing equations were solved numerically in the fluid and solid regions by discretisation based on finite volume method in [62], [63]. Finite volume method can be applied to any type of grid including complex geometries. The domain for discretisation is divided into several control volumes such that one control volume surrounds each grid point located at the centre of a control volume. An algebraic equation containing the grid point values of the dependent variable is derived by integrating the governing equation over each control volume. The conservation of mass, momentum and energy is satisfied in the whole domain just as their integral solutions are satisfied in the control volumes.

Coupled algorithm was adopted for the solution of the pressure-velocity coupling (two-phase flow) of the conjugate heat transfer problem. Second order upwind scheme was employed for the discretisation of momentum and energy equations. For the single-phase simulations, the SIMPLE algorithm was used to resolve the pressure-velocity coupling. The algebraic equations resulting thereof were solved using a line by line Tri-Diagonal Matrix Algorithm. The solutions were considered converged when continuity, momentum and energy residuals were less than 10^{-5}, 10^{-7} and 10^{-7} respectively.

3.5. Optimisation methods

3.5.1. Introduction

Optimisation can be defined as the process of determining the best design to satisfy a particular goal or a set of goals. Optimisation methods can be classified broadly as gradient based (for local optimum problems) e.g., Mixed-Integer Sequential Quadratic Programming (MISQP), Nonlinear Programming by Quadratic Lagrangian (NLPQL)) or non-gradient based (evolutionary, for global optimum problems) e.g., Multi-Objective Genetic Algorithm (MOGA), Adaptive Multi-Objective (AMO)) [156]. The computer-based optimisation of any

of the methods allows the designer to use a computer optimisation algorithm to search the design space of a computer model for the optimal designs according to the specified criteria (objectives and constraints). Obtaining a valid and accurate initial model for the design problem is a very crucial step in the optimisation process.

For example, in order to maximise the thermal performance of a microchannel heat sink, the search variables or design variables are the parameters for optimisation (e.g., velocity, geometric parameters and heat flux) and the objective function is the thermal resistance. The constraints are also specified to achieve the desired goal. The thermal resistance can be defined as being influenced as follows for a rectangular microchannel heat sink:

$$R_{th} = f(u_{in}, T_{f,in},\ T_{b,max},\ q,\ w_{ch},\ H_{ch},\ l_{ch},\ D_h,\ w_s,\ H_s,\ l_s) \tag{3.43}$$

subject to:

fixed volume of microchannel heat sink ($w_s . H_s . L_s$)

fixed volume of microchannel ($w_{ch} . H_{ch} . L_{ch}$)

where

$\mathrm{R_{th}} = \text{thermal resistance}$

$\mathrm{u_{in}} = \text{fluid inlet velocity}$

$\mathrm{T_{f,in}} = \text{fluid inlet temperature}$

$\mathrm{T_{b,max}} = \text{maximum base temperature}$

$\mathrm{q} = \text{heat flux}$

$\mathrm{L_{ch}} = \mathrm{L_s} = \text{length of microchannel, length of heat sink}$

$\mathrm{w_{ch}} = \text{width of microchannel}$

$\mathrm{H_{ch}} = \text{height of microchannel}$

$\mathrm{D_h} = \text{hydraulic diameter}$

$\mathrm{w_s} = \text{width of heat sink}$

$\mathrm{H_s} = \text{height of heat sink}$

The search for the optimal combination of design variables values that will give the minimum thermal resistance continues until the global minimum thermal resistance is obtained.

In the context of this study, ANSYS Design Explorer uses design exploration for designing and understanding the response and analysis of geometric and flow parameters to an applied heat flux. Goal driven optimisation can be defined as a constrained, multi-objective optimisation

technique in which the optimal (best) designs are obtained from a sample set given the objectives and/or constraints that have been set for the parameters. There are two goal driven optimisation systems, viz., Response Surface Optimisation and Direct Optimisation. The response surface optimisation has three components: design of experiments, response surface and optimisation. It draws its information from its own response surface; therefore, it is dependent on the quality of the response surface. Direct optimisation has only one component, viz., optimisation, which utilises direct solves method. It does not have an associated response surface component; however, it can draw its information from any other component which contains design point data. Response surface optimisation was used in this work because it is more flexible and the design of experiments can be used as many times as possible. All the geometric and flow parameters were considered very important in the optimisation procedure. The geometric and numerical optimisation suggests that optimisation was done for optimal geometric parameters; it was also done numerically at the same time to obtain optimal flow parameters. The relationship between the design variables (velocity, geometric parameters) and the performance (thermal resistance, pumping power) of a product (microchannel heat sink) can be described by design exploration using design of experiment (DOE) together with response surfaces, which provides all information required to achieve simulation driven product development. The influence of design variables on the performance of the product is quantified exhaustively to answer the "what if" question (for example, what parameters should be varied if performance can be enhanced at a reduced cost?) [156].

For a response surface optimisation scheme, after creating the initial design and the geometric parameters are defined, then response surface is created. A response surface system is inserted in the project and the design space is defined by assigning minimum and maximum values to be considered for each of the input variables. The information provided is used by the design of experiment part of the response surface system to create the design space sampling. DOE schemes are: Central Composite Design (CCD), Optimal Space-Filling Design (OSF), Box-Behnken Design, Sparse Grid Initialisation, Custom, Custom plus Sampling and Latin Hypercube Sampling Design (LHS). The response surfaces (meta-models) available in ANSYS are: Genetic Aggregation, Standard Response Surface-Full 2^{nd} Order Polynomial, Kriging, Non-Parametric Regression, Neural Network and Sparse Grid. The following types of algorithms are available for optimisation: Multi-Objective Genetic Algorithm (MOGA), Shifted Hammersley Sampling (screening), Mixed-Integer Sequential Quadratic Programming

(MISQP), Nonlinear Programming by Quadratic Lagrangian (NLPQL), Adaptive Single-Objective Optimisation (ASO) and Adaptive Multi-Objective Optimisation (AMO) [156].

Response Surface Optimisation and Direct Optimisation are the two Goal Driven Optimisation (GDO) that provide access to optimisation techniques which find design candidates from the response surfaces or other components like DOE containing design points. After introducing a GDO scheme, the optimisation study is defined and the optimisation technique, the objectives and constraints are chosen and the domain is specified.

In this study, the response surface optimisation combined the finite volume method (FVM, to carry out the flow analysis) with multi-objective genetic algorithm (MOGA) as the optimisation algorithm. This optimisation method was used to obtain optimal geometric and flow parameters. For each of the components in the response surface optimisation namely, design of experiment, response surface and optimisation, the following combination of algorithms was used because of their accuracy and peculiarity to the study (global optimum):

Design of experiment	Central composite design (CCD)
Response surface	Genetic aggregation (GA)
Optimisation	Multi-objective genetic algorithm (MOGA)

Multi-objective genetic algorithm was chosen over the default, Shifted Hammersley sampling (screening), because of its accuracy and adaptability to single objective with multiple constraints. The flow chart for response surface optimisation algorithm is shown in Figure 3.6

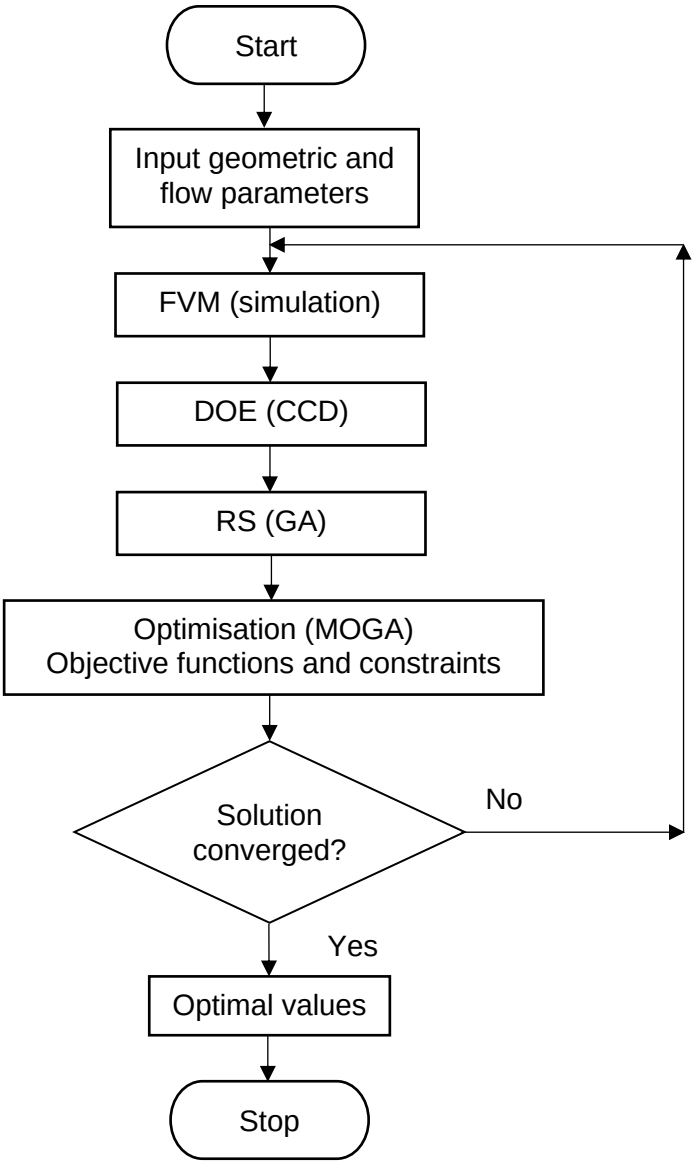

Figure 3.6. Response surface optimisation algorithm.

Note: FVM-Finite volume method, DOE-Design of experiment, RS-Response surface.

3.6. Single-phase flow

Multi-parameters optimisation approach for microchannel heat sinks was used by Wang et al. [159]. Simplified conjugate-gradient scheme together with a fully developing three-dimensional heat transfer and flow model were integrated. The search variables were the number of channels, aspect ratio, and the ratio of channel width to pitch. Thermal resistance was minimised subject to fixed pumping power and heat flux. They observed that there was a reduction in the overall thermal resistance of the optimal design when the pumping power was increased. The same method had been used by Chen et al. [160] and Kou et al. [161]. Also,

optimisation procedure consisting of conjugate-gradient method and a three-dimensional fluid flow together with heat transfer model was used by Hung et al. [162] to study the optimal geometric parameters of a double-layered microchannel heat sink. Their objective function (thermal resistance), constraints (fixed pumping power and heat flux) and search variables were similar to those of Wang et al. [159] except for the lower and upper aspect ratios that were used. It was reported that the optimal values of the channels and the aspect ratios increased whereas the optimal channel width ratio decreased, as the pumping power increased. They also observed the same trend in the optimal thermal resistance; as the pumping power increases, the overall thermal resistance decreases and later tends to a constant value. Random search technique was used by Ryu et al. [163] for the thermal optimisation of a microchannel. The design variables were the geometric parameters while the objective function that was minimised was the thermal resistance of the microchannel heat sink.

Koga et al. [164] studied topology optimisation technique in a microchannel heat sink. Optimisation was done by minimising pressure drop in the fluid flow and maximising heat dissipation. Finite element method was used for the numerical analysis with sequential linear programming as the optimisation algorithm. A comprehensive review of engineering design of optimal heat transfer systems using topology optimisation was carried out by Dbouk [165]. Arie et al. [65] studied an approximation-based multi objective optimisation to design an optimal manifold microchannel plate heat exchanger by determining the design parameters that yielded the optimal performance of the heat exchanger. The aim was to minimise pressure drop while enhancing heat transfer. It was reported that the optimal manifold microchannel plate heat exchanger had more heat transfer efficiency than chevron plate heat exchanger designs. Pareto based multi objective optimisation was used by Amanifard et al. [166] for heat transfer and flow coefficients in a microchannel; the same approach was used for the optimisation of a counterflow double-layered microchannel heat sinks by Shen et al. [167]. Multi objective performance optimisation of rectangular and trapezoidal microchannel heat sinks using evolutionary algorithm was studied by Husain and Kim [168]. Widths, heights and fin widths of the microchannels were the design variables while the objective functions were thermal resistance and pumping power. Their result showed the existence of trade-off between the thermal resistance and pumping power to optimise the microchannel heat sinks. The same authors [169] had also carried out optimisation study on a microchannel heat sink for microelectronic cooling, using shape optimisation.

Bello-Ochende et al. [71], [72], [170], [171] reported the geometric optimisation of a three-dimensional microchannel heat sink while minimising the peak temperature from the walls of the microchannel to the fluid. Finite volume method was used while numerical simulation was carried out on a unit cell of length 10 mm with volume ranging from 0.1 mm^3 to 0.9 mm^3 and pressure drop was between 10 kPa and 75 kPa. The effects of total solid volume fraction and pressure drop on aspect ratio, channel hydraulic diameter and peak temperature while the cross-sectional area of the microchannel heat sink was free to morph with respect to the degrees of freedom provided by the aspect ratio and the solid volume fraction were investigated numerically. Their results showed that there was a strong effect of degrees of freedom on peak temperature and the maximum thermal conductance. The aspect ratio and optimal hydraulic diameter obtained were reported to be in good agreement with those obtained from approximate relationships using scale analysis. Bello-Ochende et al. [170]-[172] also reported numerical optimisation results for three-dimensional heat transfer and fluid flow in a microchannel heat sink using water as the cooling fluid. Silicon wafer was used as the heat sink material. The volume of the unit channel considered was 0.9 m^3 with axial length of 10 mm. The results showed that there was agreement between the behaviour of the optimal volume and the constructal method in which the objective was to minimise the peak temperature subject to the constraints of fixed total volume of the microchannel and the silicon wafer. Geometric optimisation of a silicon based microchannel heat sink was also studied using combined numerical optimisation and constructal theory with the aim of minimising the wall temperature subject to various constraints. The results showed that as the dimensionless pressure drop increased the maximised global thermal conductance also increased. Hung et al [173] also carried out optimisation study for various configurations of microchannels with the aim of comparing the pumping power requirements and thermal resistances of the heat sinks. It was concluded that T-channel was the best design considering the thermal resistance and temperature uniformity. Optimal design of a rectangular microchannel heat sink was investigated by Shao et al. [174]. Sequential quadratic programming (SQP) algorithm was used to optimise the shapes of microchannel heat sinks, while finite volume method was used to simulate the cooling performance of the optimal rectangular microchannel heat sink. The heat flux in their study was 278 W/cm^2 and through optimisation, the highest temperature in the chip was below 42 °C which was about half of the temperature without optimisation.

Adewumi et al. [175] investigated the thermal performance of combined microchannel heat sink with micro pin fins with different cross-sectional shapes so as to study the best geometric configuration that maximised heat transfer from the heated base when the combined heat sink was subjected to a steady, laminar, incompressible convective fluid flow and heat transfer. They observed that the best performance was obtained with a sixth row of circular-shaped micro pin-fins for the optimal combination of the microchannel and micro pin-fin heat sink. The same authors [176] used constructal design technique to optimise the geometry of a multi-layered microchannel heat sink with the aim of minimising the peak temperature of the solid substrate into which the microchannel was embedded. Parallel and counter flow arrangements of fluid through the microchannel were considered. They reported that as the pressure drop increased, the minimised peak temperature decreased and the maximum thermal conductance increased and when the number of layers of the microchannel was increased from two to three, the results of the thermal conductance was worse. It was also reported that two-layered microchannel with counter flow arrangement was the best design in minimising the peak temperature and maximising the thermal conductance when the pressure drop was between 20 kPa and 60 kPa. Salimpour et al. [177] carried out geometric and numerical optimisation of an array of circular, square and isosceles right triangle microchannels with air as the coolant. The aim was to investigate heat transfer in these channels subject to fixed volume and pressure constraints. They observed that square microchannel had the highest heat transfer per unit volume. Simulated annealing method was adopted by Kou et al. [161] to achieve minimum thermal resistance and optimal microchannel width with various pumping power requirements and microchannel heights. The same method and other optimisation algorithms were used by Cruz et al. [178] to optimise a rectangular microchannel in the presence of spreading resistance.

Ighalo et al. [179] investigated numerically the geometric optimisation of a microchannel heat sink with the aim of optimising the wall peak temperature of the heat sink subject to the constraints of manufacturing restraints, fixed pressure drop and total volume. A gradient based optimisation algorithm was used for the simulation. They also reported that the effects of pressure drop on aspect ratio, solid volume fraction, channel hydraulic diameter, minimised peak temperature and thermal conductance were in agreement with previous studies in the literature.

Kim [180] presented three optimisation methods which include: fin model, porous medium model and numerical optimisation methods. Optimal design variables and the corresponding

thermal resistances using porous medium and numerical simulation under the constraint of maximum pumping power were presented because assumptions used (one dimensional conduction only along the fin height, constant heat transfer coefficient, and uniform fluid temperature) in the fin model were shown to be invalid for large aspect ratios.

Ma et al. [181] carried out multi-parameter optimisation for a rectangular microchannel heat sink. The constraints were: fixed inlet volume flow rate, fixed pressure drop, and fixed pumping power. The results showed low thermal resistance at individual constraint condition with a pressure drop of 350 kPa and when multiple constraint conditions were applied, pressure drop and channel height less than 50 kPa and 350 μm respectively were achieved.

Other authors [80], [182]-[185] also used various methods of optimisation in single-phase flow.

3.7. Two-phase flow

Information is scarce in the open literature on optimisation of microchannel heat sinks using any of the methods stated above in two-phase flow and also in the way that it has been done in the present study. This creates a big gap that this study has explored to optimise four different microchannel heat sink configurations (circular, equilateral triangular, rectangular and square) at high heat fluxes for optimal performances. The optimisation of microchannel heat sinks in single-phase flow was also done to enhance performance at moderate heat fluxes. The pressure drops were lower compared to those available for microchannels of similar configurations and sizes in the open literature. It is a well-known fact that the performance of two-phase flow in microchannel is better than single-phase flow at the same operating conditions of applied heat flux and velocity, but comparisons of optimal performances of microchannel heat sinks in two-phase flow and single-phase flow with their optimal geometries having the same fixed volumes of microchannel and heat sink have not been done before as in this study. At different optimal velocities, the volumes of optimal microchannels and heat sinks were the same in two-phase and single-phase flow. The fixed volume constraints for the microchannel and heat sink were necessary for accurate comparisons of all the optimal microchannel heat sinks in this study.

The flow charts for single phase and two-phase flow simulations are shown in Figure 3.7 [186] and Figure 3.8 while the concept of single-phase and two-phase flow cooling for this research is shown in Figure 3.9.

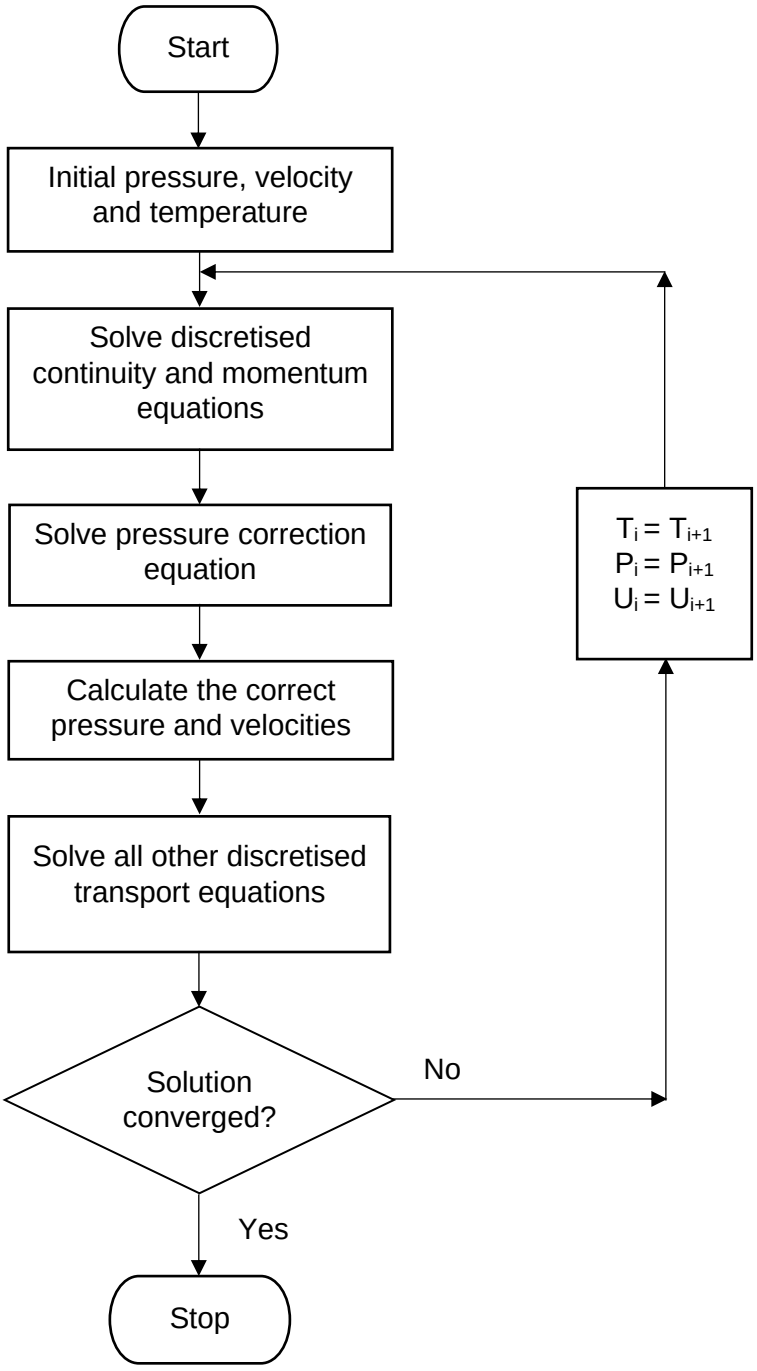

Figure 3.7. SIMPLE algorithm by Patankar [186].

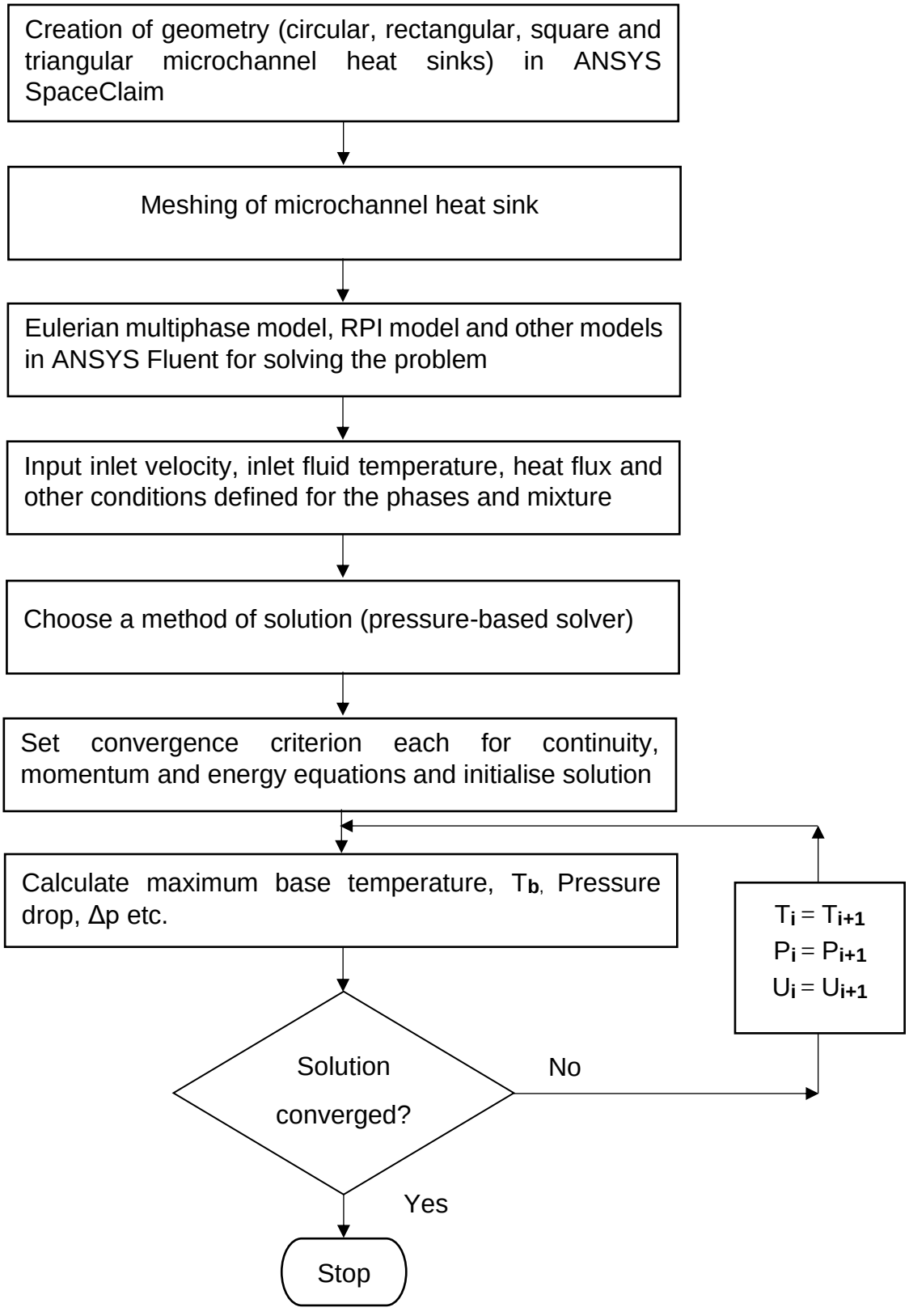

Figure 3.8. Simulation of subcooled flow boiling in microchannels.

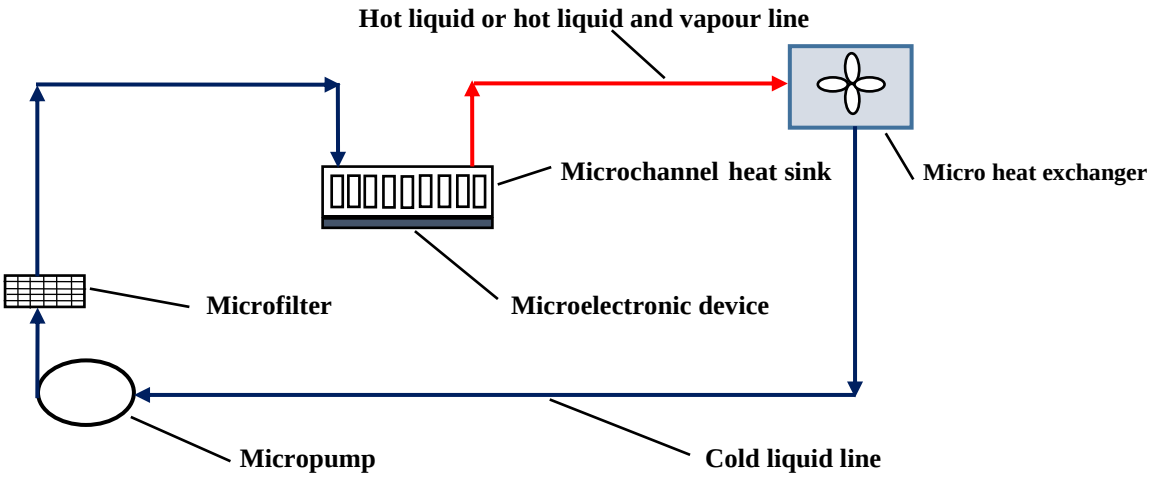

Figure 3.9. Concept of single-phase and two-phase flow cooling of electronic devices.

CHAPTER 4
SUBCOOLED BOILING MODELS AND CORRELATIONS

4.1. Wall boiling model

Subcooled boiling in the microchannel can be described as a situation where the wall temperature is high enough to cause boiling of the liquid in contact with it while the bulk liquid average temperature is less than the saturation temperature. The wall heat flux partitioning (RPI) model proposed by Kurul and Podowski [187] which is normally used to model subcooled boiling heat transfer at the wall of the microchannel was employed in this work. The liquid phase is the continuous phase while the vapour phase is the dispersed phase. Figure 4.1 shows the mechanism for subcooled flow boiling in a one-sided heated microchannel which was the concept used in this study.

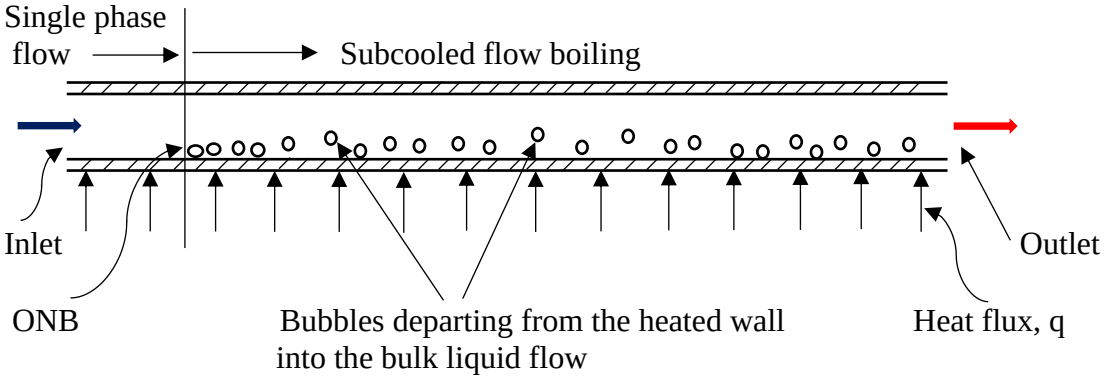

Figure 4.1. Schematic diagram of nucleation and departure of bubbles in subcooled flow boiling (heated at the bottom/base).

The wall heat flux partitioning model has total heat flux from the heated wall to the fluid which is partitioned into three components: single phase convective heat flux, q_C, wall quenching heat flux q_Q and evaporative heat flux, q_E such that

$$q_W = q_C + q_Q + q_E \tag{4.1}$$

The heat fluxes are expressed as follows:

$$q_C = h_{Cl}(T_w - T_l)(1 - A_b) \tag{4.2}$$

The heated wall surface is divided into A_b and $(1 - A_b)$; A_b represents area covered by the nucleating bubbles while $(1 - A_b)$ is the area covered by the liquid, h_{Cl} is the single-phase

heat transfer coefficient, T_w and T_l denote wall and liquid temperatures respectively. The vapour phase is dispersed in the liquid phase.

The cyclic averaged transient energy transfer related to liquid filling the wall vicinity after bubble detachment is modelled by quenching heat flux and it is expressed as

$$q_Q = \frac{2k_l}{\sqrt{\pi\lambda_l T}}(T_w - T_l) \tag{4.3}$$

where $T = \frac{1}{f}$ is the periodic time, f is the bubble departure frequency and λ_l is the diffusivity, which is defined as

$$\lambda_l = \frac{k_l}{\rho_l C_{pl}} \tag{4.4}$$

Substituting for T and λ_l in Equation (4.3) and rearranging,

$$q_Q = 2\,.\sqrt{\frac{k_l \rho_l C_{pl} f}{\pi}}(T_w - T_l) \tag{4.5}$$

The evaporative heat flux is expressed as

$$q_E = V_d N_w \rho_v h_{lv} f \tag{4.6}$$

where ρ_l and ρ_v are the densities of liquid and vapour phases respectively, h_{lv} is the latent heat of evaporation, V_d is the volume of the bubble based on the bubble departure diameter, C_{pl} and k_l are the specific heat and thermal conductivity of the liquid phase respectively. The proportion of the heated wall covered by the nucleating bubbles, A_b is expressed as

$$A_b = K_{emp}\frac{N_w \pi {d^2}_{bw}}{4} \tag{4.7}$$

The area of influence is limited as follows to avoid numerical instabilities as a result of unbound empirical correlations for the nucleate site density:

$$A_b = \min\left(1, K_{emp}\frac{N_w \pi {d^2}_{bw}}{4}\right) \tag{4.8}$$

where d_{bw} is the bubble departure diameter given as [188]:

$$d_{bw} = \min\left(0.0014, 0.0006.\, e^{-\frac{\Delta T_{sub}}{45}}\right) \tag{4.9}$$

K_{emp} is an empirical constant estimated by [189] as

$$K_{emp} = 4.8\exp\left(-\frac{\rho_l C_{p,l}(T_w - T_l)}{80\rho_g h_{lv}}\right) \tag{4.10}$$

N_w is the active nucleate site density given by [190] as

$$N_w = 210^{1.805}(T_w - T_s)^{1.805} \quad (4.11)$$

where T_s is the saturation temperature, f is the frequency of bubble departure given by [191] as

$$f = \frac{1}{T} = \sqrt{\frac{4g(\rho_l - \rho_v)}{3\rho_l d_{bw}}} \quad (4.12)$$

where g is acceleration due to gravity.

4.2. Non-equilibrium subcooled boiling

Critical heat flux condition in microchannel flow boiling is as a result of the excursion of wall surface temperatures because of sharp reduction in local heat transfer coefficients. The heated surface (one-sided heating in this work) or surfaces (heated at more than one side) are no longer wetted by the liquid and the vapour replaces the liquid in direct contact with the walls. At this stage, subcooled boiling departs from the bubbly flow regime. Heat is transferred directly to the vapour; the heat capacity is much less than that of the liquid, hence there is a sharp reduction in heat removal efficiency which results in high wall temperatures.

Non-equilibrium subcooled boiling model is used to model departure from nucleate boiling (critical heat flux) in subcooled boiling. The vapour temperature is included in the modified wall heat flux partition and it is expressed as follows:

$$q_W = (q_C + q_Q + q_E)f(\alpha_l) + (1 - f(\alpha_l))q_{cv} \quad (4.13)$$

where q_C is the single-phase convective heat flux, q_Q is the wall quenching heat flux, q_E is the evaporative heat flux, q_{cv} is the convective heat flux of the vapour phase and α_l is the volume fraction of the liquid phase. The additional heat flux, q_{cv} is expressed as

$$q_{cv} = h_{cv}(T_w - T_v) \quad (4.14)$$

where T_w represents the wall temperature, T_v is the vapour temperature, h_{cv} is the convective heat transfer coefficient of vapour.

The function $f(\alpha_l)$ is expressed as [192]:

$$f(\alpha_l) = \begin{cases} 1 - \frac{1}{2}e^{-20(\alpha_l - \alpha_{l,crit})} \\ \frac{1}{2}\left(\frac{\alpha_l}{\alpha_{l,crit}}\right)^{20\alpha_{l,crit}} \end{cases} \quad (4.15)$$

The critical value for the liquid phase volume fraction, $\alpha_{l,crit} = 0.2$. For the first case, $\alpha_l > \alpha_{l,crit}$ and $\alpha_l < \alpha_{l,crit}$ for the second case.

4.3. Interfacial area concentration

Interfacial area concentration is used to predict mass, momentum and energy transfers through the interface between the phases. This model uses a single transport equation per secondary phase and it is specific to bubbly flow. The transport equation allows for distribution of bubble diameters, coalescence and breakage effects. The equation is expressed as [62]:

$$\frac{\partial}{\partial t}(\rho_v \chi_{int}) + \nabla.(\rho_v \vec{v}_v \chi_{int}) = \frac{1}{3}\frac{D\rho_v}{Dt}\chi_{int} + \frac{2}{3}\frac{\dot{m}_v}{\alpha_v}\chi_{int} + \rho_v(S_{RC} + S_{WE} + S_{TI}) \quad (4.16)$$

where χ_{int} represents interfacial area concentration (m^2/m^3) and α_v is the vapour volume fraction. The vapour bubble expansion due to compressibility and phase change is represented by the first two terms on the right of Equation (4.16). The mass transfer rate to the vapour phase per unit mixture volume is $\dot{m}_v$ $(kg/m^3/s)$. Coalescence sink terms due to random collision and wake entrainment are represented by S_{RC} and S_{WE} while S_{TI} is the breakage source term due to turbulent impact.

Hibiki and Ishii [193] modelled the effects as follows:

$$S_{RC} = -\frac{1}{3\varphi}\left(\frac{\alpha_v}{\chi_{int}}\right)^2 f_c n_b \lambda_c \quad (4.17)$$

where f_c, n_b and λ_c are the frequency of bubble collision, the number of bubbles per unit mixture volume and the efficiency of coalescence from the collision respectively.

$$S_{TI} = \frac{1}{3\varphi}\left(\frac{\alpha_v}{\chi_{int}}\right)^2 f_b n_e \lambda_b \quad (4.18)$$

where $f_{b,}$ n_e and λ_b are the frequency of collision between bubbles and turbulent eddies of the liquid phase, the number of turbulent eddies per unit mixture volume and the efficiency of breakage from the impact respectively. The shape factor, $\psi = 6$, and it is defined for spherical bubbles as

$$\varphi = \frac{1}{36\pi} \quad (4.19)$$

The coalescence term in the volumetric interfacial area transport was modelled by Yao and Morel [194] as

$$\Phi^{CO} = \frac{1}{2}\frac{\eta_c n}{T_{cf}+T_{ci}} \tag{4.20}$$

where T_{cf} and T_{ci} represent the free travelling time and interaction time for coalescence, η_c is the bubble coalescence efficiency and n is the bubble number density. The equation above can also be expressed as

$$\Phi^{CO} = -K_{c1}\frac{\varepsilon^{\frac{1}{3}}\alpha^2}{d_{bv}^{\frac{11}{3}}}\frac{1}{g(\alpha)+K_{c2}\alpha\sqrt{\frac{We}{We_c}}}\exp\left(-K_{c3}\sqrt{\frac{We}{We_c}}\right) \tag{4.21}$$

where the critical Weber number, $We_c = 1.24$, the coefficients K_{c1}, K_{c2} and K_{c3} have the values 2.86, 1.922 and 1.017 respectively. The diameter of vapour bubble is d_{bv}, We is the Weber number and ε is the dissipation which is obtained from k-epsilon turbulence model. The modification factor is defined as

$$g(\alpha) = 1 - (\alpha/\alpha_{max})^{1/3} \tag{4.22}$$

where $\alpha_{max} = 0.52$ is the packing limit.

The final expression of breakage term modelled by Yao and Morel [194] is written as

$$\Phi^{BK} = K_{b1}\frac{\varepsilon^{\frac{1}{3}}\alpha(1-\alpha)}{d_{bv}^{\frac{11}{3}}}\frac{1}{1+K_{b2}(1-\alpha)\sqrt{\frac{We}{We_c}}}\exp\left(-\frac{We_c}{We}\right) \tag{4.23}$$

where the values of the coefficients, K_{b1} and K_{b2} are 1.6 and 0.42 respectively.

S_{RC} and S_{WE} in Equation (4.16) can be combined and expressed as follows:

$$S_{RC} + S_{WE} = \frac{1}{3\varphi}\left(\frac{\alpha}{\chi_{int}}\right)^2 \Phi^{CO} \tag{4.24}$$

A new source term is included when source terms due to bubble nucleation at the heated wall are added and it is expressed as

$$\Phi^{NUC} = \pi d_{bv}^2 N_w f \frac{A_{heated}}{Volume} \tag{4.25}$$

where f is the frequency of bubble departure, N_w represents nucleation site density and the diameter of the nucleating bubble is d_{bv}.

4.4. Interfacial mass transfer

It is assumed that vapour retains the saturation temperature by rapid evaporation or condensation such that when the evaporation mass flow is applied at the cell near the wall the equation can be expressed as

$$\dot{m}_E = \frac{q_E}{h_{lv}+C_{p,l}\Delta T_{sub}} \tag{4.26}$$

where ΔT_{sub} is the difference between local saturation temperature and the temperature of the bulk fluid, $C_{p,l}$ is the isobaric specific heat capacity and h_{lv} is the latent heat of evaporation.

If all the heat transferred to the interface is used in mass transfer, the interfacial mass transfer, $\dot{m}$ can be expressed as

$$\dot{m} = \dot{m}_{t,l} + \dot{m}_{t,v} = \frac{q_{t,l}+q_{t,v}}{h_{lv}} \tag{4.27}$$

where $\dot{m}_{t,l}$, $\dot{m}_{t,v}$, $q_{t,l}$ and $q_{t,v}$ represent mass transfer rate of liquid, mass transfer rate of vapour, heat transfer rate of liquid and heat transfer rate of vapour respectively. subscripts l, v and t denote liquid, vapour and transfer respectively.

4.5. Interfacial momentum transfer

The **drag force** is expressed as [62]:

$$\vec{F}_d = \frac{\rho_v f_d d_{bv} A_i}{6\tau_v}(\vec{v}_l - \vec{v}_v) \tag{4.28}$$

where

$$f_d = \frac{C_D Re}{24} \tag{4.29}$$

is known as drag force coefficient and τ_v is the dispersed phase relaxation time.

The drag coefficient model of Ishii [195] was used in the simulations. It is expressed as

$$C_D = \min\left(C_D^{vis}, C_D^{dis}\right) \tag{4.30}$$

where C_D is the drag coefficient which is determined by choosing the minimum of the viscous regime C_D^{vis} and the distorted regime C_D^{dis}; C_D^{vis} and C_D^{dis} are expressed as follows:

$$C_D^{vis} = \frac{24}{Re}(1 + 0.15Re^{0.75}) \tag{4.31}$$

$$C_D^{dis} = \frac{2}{3}\frac{d_{bv}}{\sqrt{\frac{\sigma}{g|\rho_v-\rho_l|}}} \tag{4.32}$$

where g is acceleration due to gravity, σ represents surface tension, Re is relative Reynolds number and d_{bv} is bubble diameter.

The **lift force** is expressed as [62]:

$$\vec{F}_{lift} = -C_{lift}\rho_l\alpha_v(\vec{v}_l - \vec{v}_v).(\nabla.\vec{v}_l) \tag{4.33}$$

where C_{lift} is the lift force coefficient. The modified model of Tomiyama [196] was used for the lift force coefficient. It is expressed as

$$C_{lift} = \begin{cases} \min\{0.288\tanh(0.121Re_l), f(Eo)\} & Eo \leq 4 \\ f(Eo) & 4 < Eo \leq 10 \\ -0.27 & 10 < Eo \end{cases} \tag{4.34}$$

where

$$f(Eo) = 0.00105Eo^3 - 0.0159Eo^2 - 0.0204Eo + 0.474 \tag{4.35}$$

Based on the long axis of the deformable bubble d_{db}, Eo is a modified $Eötvös$ number and it is expressed as

$$Eo = \frac{g(\rho_l - \rho_v)d_{db}^2}{\sigma} \tag{4.36}$$

$$d_{db} = \frac{d_{bv}}{(1+0.163Eo^{0.757})^{1/3}} \tag{4.37}$$

The **wall lubrication force** is expressed as [62]:

$$\vec{F}_{wl} = C_{wl}\rho_l\alpha_v|(\vec{v}_l - \vec{v}_v)|^2 n_w \tag{4.38}$$

where n_w represents the unit normal pointing away from the wall surface and $|(v_l - v_v)|$ denotes the phase relative velocity component tangential to the wall surface.

The model of Antal et al. [197] was used to model the wall lubrication coefficient; it is expressed as follows:

$$C_{wl} = \max\left(0, \frac{C_{w1}}{d_{bv}} + \frac{C_{w2}}{y_w}\right) \tag{4.39}$$

where y_w is the distance to the nearest wall, $C_{w1} = -0.01$ and $C_{w2} = 0.05$.

C_{wl} is non zero within a thin layer adjacent to the wall such that

$$y_w \leq -\left(\frac{C_{w2}}{C_{w1}}\right) d_{bv} \tag{4.40}$$

The model of Lopez de Bertodano [198] was used for **turbulent dispersion force**. The model is defined as

$$\vec{F}td_{,l} = -\vec{F}td_{,v} = C_{TD}\rho_l k_l \nabla\alpha_v \tag{4.41}$$

where ρ_l is the continuous (liquid) phase density, $\nabla\alpha_v$ represents the gradient of the dispersed (vapour) phase volume fraction, k_l represents the turbulent kinetic energy in the continuous phase and C_{TD} is a user modifiable constant which is equal to 1 by default.

Virtual mass occurs when vapour accelerates relatively to liquid. The virtual mass effect is expressed as [199]:

$$\vec{F}_{vm} = 0.5\alpha_v\rho_l\left(\frac{\partial v_l}{\partial t} + (v_l.\nabla)v_l - \left(\frac{\partial v_v}{\partial t} + (v_v.\nabla)v_v\right)\right) \tag{4.42}$$

$$\vec{F}_{vm,l} = -\vec{F}_{vm,v} \tag{4.43}$$

The **body force ($\vec{F}$)** which is the force due to gravity is assumed to be negligible because the microchannel heat sinks are horizontal.

4.6. Interfacial energy transfer

The volumetric energy transfer rate between the phases, q_{vl} is assumed to be a function of the interfacial area, A_{int} and the temperature difference. It is expressed as

$$q_{vl} = h_{vl}A_{int}(T_v - T_l) \tag{4.44}$$

where the volumetric heat transfer coefficient between the vapour phase and liquid phase is defined as

$$h_{vl} = h_{lv} \tag{4.45}$$

The heat transfer coefficient is defined as

$$h_{vl} = \frac{k_l Nu_v}{d_{bv}} \tag{4.46}$$

where k_l is the thermal conductivity of the liquid and d_{bv} is the bubble diameter.

Ranz and Marshall [200], [201] model was used to compute Nusselt number as shown:

$$Nu_v = 2.0 + 0.6Re_v^{1/2}Pr^{1/3} \tag{4.47}$$

where Re_v is the relative Reynolds number based on bubble diameter, the relative velocity is defined as

$$|\vec{v}_v - \vec{v}_l| \tag{4.48}$$

The Prandtl number of the liquid phase is defined as

$$Pr = \frac{c_{p,l}\mu_l}{k_l} \tag{4.49}$$

4.7. Turbulence kinetic energy and dissipation rate

Realizable k-ε model was used to model turbulence in the flow. The model is realizable for satisfying certain mathematical constraints on the Reynolds stresses which is consistent with the physics of the flow. The turbulence kinetic energy is k and its dissipation rate is ε. The governing equations for realizable k-ε model are as follows [62], [63]:

$$\frac{\partial}{\partial t}(\rho k) + \frac{\partial}{\partial x_l}(\rho k u_l) = \frac{\partial}{\partial x_l}\left(\left(\mu + \frac{\mu_t}{\sigma_k}\right)\frac{\partial k}{\partial x_l}\right) + G_k + G_b - \rho\varepsilon - Y_M + S_k \tag{4.50}$$

$$\frac{\partial}{\partial t}(\rho \varepsilon) + \frac{\partial}{\partial x_l}(\rho \varepsilon u_l) = \frac{\partial}{\partial x_l}\left(\left(\mu + \frac{\mu_t}{\sigma_\varepsilon}\right)\frac{\partial \varepsilon}{\partial x_l}\right) + \rho C_1 S_\varepsilon - \rho C_2 \frac{\varepsilon^2}{k+\sqrt{\nu\varepsilon}} + C_{1\varepsilon}\frac{\varepsilon}{k}C_{3\varepsilon}G_b + S_\varepsilon \tag{4.51}$$

where

$$C_1 = \max\left(0.43,\ \frac{\eta}{\eta+5}\right) \tag{4.52}$$

$$\eta = S\frac{k}{\varepsilon} \tag{4.53}$$

G_k denotes generation of turbulence kinetic energy as a result of mean velocity gradients, G_b represents generation of turbulence kinetic energy due to buoyancy, Y_M is the contribution of the fluctuating dilation in compressible turbulence to the overall dissipation rate, C_2, $C_{3\varepsilon}$ and $C_{1\varepsilon}$ are constants, S_k and S_ε are user-defined source terms, σ_k and σ_ε represent turbulent Prandtl numbers for k and ε respectively and S is the scalar measure of the deformation tensor.

The Menter-Lechner [62], [63] near wall treatment modifies the k-ε model to account for near-wall effects as shown:

$$\frac{\partial}{\partial t}(\rho k) + \frac{\partial}{\partial x_l}(\rho k u_l) - \frac{\partial}{\partial x_v}\left(\left(\mu + \frac{\mu_t}{\sigma_k}\right)\frac{\partial k}{\partial x_v}\right) = G_k - \rho\varepsilon + S_{near-wall} \tag{4.54}$$

$$\frac{\partial}{\partial t}(\rho \varepsilon) + \frac{\partial}{\partial x_l}(\rho \varepsilon u_l) - \frac{\partial}{\partial x_v}\left(\left(\mu + \frac{\mu_t}{\sigma_\varepsilon}\right)\frac{\partial \varepsilon}{\partial x_v}\right) = C_{1\varepsilon}\frac{\varepsilon}{k}G_k - C_{2\varepsilon}\rho\frac{\varepsilon^2}{k} \tag{4.55}$$

$$\mu_t = \rho C_\mu \frac{k^2}{\varepsilon} \tag{4.56}$$

where

$C_{1\varepsilon} = 1.44$, $C_{2\varepsilon} = 1.92$, $C_{\mu} = 0.09$, $\sigma_k = 1.0$, $\sigma_{\varepsilon} = 1.3$, ρ is the density of the liquid and $S_{near-wall}$ is a source term that accounts for near-wall effects.

The model of Troshko-Hassan [202] was used for the influence of the vapour phase on the turbulence equations and it is expressed as:

$$\Pi_{kv} = C_{ke}\alpha_v K_{vl}\left|\vec{U}_v - \vec{U}_l\right|^2 \tag{4.57}$$

$$\Pi_{\varepsilon v} = C_{td}\frac{1}{\tau_v}\Pi_{kv} \tag{4.58}$$

where

Π_{kv}, $\Pi_{\varepsilon v}$ are the source terms, $C_{ke} = 0.75$, $C_{td} = 0.45$. The characteristic time of the induced turbulence is expressed as:

$$\tau_v = \frac{2C_{VM}d_b}{3C_D|\vec{U}_v - \vec{U}_l|} \tag{4.59}$$

where C_{VM} represents virtual mass coefficient and C_D denotes drag coefficient.

Bubble diameter

The model for bubble diameter can be expressed as a function of the local subcooling, ΔT_{sat} $(= T_{sat} - T_l)$ as [62]:

$$d_{bv} = \begin{cases} \max\left(1.0x10^{-5}, d_{min}.e^{\left(\frac{-(K(\Delta T_{sub} - \Delta T_{max})}{d_{min}}\right)}\right) & \Delta T_{sub} > 13.5\ K \\ d_{max} - K(\Delta T_{sub} - \Delta T_{min}) & \Delta T_{sub} \leq 13.5\ K \end{cases} \tag{4.60}$$

where

ΔT_{sat} is the degree of subcooling, T_{sat} is the saturation temperature at the prevailing pressure, T_l is the bulk liquid temperature, $d_{min} = 0.00015\ m$ (this was adjusted to $10^{-10}m$ because of the sizes of microchannels) , $d_{max} = 0.001m$ (this maximum was not reached, hence it was safe to leave the value as it is), $\Delta T_{min} = 0\ K$, $\Delta T_{max} = 13.5\ K$ (the maximum temperature variation between the inlet and outlet can be less or greater than 13.5 K depending on the heat flux). K in (4.60) is expressed as:

$$K = \frac{d_{max} - d_{min}}{\Delta T_{max} - \Delta T_{min}} \tag{4.61}$$

CHAPTER 5
SIMULATION AND OPTIMISATION IN SUBCOOLED FLOW BOILING

5.1. Computational models and description of physical models

The microchannel heat sinks are subjected to constant heat fluxes at their bottoms and water flows inside the microchannels to remove heat conducted to the inner surfaces of the microchannels from the electronic devices which are attached to the bottoms of the microchannel heat sinks. Water enters the microchannels in single phase at 25 °C and nucleation of vapour bubbles start at ONB, which is the lower limit for two-phase flow in the microchannels, and there is continuous generation of bubbles thereafter. For single-phase flow, there is no phase change as the fluid flows through the microchannels from their inlets to the outlets, hence no generation of vapour bubbles. Two-phase flow encompasses sensible and latent heats, hence high heat flux is removed from the devices being cooled compared to single-phase flow which involves only sensible heat. Also, latent heat maintains temperature uniformity of the heat sinks because it occurs at constant temperature. Figure 5.1(a)-Figure 5.1(d) show heat sinks with many microchannels where H_{ch} (D_h), W_{ch} and L are the height, width and axial length of each microchannel in the various configurations. The microchannels were arranged symmetrically in the heat sinks and this advantage was taken to select any unit cell microchannel heat sink (Figure 5.2(a)-Figure 5.2(d)) so as to save computational time. The volumes of microchannel heat sinks and microchannels are the same (fixed) for all the heat sinks and microchannel configurations. These enabled accurate and reliable comparisons of the optimal microchannel heat sink configurations. Each heat flux is fixed for all the velocity ranges considered. The volume constraints for the computational domains are defined as:

$$V_s = W_s . H_s . L\ (constant) \tag{5.1}$$

$$V_{ch} = V_s - V_{sub}\ (constant) \tag{5.2}$$

The manufacturing constraints are:

$$H_b \geq 50\ \mu m \tag{5.3}$$

$$H_{cp} \geq 50\ \mu m \tag{5.4}$$

$$W_w \geq 45\ \mu m \tag{5.5}$$

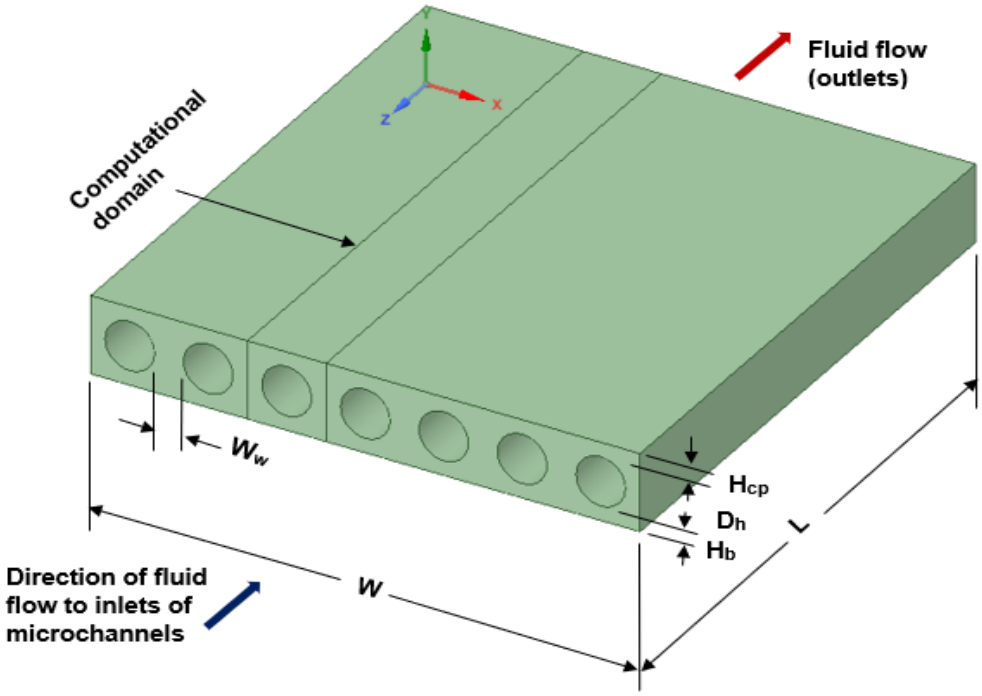

(a) Circular microchannel heat sink

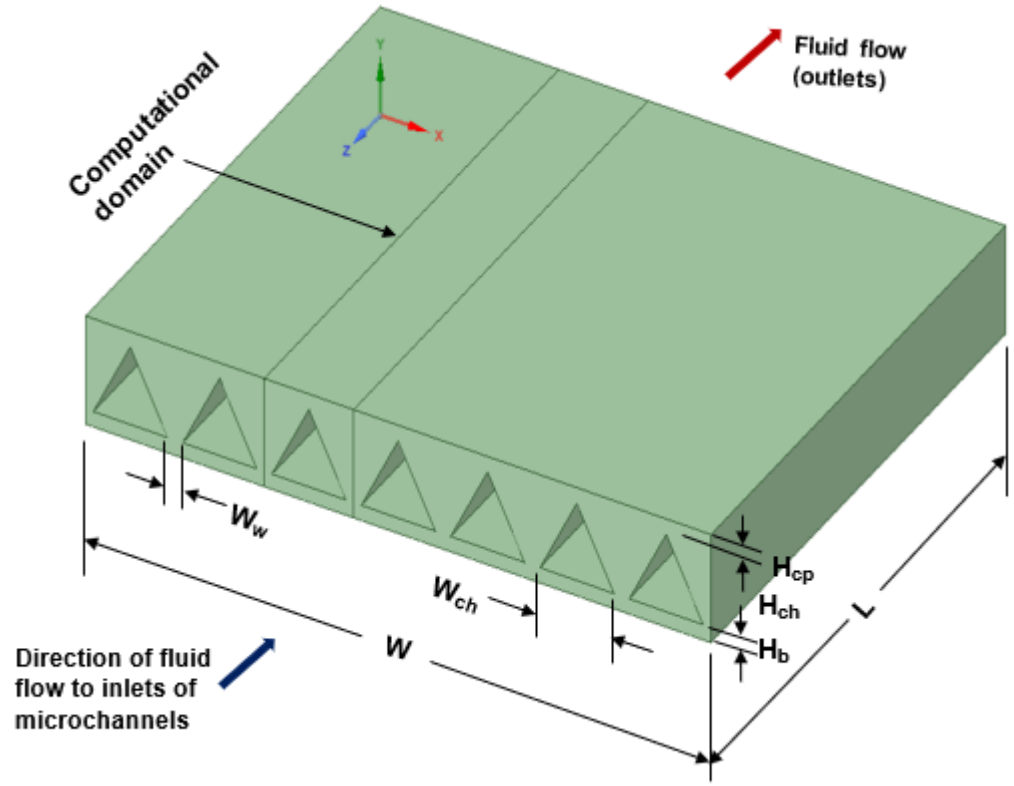

(b) Equilateral triangular microchannel heat sink

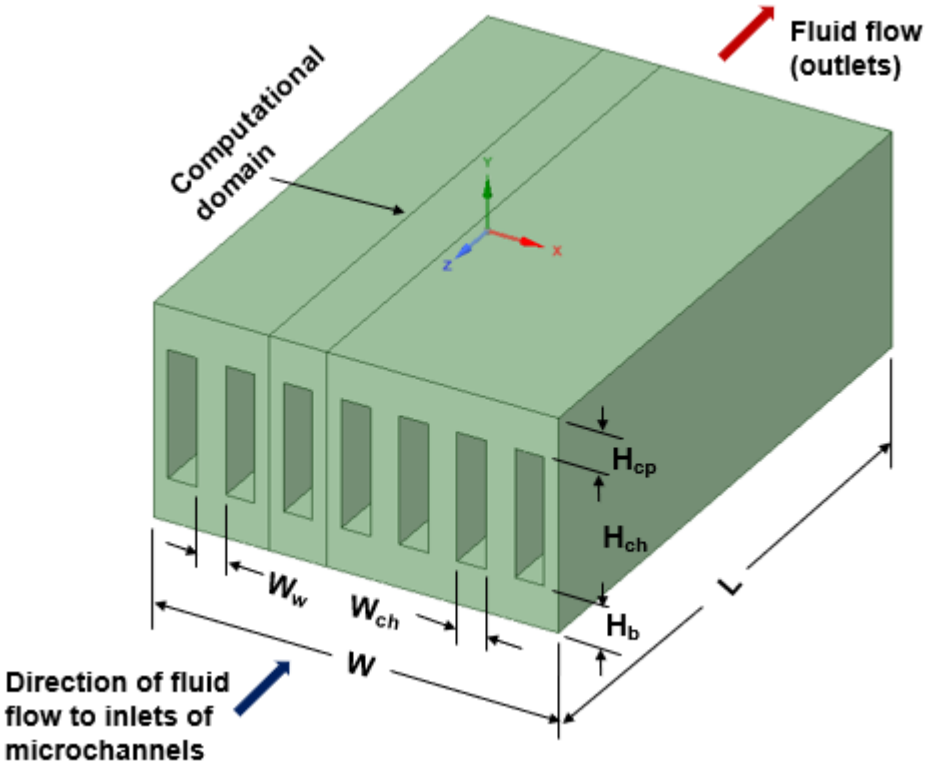

(c) Rectangular microchannel heat sink

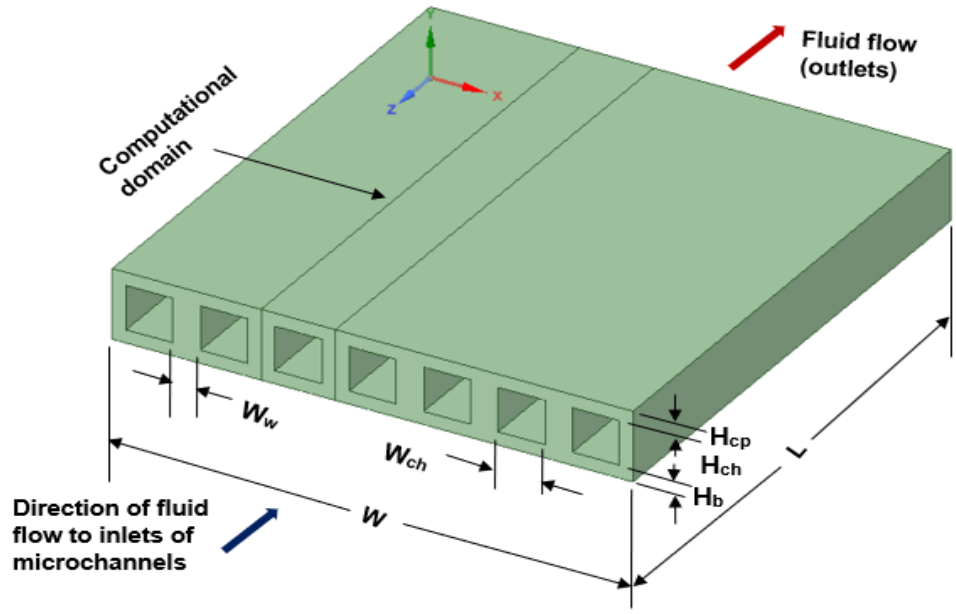

(d) Square microchannel heat sink

Figure 5.1. Multichannel heat sinks.

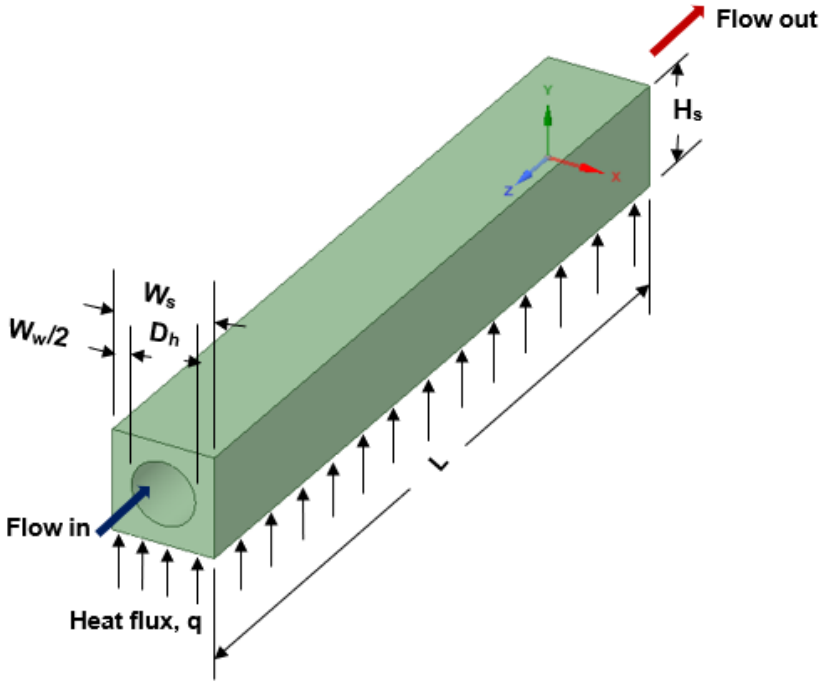

(a) Circular microchannel heat sink computational domain

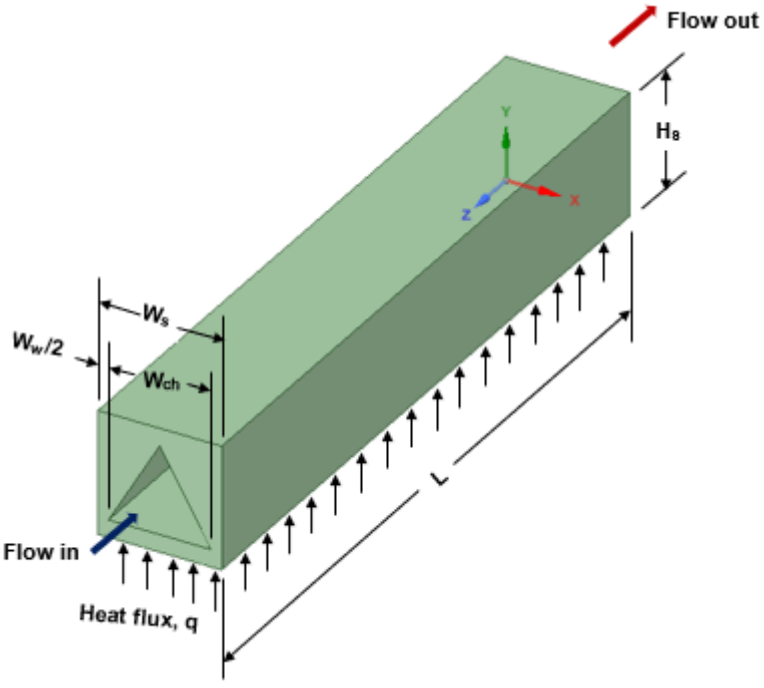

(b) Equilateral triangular microchannel heat sink computational domain

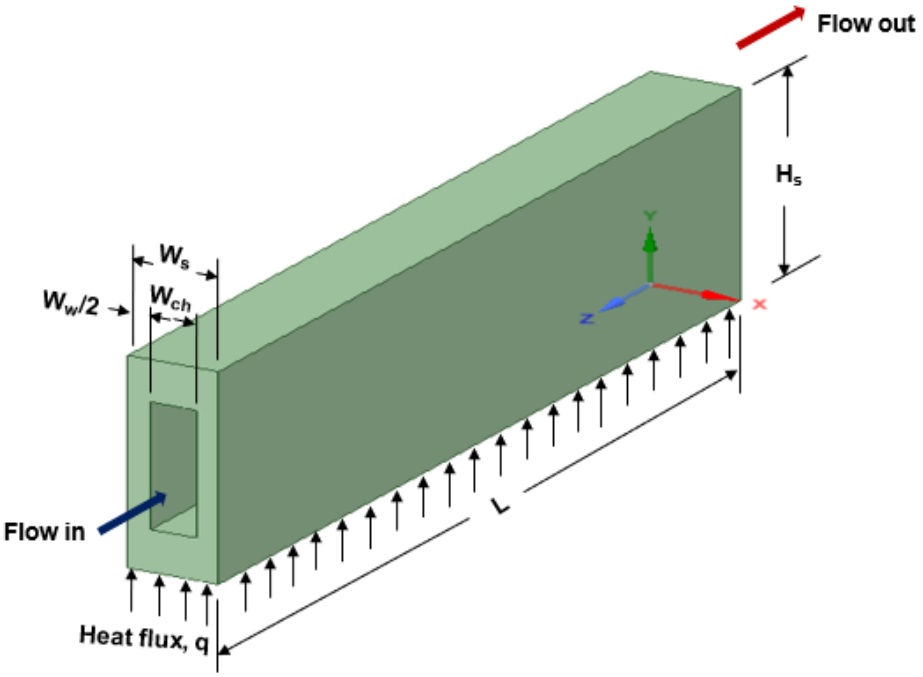

(c) Rectangular microchannel heat sink computational domain

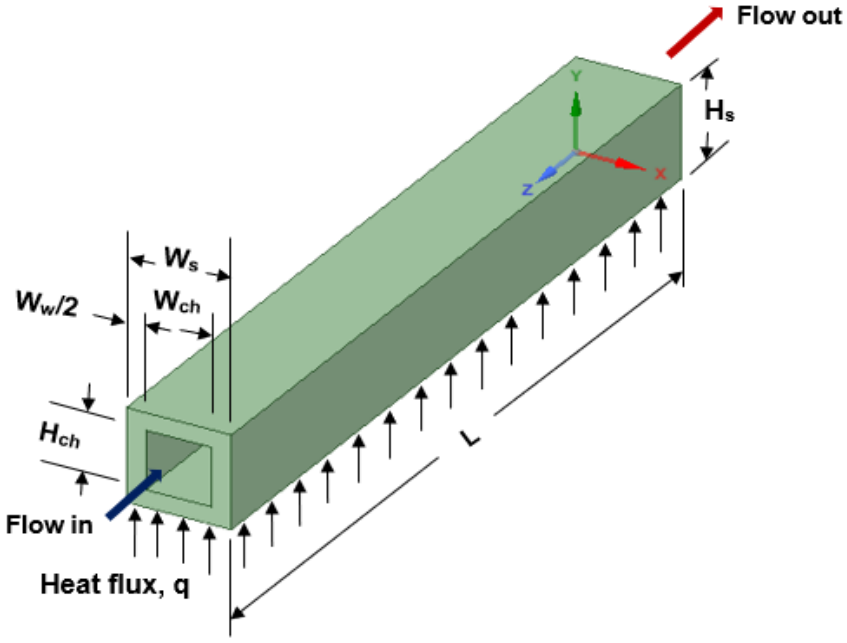

(d) Square microchannel heat sink computational domain

Figure 5.2. Microchannel heat sinks computational domains.

5.2. Computational fluid dynamics (CFD) modelling

The heat transfer was conjugate in nature with conduction in the solid and convection in the fluid. Numerical analysis is not meant to replace experimental analysis but supportive to it [203]. Also, numerical predictions have proved to be cost effective. The CFD modelling consists of geometry creation, meshing and setting up of boundary conditions to solve the problem numerically. The steps consist of:

Pre-processing
Processing
Post-processing

5.2.1. Pre-processing

This involves design of microchannel heat sinks using SpaceClaim within ANSYS FLUENT. Tiny control volumes are then created through meshing, where discretised versions of the governing equations are solved. A fine mesh generation may be required for accurate results. Hexahedral, tetrahedral, structured and unstructured meshes were used. Grid refinement tests were performed to ensure that the results were independent of the mesh size.

5.2.2. Processing

The single-phase pressure-velocity coupling problem was solved by adopting Semi-Implicit Method for Pressure Linked Equations (SIMPLE) algorithm developed by Patankar [186]. The liquid water and water vapour properties were chosen from Fluent database and these were used in the simulations. The Eulerian multiphase model was used for the two phase (subcooled boiling) and critical heat flux simulations. The pressure-velocity coupling was solved by adopting coupled algorithm with pseudo transient option. Numerical parameters and other solution algorithms were defined. Initial conditions were defined to initiate the iteration process. Discretised forms of the equations were solved iteratively by making use of the initial guesses.

5.2.3. Post-processing

Post-processing was done with FLUENT inbuilt capability for obtaining thermal and fluid flow fields.

5.3. Grid refinement

Grid independence tests were carried out for the microchannel configurations presented for the simulations and optimisations at heat flux of 200 W/cm^2 and velocity of 4 m/s in two-phase flow. The fourth row of number of nodes and number of elements for each microchannel configuration was chosen because of consistent base temperature ($T_{b,stable}$) to save computation time. The same results were adopted for single-phase flow having discovered that consistent base temperatures were obtained. The results are summarised in Table 5.1-Table 5.4.

Table 5.1. Grid refinement for circular microchannel heat sink design.

Number of nodes	Number of elements	Maximum base temperature, T_b (K)	Deviation $\left\|\frac{(T_{b,stable} - T_b)}{T_{b,stable}} \mathbf{x100}\right\|$ (%)
21706	16885	334.0368	7.6345 x 10^{-3}
58584	48540	334.0294	5.4190 x 10^{-3}
180733	159969	334.0235	3.6526 x 10^{-3}
282724	251924	334.0113	-
502586	460323	334.0112	2.9939 x 10^{-5}

Table 5.2. Grid refinement for equilateral triangular microchannel heat sink design.

Number of nodes	Number of elements	Maximum base temperature, T_b (K)	Deviation $\left\|\frac{(T_{b,stable} - T_b)}{T_{b,stable}} \mathbf{x100}\right\|$ (%)
19019	13064	332.8201	0.4050
46535	34680	331.9335	0.1376
122720	98196	331.6421	0.0497
295136	248800	331.4775	-
355312	302445	331.4775	0

Table 5.3. Grid refinement for rectangular microchannel heat sink design.

Number of nodes	Number of elements	Maximum base temperature, T_b (K)	Deviation $\left\|\frac{(T_{b,stable} - T_b)}{T_{b,stable}} \mathbf{x100}\right\|$ (%)
20306	13774	316.6475	0.1724
44690	31008	317.6919	0.1569
118590	90552	317.2618	0.0213
279898	228000	317.1943	-
359976	302445	317.1942	3.1526×10^{-5}

Table 5.4. Grid refinement for square microchannel heat sink design.

Number of nodes	Number of elements	Maximum base temperature, T_b (K)	Deviation $\left\|\frac{(T_{b,stable} - T_b)}{T_{b,stable}} \mathbf{x100}\right\|$ (%)
17160	11502	332.7761	0.1895
44075	33252	332.5599	0.1244
127440	103782	332.2318	0.0257
288720	245200	332.1466	-
320544	272412	332.1466	0

5.4. Model validation

The single-phase and two-phase models used for the simulations were validated with the available and reliable experimental data. The validation processes are discussed in the following sections.

5.4.1. Single-phase flow

Single-phase model in ANSYS code was validated with the experiment of Tuckerman and Pease [8] using the same operating conditions. The refinements of mesh (grid) were done gradually until stable base (bottom) wall temperatures were achieved. The number of nodes

and elements that produced stable temperatures are shown in Table 5.5. The results were compared with the experimental data as shown in Table 5.6. The percentage error was calculated as

$$\frac{(Exp-Num)}{Exp} \text{ x } 100 \quad (5.6)$$

where Exp and Num are experimental and numerical values of thermal resistance. The experimental and numerical results are in close agreements; hence the model is reliable.

Table 5.5. Maximum stable base temperatures.

Number of nodes	Number of elements	Maximum base temperature (K)
271201	200750	316.01
266084	198560	327.34
271943	202032	367.65

Table 5.6. Comparison of experimental data of Tuckerman and Pease [8] with numerical data [$T_{f,in}$ =296.15 K, L_s=10000 μm].

Exp	Width of channel W_{ch} (μm)	Fin thickness W_w (μm)	Height of channel H_{ch} (μm)	Pressure drop Δp (N/m^2)	Heat flux q (W/cm^2)	Thermal resistance Exp (°C /W)	Thermal resistance Num (°C /W)	Deviation (%)
1	56	44	320	103421	181	0.110	0.1097	0.273
2	55	45	287	117211	277	0.113	0.1126	0.354
3	50	50	302	213737	790	0.090	0.0905	0.556

5.4.2. Two-phase flow (subcooled flow boiling)

The wall heat flux partitioning (RPI) model for subcooled flow boiling was compared with the work of Qu and Mudawar [154] for validation of the ANSYS code. The experimental geometric parameters for validation are shown in Table 5.7. The numerical results were compared with the experimental data for outlet subcooling at boiling incipience for various inlet velocities and rise in temperature at different Reynolds numbers with inlet temperature of 30 ^{o}C. Domain discretisation was initially performed with a fine mesh of 3762 nodes and 1885 elements. This was refined gradually until a stable outlet temperature was achieved with 312156 nodes and 242018 elements. The maximum error of 2.5045% between experimental data and numerical data for the outlet temperature occurred at point 3 in Figure 5.3(a) and Figure 5.3(b). The numerical results were in good agreement with the experimental data; hence this shows that the model is reliable. The details of the grid refinement results are shown in Table 5.8. The comparison of numerical results with experimental data are shown in Figure 5.3(a) and Figure 5.3(b). The dimensionless liquid velocity and temperature profiles are shown in Figure 5.4(a)-Figure 5.4(c). The numerical results and experimental data are in good agreement.

Table 5.7. Dimensions of a unit cell microchannel heat sink (μm) [154].

Height of sink H_s	Height of channel H_{ch}	Width of sink W_s	Width of channel W_{ch}	Height of cover plate H_{cp}	Base thickness of channel H_b	Length of sink/channel L_s	Hydraulic diameter D_h
15877	713	467	231	12700	2464	44800	348.95

Table 5.8. Grid independence result.

Number of nodes	Number of elements	Maximum outlet temperature (K)	Deviation $\left\|\frac{(T_{max,stable} - T_{max})}{T_{max,stable}} x100\right\|$ (%)
3762	1885	369.36	0.58
14300	7224	369.57	0.52
43485	27742	370.59	0.25
110148	79443	371.507	8.075×10^{-4}
288948	223908	371.508	5.383×10^{-4}
312156	242018	371.51	-
325312	254395	371.51	0
542300	441816	371.51	0

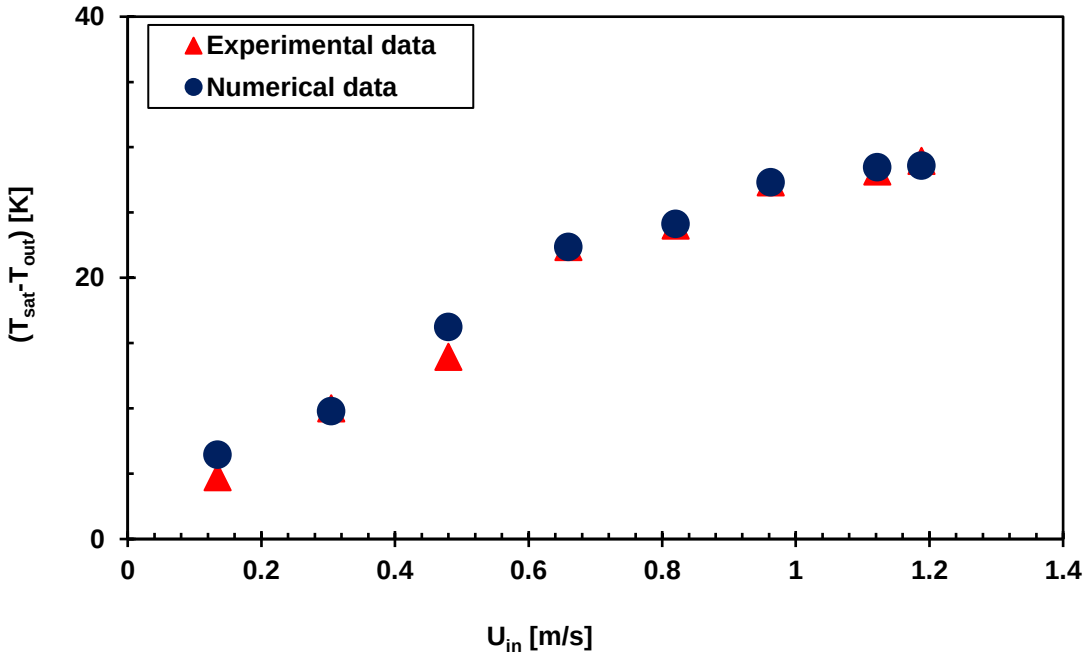

(a) Comparison of numerical results and experimental data of outlet subcooling at boiling incipience [154]

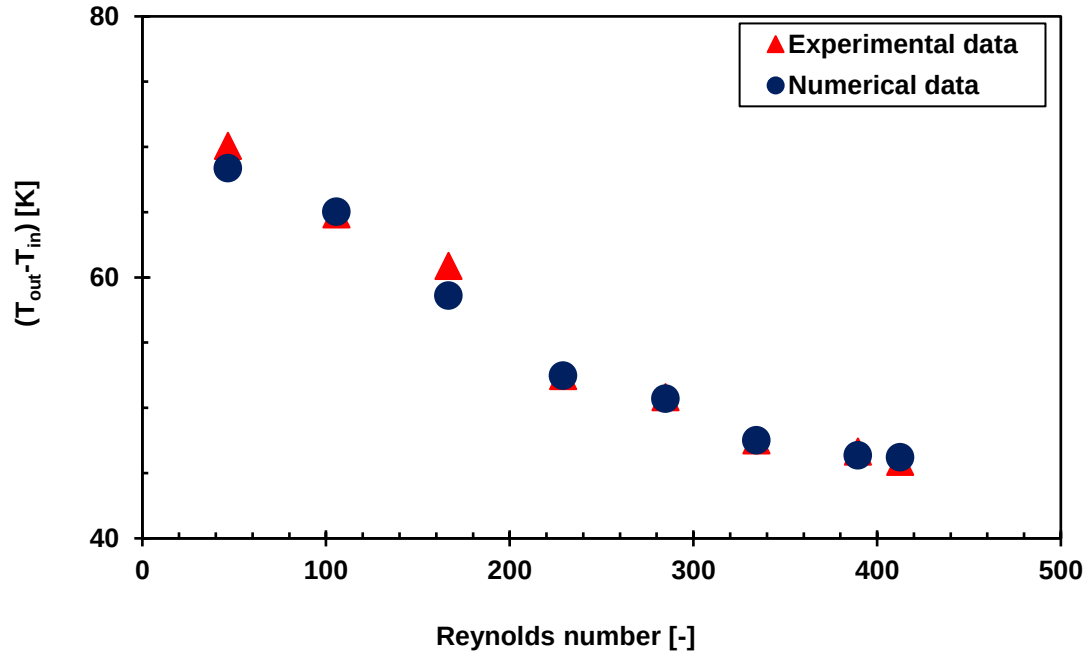

(b) Comparison of numerical results and experimental data of temperature rise in the microchannel [154]

Figure 5.3. Comparison of numerical results with experimental data.

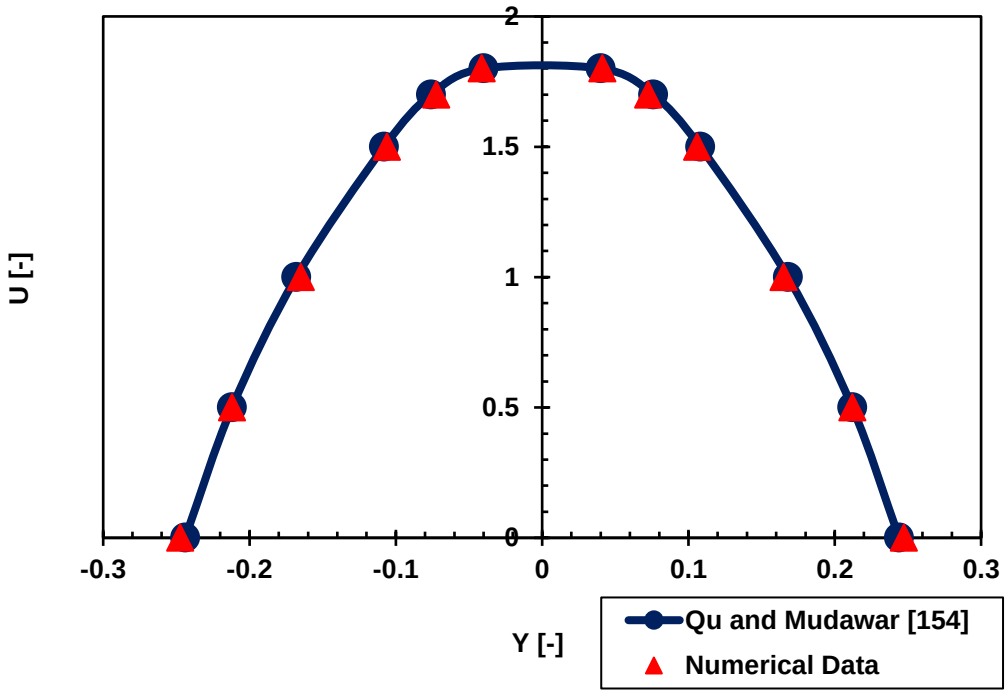

(a) Comparison of numerical results of dimensionless liquid velocity profile along y-axis with [154]

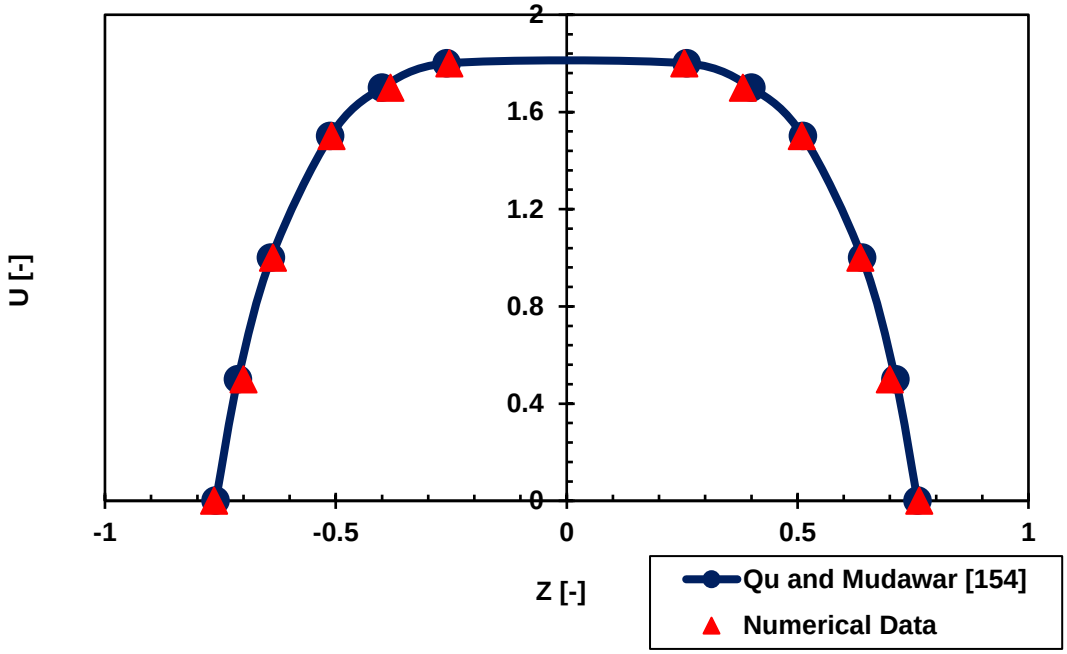

(b) Comparison of numerical results of dimensionless liquid velocity profile along z-axis with [154]

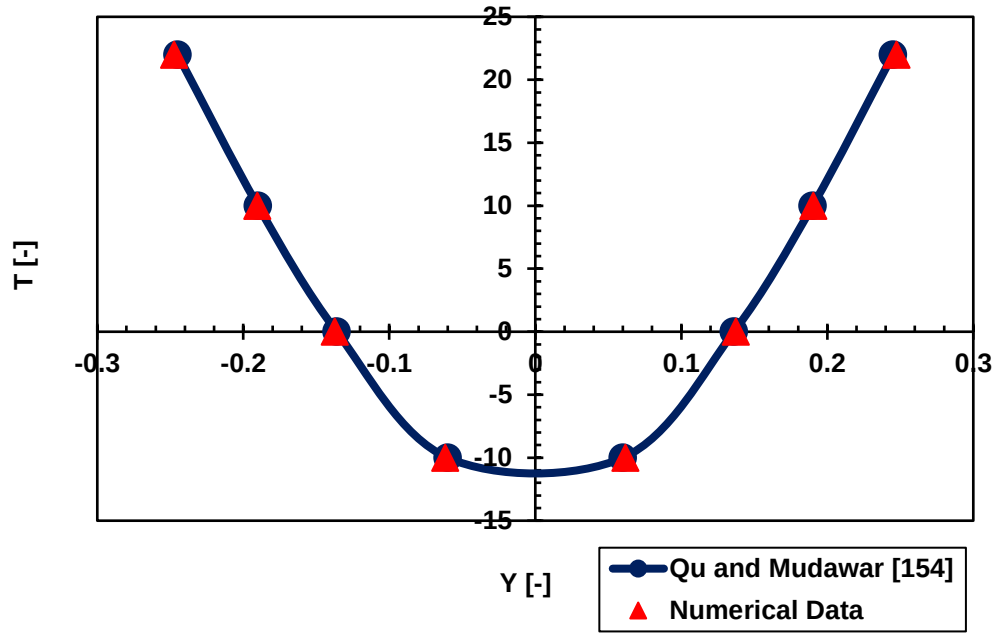

(c) Comparison of numerical results of dimensionless liquid temperature profile along y-axis with [154]

Figure 5.4. Water velocity and temperature profiles at the microchannel exit.

5.5. Optimisation procedure

Design exploration describes the relationship between the design variables (geometric and flow parameters) and the thermal performance of the microchannel heat sink. Goal driven optimisation (GDO) is a constrained, multi-objective optimisation technique which gives the best possible designs from a set of samples, given the objectives and constraints specified for the geometric and flow parameters. Response surface optimisation which is a goal driven optimisation in ANSYS 18.1 Design Explorer [156] was used in this study. The aim was to minimise the thermal resistance of each of the microchannel heat sink configurations and in doing so, the maximum outlet wall temperatures were minimised. The volumes of microchannel heat sinks and microchannels were fixed for the range of velocity and each heat flux considered. As an example, for heat flux of 100 W/cm^2 and velocities of 0.1-0.5 to 4.0-4.5 m/s, the heat flux was fixed throughout.

After creating initial model and initial parameters are defined, a response surface system is inserted in the project. Based on the information provided, the design of experiment (DOE) part of the response surface system creates design space sampling. Once a goal driven optimisation has been introduced, the optimisation study which includes optimisation method, setting the objectives and constraints and specifying the domain, is defined.

All the geometric parameters viz., height, width and length of each of the microchannel heat sinks; height, width and length of each of the microchannels (length of microchannel heat sink is the same as the length of microchannel) were allowed to morph so as to obtain optimal parameters within each velocity range. The velocities varied in each range, for the microchannel heat sinks to obtain their optimal values. Approximate values of geometric parameters of each of the unit cell microchannel heat sinks used for the optimisations are given in Table 5.9-Table 5.12. The length of microchannel heat sinks in Table 5.9-Table 5.12 is exact while other geometric parameters have been approximated for circular, equilateral triangular and square microchannel heat sinks to two decimal places here because of space. The exact values were used in the simulations and optimisations.

Table 5.9. Geometric parameters of a unit cell circular microchannel heat sink (μm).

Height of sink	Width of sink	Height of channel	Width of channel	Length of sink/channel
H_s	W_s	H_{ch}	W_{ch}	L_s
588.96	588.96	401.92	401.92	9750

Table 5.10. Geometric parameters of a unit cell equilateral triangular microchannel heat sink (μm).

Height of sink	Width of sink	Height of channel	Width of channel	Length of sink/channel
H_s	W_s	H_{ch}	W_{ch}	L_s
588.96	588.96	468.78	541.30	9750

Table 5.11. Geometric parameters of a unit cell rectangular microchannel heat sink (μm).

Height of sink	Width of sink	Height of channel	Width of channel	Length of sink/channel
H_s	W_s	H_{ch}	W_{ch}	L_s
925	375	725	175	9750

Table 5.12. Geometric parameters of a unit cell square microchannel heat sink (μm).

Height of sink	Width of sink	Height of channel	Width of channel	Length of sink/channel
H_s	W_s	H_{ch}	W_{ch}	L_s
588.96	588.96	356.2	356.2	9750

The velocities were ranged from (0.1-0.5 m/s) to (6.5-7.0 m/s). Mass velocity (Mass flux) was not used in this work but could be obtained through multiplication of the velocity of flow by the density of deionised water.

Most of the geometric parameters and velocities used in the optimisation procedure had also been used for parametric analysis and other studies for microchannel heat sinks, in the literature [89], [204]-[206]. Heat fluxes between 100 W/cm^2 and 1200 W/cm^2 were achieved in this study, the target being the cooling of microelectronic devices. Optimisation was done to obtain the best geometric and flow parameters for the microchannel heat sinks in each velocity range and for each heat flux.

5.6. Critical heat flux simulation procedure

Non-equilibrium boiling model in ANSYS 18.1 [62], [63], which is an extension of wall heat flux partitioning (RPI) model for modelling up to departure from nucleate boiling (critical heat flux) in subcooled flow boiling was used for the simulations. The simulations were based on optimal microchannel heat sinks at velocities of 2.0-2.5 to 3.5-4.0 m/s and heat flux of 100 W/cm^2. Optimal velocities for the heat flux were used in the simulations for each of the microchannel configurations. The highest inner wall temperatures at the exits of the microchannel heat sinks were used in the computation of wall superheat defined as $(T_{wall} - T_{sat})$. Optimal velocity in each range was used and heat flux was increased at intervals of 50 W/cm^2 until the last stable outlet temperature corresponding to the critical heat flux was reached. The saturation temperature of water at 1.01325 bar (outlet pressure) was used in the computations.

CHAPTER 6
RESULTS AND DISCUSSION

6.1. Introduction

Consistency and accuracy in the generation of results were ensured for all the velocities and heat fluxes considered. This process was monitored by comparing the temperature of the previous velocity range with the current velocity range to ensure that the value of temperature had decreased from the previous value while that of pressure drop had increased from the previous value. Also, going from a low heat flux to a high heat flux, the temperature value should increase for the same velocity range. Typical examples for subcooled flow boiling in optimal circular microchannel heat sinks are given in Table 6.1 and Table 6.2.

Table 6.1. Generated optimal values at 100 W/cm^2.

Velocity (m/s)	Pressure drop (N/m^2)	Base temperature (K)	Outlet water temperature (K)
1.4999	4413.7739	330.2045	312.5746
1.9968	6670.4912	325.3316	308.9030
2.4863	9268.0352	322.0667	306.7246
↓	↓	↓	↓
Velocity increases	Pressure drop increases	Temperature decreases	Temperature decreases

Table 6.2. Generated optimal values at 200 W/cm^2.

Velocity (m/s)	Pressure drop (N/m^2)	Base temperature (K)	Outlet water temperature (K)
1.4992	4453.5786	362.0171	329.1421
1.9865	6624.3550	352.5494	320.8571
2.4972	9240.1934	345.6634	317.1181
↓	↓	↓	↓
Velocity increases	Pressure drop increases	Temperature decreases	Temperature decreases

From a low heat flux to a high heat flux, the outlet temperatures must increase as can be observed from the tables whereas it is not the same for pressure drop because atmospheric pressure was assumed at the outlet and it was observed that optimal geometric parameters and velocity had significant influence on pressure drop. Therefore, it is possible to have the pressure drop situations shown in Table 6.1 and Table 6.2. The velocities were ranged from 0.1-0.5 m/s to 6.5-7.0 m/s at intervals of 0.5 m/s. Different global optimal velocities were obtained at each range going from one heat flux to another. The explanation for the optimal temperatures, pressure drops and velocities here is valid for the remaining three configurations used in this study. The lengths considered in the simulations and optimisations were between 9200 and 12400 μm for all the configurations. Other geometric parameters were ranged appropriately to ensure that fixed volumes of microchannels and heat sinks were obtained in the computer experiments (DOE) and optimisations. The best optimal geometric and flow parameter results for each microchannel configuration were used in plotting the graphs. Examples of local and global optima are shown in Figure 6.1.

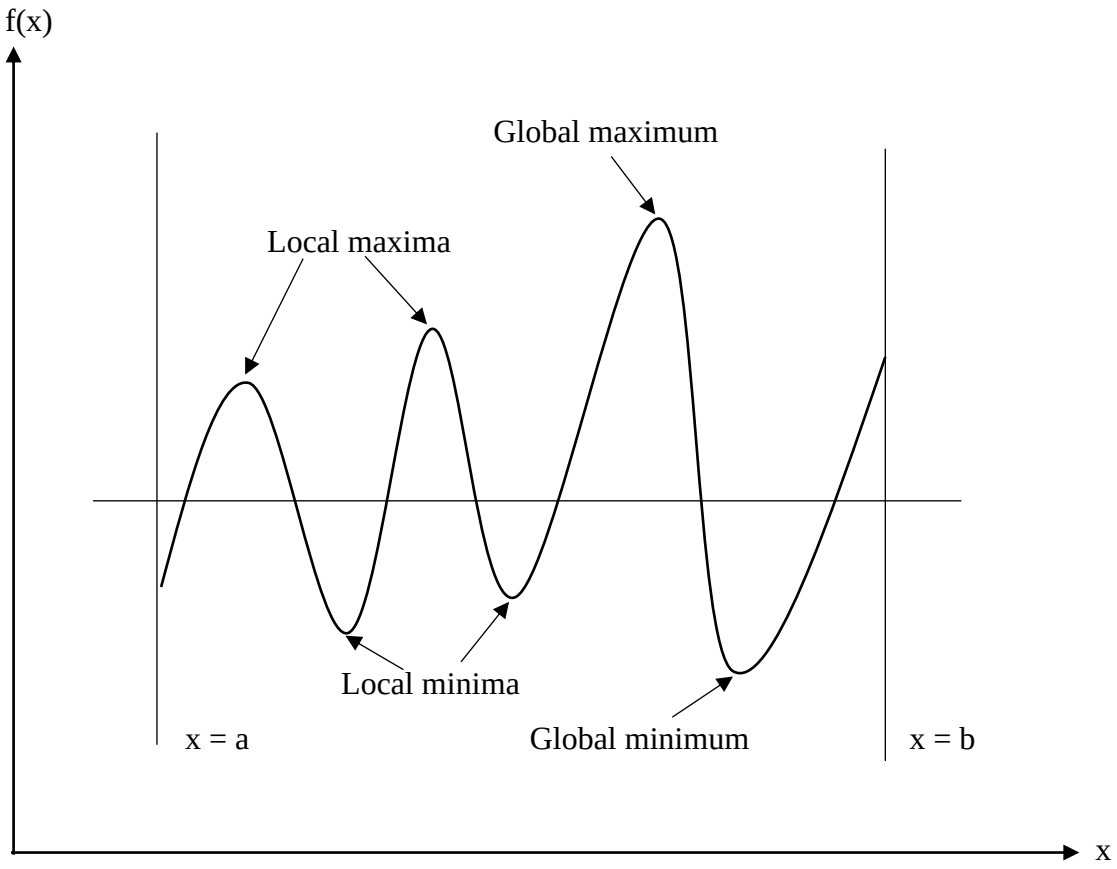

Figure 6.1. Minimum and maximum optimal values.

The independent variable x, and f(x) are allowed to have any values between a and b. The global maximum and minimum are the points of best performance of the parameters being optimised depending on whether they are to be maximised or minimised while a to b represents the range considered in the optimisation.

6.2. Optimal geometric and flow parameters

The thermal resistances of the microchannel configurations were minimised; hence the maximum base temperatures were minimised. The geometric and flow parameters were optimised for the velocities and heat fluxes considered. This is in line with constructal design principle which states that for a finite-size flow system to persist in time (live), it must evolve in such a way that it provides easier access to the imposed (global) currents that flow through it. If a system is free to morph under global constraints, the better flow architecture is the one that minimises the global flow resistances or maximises the global flow access [97], [171], [207], [208].

In this study, numerical analyses and optimisations were done to obtain microchannel heat sinks that performed optimally at high heat fluxes not familiarly reported for similar geometries in the open literature. It was also the aim of this study to have many microchannel heat sinks that performed optimally in subcooled flow boiling by ensuring that the flow did not exceed bubbly flow in the simulations. Where the results were unstable and there were convergence issues in the simulations and they could not be resolved, simulations were normally terminated. For each heat flux and velocities from 0.1-0.5 to 4.0-4.5 m/s for example, there were nine optimal microchannel heat sinks which could be used in the cooling of electronic devices.

6.2.1. Circular microchannel heat sinks

6.2.1.1. Subcooled flow boiling (Two-phase flow)

The thermal resistances of optimal circular microchannel heat sinks are shown in Figure 6.2 for heat fluxes between 100 and 500 W/cm^2. As can be observed, the thermal resistance followed the same trend and the base temperature which is the temperature of the device being cooled increased from a low heat flux to a high heat flux in Figure 6.3. The thermal resistances of optimal microchannel heat sinks decrease as Reynolds number increases which is a common trend in the open literature. Each point on the curves in Figure 6.2 represents an optimal microchannel heat sink with complete optimal geometric and flow parameters. This gives room for flexibility in the choice of microchannel heat sinks with different thermal resistances and Reynolds numbers. Base temperatures at 400 and 500 W/cm^2 are not shown in Figure 6.3 as a result of turbulent flow. Figure 6.3 presents the operating temperatures of optimal microchannel heat sinks at the heat fluxes shown. The operating temperatures are within those for modern electronics [5]. The temperatures of optimal heat sinks at a higher heat flux are higher than those at a lower heat flux which is expected. The velocity ranges for which optimal values were obtained were 0.1-0.5, 0.5-1.0 …., 4.0-4.5 m/s (intervals of 0.5 m/s which is applicable to other heat fluxes) for 100 W/cm^2, 1.0-1.5 to 4.0-4.5 m/s for 200 W/cm^2, 2.5-3.0 to 5.0-5.5 m/s for 300 W/cm^2, 4.5-5.0 to 6.5-7.0 m/s for 400 W/cm^2 and 5.5-6.0 to 6.5-7.0 m/s for 500 W/cm^2. Each velocity range produced an optimal velocity corresponding to optimal geometric and flow parameters.

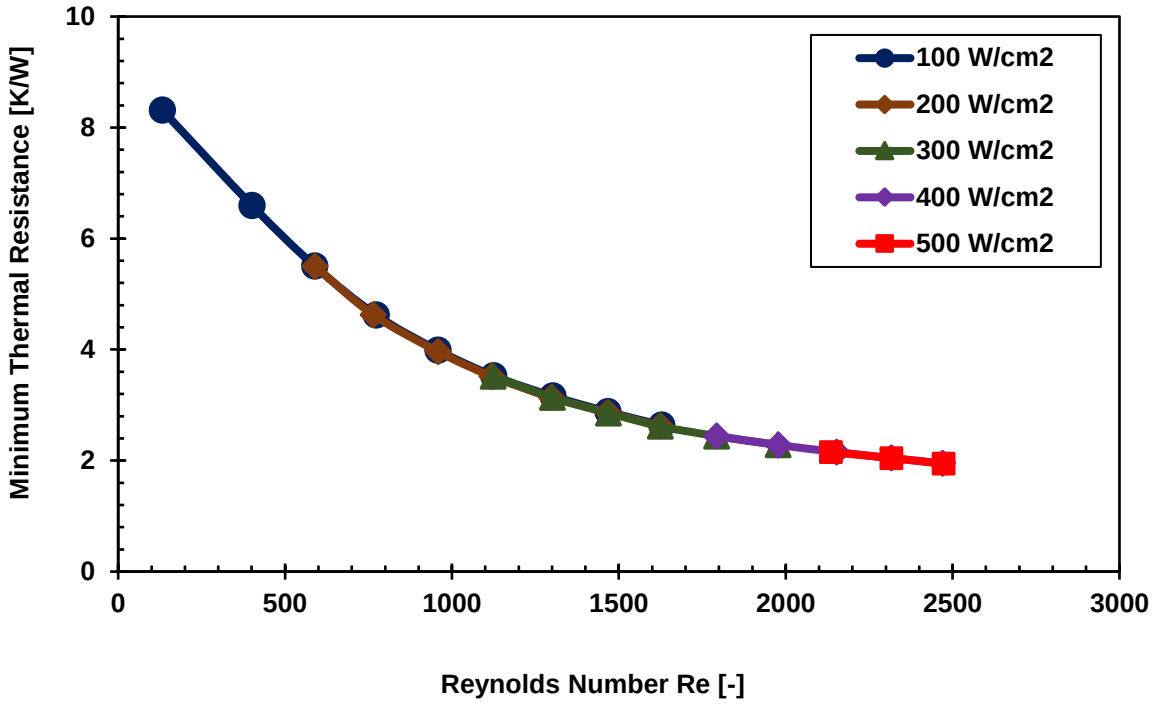

Figure 6.2. Thermal resistances of microchannel heat sinks.

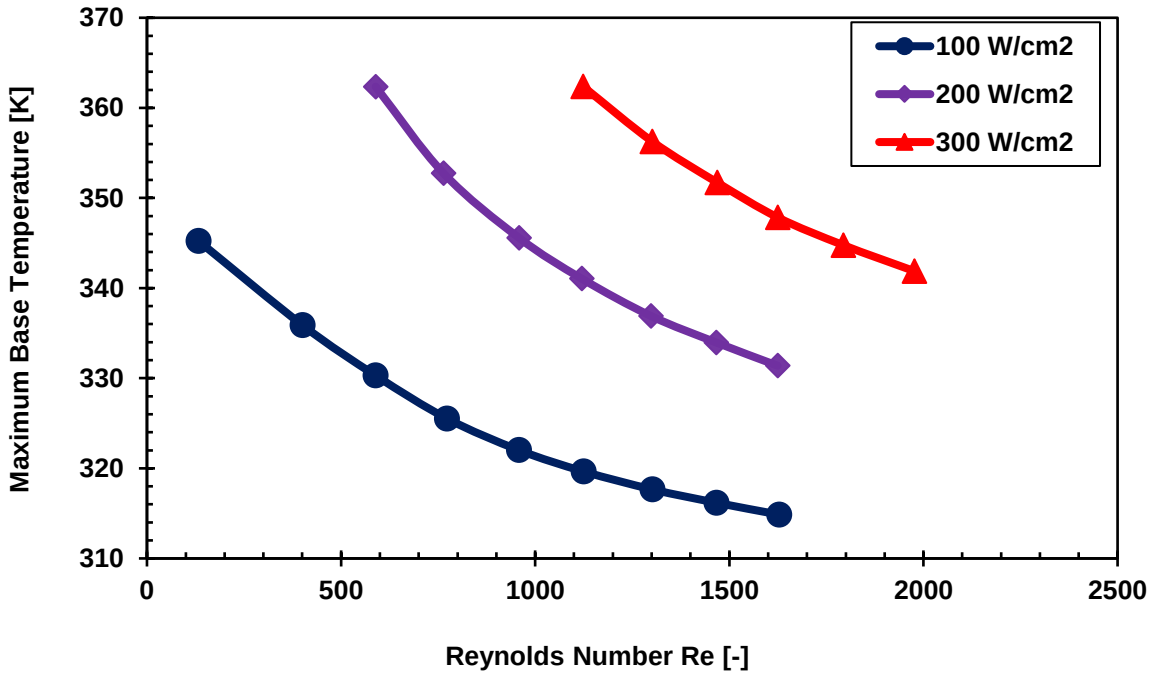

Figure 6.3. Maximum base temperatures of optimal microchannel heat sinks.

The pumping power represents the energy per second required to drive the coolant from the micropump through an optimal microchannel. Micropumps are for cooling application in microelectronics because the use of liquid cooling is necessary to ease the challenging cooling constraints posed by the need to remove high heat flux beyond the limit of air cooling. The pumping power requirements for the optimal microchannels are shown in Figure 6.4. The pressure drop increases as Reynolds number increases which translates to increase in pumping power for the microchannels in Figure 6.4 and this could provide flexibility in the choice of microchannel heat sinks because of the uniqueness of the pumping power requirements. Pressure drop increases as vapour bubble formation increases. It also increases with velocity which is consistent with literature [112], [116].

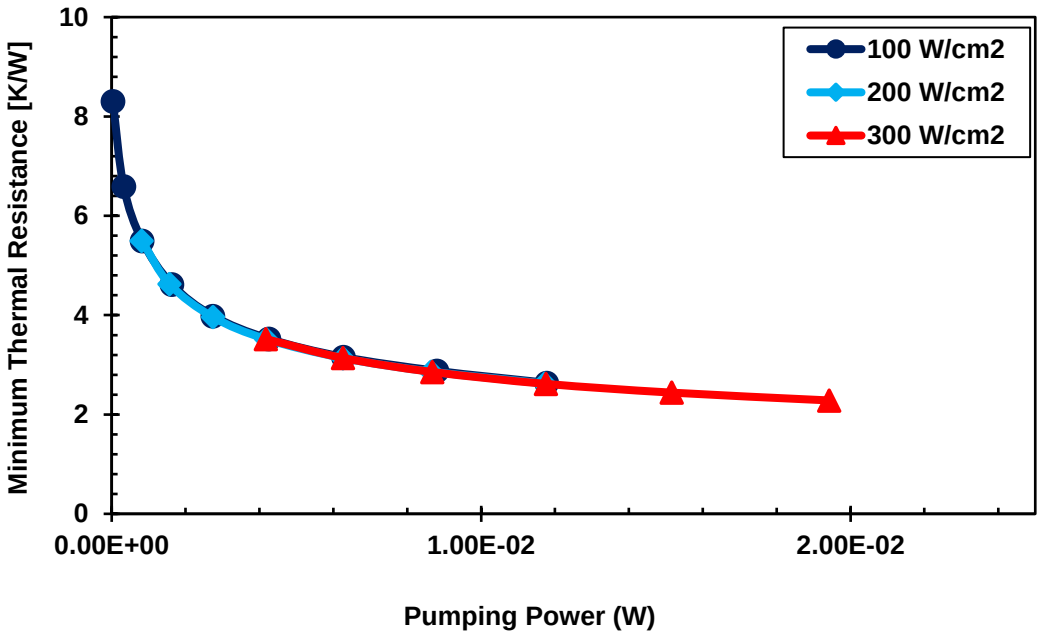

Figure 6.4. Pumping power of optimal microchannel heat sinks.

Velocity of flow and length influence Reynolds number, pressure drop and thermal performances of the microchannels. As the length and velocity increase at a particular heat flux, pressure drop and Reynolds number increase. The effects of optimal length on optimal microchannel heat sinks are shown in Figure 6.5. As length increases, Reynolds number increases and base temperature decreases. The influence of Bejan number, a dimensionless

pressure drop on optimal microchannel heat sinks are shown in Figure 6.6. Optimal length increases as Bejan number increases to achieve the desired cooling effect.

Figure 6.7 and Figure 6.8 show the effects of hydraulic diameter on optimal microchannel heat sinks. Wide variations of hydraulic diameters were not witnessed, yet low thermal resistances and pumping power were achieved with the operating temperatures in the acceptable range as discussed earlier. As the length increases, hydraulic diameter of the microchannel decreases; these variations are expected because the volumes of microchannels and heat sinks are fixed. The hydrodynamic boundary layer thickness grows from the inlet of the microchannel to full size of the microchannel at the entrance length where the velocity is fully developed. The entrance length together with the ratio of length of microchannel to its hydraulic diameter can have effect on the optimal efficiency of the microchannel heat sink [76]. The boundary layer flattens as length increases.

Figure 6.9 and Figure 6.10 show the variation of pressure drop and dimensionless pressure drop on Reynolds number. It is obvious that the trend in Figure 6.9 is the same with that in Figure 6.10 which is indicative of the correctness of the computation of Bejan number. As Reynolds number increases, pressure drop and Bejan number increase which have positive effects on the thermal characteristics of the optimal heat sinks.

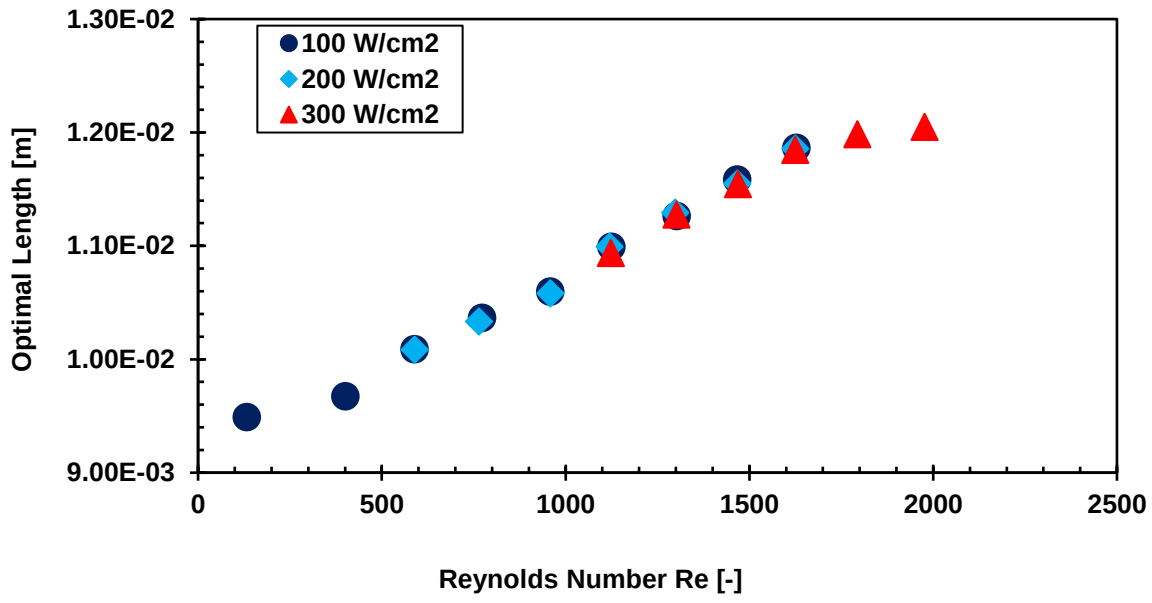

Figure 6.5. Effect of length on optimal microchannel heat sinks.

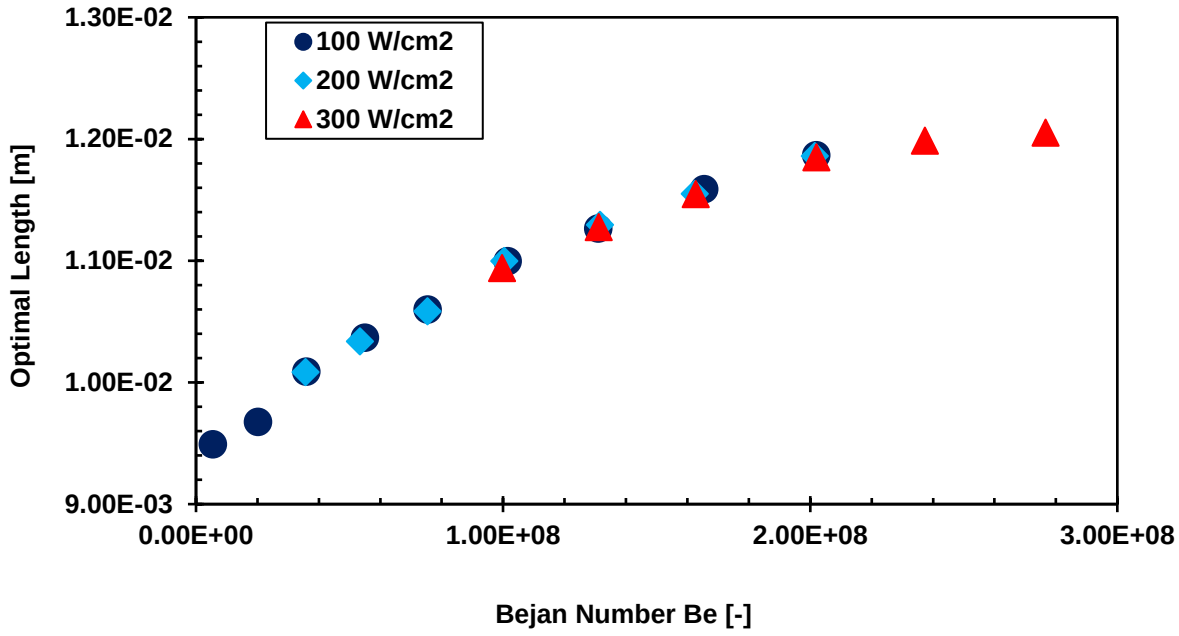

Figure 6.6. Effect of dimensionless pressure drop on optimal length.

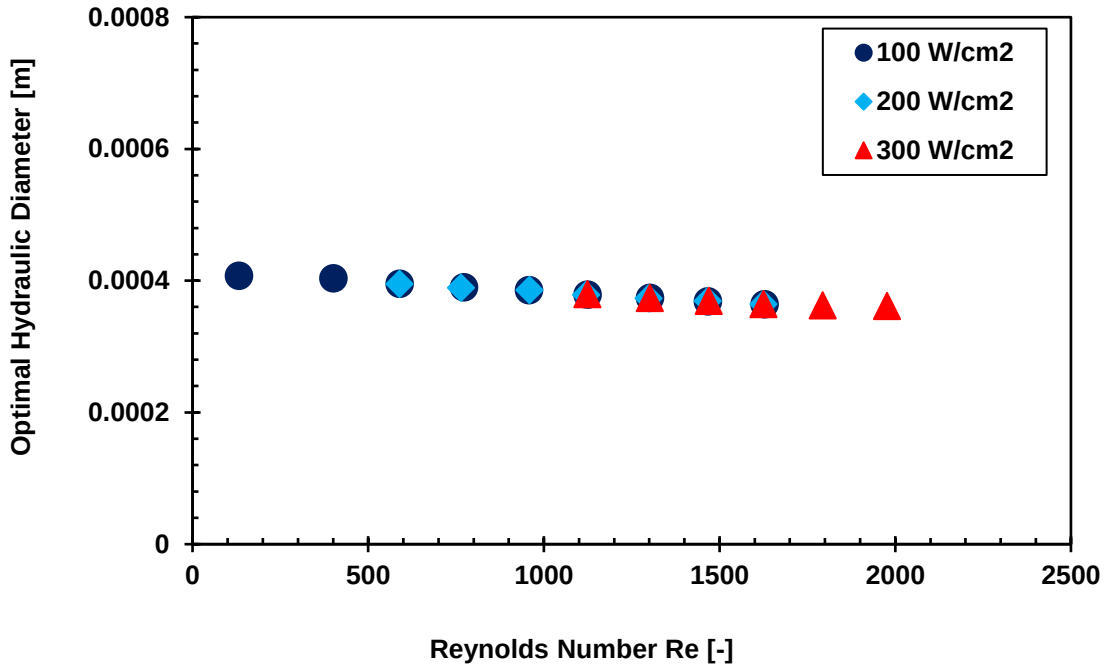

Figure 6.7. Effect of hydraulic diameter on optimal microchannel heat sinks.

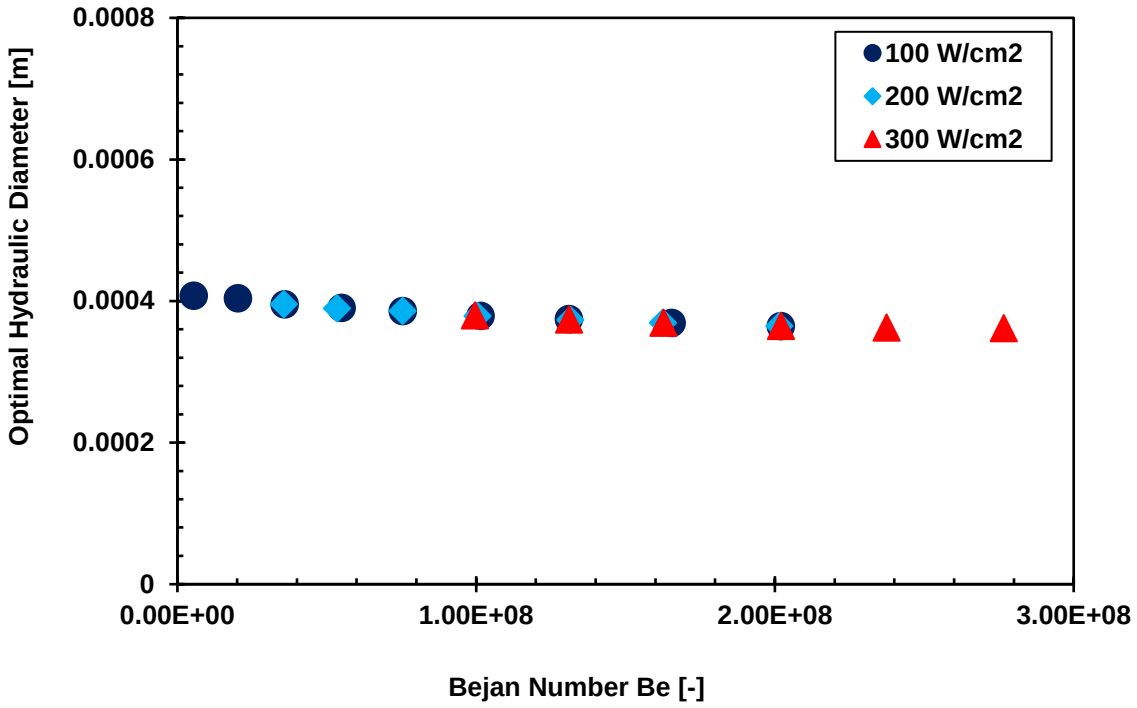

Figure 6.8. Effect of dimensionless pressure drop on optimal hydraulic diameter.

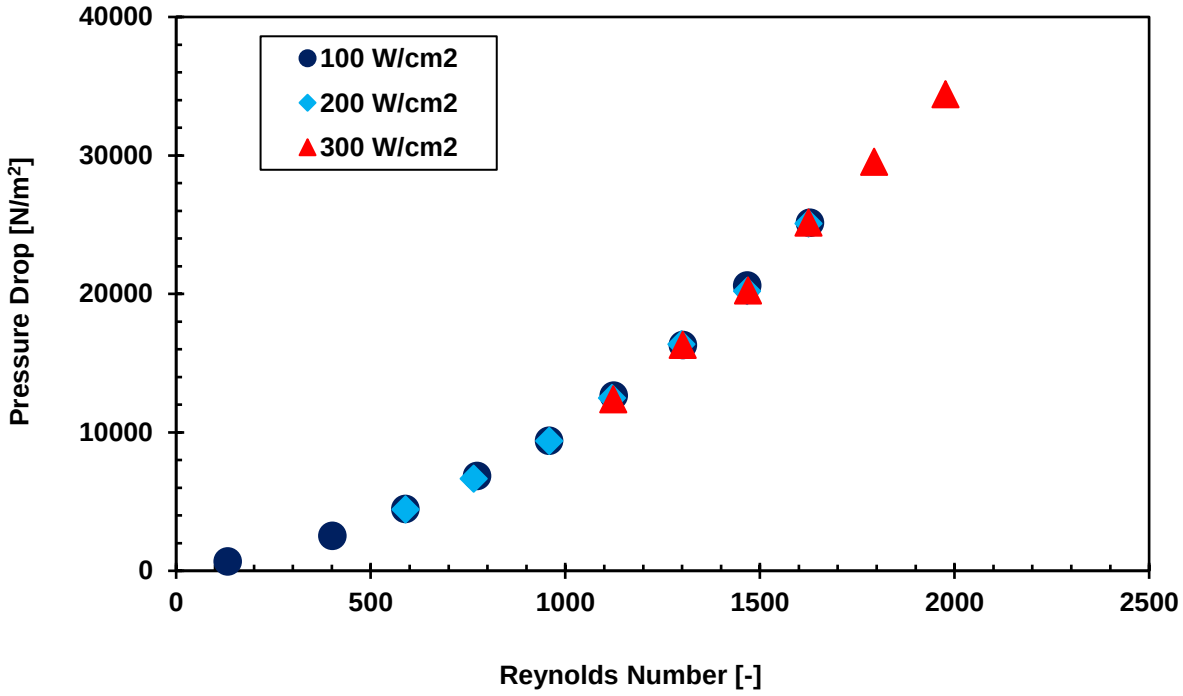

Figure 6.9. Effect of pressure drop on Reynolds number.

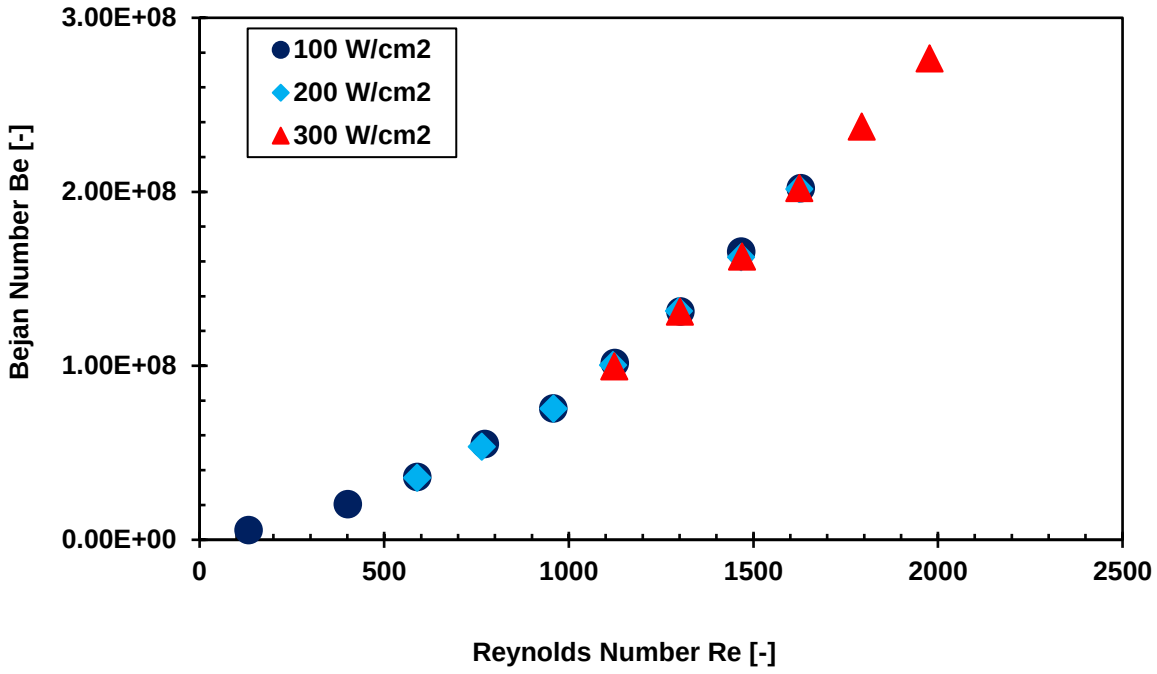

Figure 6.10. Effect of dimensionless pressure drop on Reynolds number.

Temperature contours

The heat flux for the temperature contours shown in Figure 6.11- Figure 6.15 is 100 W/cm^2 in subcooled flow boiling. In Figure 6.11, the wall temperature range between inlet and outlet of the heat sink is approximately 311.6 to 322 K. The highest base temperature recorded was 322.0134K. Figure 6.12(a) and Figure 6.12(b) attest to wall temperature difference across the optimal microchannel heat sink. The temperature distribution in Figure 6.12(a) and Figure 6.12(b) corresponds to the legend in Figure 6.11. Figure 6.13, Figure 6.14(a) and Figure 6.14(b) show water temperature contours in the microchannel and inlet and outlet water temperature contours respectively. Water entered at 298.15 K and exited at 307.095 K at an optimal velocity of 2.498 m/s. Figure 6.15 is indicative of the fact that water entered in single phase and this was maintained for a short distance before the onset of continuous generation of vapour when the inner wall temperature was more than the saturation temperature of the liquid.

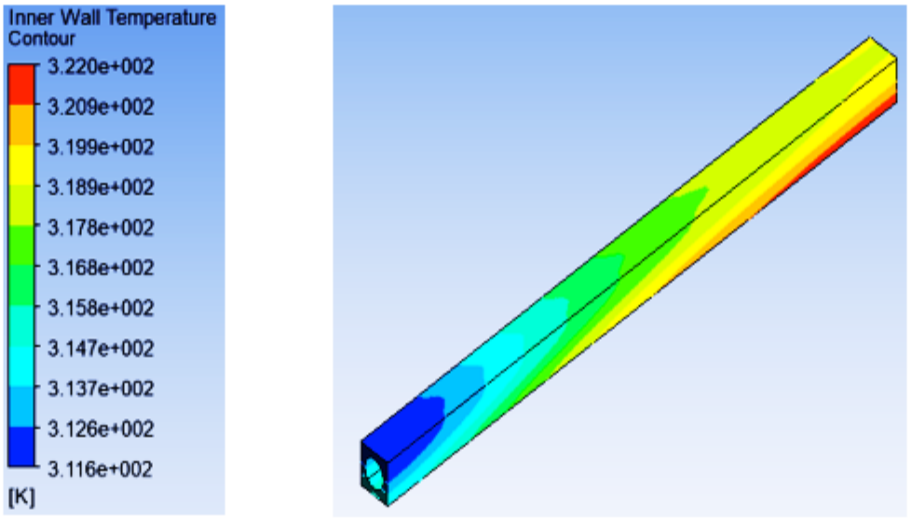

Figure 6.11. Inner wall temperature contour (base temperature = 322.013 K).

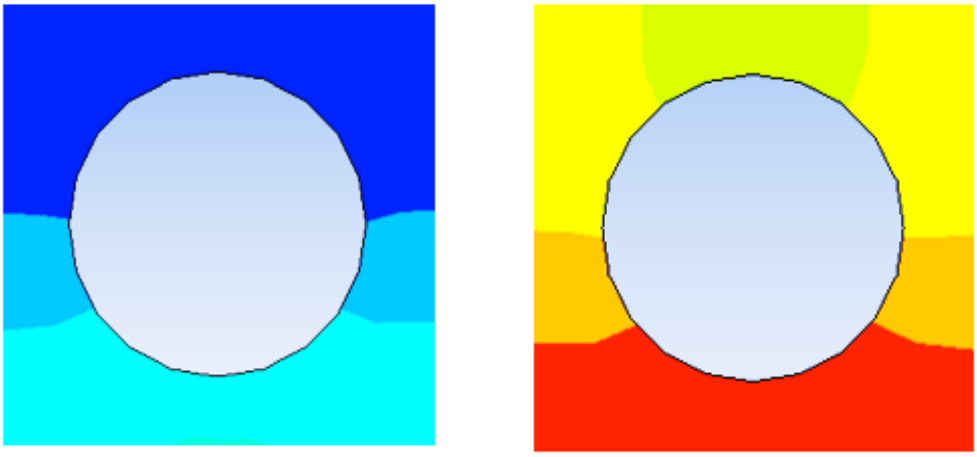

(a) Inlet wall temperature contour (b) Outlet wall temperature contour

Figure 6.12. Inlet and outlet wall temperature contours.

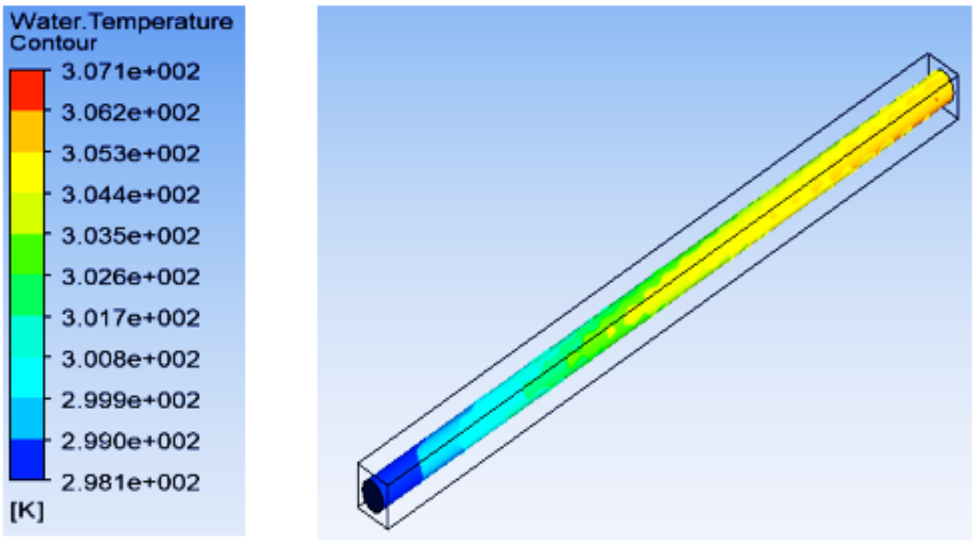

Figure 6.13. Water temperature contour.

(outlet water temperature = 307.095 K, optimal velocity = 2.498 m/s)

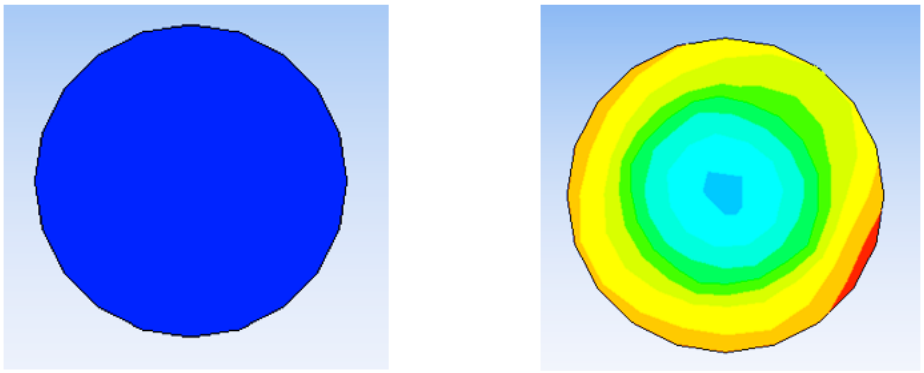

(a) Inlet water temperature contour (b) Outlet water temperature contour

Figure 6.14. Inlet and outlet water temperature contours.

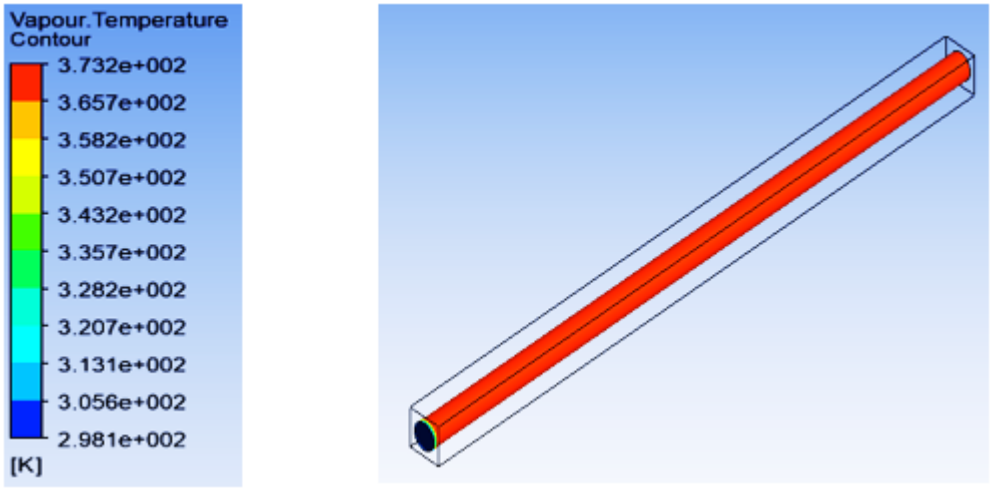

Figure 6.15. Vapour temperature contour.

6.2.1.2. Comparisons of two-phase and single-phase flow

The characteristics of optimal microchannel heat sinks in subcooled flow boiling and single-phase flow are compared at 100 and 200 W/cm^2 for which results were available in single-phase flow. Results were not available for single-phase flow at other heat fluxes because of high base temperatures outside the range for modern electronic devices. Results were available for two-phase flow (subcooled flow boiling) between 0.1-0.5 and 4.0-4.5 m/s and single-phase flow between 0.5-1.0 and 4.0-4.5 m/s, both at 100 W/cm^2, while for 200 W/cm^2, results were available between 1.0-1.5 to 4.0-4.5 m/s for two-phase flow and 3.0-3.5 to 5.0-5.5 m/s for single-phase flow. Results were obtained at Reynolds numbers below 2000.

Comparisons at 100 W/cm^2

Figure 6.16 to Figure 6.24 show the comparisons between two-phase flow and single-phase flow at 100 W/cm^2. Figure 6.16 shows the comparison of thermal resistances of optimal microchannel heat sinks while Figure 6.17 gives the corresponding maximum operating base temperatures equivalent to electronic device temperatures. From the figures, it can be seen that two-phase flow has superior thermal characteristics than single-phase flow as a result of latent heat involved in the removal of heat in the microchannels. The pumping power is slightly higher at high Reynolds number as shown in Figure 6.18 because of high pressure drop in two-phase flow, however the cooling advantage is overwhelming. One of the advantages of this optimisation study is that the microchannel heat sinks shown in the figures have optimal geometric and flow parameters.

Figure 6.19 and Figure 6.20 show the effects of length on optimal microchannel heat sinks. As lengths of microchannels in two-phase and single-phase flow increase, Reynolds number and pressure drop increase. Also, thermal resistances and base temperatures decrease to achieve the optimal geometric and flow parameters. Optimal hydraulic diameters adjusted in such a way that there were no wide variations in the optimal values for two-phase flow and single-phase flow as shown in Figure 6.21 and Figure 6.22, and optimal microchannel heat sinks were produced. In the optimisation, a different set of optimal geometric and flow parameters was obtained for each optimal velocity.

Figure 6.23 and Figure 6.24 show the effects of Reynolds number on pressure drop and Bejan number where it can be seen that pressure drops are higher for two-phase flow at high Reynolds number. As velocity increases, pressure drop and Bejan number increase and thermal performance is enhanced.

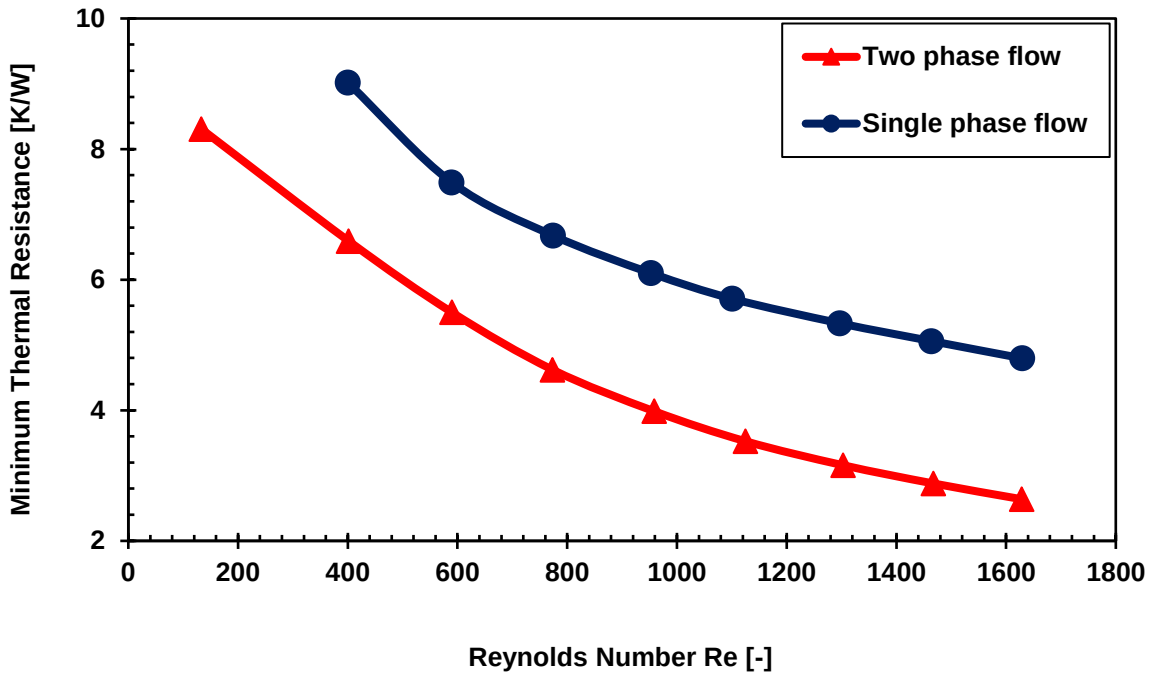

Figure 6.16. Thermal resistances of optimal microchannel heat sinks at 100 W/cm^2.

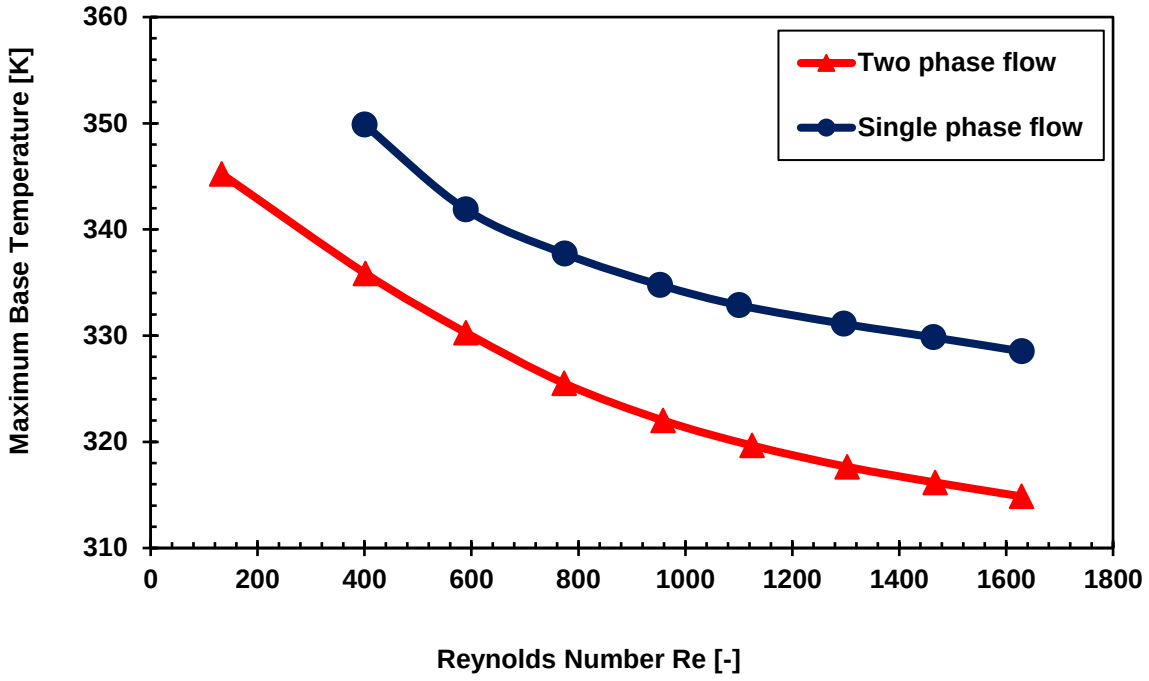

Figure 6.17. Maximum base temperatures of optimal microchannel heat sinks at 100 W/cm^2.

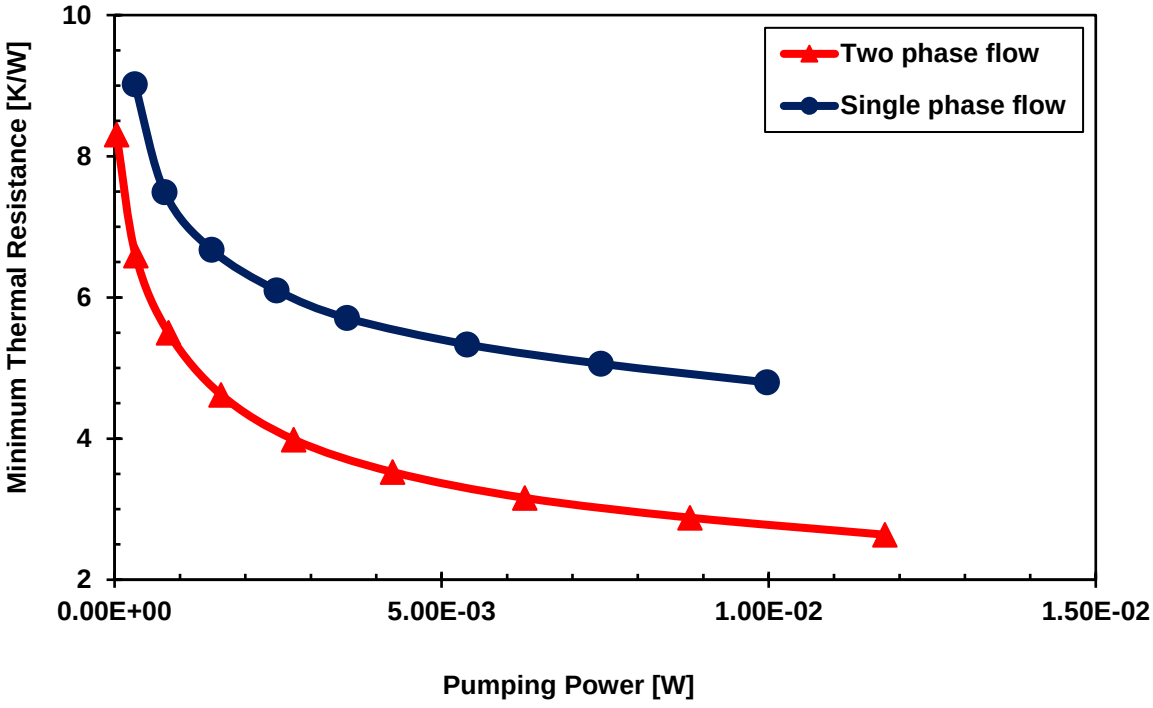

Figure 6.18. Pumping power of optimal microchannel heat sinks at 100 W/cm^2.

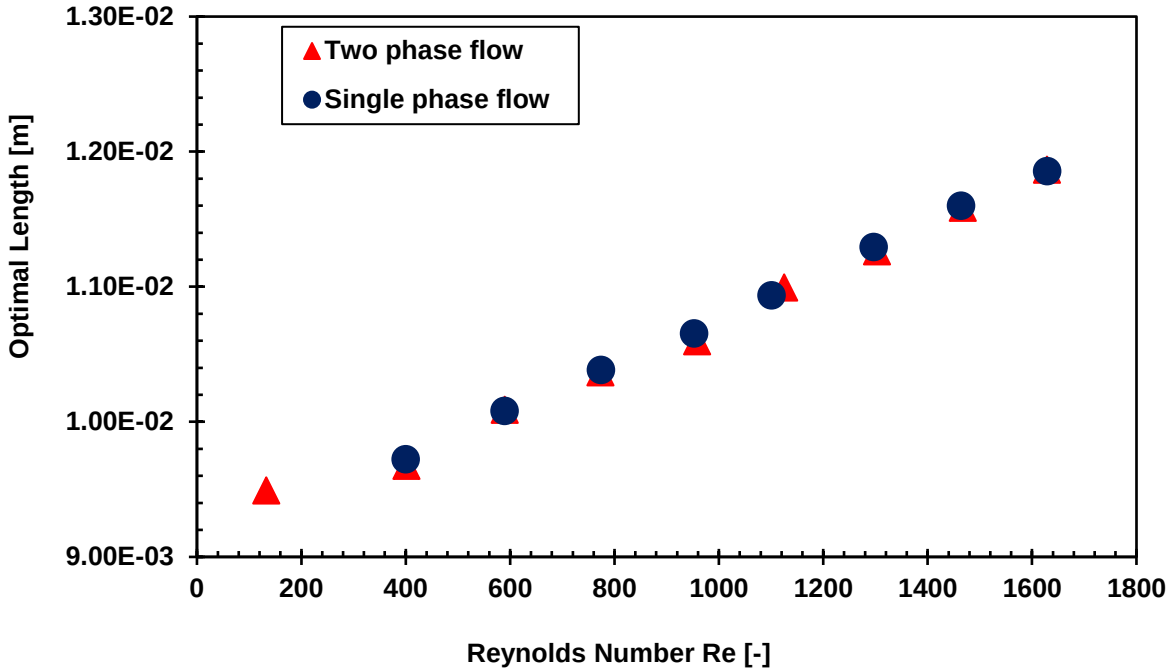

Figure 6.19. Effect of length on optimal microchannel heat sinks at 100 W/cm^2.

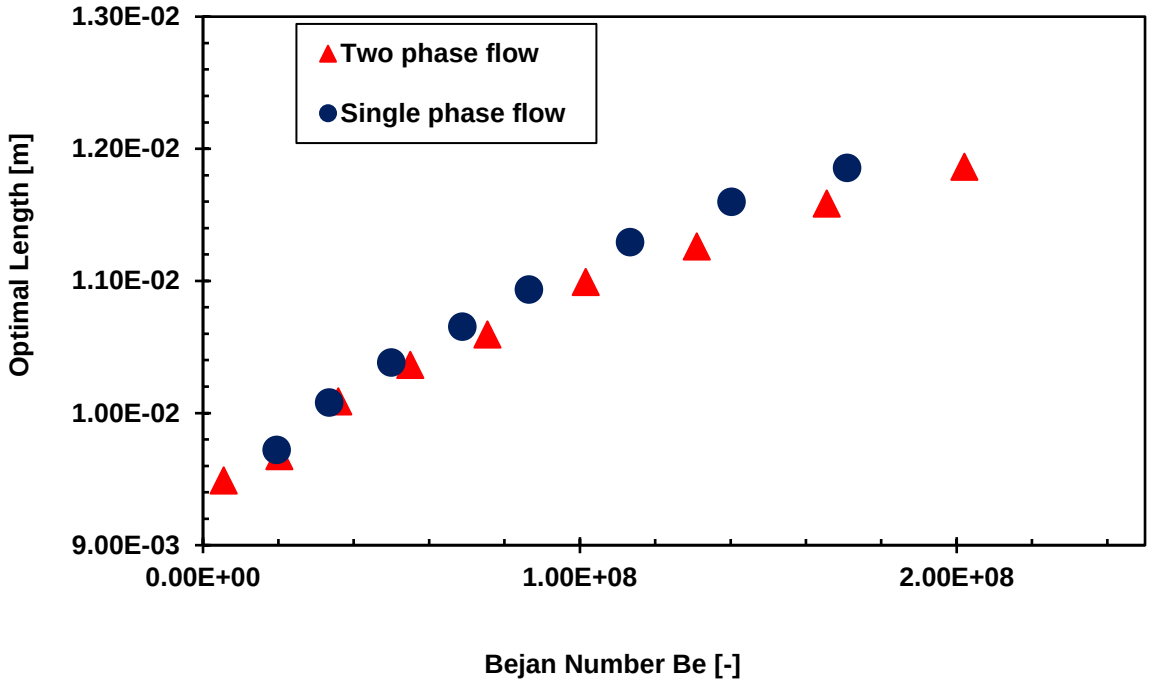

Figure 6.20. Effect of dimensionless pressure drop on optimal length at 100 W/cm^2.

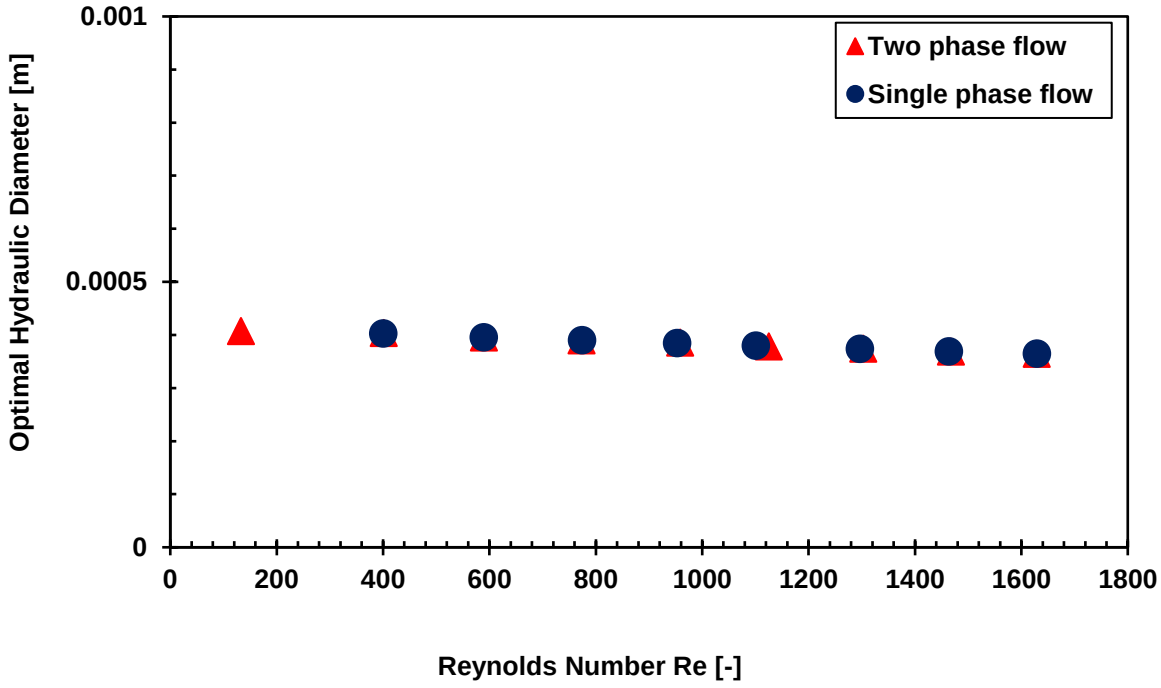

Figure 6.21. Effect of hydraulic diameter on optimal microchannel heat sinks at 100 W/cm^2.

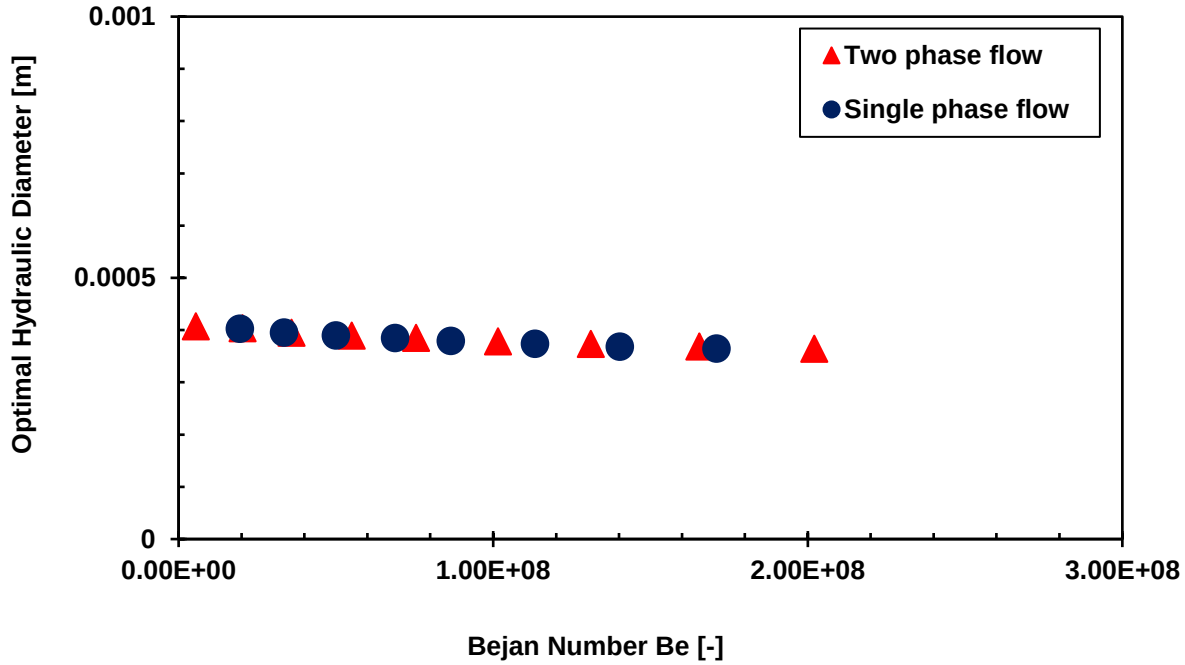

Figure 6.22. Effect of dimensionless pressure drop on optimal hydraulic diameter at 100 W/cm^2.

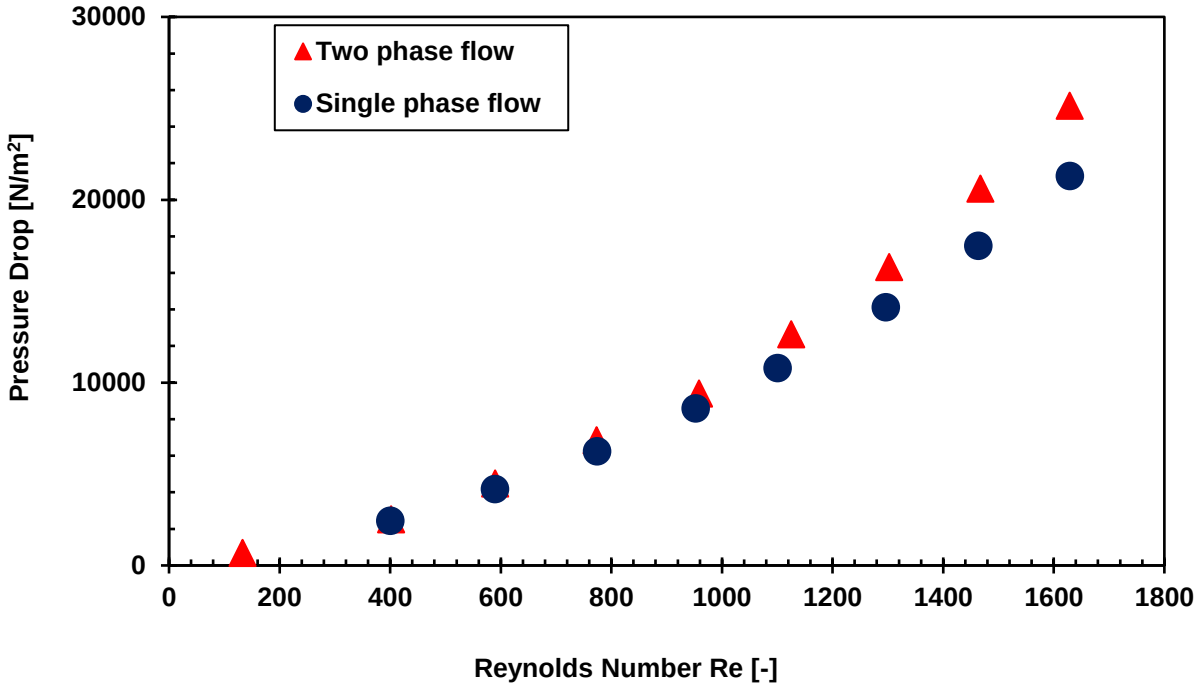

Figure 6.23. Effect of pressure drop on Reynolds number at 100 W/cm^2.

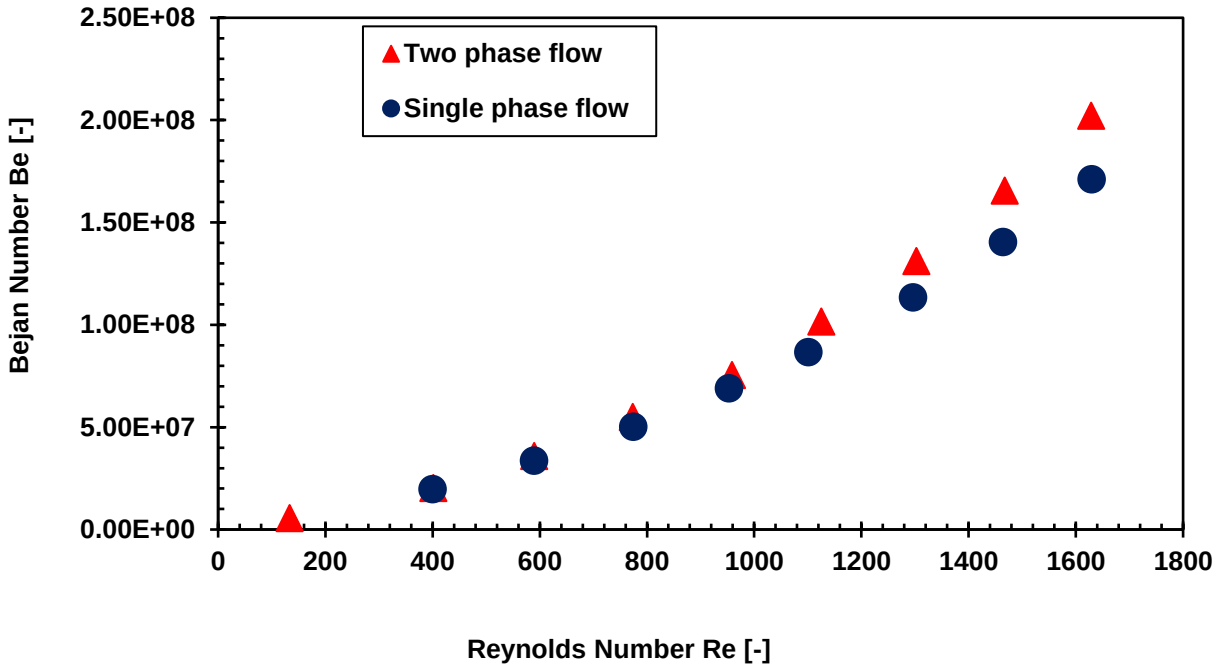

Figure 6.24. Effect of dimensionless pressure drop on Reynolds number at 100 W/cm^2.

Comparisons at 200 W/cm^2

Figure 6.25 to Figure 6.33 show the comparisons between two-phase and single-phase flow at 200 W/cm^2. Thermal characteristics are shown in Figure 6.25 and Figure 6.26. It is absolutely clear that the performance of two-phase flow is better than single-phase flow as expected. The velocities for which optimal values were obtained are: 1.0-1.5 to 4.0-4.5 for two-phase flow and 3.0-3.5 to 5.0-5.5 for single-phase flow. The value of pumping power for each optimal microchannel heat sink is shown in Figure 6.27. The beauty of the optimisation is that there are optimal microchannel heat sinks with different pumping power requirements.

The effects of increase in length on Reynolds number and Bejan number are shown in Figure 6.28 and Figure 6.29. As velocity increases and length morphs, Reynolds number and Bejan number increase until optimal values of geometric and flow parameters are obtained.

Figure 6.30 and Figure 6.31 show the relationships between hydraulic diameter, Reynolds number and Bejan number. The hydraulic diameter adjusts just like other heat sink parameters and slight decreases can be seen for two-phase and single-phase flow consistent with Figure 6.21 and Figure 6.22.

The effects of pressure drop and Bejan number on Reynolds number are shown in Figure 6.32 and Figure 6.33. Again, the pressure drops for two-phase flow are higher than single-phase flow in the same velocity range, which is consistent with the results obtained at 100 W/cm^2.

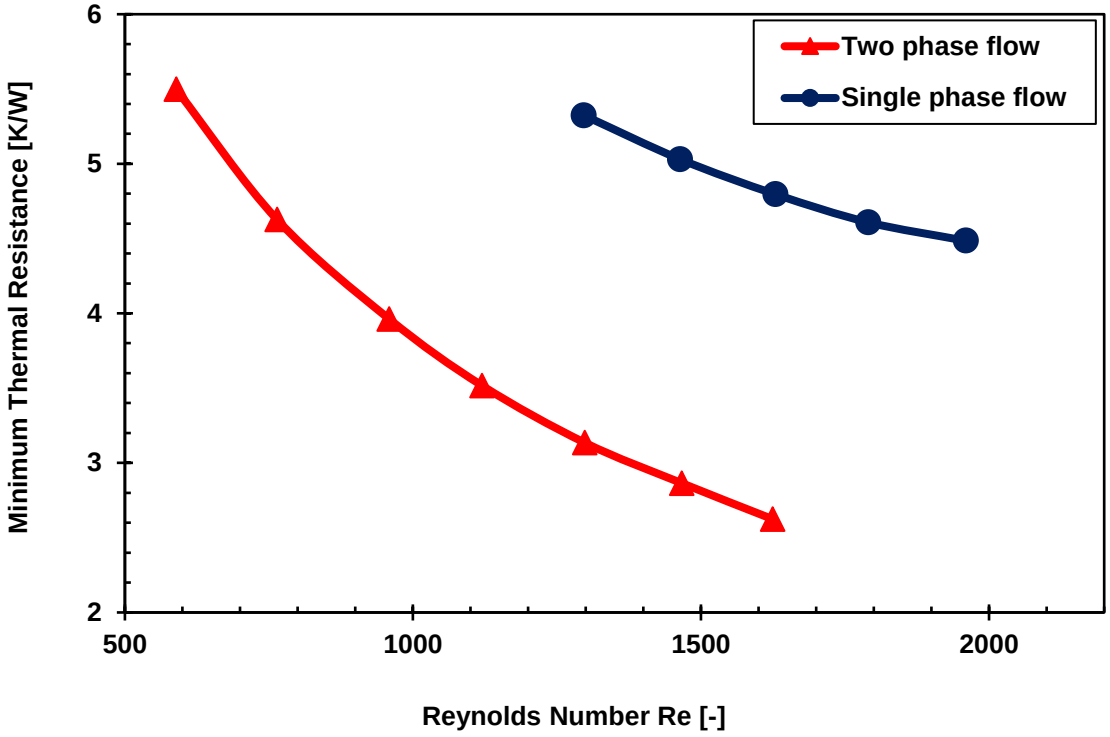

Figure 6.25. Thermal resistances of optimal microchannel heat sinks at 200 W/cm^2.

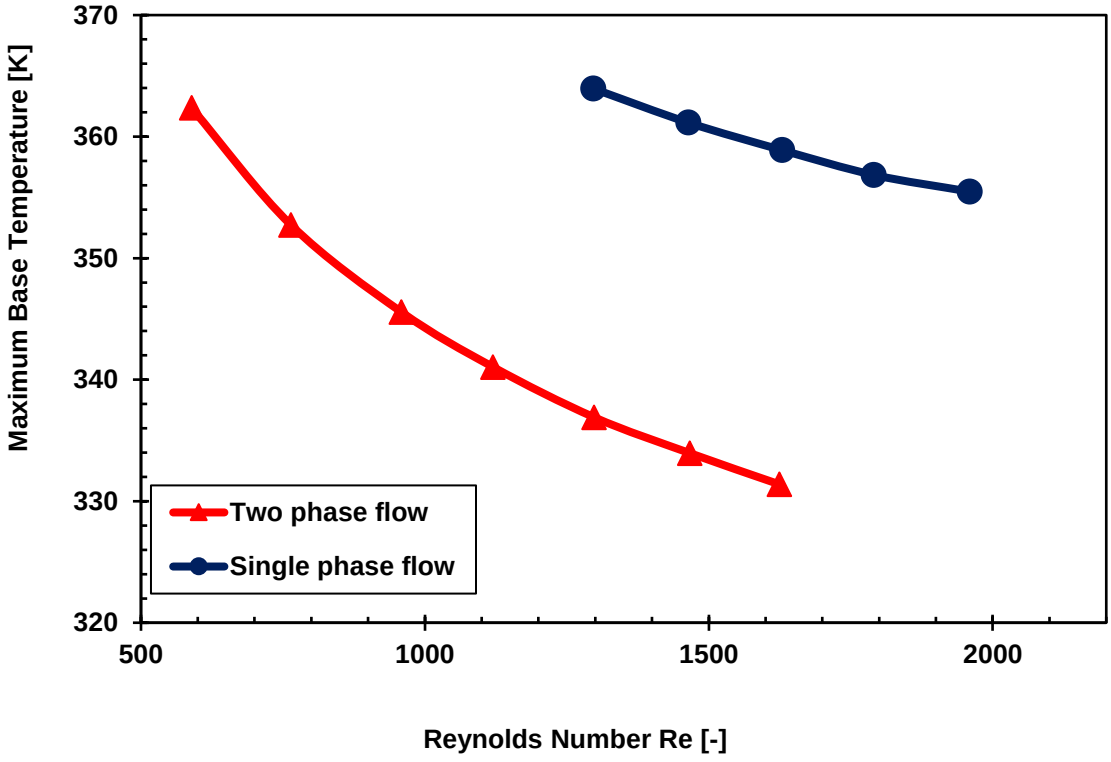

Figure 6.26. Maximum base temperatures of optimal microchannel heat sinks at 200 W/cm^2.

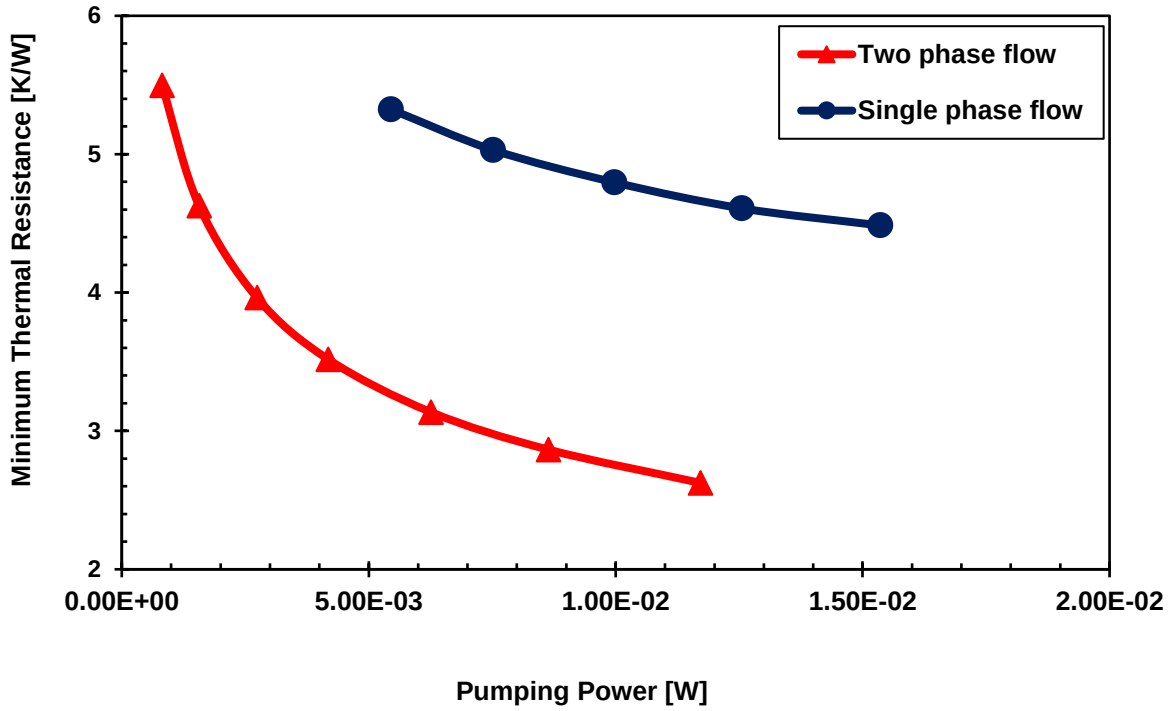

Figure 6.27. Pumping power of optimal microchannel heat sinks at 200 W/cm^2.

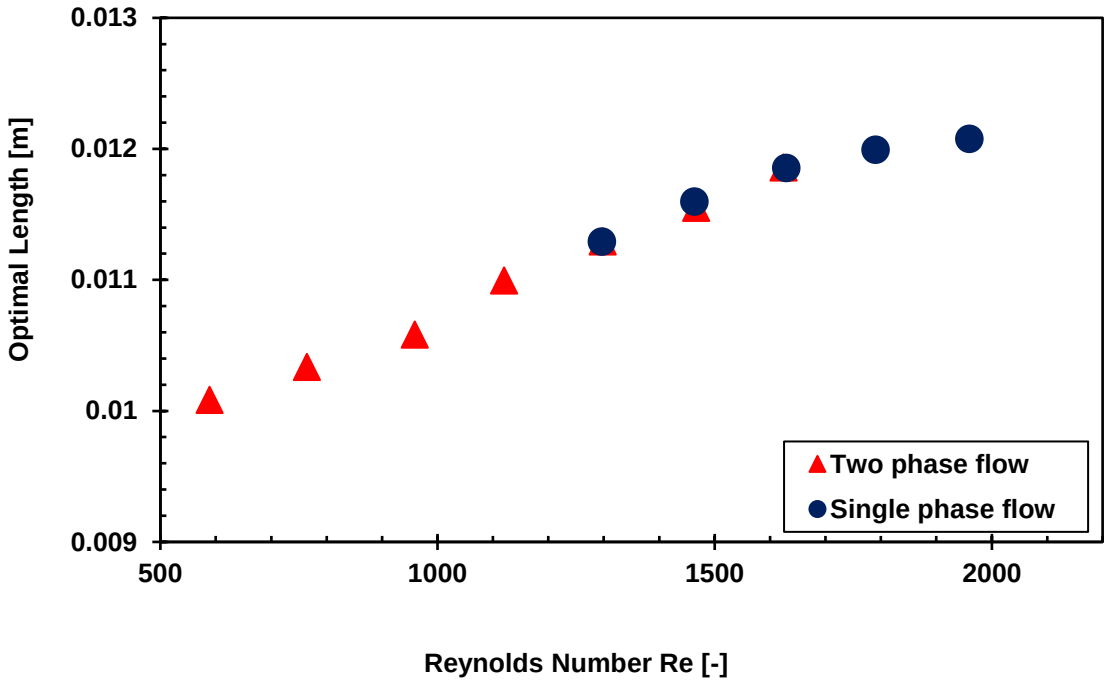

Figure 6.28. Effect of length on optimal microchannel heat sinks at 200 W/cm^2.

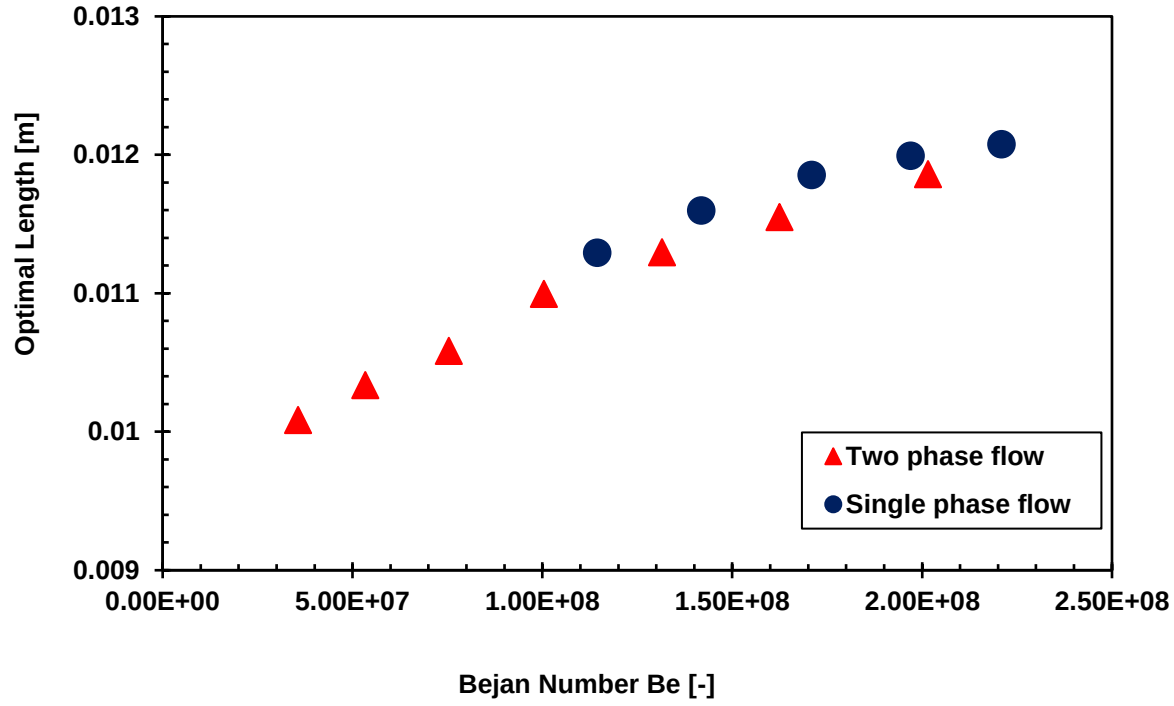

Figure 6.29. Effect of dimensionless pressure drop on optimal length at 200 W/cm^2.

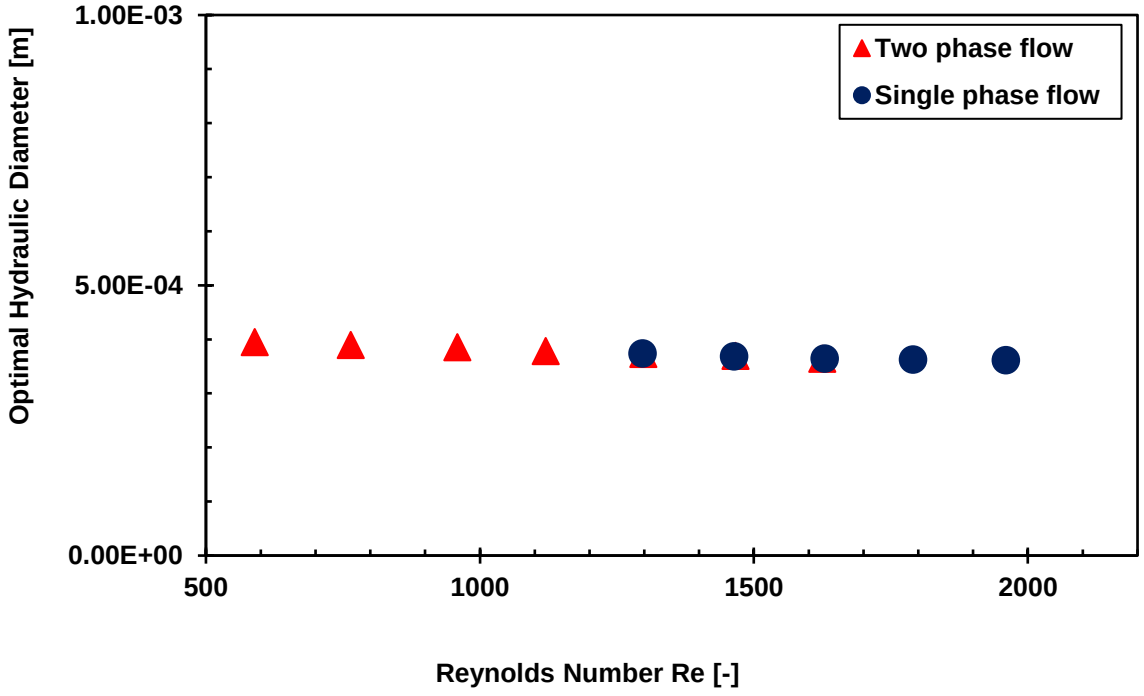

Figure 6.30. Effect of hydraulic diameter on optimal microchannel heat sinks at 200 W/cm^2.

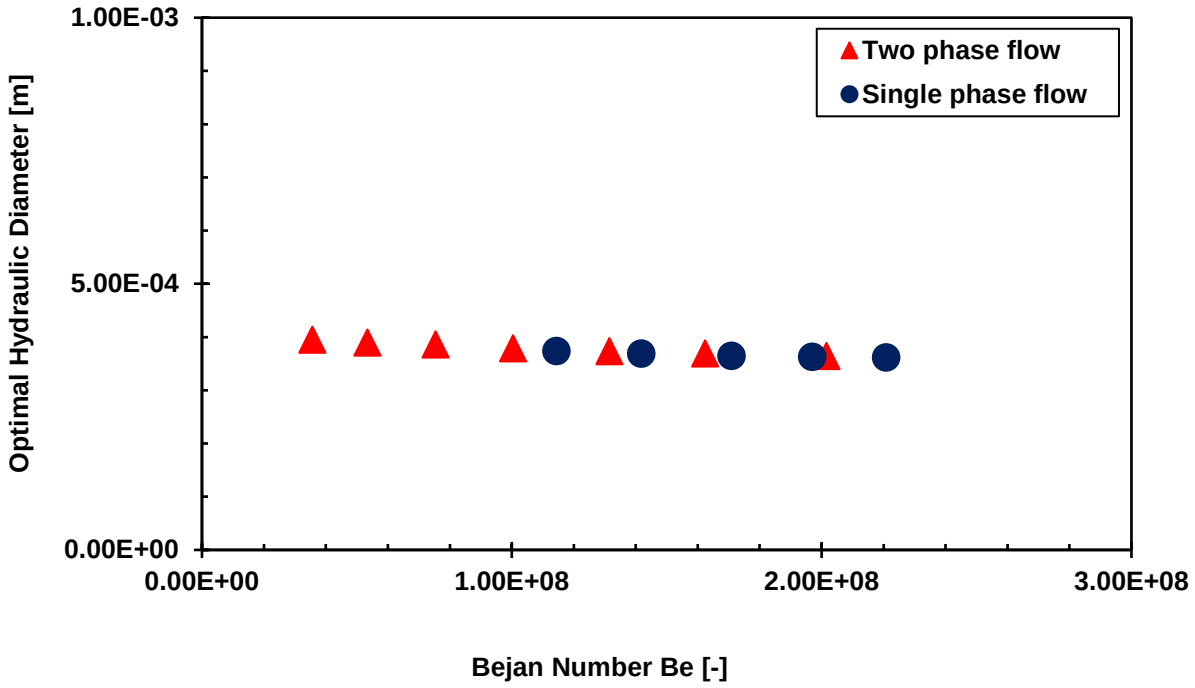

Figure 6.31. Effect of dimensionless pressure drop on optimal hydraulic diameter at 200 W/cm^2.

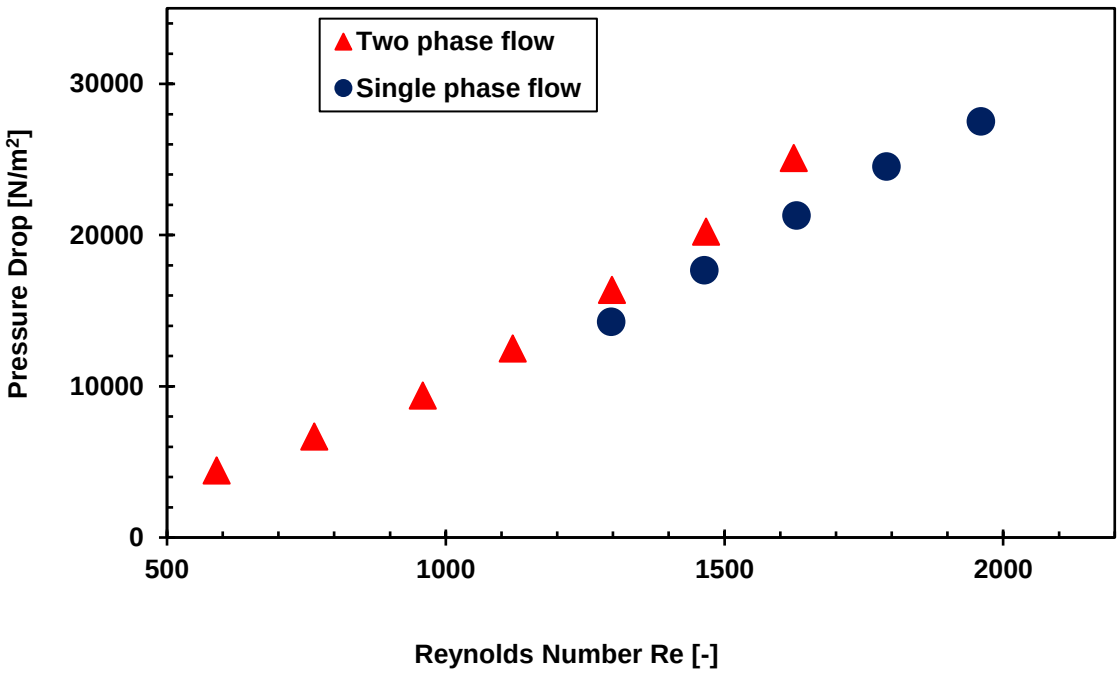

Figure 6.32. Effect of pressure drop on Reynolds number at 200 W/cm^2.

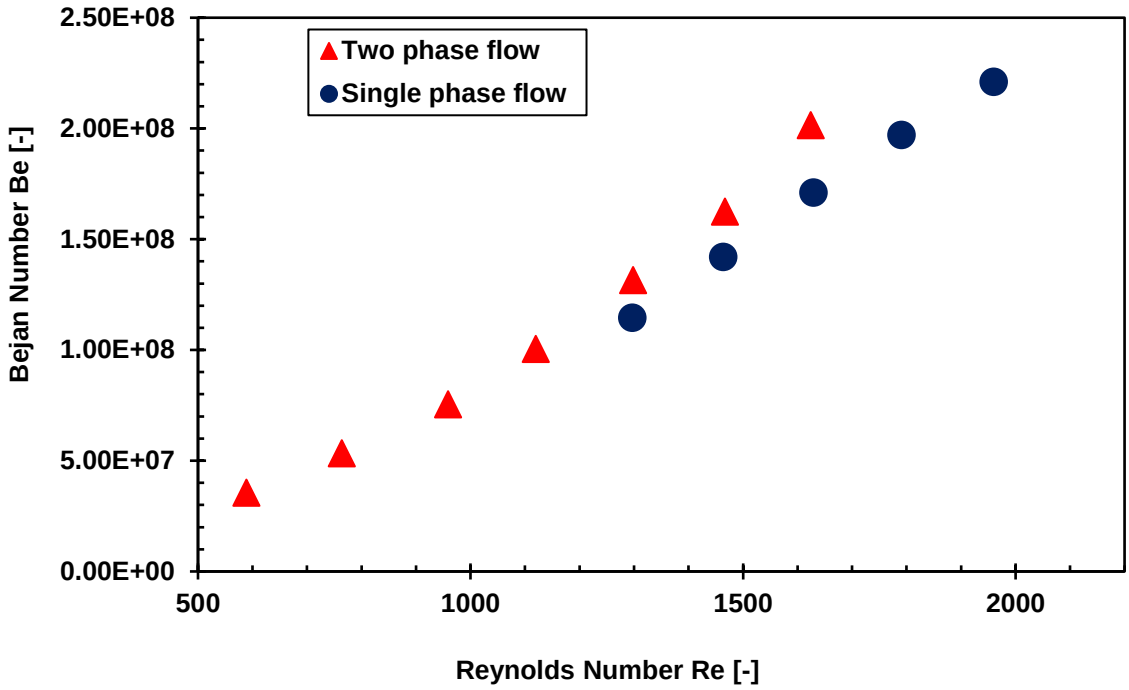

Figure 6.33. Effect of dimensionless pressure drop on Reynolds number at 200 W/cm^2.

6.2.1.3. Comparisons of single-phase flow at 100 and 200 W/cm^2

Single-phase flow at 100 and 200 W/cm^2 were compared to show the behaviour of optimal microchannel heat sinks. Figure 6.34 and Figure 6.35 show thermal characteristics of optimal microchannel heat sinks. The velocities are: 0.5-1.0 to 4.0-4.5 m/s for 100 W/cm^2 and 3.0-3.5 to 5.0-5.5 m/s for 200 W/cm^2. The difference between the thermal resistances at the same velocity range is small, however the base temperatures are not close as a result of higher heat flux. The reason for the closeness of thermal resistances may not be unconnected with the minimisation of same in the optimisation process. Highest operating temperatures of the optimal heat sinks are shown in Figure 6.35.

The pumping power requirements are shown in Figure 6.36. At higher velocities, the pumping power requirements at 200 W/cm^2 are higher, this is expected because higher velocities results in greater pressure drops. There are eight and five microchannel heat sinks at 100 and 200 W/cm^2 respectively, that performed optimally in the laminar flow regime.

The effects of length on Reynolds number and Bejan number are shown in Figure 6.37 and Figure 6.38. As length and velocity increase, Reynolds number and Bejan number increase to produce optimal microchannel heat sinks.

Figure 6.39 and Figure 6.40 depict the influence of hydraulic diameter on Reynolds number as a result of change in velocity, and on Bejan number as a result of pressure drop. These effects became necessary in producing the desired microchannel heat sinks.

The effects of pressure drop and Bejan number are shown in Figure 6.41 and Figure 6.42. The pressure drops at coincidental velocity ranges are similar with slightly higher values at 200 W/cm^2. This same trend was witnessed when optimal microchannel heat sinks were compared at different heat fluxes in two-phase flow (Figure 6.9 and Figure 6.10).

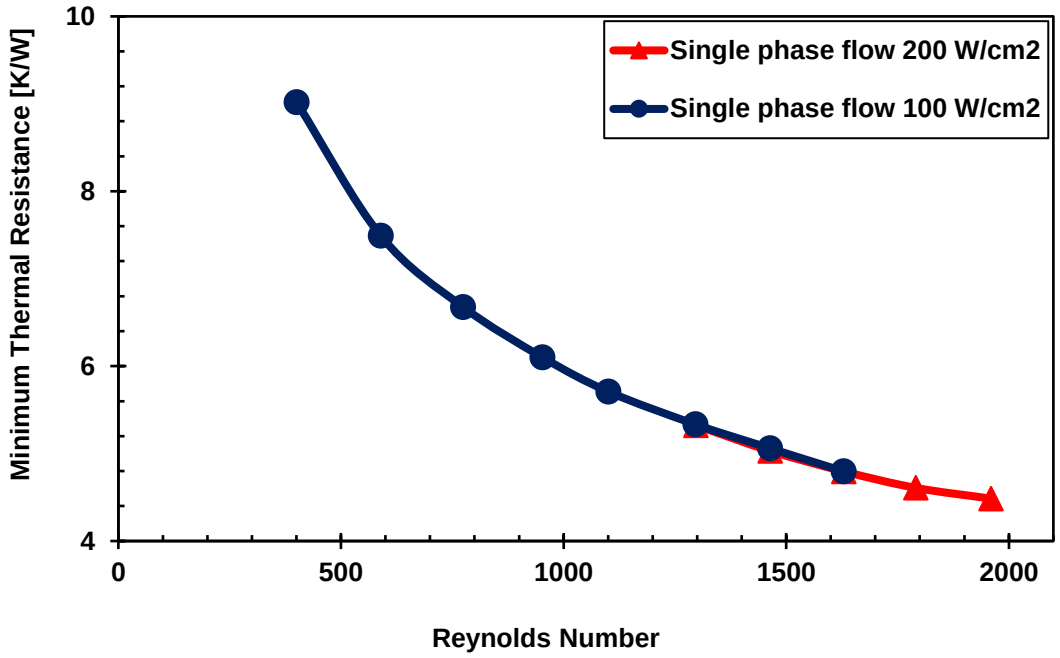

Figure 6.34. Thermal resistances of optimal microchannel heat sinks at 100 and 200 W/cm^2.

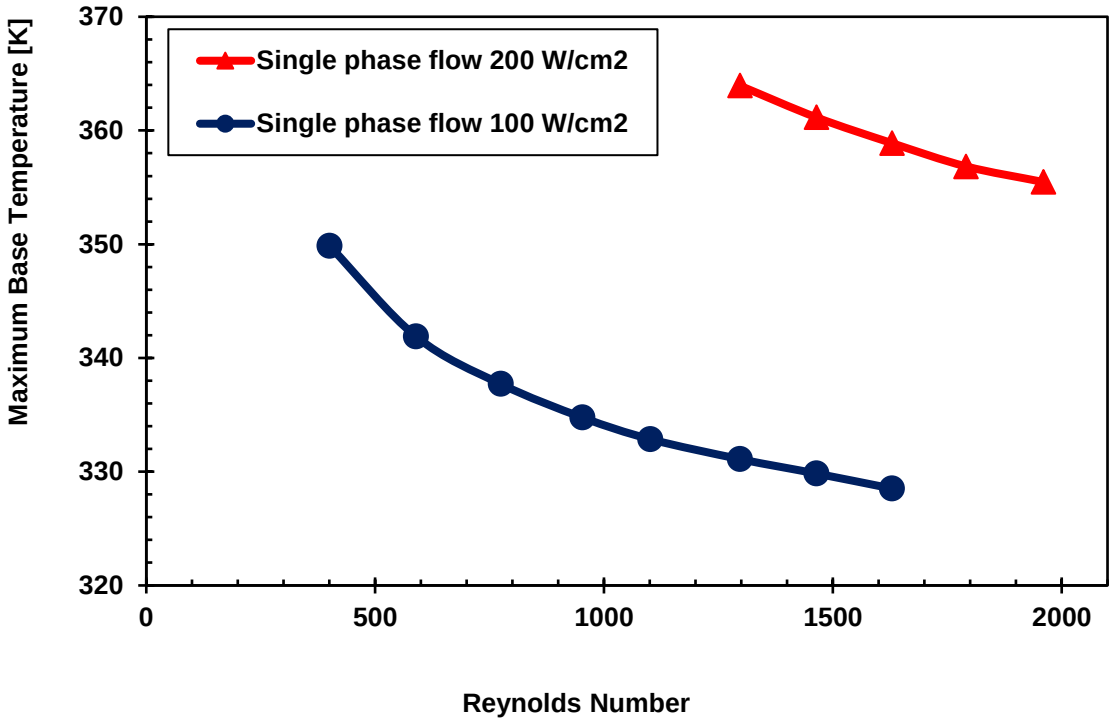

Figure 6.35. Maximum base temperatures of optimal microchannel heat sinks at 100 and 200 W/cm^2.

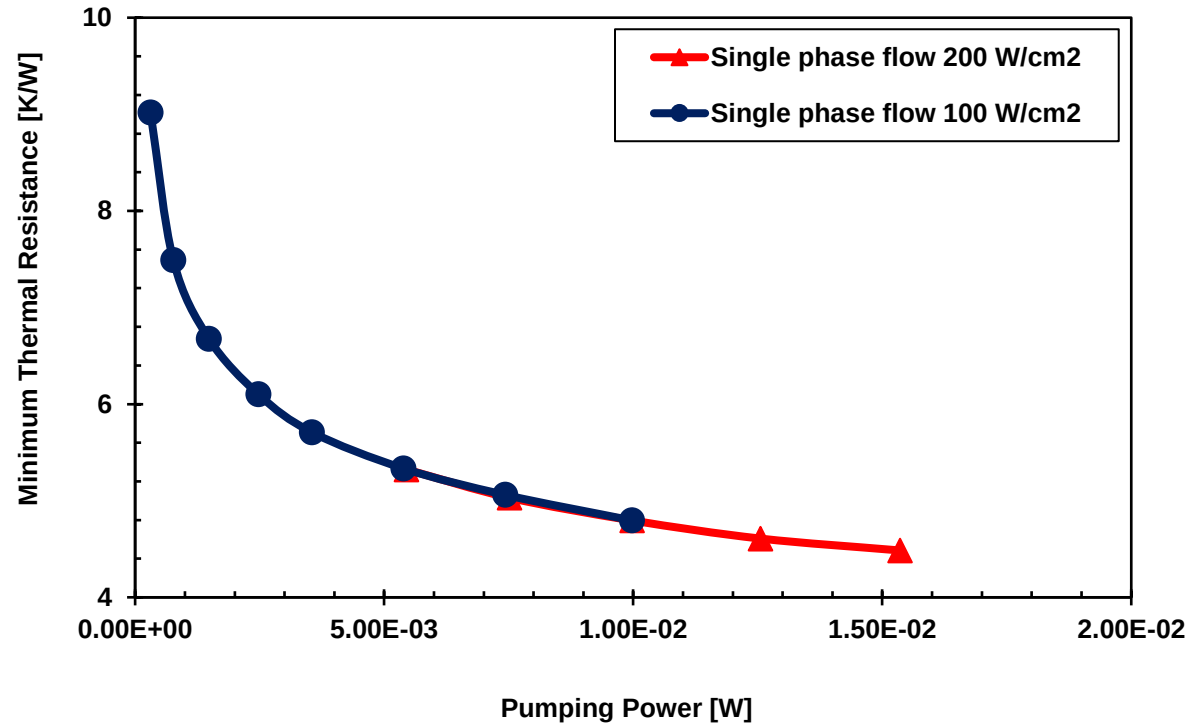

Figure 6.36. Pumping power of optimal microchannel heat sinks at 100 and 200 W/cm^2.

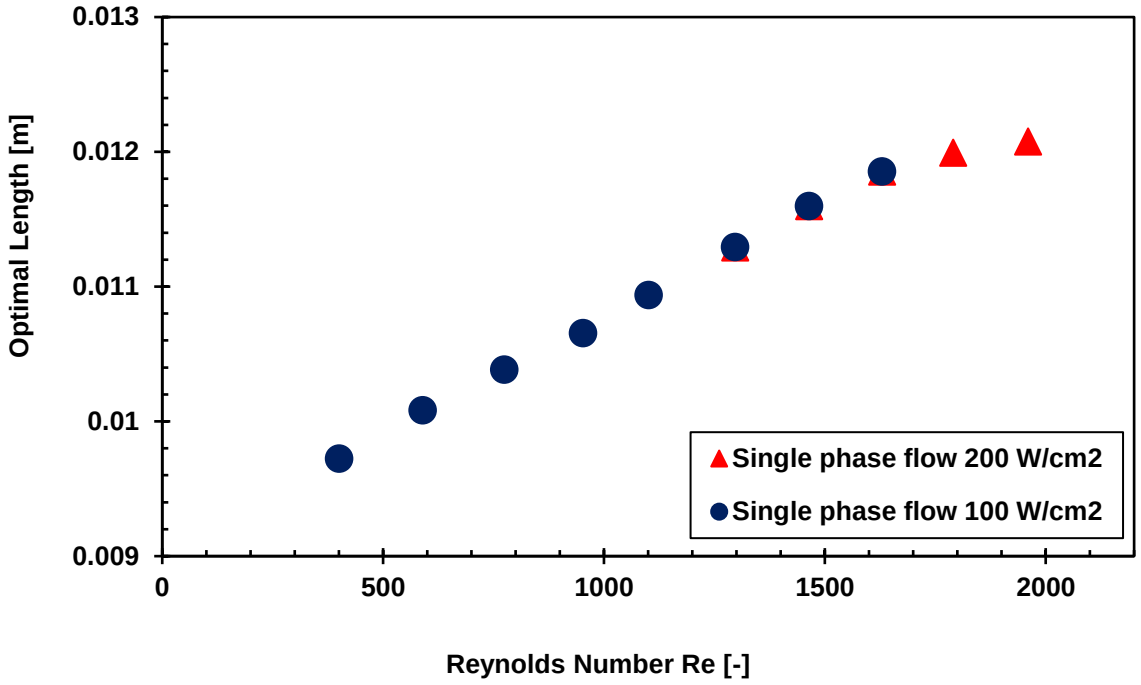

Figure 6.37. Effect of length on optimal microchannel heat sinks at 100 and 200 W/cm^2.

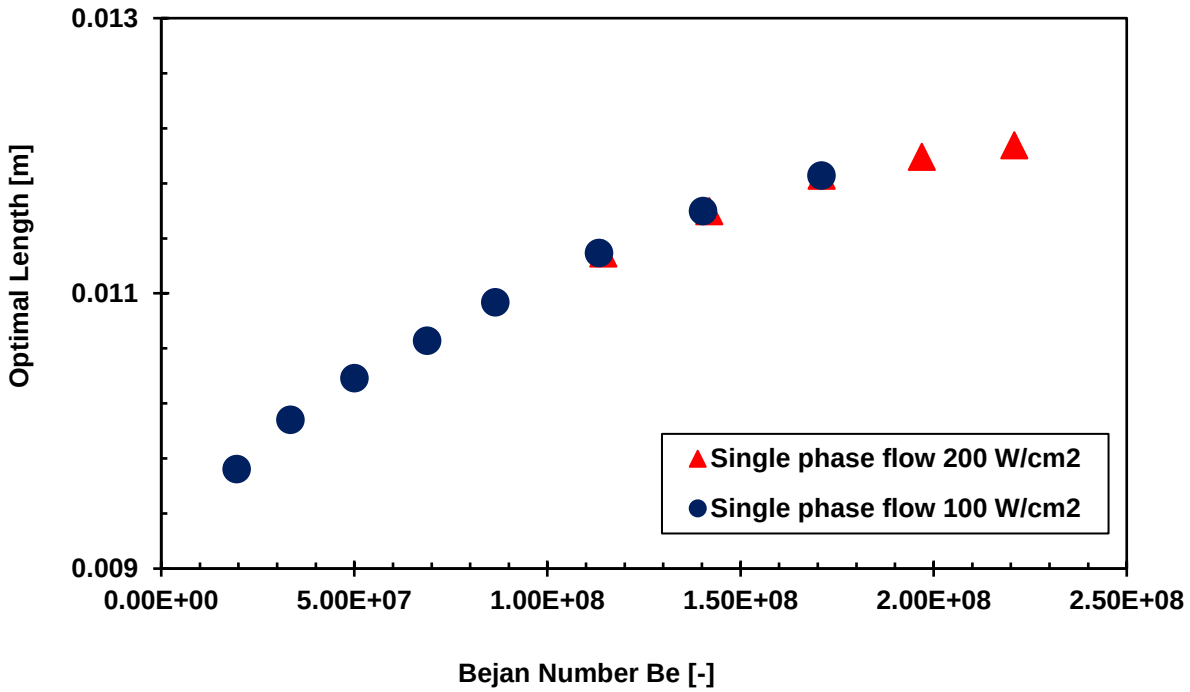

Figure 6.38. Effect of dimensional pressure drop on optimal length at 100 and 200 W/cm^2.

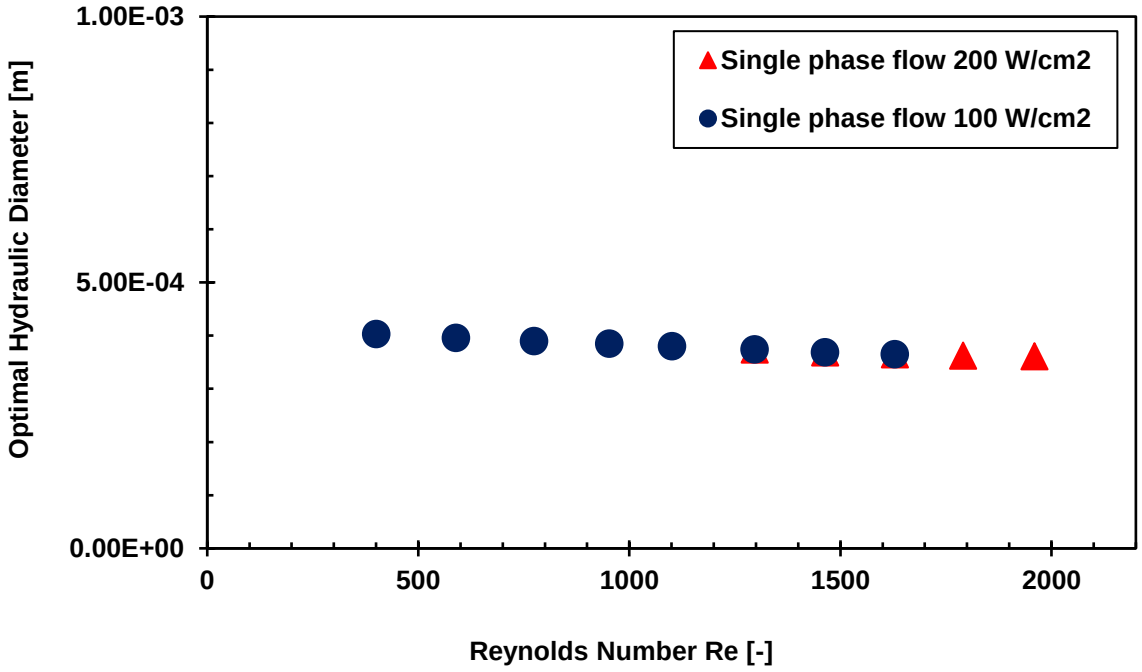

Figure 6.39. Effect of hydraulic diameter on optimal microchannel heat sinks at 100 and 200 W/cm^2.

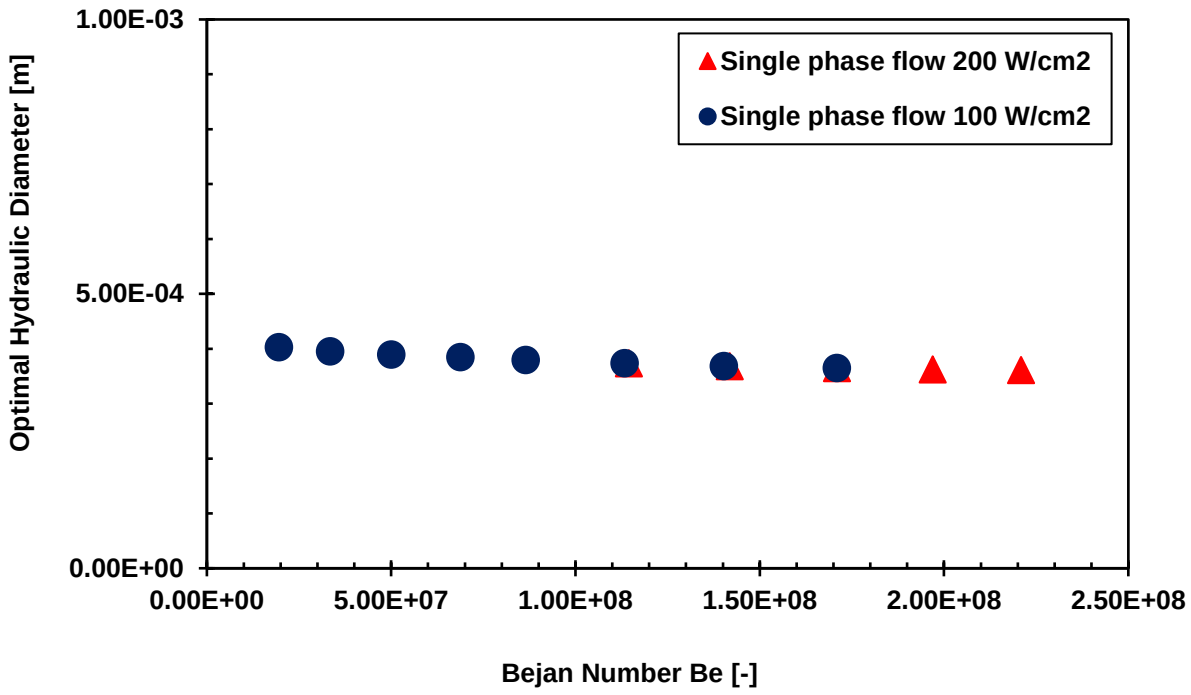

Figure 6.40. Effect of dimensionless pressure drop on optimal hydraulic diameter at 100 and 200 W/cm^2.

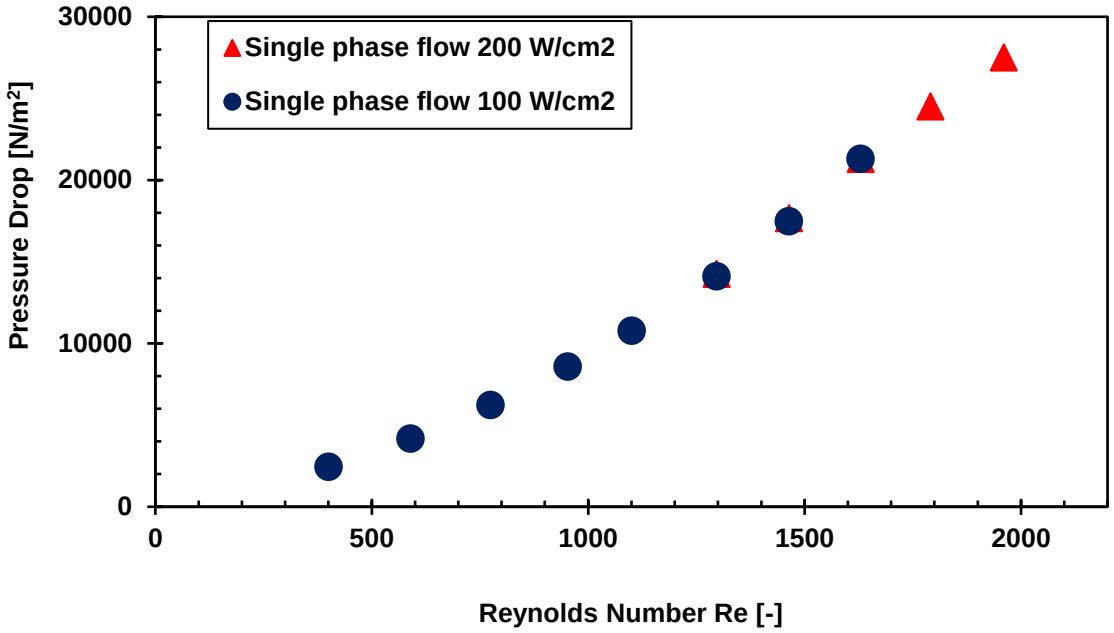

Figure 6.41. Effect of pressure drop on Reynolds number at 100 and 200 W/cm^2.

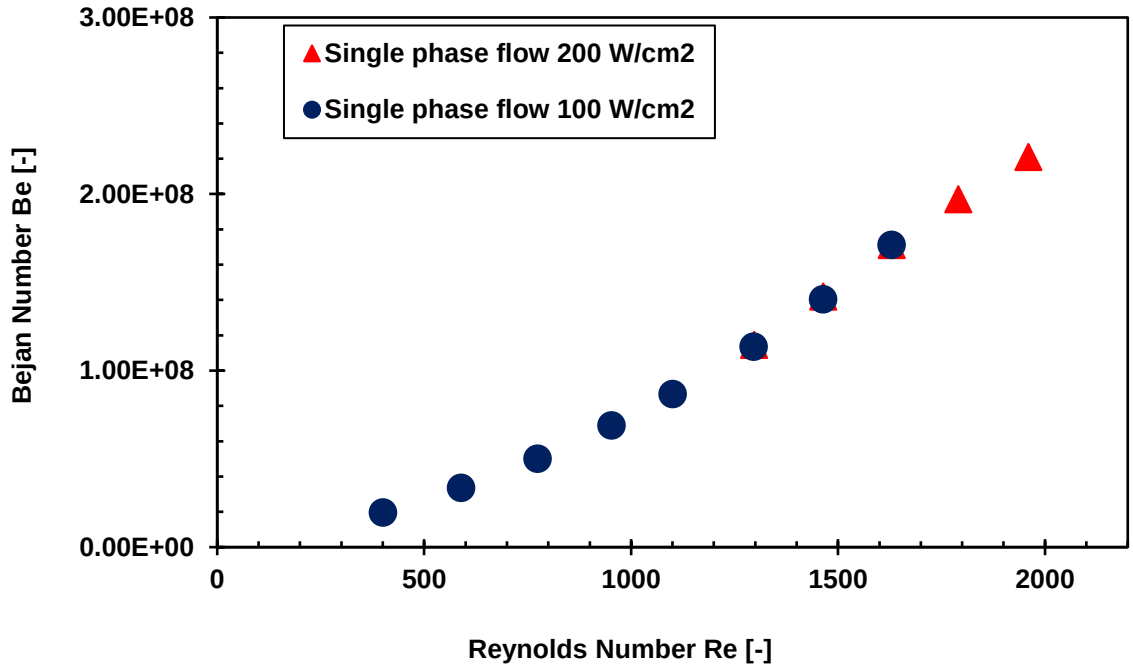

Figure 6.42. Effect of dimensionless pressure drop on Reynolds number at 100 and 200 W/cm^2.

Temperature contours

The heat flux for the contours shown in Figure 6.43-Figure 6.46 is 100 W/cm^2 at 2.49 m/s in single phase flow. The wall temperature contours are shown in Figure 6.43 and Figure 6.44. The maximum base temperature is slightly higher than the highest inner wall temperature at 334.764 K and this is below the maximum operating temperature for modern electronic devices. The inner wall temperature range as shown in Figure 6.11 is 311.6 to 322 K while that of water temperature is 298.15 to 307.095 K (Figure 6.13). Here, in single phase flow at the same heat flux and velocity range, the inner wall temperature range is 318.1 to 334.7 K in Figure 6.43 while that of water temperature is 298.15 to 319.347 K in Figure 6.45. Figure 6.44(a) and Figure 6.44(b) depict the wall temperature distribution at inlet and outlet of the microchannel heat sink. Figure 6.46(a) and Figure 6.46(b) show inlet and outlet water temperature contours.

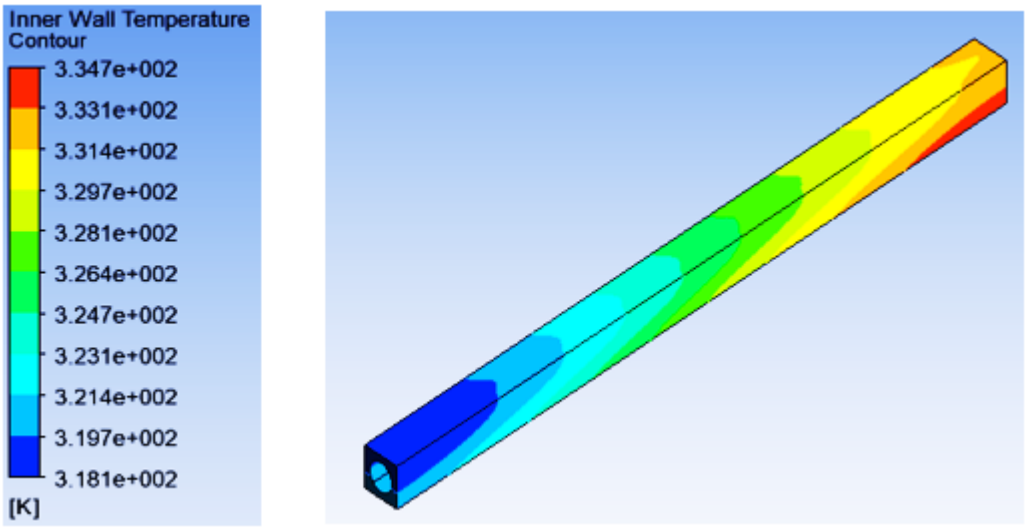

Figure 6.43. Inner wall temperature contour (base temperature = 334.764 K).

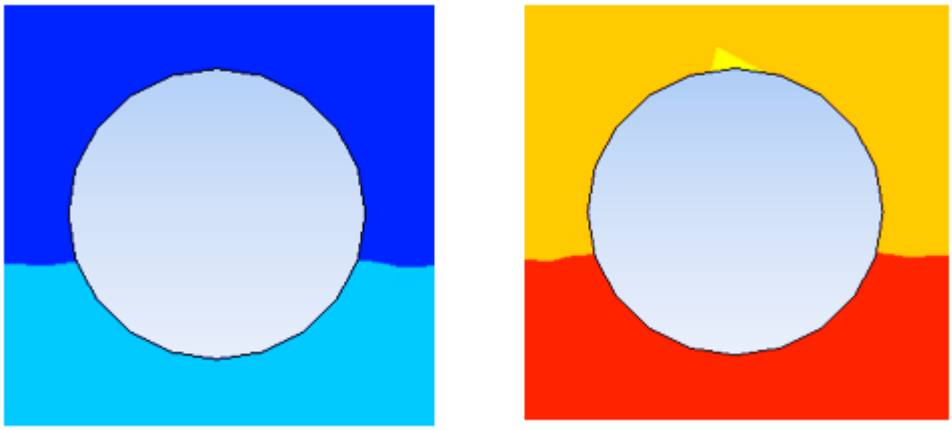

(a) Inlet wall temperature contour (b) Outlet wall temperature contour

Figure 6.44. Inlet and outlet wall temperature contours.

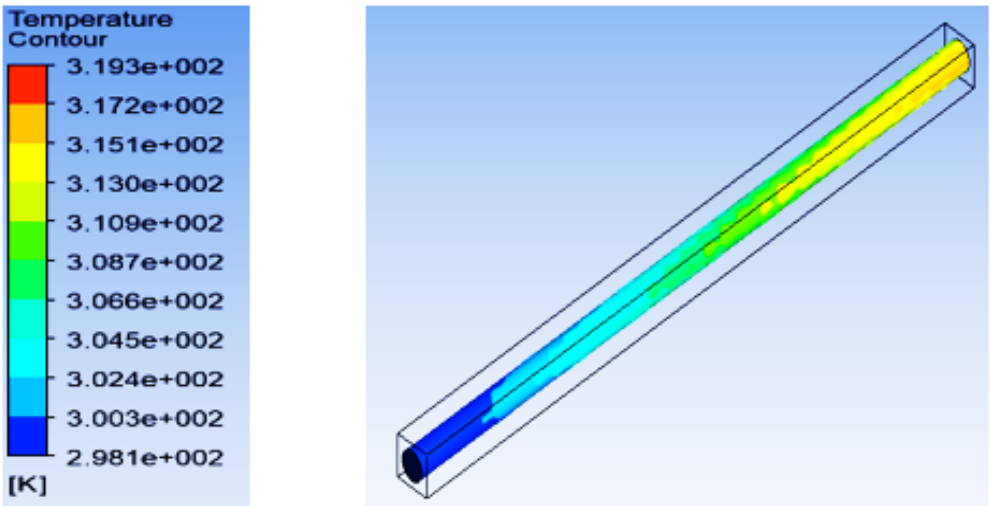

Figure 6.45. Water temperature contour.

(outlet water temperature = 319.347 K, optimal velocity = 2.490 m/s)

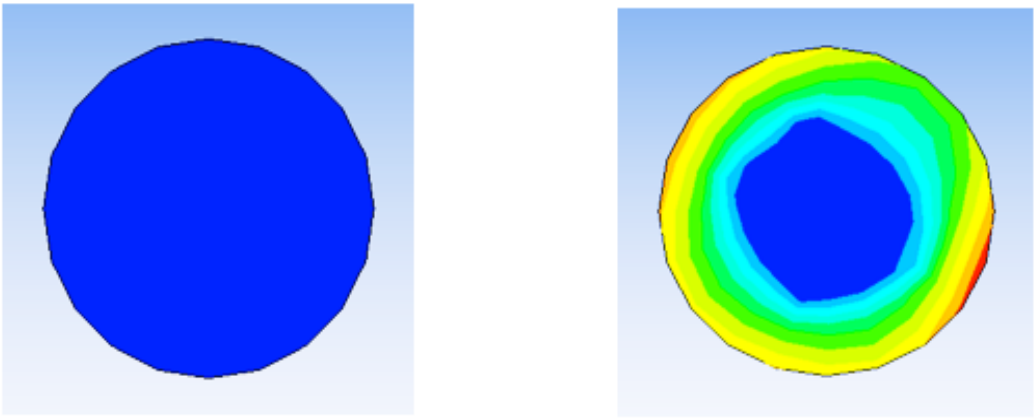

(a) Inlet water temperature contour (b) Outlet water temperature contour

Figure 6.46. Inlet and outlet water temperature contours.

6.2.2. Equilateral triangular microchannel heat sinks

6.2.2.1. Subcooled flow boiling (Two-phase flow)

Equilateral triangular microchannel was also considered a viable flow path in a micro heat sink. Optimal microchannel heat sinks were obtained up to 500 W/cm^2 as shown in Figure 6.47. The thermal resistances at each velocity range are close but not the same. However, the base temperatures are not close as seen in Figure 6.48. The thermal resistance decreases as Reynolds number increases as expected and the desired cooling is achieved optimally. Figure 6.47 and Figure 6.48 provide optimal microchannel heat sinks operating at different thermal resistances and base temperatures. The velocities for which optimal parameters were obtained are: 0.1-0.5 to 4.0-4.5 m/s at 100 W/cm^2, 1.0-1.5 to 4.0-4.5 m/s at 200 W/cm^2, 2.0-2.5 to 6.5-7.0 m/s at 300 W/cm^2, 4.0-4.5 to 6.5-7.0 m/s at 400 W/cm^2 and 5.5-6.0 to 6.5-7.0 m/s at 500 W/cm^2. The microchannel heat sinks are compared between 100 and 300 W/cm^2 consistent with what was done for circular microchannel heat sinks.

Figure 6.49 provides the pumping power for the optimal microchannel heat sinks. The pumping power requirements at 300 W/cm^2 are higher due to the fact that optimal parameters were obtained at high velocities, hence pressure drops were high.

Figure 6.50 and Figure 6.51 give the variation of Reynolds number and Bejan number with optimal length. It can be seen that optimal microchannel heat sinks with greater lengths were

obtained at high Bejan numbers at 300 W/cm^2 because of high velocities. Despite these, Reynolds number stayed below 2000.

Figure 6.52 and Figure 6.53 show that optimal hydraulic diameters are within a narrow range. Optimal hydraulic diameters decrease slightly as Reynolds number and Bejan number increase, which is consistent with the trend for optimal circular microchannel heat sinks (Figure 6.7 and Figure 6.8).

The functional relationships between Reynolds number, pressure drop and Bejan number are shown in Figure 6.54 and Figure 6.55. Pressure drop and Bejan number increase as Reynolds number increases showing consistency with Figure 6.9 and Figure 6.10.

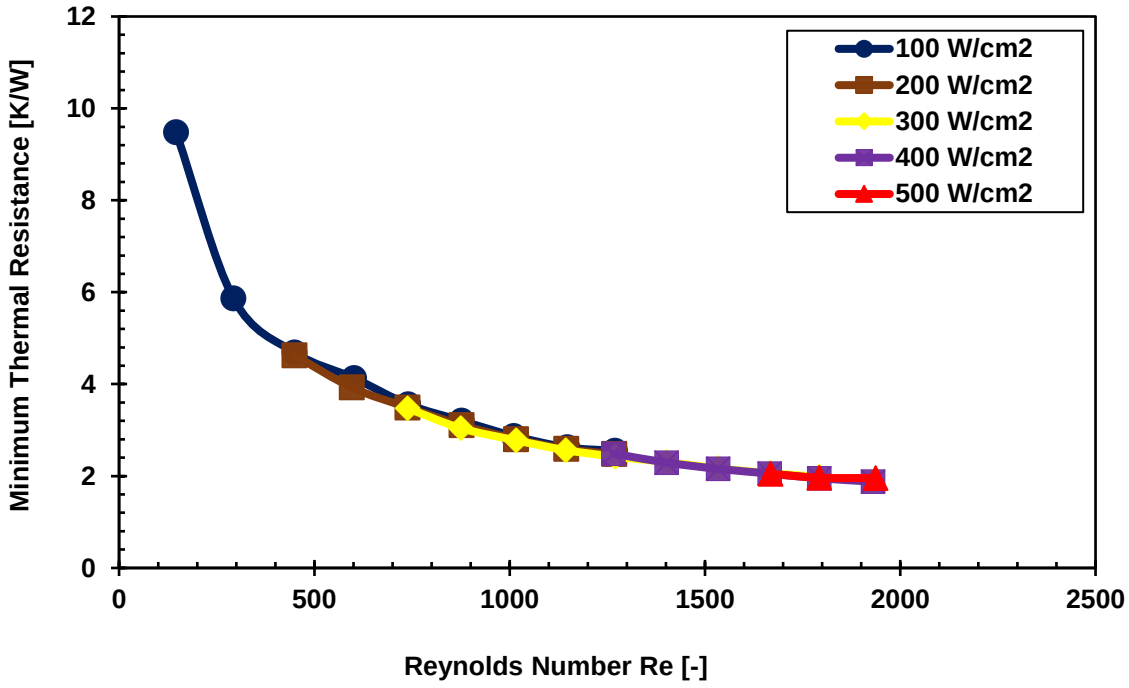

Figure 6.47. Thermal resistances of optimal microchannel heat sinks.

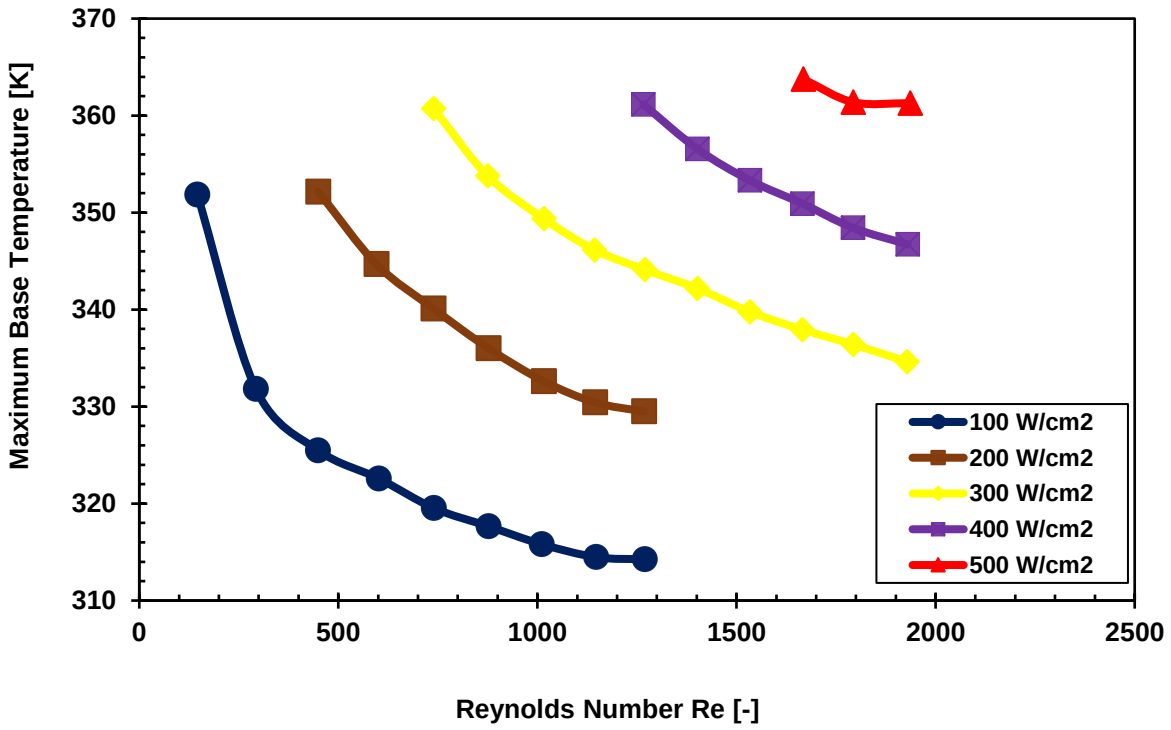

Figure 6.48. Maximum base temperatures of optimal microchannel heat sinks.

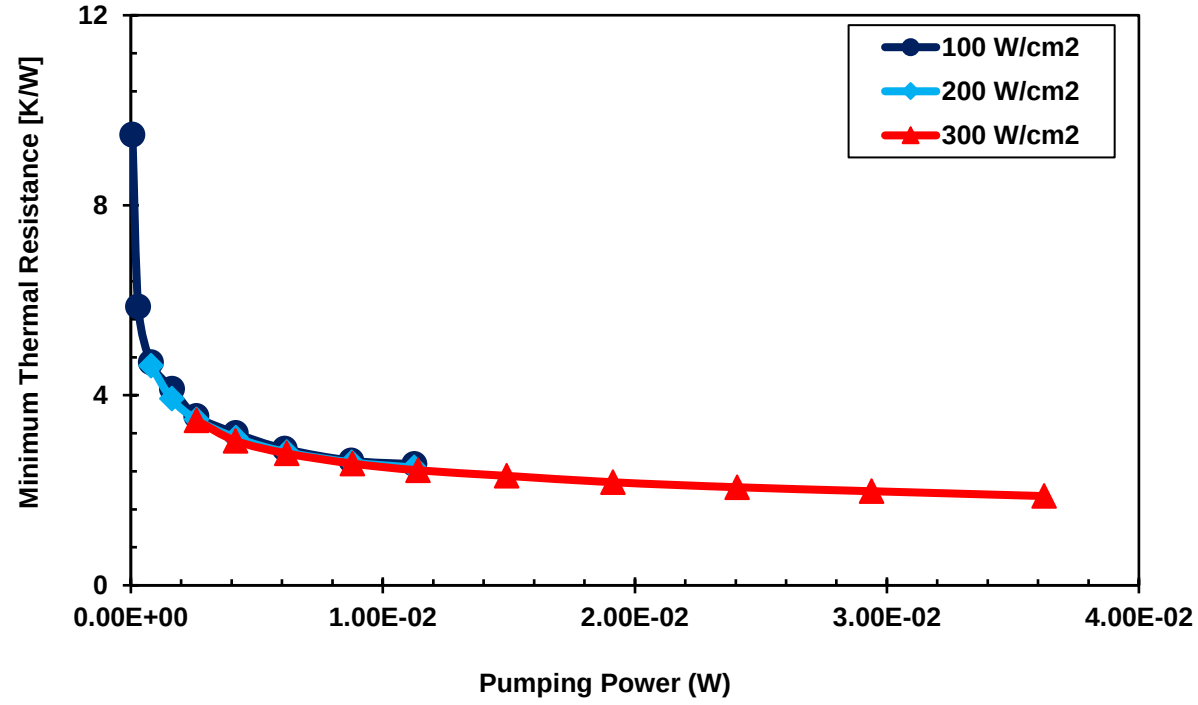

Figure 6.49. Pumping power of optimal microchannel heat sinks.

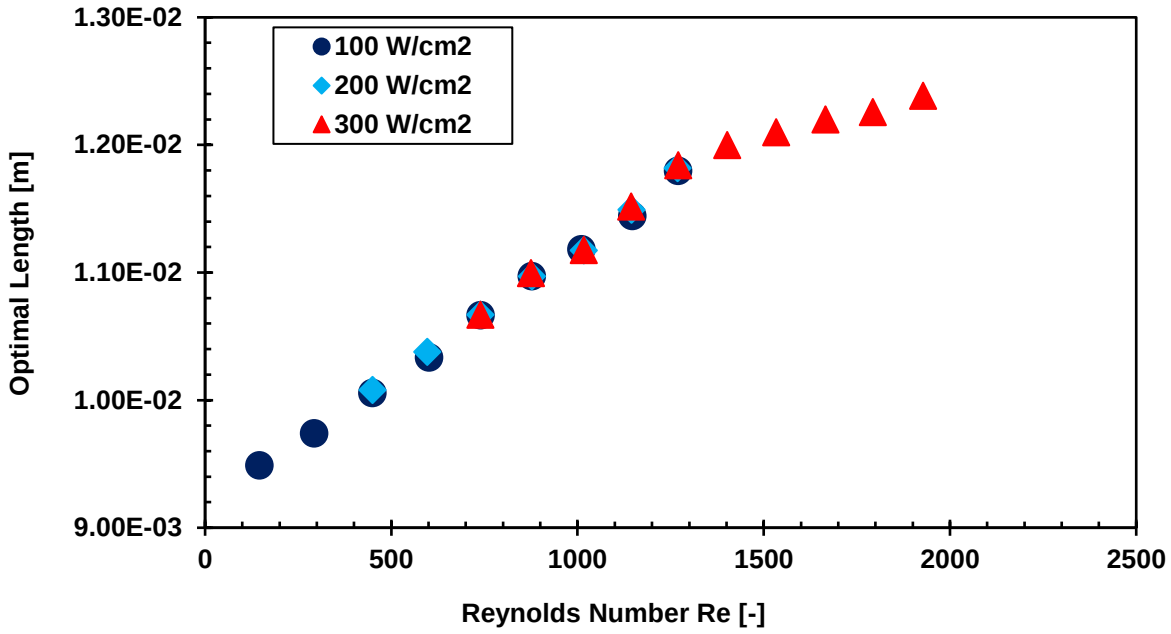

Figure 6.50. Effect of length on optimal microchannel heat sinks.

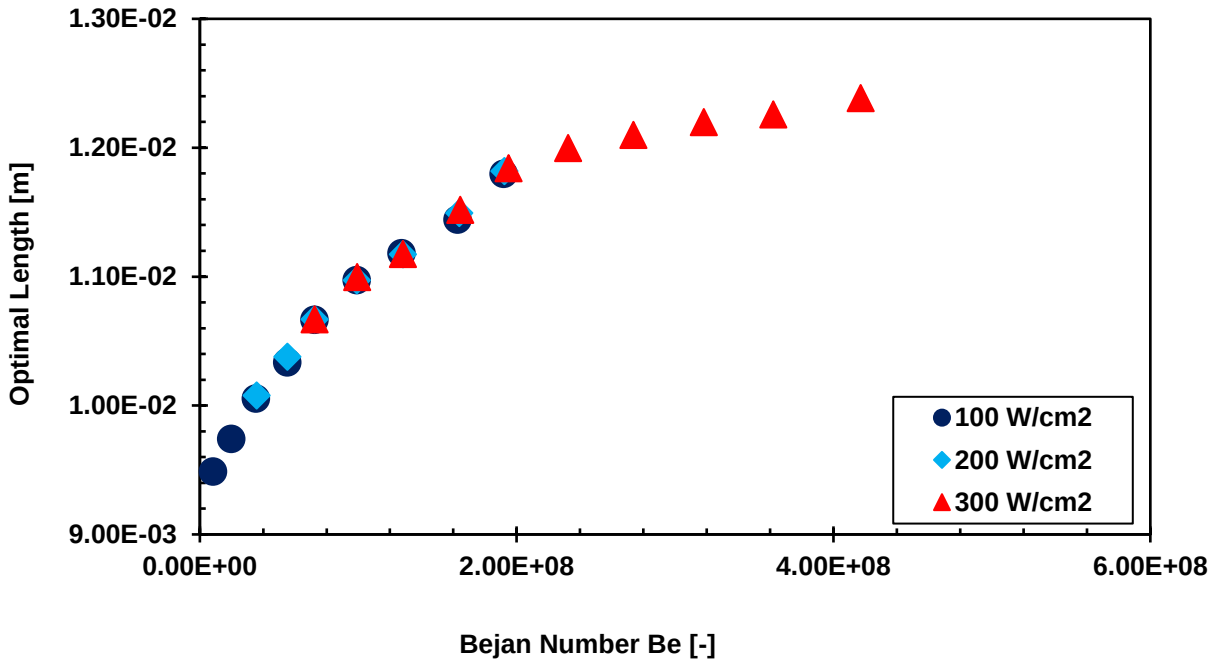

Figure 6.51. Effect of dimensionless pressure drop on optimal length.

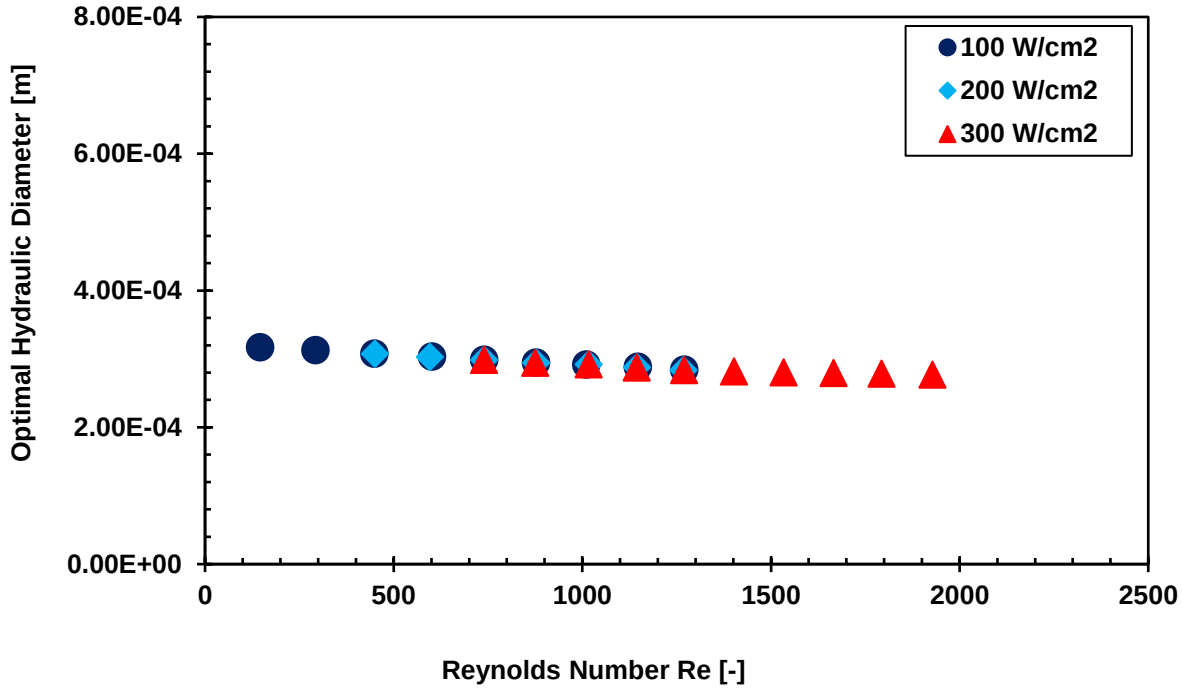

Figure 6.52. Effect of hydraulic diameter on optimal microchannel heat sinks.

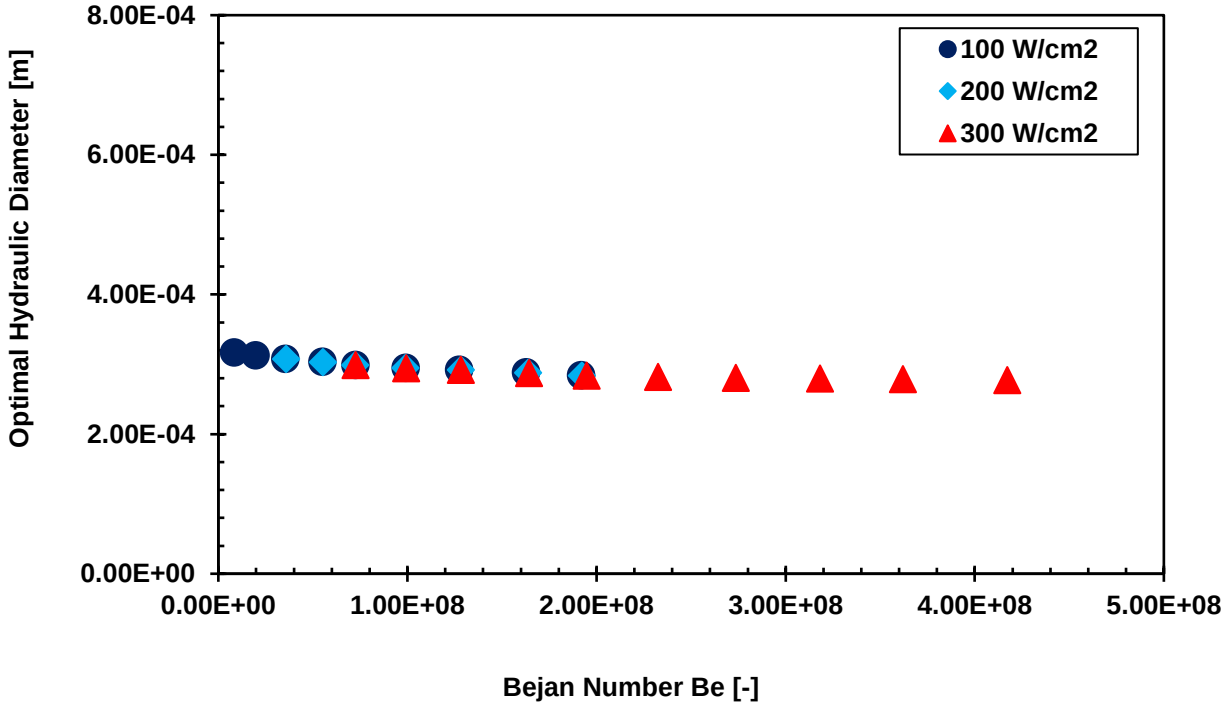

Figure 6.53. Effect of dimensionless pressure drop on optimal hydraulic diameter.

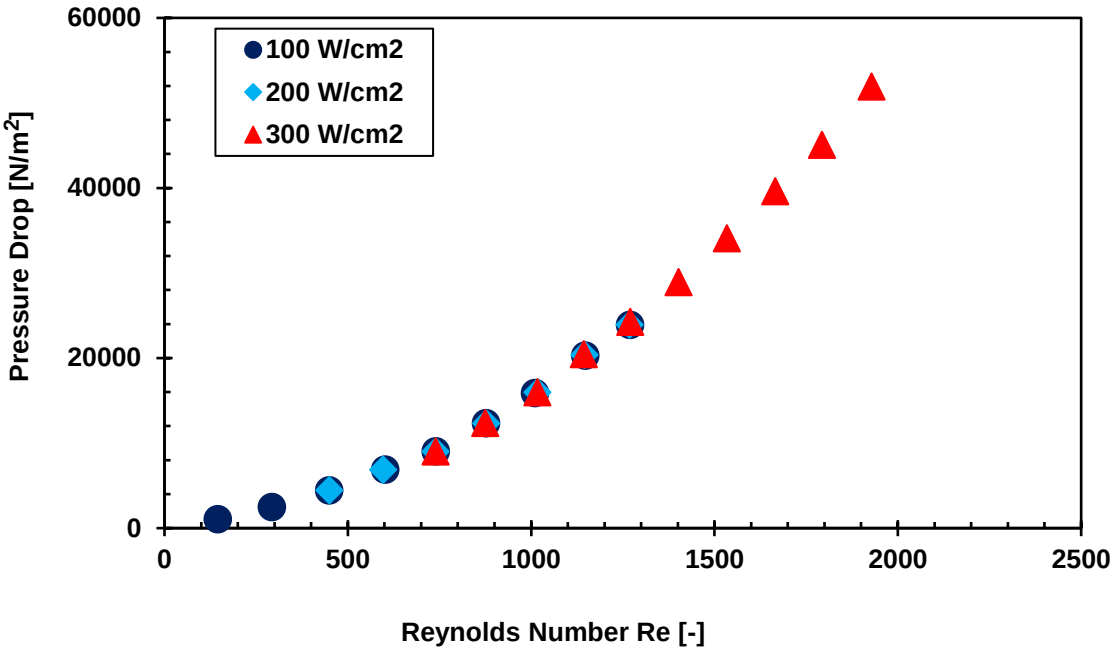

Figure 6.54. Effect of pressure drop on Reynolds number.

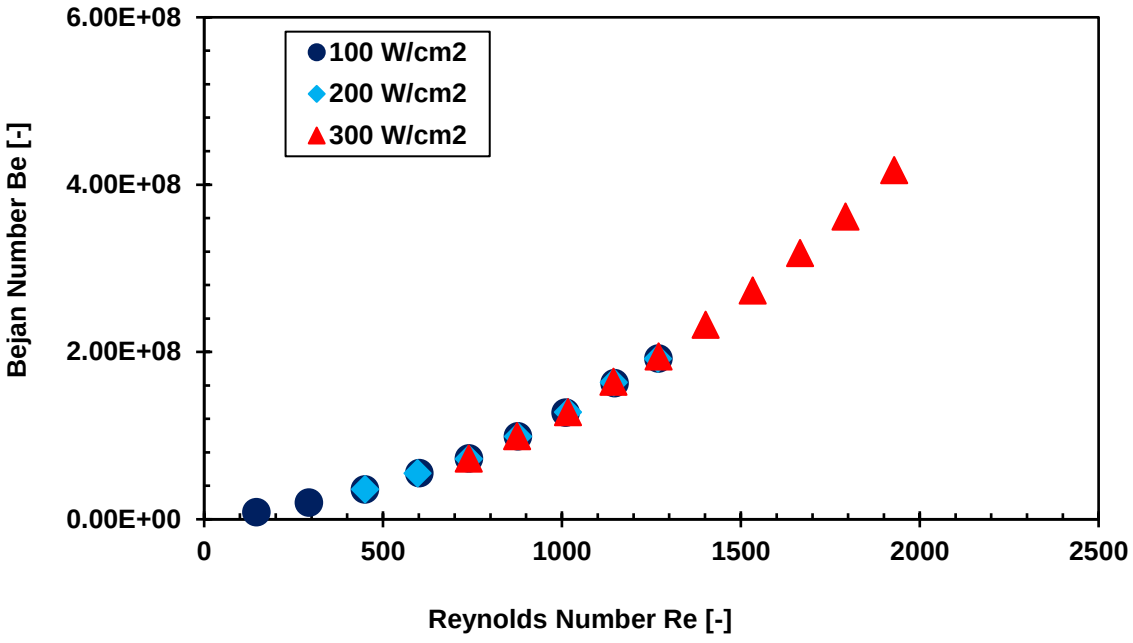

Figure 6.55. Effect of dimensionless pressure drop on Reynolds number.

Temperature contours

The heat flux for the contours in Figure 6.56-Figure 6.60 is 100 W/cm^2 at 2.489 m/s in subcooled flow boiling. Wall temperature contours are shown in Figure 6.56 and Figure 6.57. The maximum inner wall temperature at the outlet is 319.5 K compared to that of circular microchannel heat sink at the same velocity range and heat flux which is 322 K. The maximum base temperature is 319.523 K. Figure 6.57 shows the variation of wall temperature from the inlet to the outlet of the heat sink.

The water temperature contours are shown in Figure 6.58 and Figure 6.59 with the outlet maximum of 302.639 K. Figure 6.60 shows that water entered in single-phase, maintaining this for a short distance in the microchannel before onset of nucleate boiling (red part).

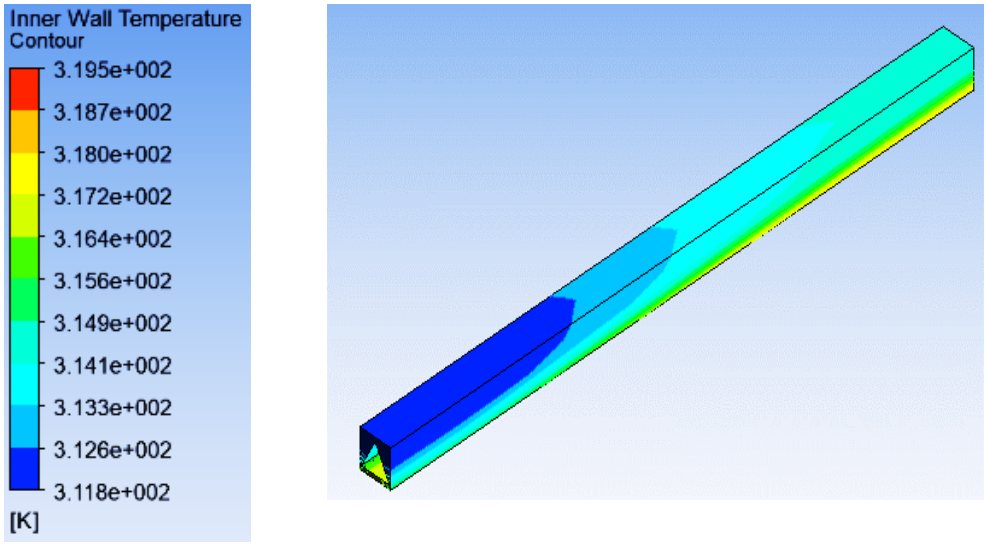

Figure 6.56. Inner wall temperature contour (base temperature = 319.523 K).

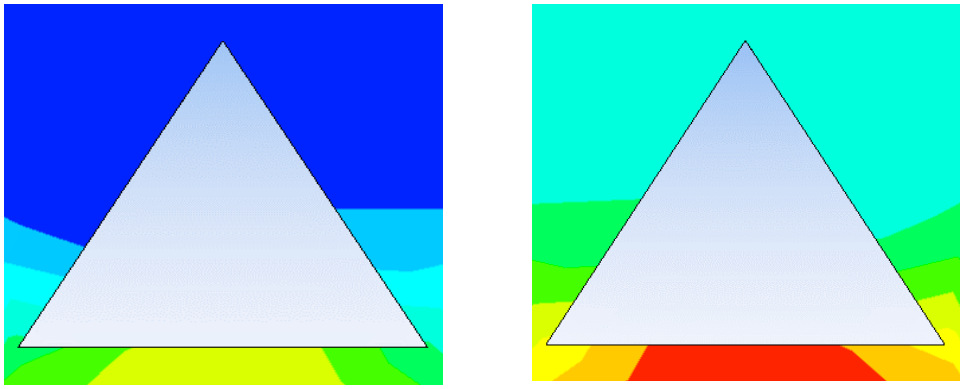

(a) Inlet wall temperature contour (b) Outlet wall temperature contour

Figure 6.57. Inlet and outlet wall temperature contours.

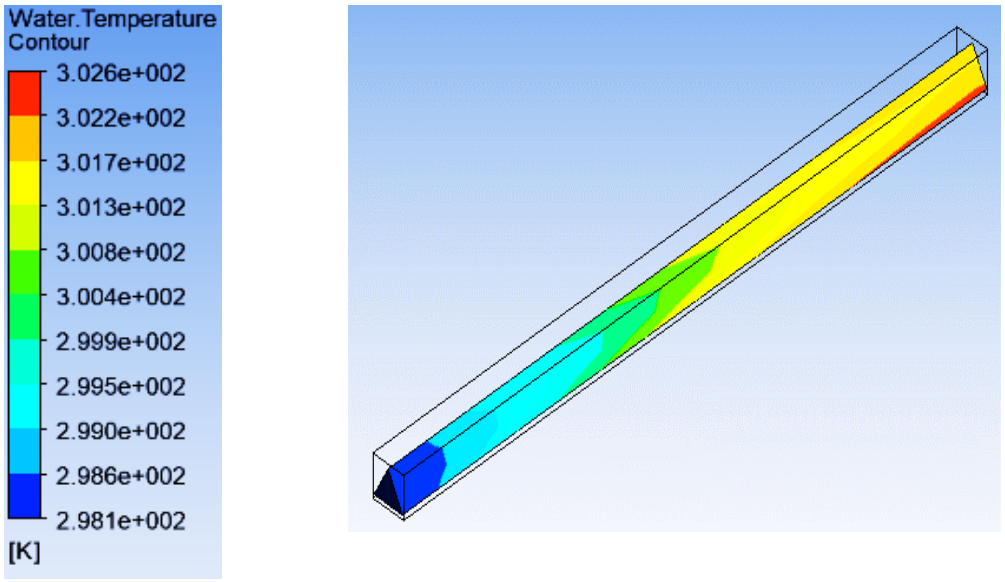

Figure 6.58. Water temperature contour.

(outlet water temperature = 302.639 K, optimal velocity = 2.489 m/s)

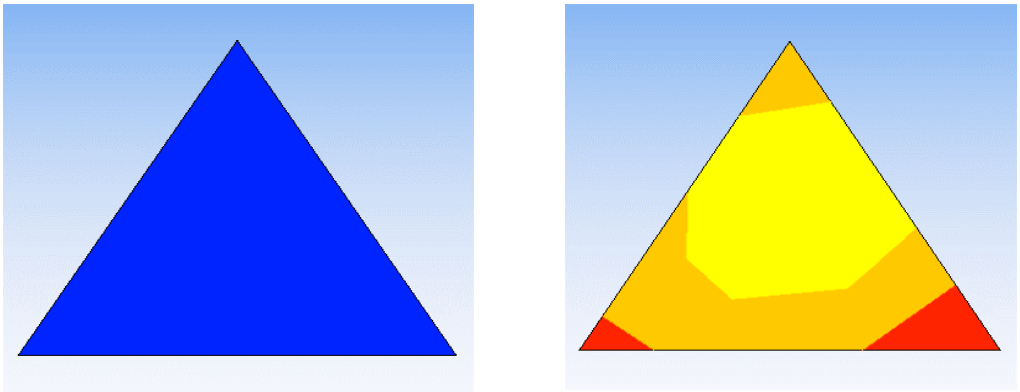

(a) Inlet water temperature contour (b) Outlet water temperature contour

Figure 6.59. Inlet and outlet water temperature contours.

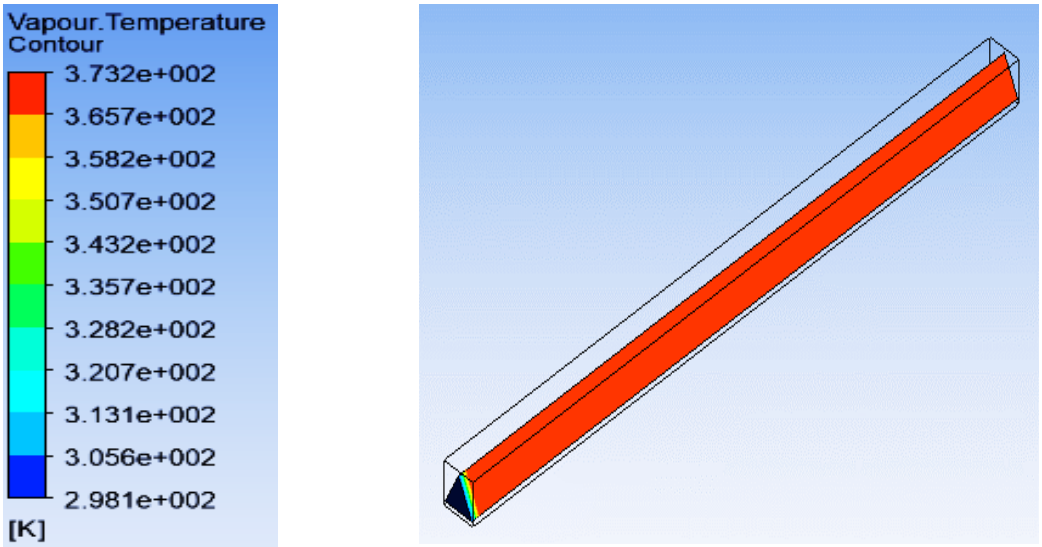

Figure 6.60. Vapour temperature contour.

6.2.2.2. Comparisons of two-phase and single-phase flow at 100 W/cm^2

Two-phase and single-phase flow are compared at 100 W/cm^2 as shown in Figure 6.61-Figure 6.69. Results are not available for other heat fluxes because of high base temperatures above the maximum for modern electronic devices. The thermal characteristics of optimal microchannel heat sinks are shown in Figure 6.61 and Figure 6.62. Optimal values were obtained at the following velocities: 0.1-0.5 to 4.0-4.5 in two-phase flow and 2.0-2.5 to 4.0-4.5

in single-phase flow. Optimal microchannel heat sinks in two-phase flow performed better than those in single-phase flow, which is expected. The base temperatures in Figure 6.62 show that the optimal microchannel heat sinks can be operated at relatively low temperatures.

The pumping power requirements are shown in Figure 6.63. The pumping power requirements are higher for two-phase flow at high pressure drops which are reflected in the last two optimal microchannel heat sinks. This same trend was obtained for the circular microchannel configuration (Figure 6.18).

Reynolds number and Bejan number relationships with optimal length are shown in Figure 6.64 and Figure 6.65. The differences in optimal lengths in two-phase and single-phase flow are small consistent with those obtained for circular configuration (Figure 6.19 and Figure 6.20). Despite the small differences, heat transfer mechanisms in two-phase and single-phase flow distinguish the rate of heat removal in the microchannels.

Optimal hydraulic diameters in Figure 6.66 and Figure 6.67 show the same trend with those of circular microchannel configuration (Figure 6.21 and Figure 6.22), with a narrow range of variation.

Figure 6.68 and Figure 6.69 show the relationships between Reynolds number, pressure drop and Bejan number. The pressure drops for two-phase flow are evidently higher than those of single-phase flow at high Reynolds numbers as shown in Figure 6.68 and Figure 6.69. This trend is consistent with Figure 6.23 and Figure 6.24.

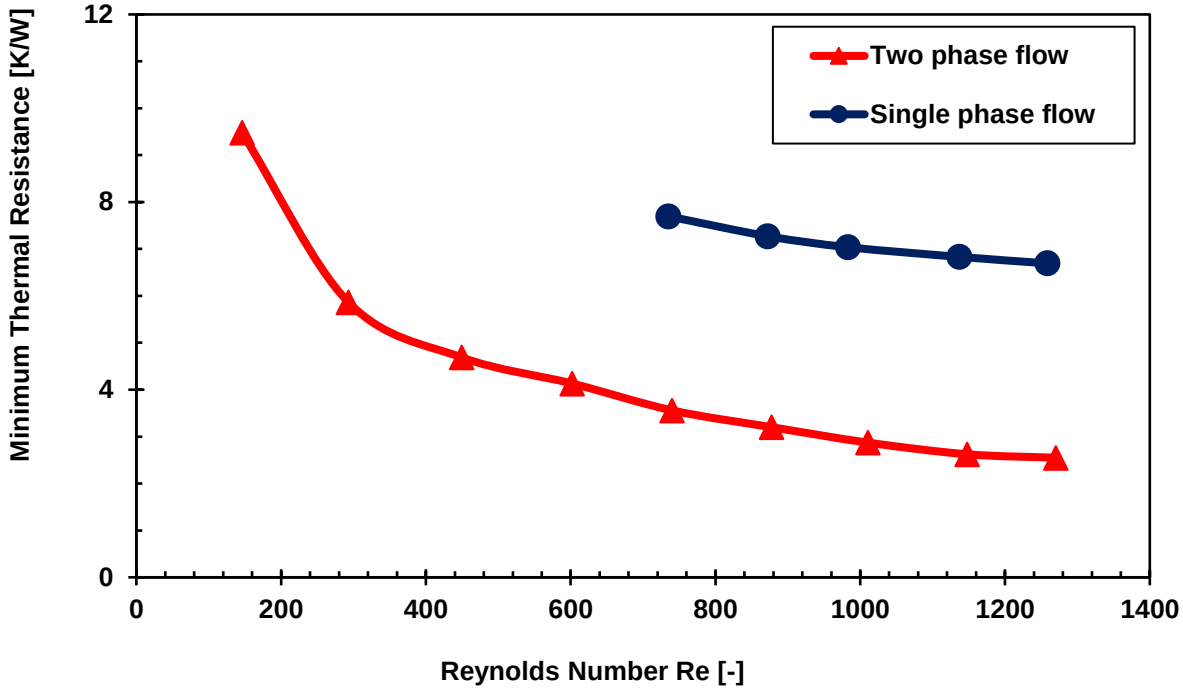

Figure 6.61. Thermal resistances of optimal microchannel heat sinks at 100 W/cm^2.

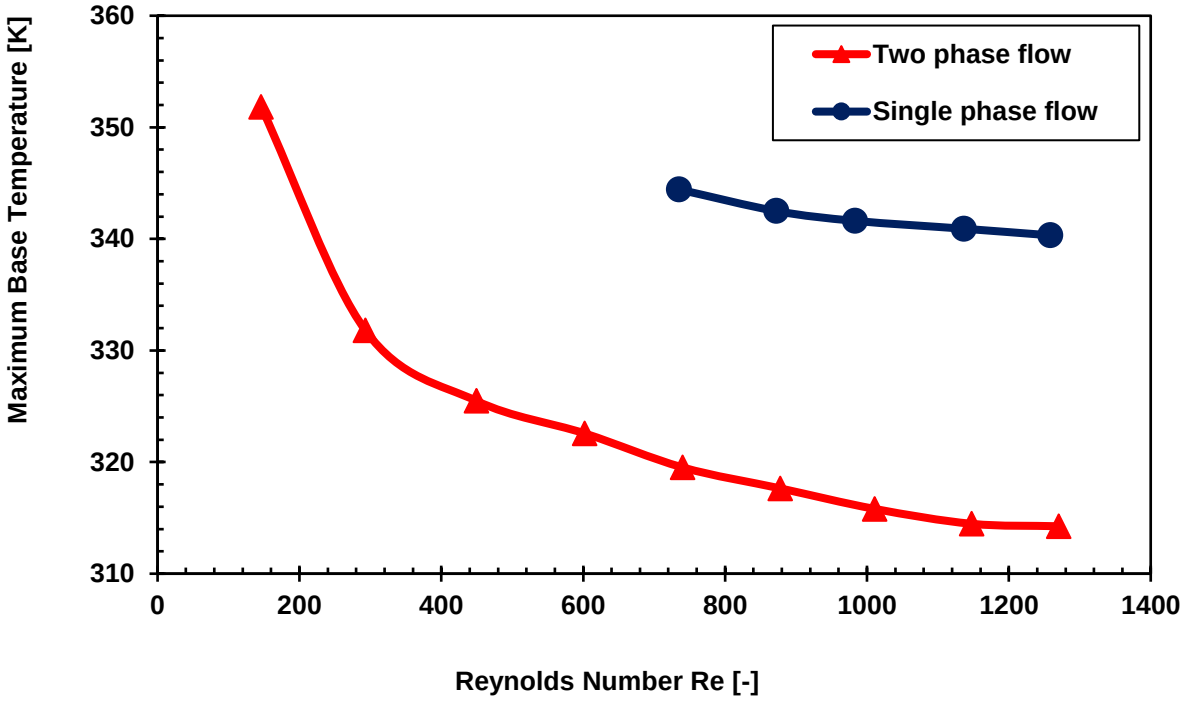

Figure 6.62. Maximum base temperatures of optimal microchannel heat sinks at 100 W/cm^2.

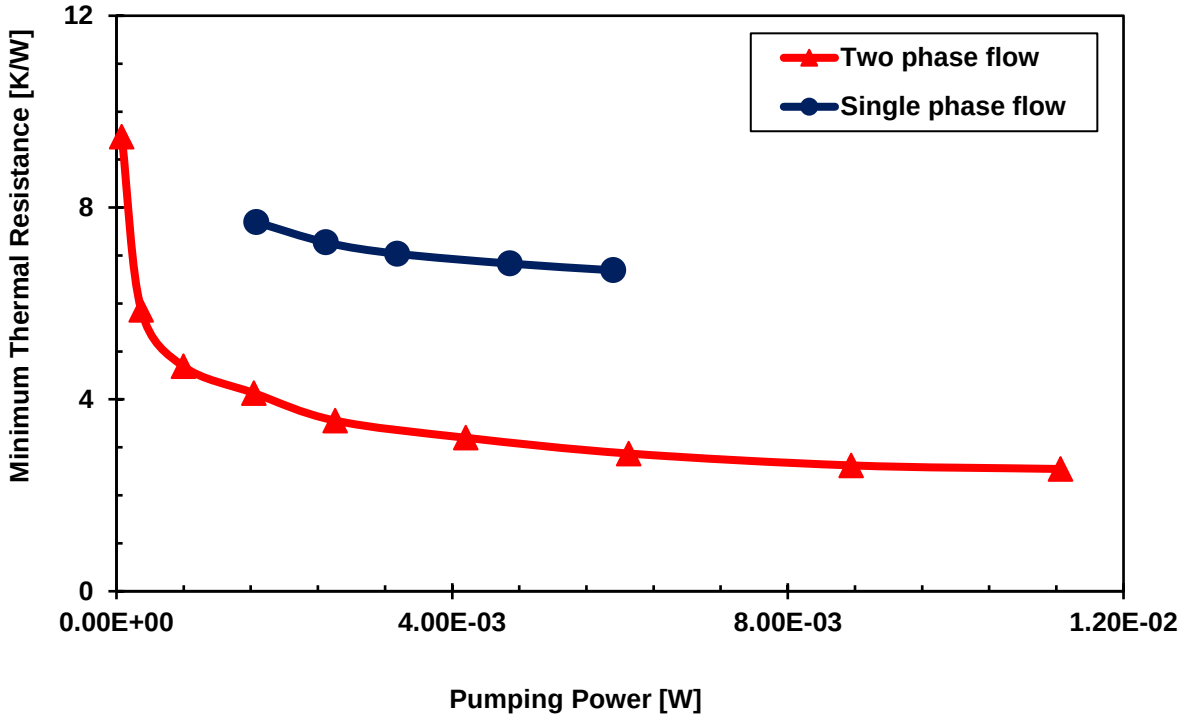

Figure 6.63. Pumping power of optimal microchannel heat sinks at 100 W/cm^2.

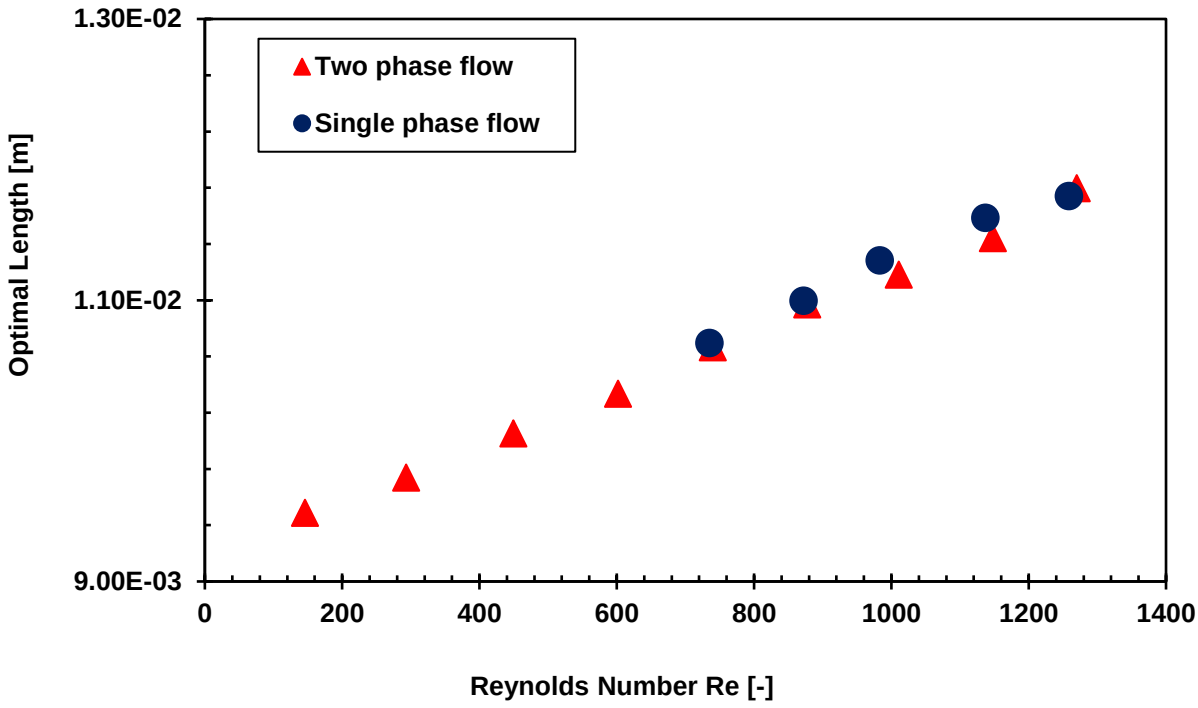

Figure 6.64. Effect of length on optimal microchannel heat sinks at 100 W/cm^2.

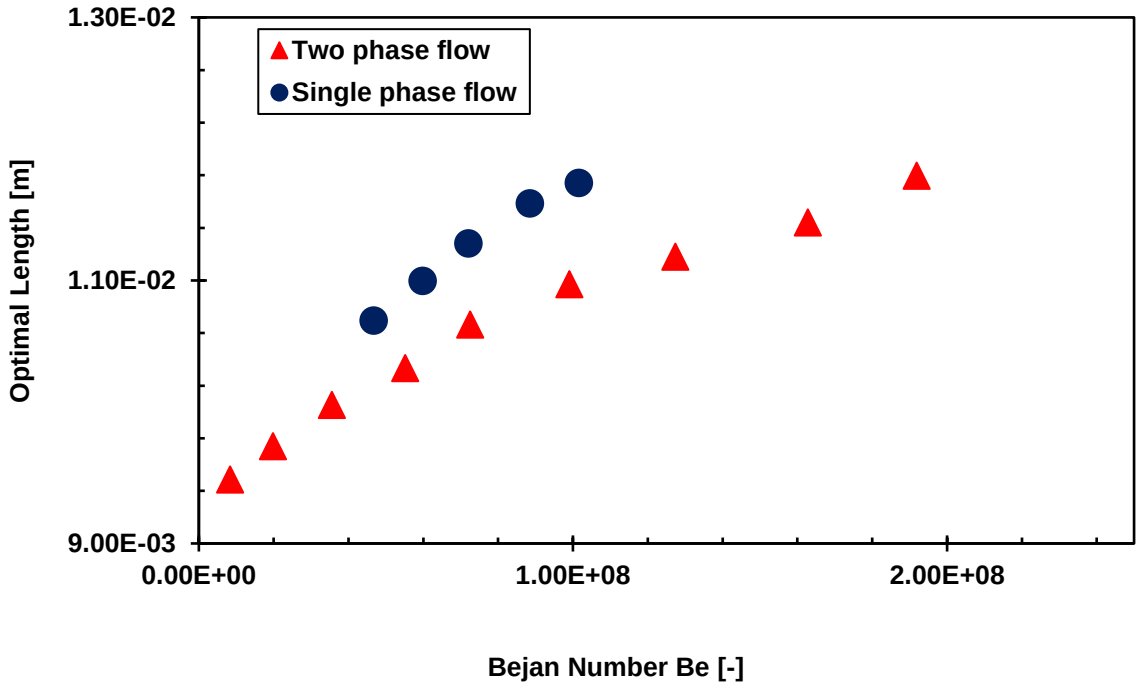

Figure 6.65. Effect of dimensionless pressure drop on optimal length at 100 W/cm^2.

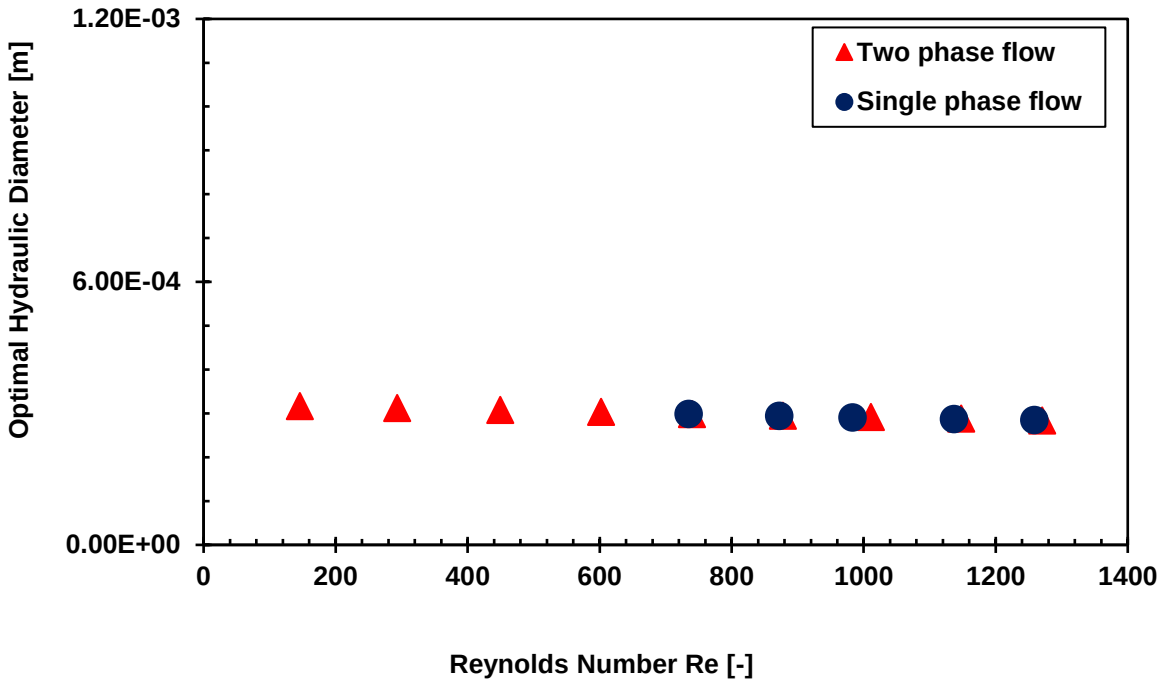

Figure 6.66. Effect of hydraulic diameter on optimal microchannel heat sinks at 100 W/cm^2.

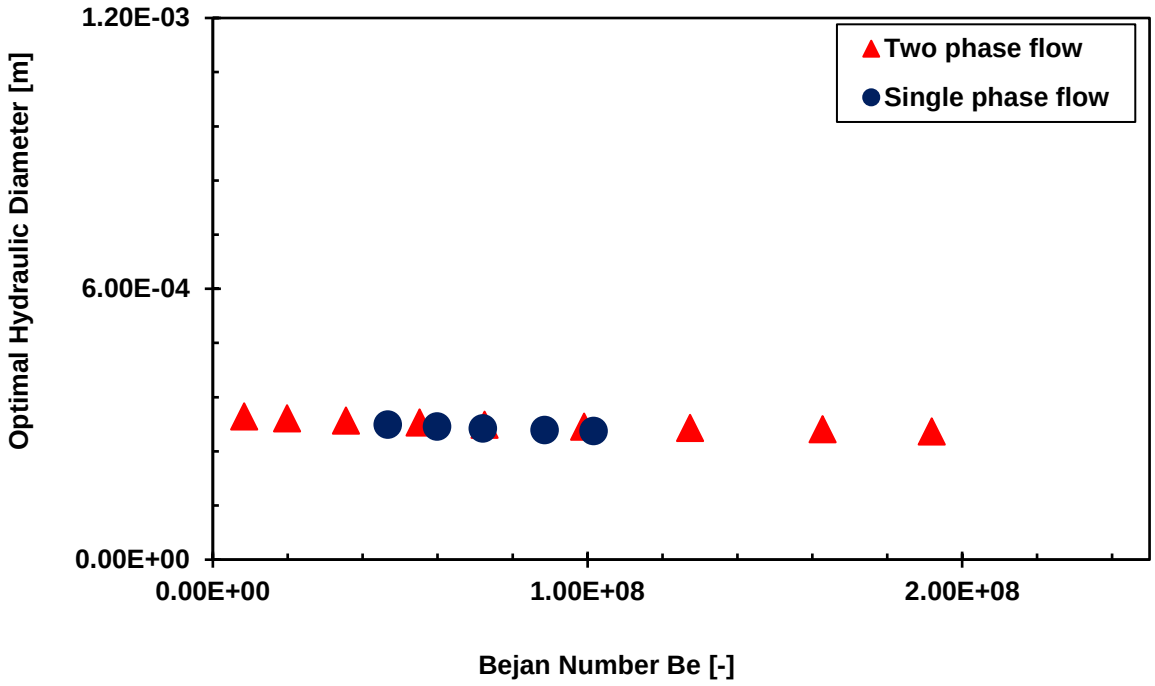

Figure 6.67. Effect of dimensionless pressure drop on optimal hydraulic diameter at 100 W/cm^2.

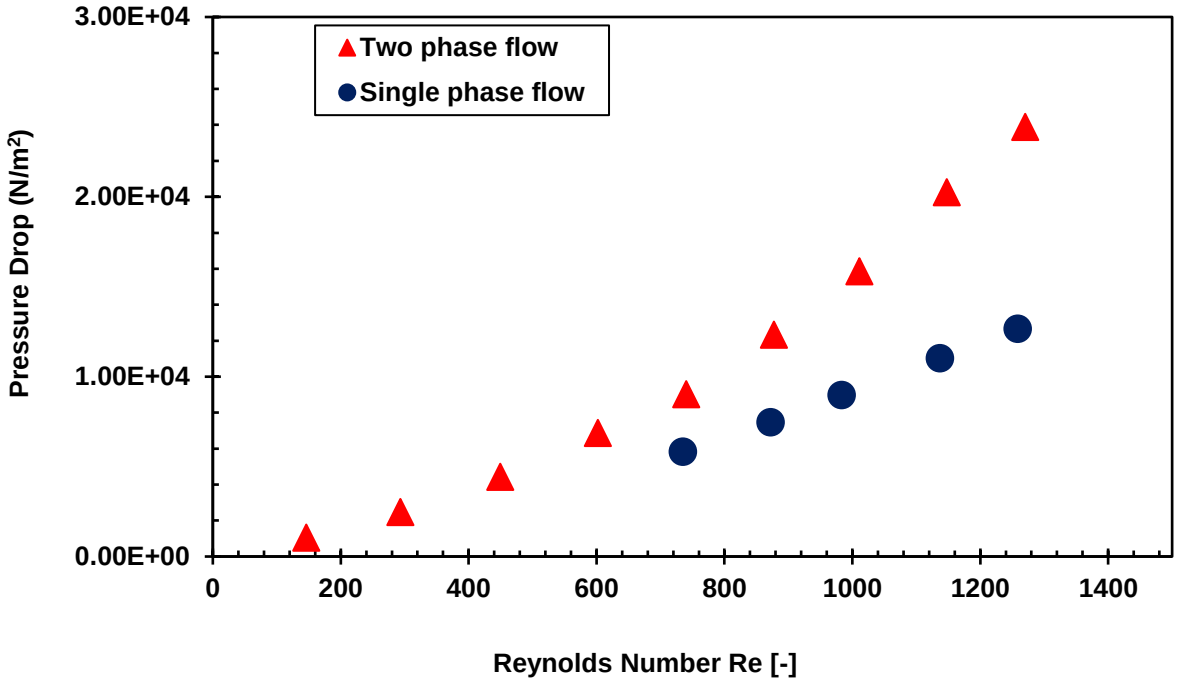

Figure 6.68. Effect of pressure drop on Reynolds number at 100 W/cm^2.

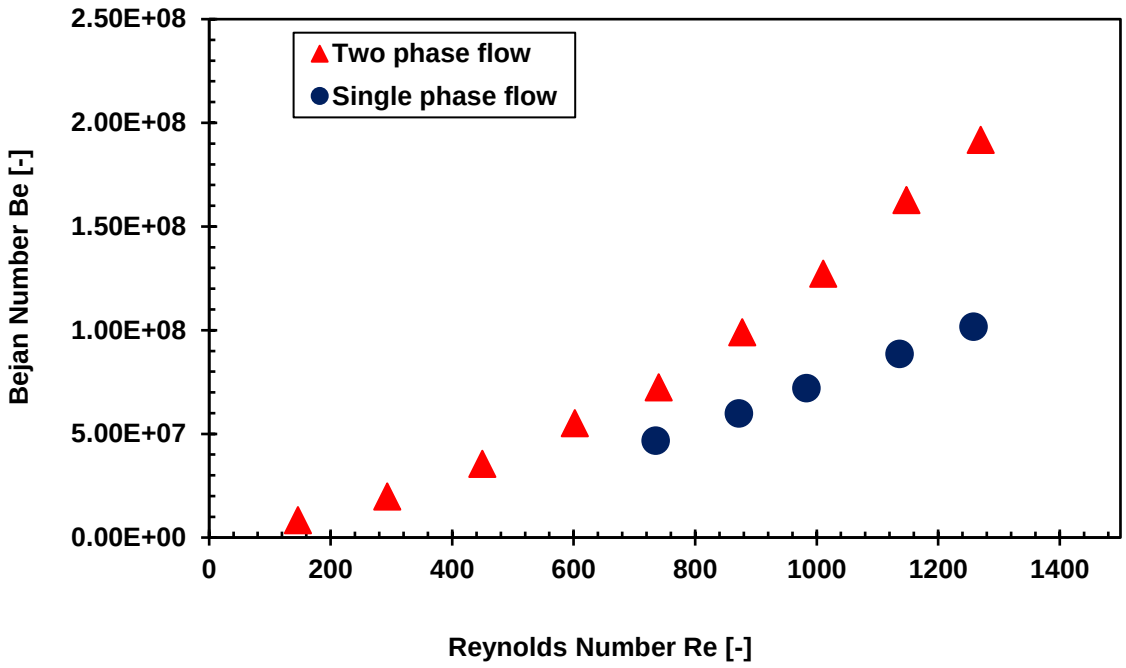

Figure 6.69. Effect of dimensionless pressure drop on Reynolds number at 100 W/cm^2.

Temperature contours

The heat flux for the contours in Figure 6.70-Figure 6.73 is 100 W/cm^2 at 2.475 m/s in single-phase flow. Two-phase flow had its inner wall temperature varying between 311.8 and 319.523 K (Figure 6.56) while that in single-phase flow varied between 334.7 and 344.4 K as shown in Figure 6.70. Figure 6.71(a) and Figure 6.71(b) show wall temperature distribution of inlet and outlet walls.

Figure 6.72 shows water temperature contour from inlet to outlet of the microchannel. The water temperature varied between 298.15 K at the inlet and 302.639 K at the outlet (Figure 6.58) while for single-phase flow, water temperature varied between 298.15 and 306.394 (Figure 6.72) from inlet to outlet of the microchannel. The corresponding temperature contours at inlet and outlet are shown in Figure 6.73(a) and Figure 6.73(b). The differences between the values of two-phase and single-phase flow show evidence of the superior performances of optimal microchannel heat sinks in two-phase flow.

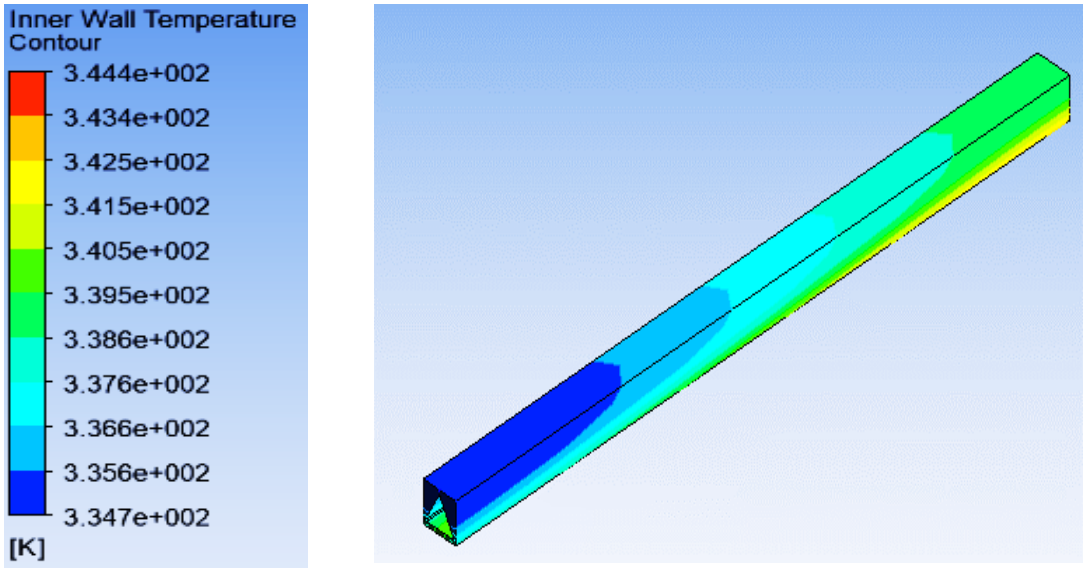

Figure 6.70. Inner wall temperature contour (base temperature = 344.425 K).

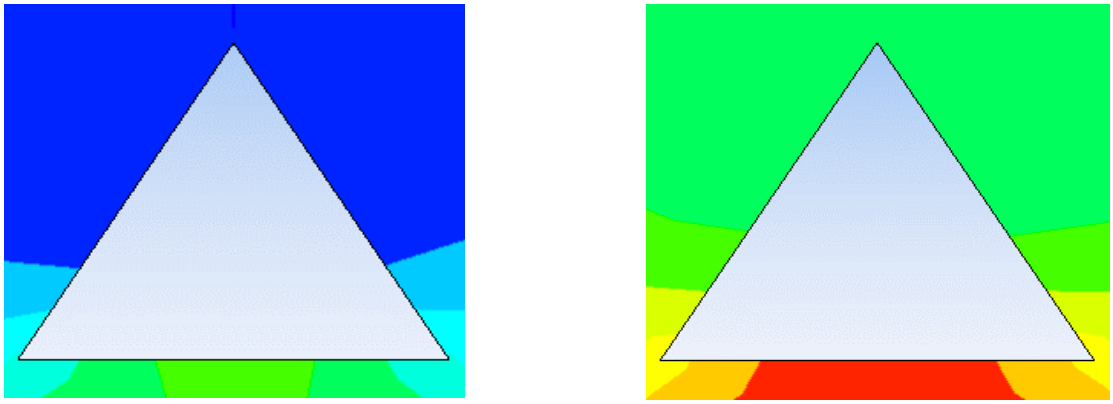

(a) Inlet wall temperature contour (b) Outlet wall temperature contour

Figure 6.71. Inlet and outlet wall temperature contours.

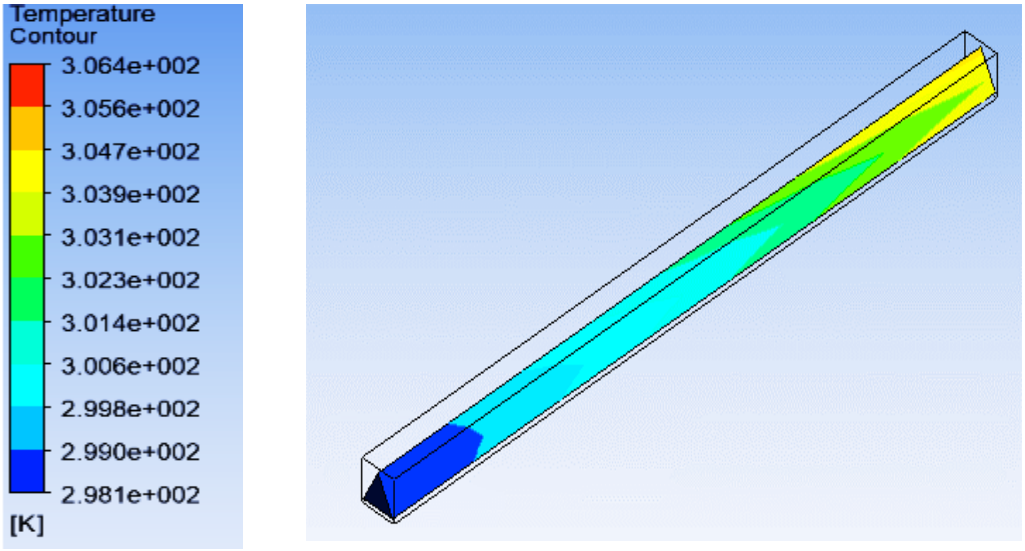

Figure 6.72. Water temperature contour.

(Outlet water temperature = 306.394 K, optimal velocity = 2.475 m/s)

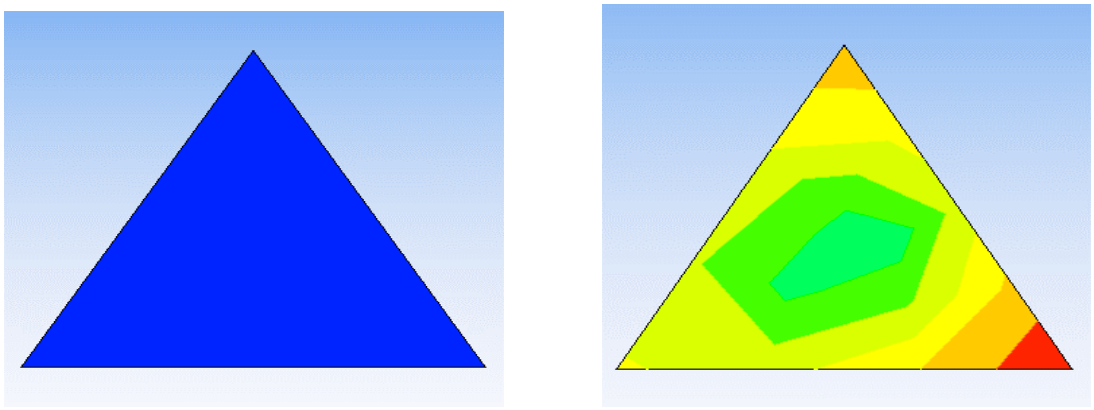

(a) Inlet water temperature contour (b) Outlet water temperature contour

Figure 6.73. Inlet and outlet water temperature contours.

6.2.3. Rectangular microchannel heat sinks

6.2.3.1. Subcooled flow boiling (Two-phase flow)

The aspect ratio of a rectangular microchannel defined as ratio of its height to width is greater than 1 in this work. Values were available for optimal microchannel heat sinks up to 700 W/cm^2 as shown in Figure 6.74-Figure 6.76. The velocities are: 0.1-0.5 to 4.0-4.5 m/s at 100 W/cm^2; 0.5-1.0 to 4.0-4.5 m/s at 200 W/cm^2; 1.0-1.5 to 4.0-4.5 m/s at 300 W/cm^2; 4.5-5.0 to 6.5-7.0

m/s at 400 W/cm^2; 4.5-5.0 to 6.5-7.0 m/s at 500 W/cm^2; 5.0-5.5 to 6.5-7.0 m/s at 600 W/cm^2; 5.5-6.0 to 6.5-7.0 m/s at 700 W/cm^2.

The curves are not as close as obtained previously for circular and equilateral microchannel heat sinks (Figure 6.2 and Figure 6.47) but are of the same trend of decreasing thermal resistance with increasing Reynolds number, hence the graphs have been split into three as shown in Figure 6.74-Figure 6.79.

Figure 6.74 shows the thermal resistances of optimal microchannel heat sinks at various Reynolds numbers. The optimal microchannel heat sinks show good thermal performances for the heat fluxes and velocities considered. The optimal microchannel heat sinks show lower thermal resistances as Reynolds number increases which is consistent with Figure 6.2 and Figure 6.47. The corresponding base temperatures are shown in Figure 6.77.

Figure 6.75 and Figure 6.76 show the thermal resistances of optimal microchannel heat sinks at higher heat fluxes than obtained previously for circular and equilateral triangular microchannel heat sinks (Figure 6.2 and Figure 6.47). This observation is crucial to the effort made to push the heat flux removal with rectangular microchannel heat sinks to 1200 W/cm^2 in this study. The corresponding base temperatures are shown in Figure 6.78 and Figure 6.79. The base temperatures are below the upper limit for modern electronic devices.

The pumping power requirements for optimal microchannel heat sinks operating between 100 and 300 W/cm^2 are shown in Figure 6.80. The pumping power requirements for most optimal rectangular microchannel heat sinks are better than those in Figure 6.4 and Figure 6.49 and are of the same trend of decreasing thermal resistance as pumping power increases. Pressure drop affects micro pumping in the microchannel because low pressure drops lead to smaller micro pumps. One of the advantages of nucleate boiling is the independence of heat transfer coefficient on velocity or mass velocity which makes it possible to use a fixed speed pump, resulting in a simpler and more reliable cooling system at a reduced cost [7]. High pressure drops are offset by low volumetric flow rates to achieve low pumping power.

The relationships between aspect ratio, Reynolds number and Bejan number are shown in Figure 6.81 and Figure 6.82. These variations allowed for flexibility in the optimisations for optimal geometric and flow parameters. The optimal aspect ratios affect subcooled flow boiling in the microchannels; the volumetric flow rate either increases or reduces because of low or

high aspect ratios. These depend on small surface area to cross sectional area ratio or large surface area to cross sectional area ratio. High aspect ratios were recorded for a few optimal microchannel heat sinks at 200 and 300 w/cm^2.

The effects of length on Reynolds number and Bejan number are shown in Figure 6.83 and Figure 6.84. Length increased with Reynolds number and Bejan number until optimal values were obtained in the optimisation. This trend is consistent with Figure 6.5 and Figure 6.6, also Figure 6.50 and Figure 6.51.

Figure 6.85 and Figure 6.86 show the influence of hydraulic diameter on Reynolds number and Bejan number. The optimal hydraulic diameters occur within a narrow range and not decreasing slightly as Reynolds number increases as seen previously (Figure 6.7 and Figure 6.8, and Figure 6.52 and Figure 6.53).

Pressure drop and Bejan number increase as Reynolds number increases to obtain optimal geometric and flow parameters as shown in Figure 6.87 and Figure 6.88. This trend is consistent with Figure 6.9 and Figure 6.10, also Figure 6.54 and Figure 6.55.

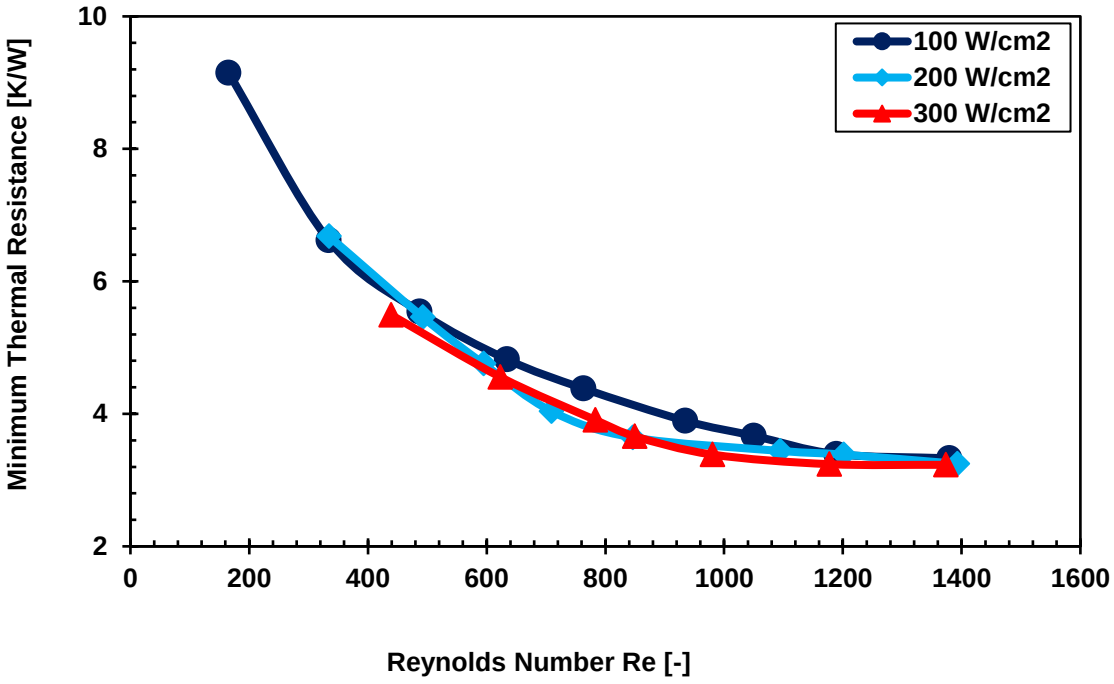

Figure 6.74. Thermal resistances of optimal microchannel heat sinks.

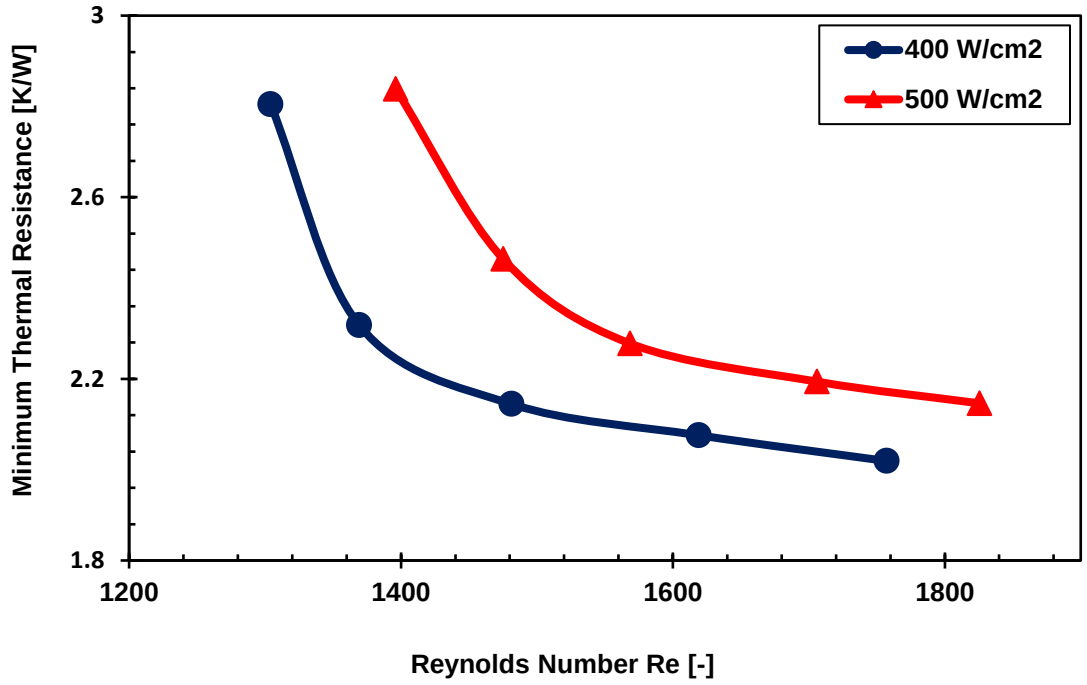

Figure 6.75. Thermal resistances of optimal microchannel heat sinks.

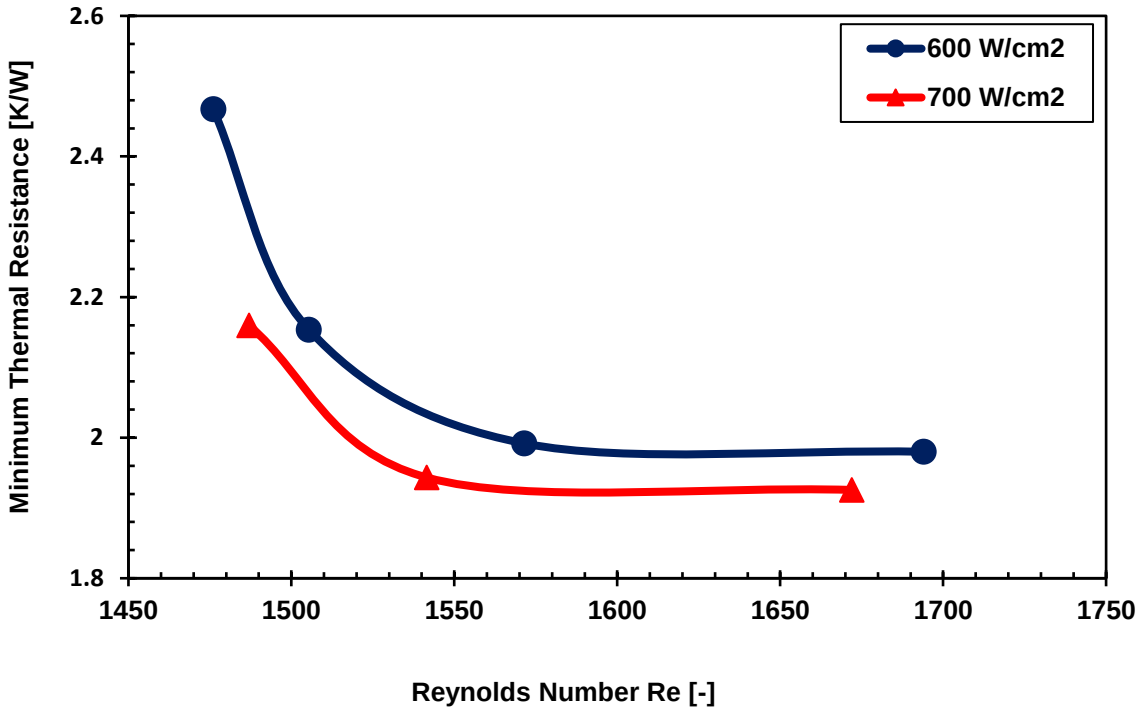

Figure 6.76. Thermal resistances of optimal microchannel heat sinks.

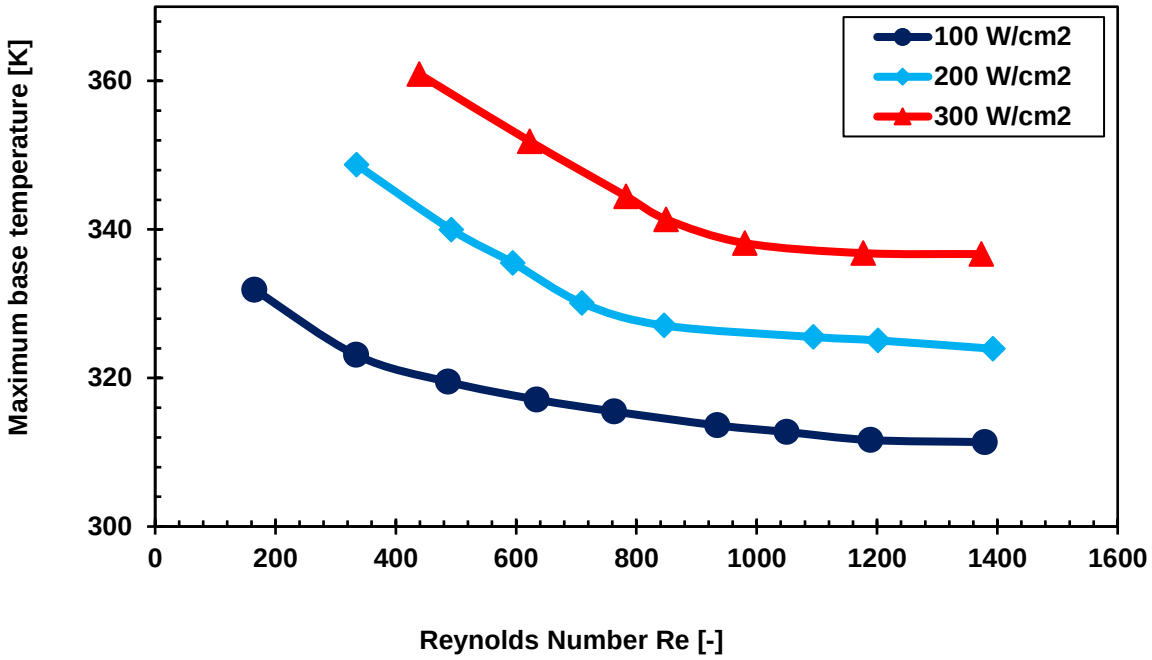

Figure 6.77. Maximum base temperatures of optimal microchannel heat sinks.

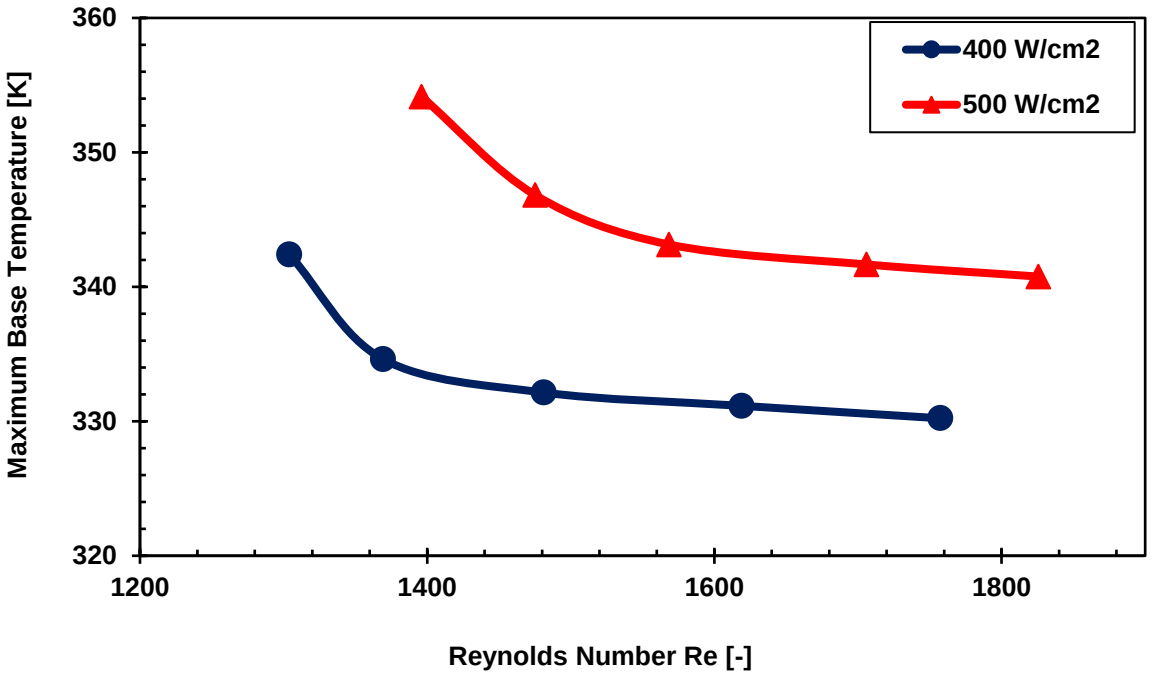

Figure 6.78. Maximum base temperatures of optimal microchannel heat sinks.

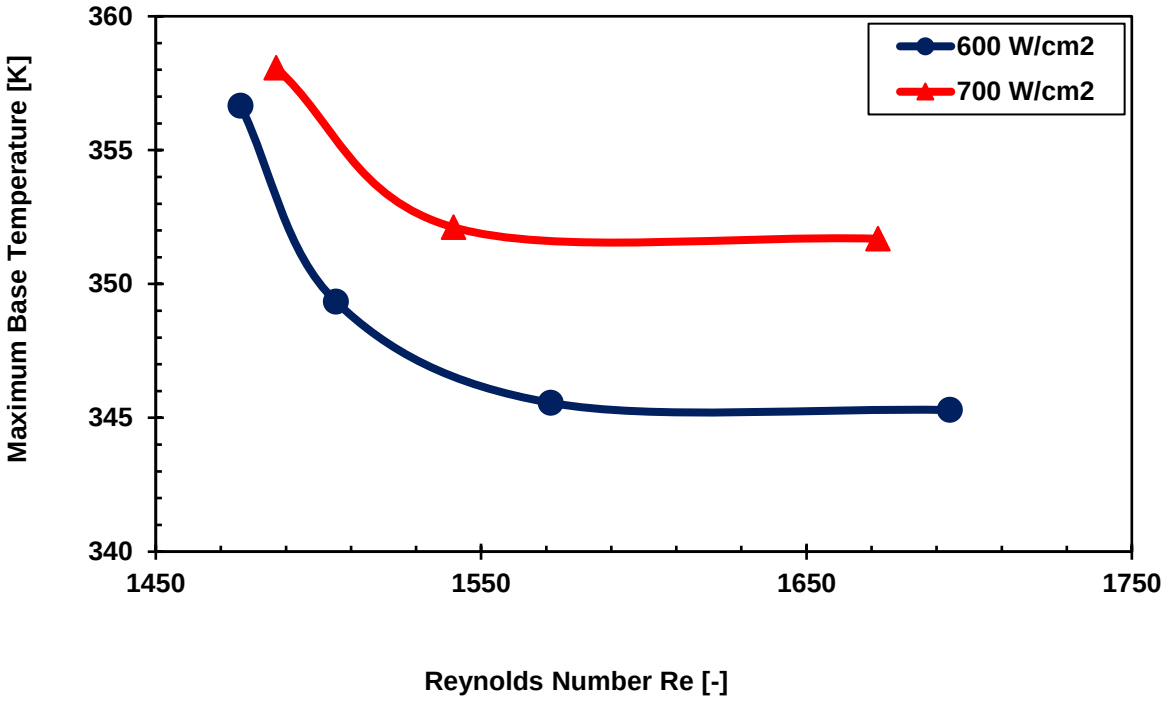

Figure 6.79. Maximum base temperatures of optimal microchannel heat sinks.

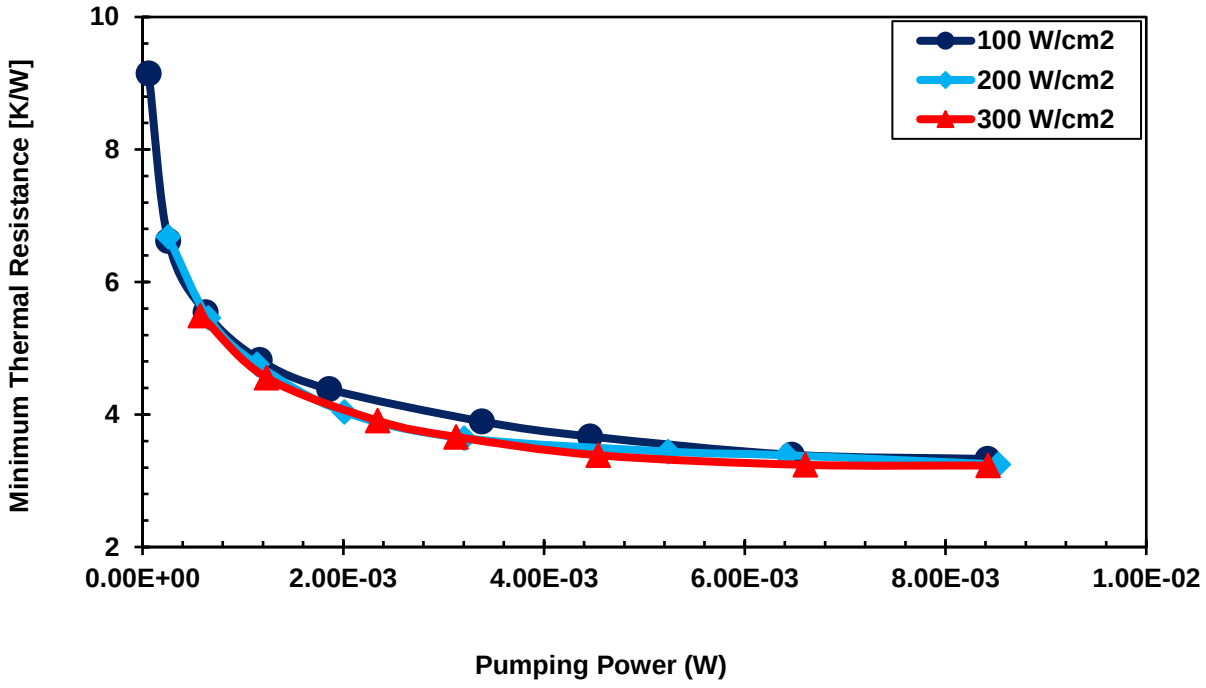

Figure 6.80. Pumping power of optimal microchannel heat sinks.

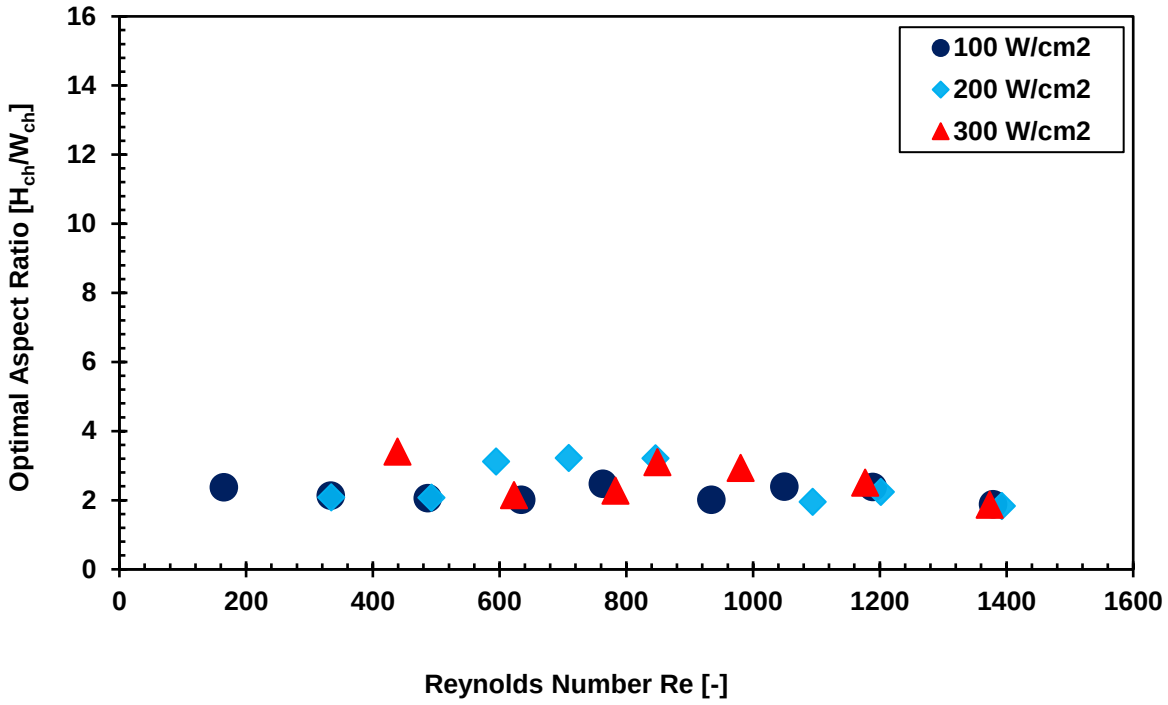

Figure 6.81. Effect of aspect ratio on optimal microchannel heat sinks.

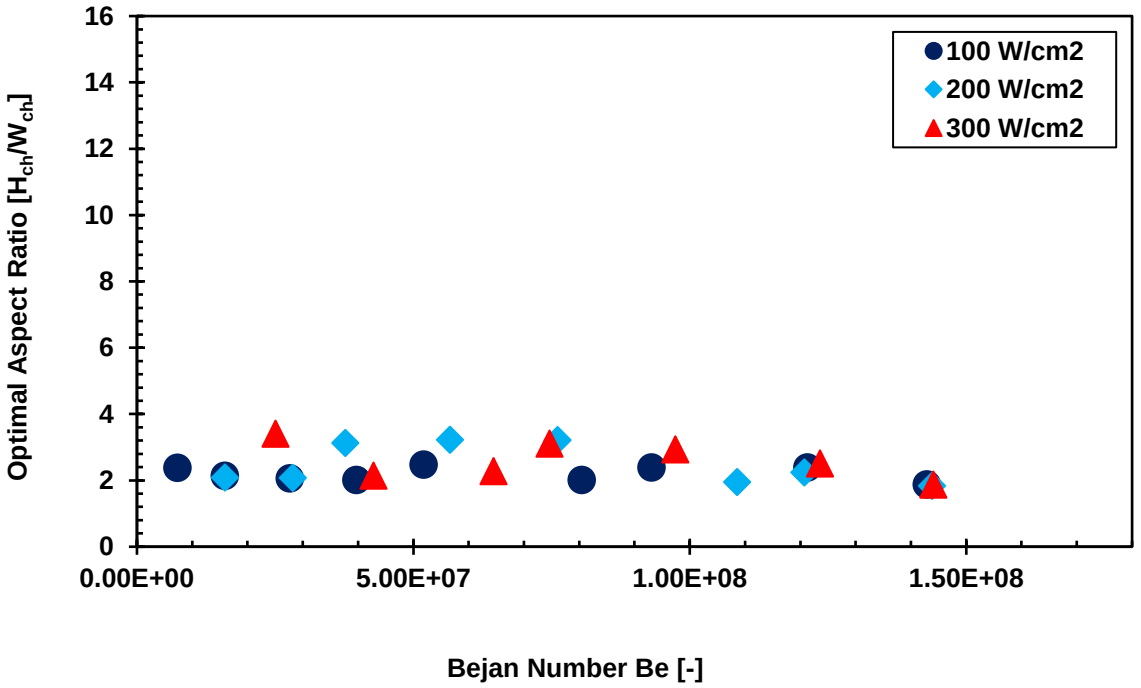

Figure 6.82. Effect of dimensionless pressure drop on optimal aspect ratio.

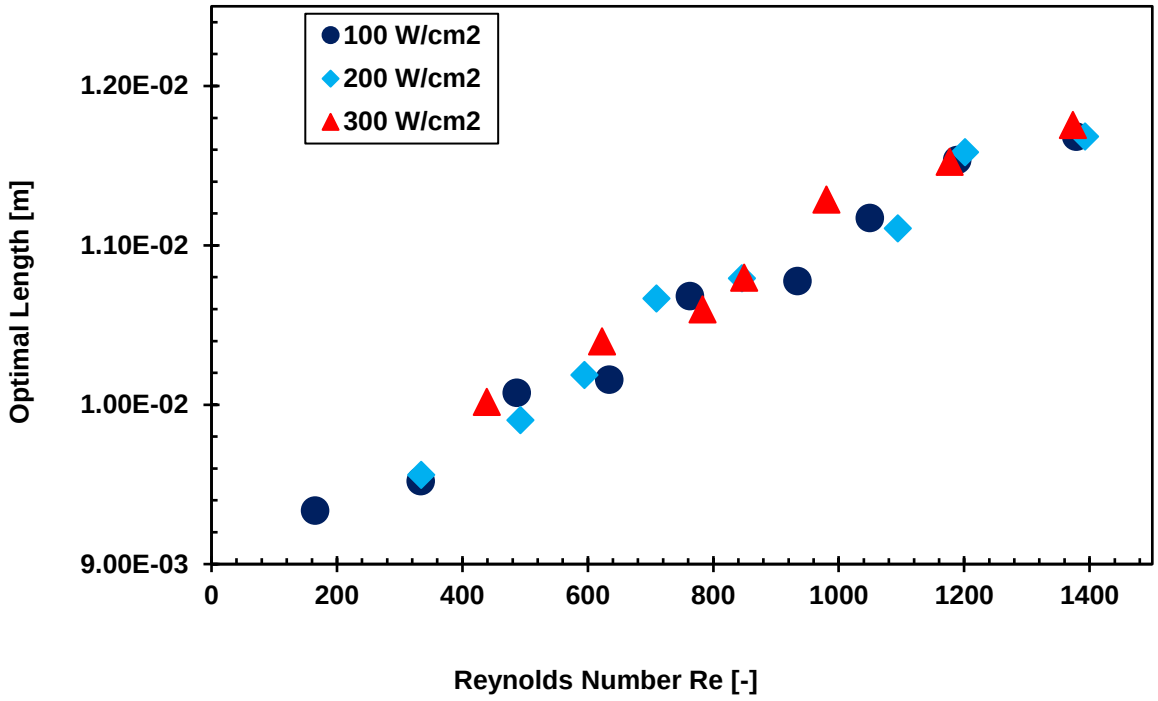

Figure 6.83. Effect of length on optimal microchannel heat sinks.

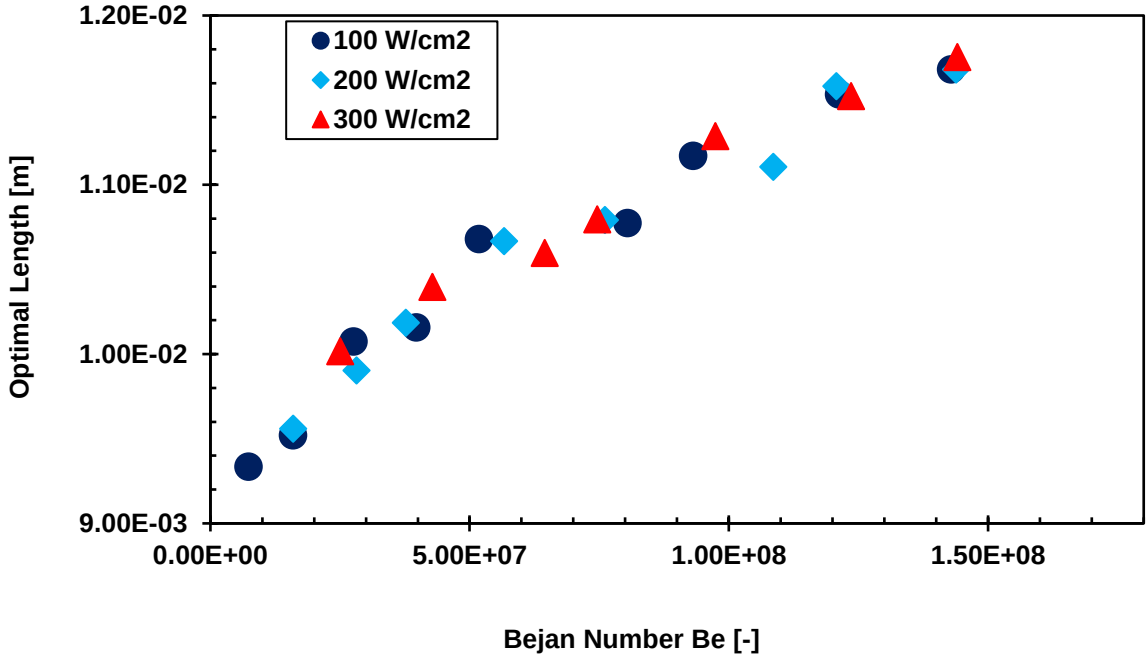

Figure 6.84. Effect of dimensionless pressure drop on optimal length.

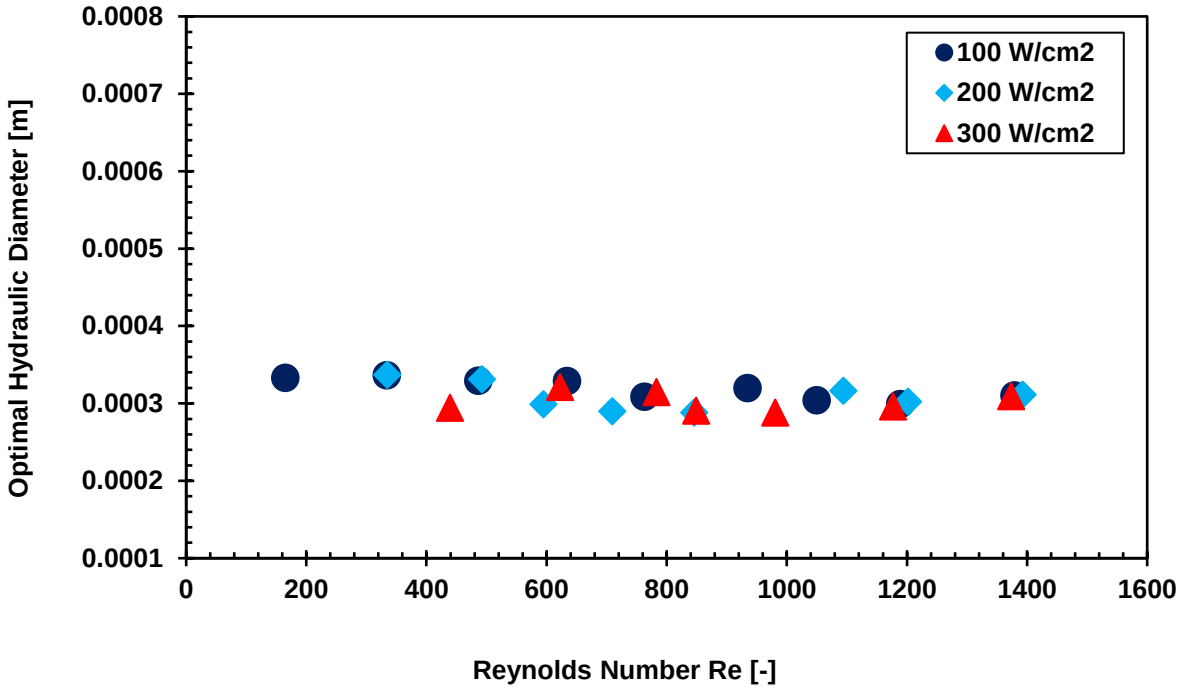

Figure 6.85. Effect of hydraulic diameter on optimal microchannel heat sinks.

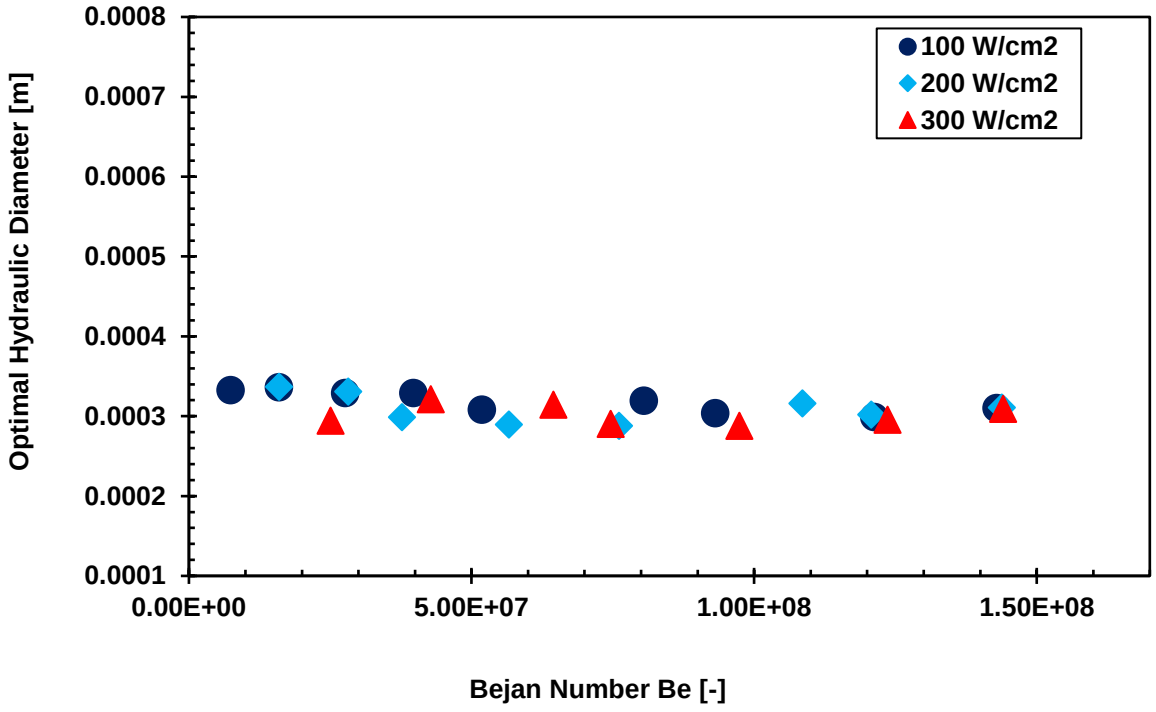

Figure 6.86. Effect of dimensionless pressure drop on hydraulic diameter.

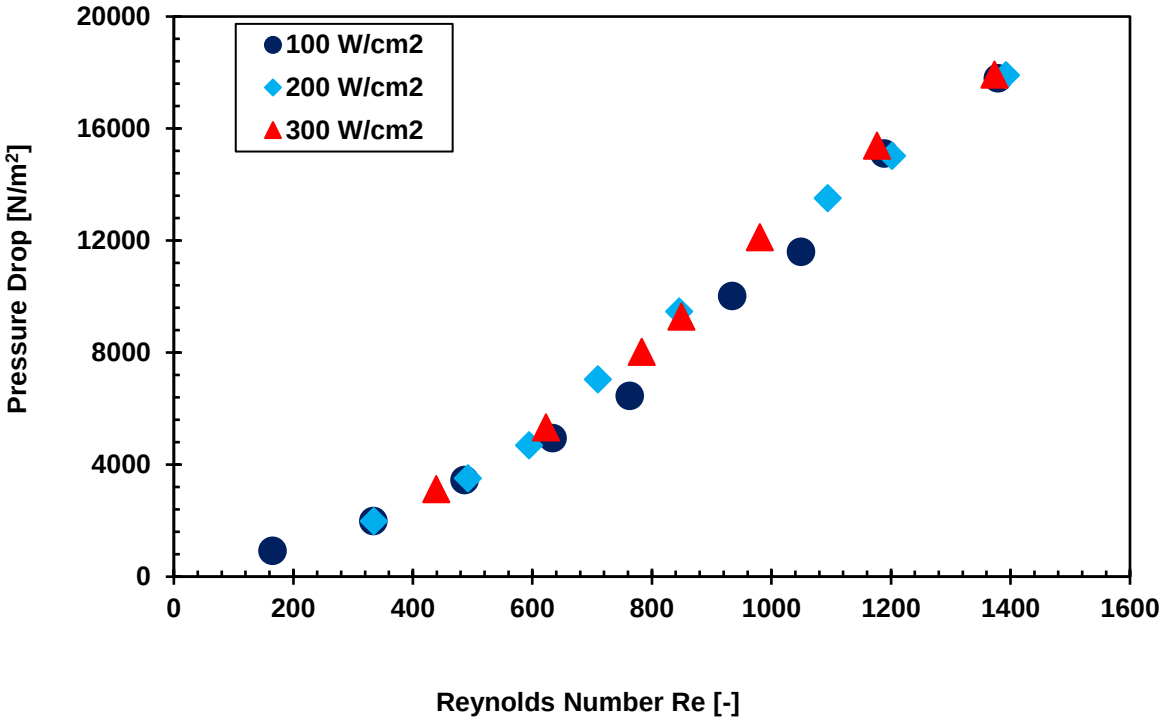

Figure 6.87. Effect of pressure drop on Reynolds number.

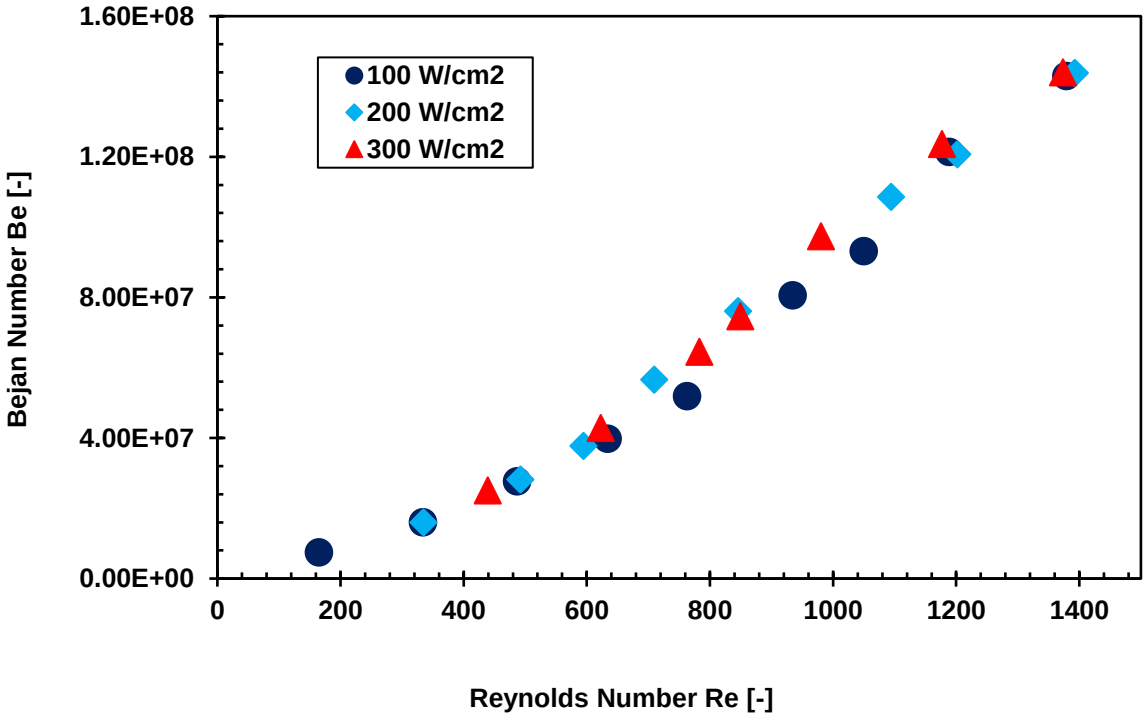

Figure 6.88. Effect of dimensionless pressure drop on Reynolds number.

Temperature contours

The heat flux for the contours in Figure 6.89-Figure 6.93 is 100 W/cm^2 in subcooled flow boiling. Temperature contours are shown in Figure 6.89 and Figure 6.90. The inner wall temperature contour shows temperature varying from 310.1 K at the inlet to 315.4 K at the outlet. The temperature contours in Figure 6.90(a) and Figure 6.90(b) provide information on wall temperature distribution at the inlet and outlet of the heat sink. Figure 6.91 and Figure 6.92 give information on water temperature distribution in the microchannel. Water temperature increases from the inlet of the microchannel to the outlet as heat is removed. Figure 6.93 gives details on when vapour starts forming in the microchannel at 373.15 K.

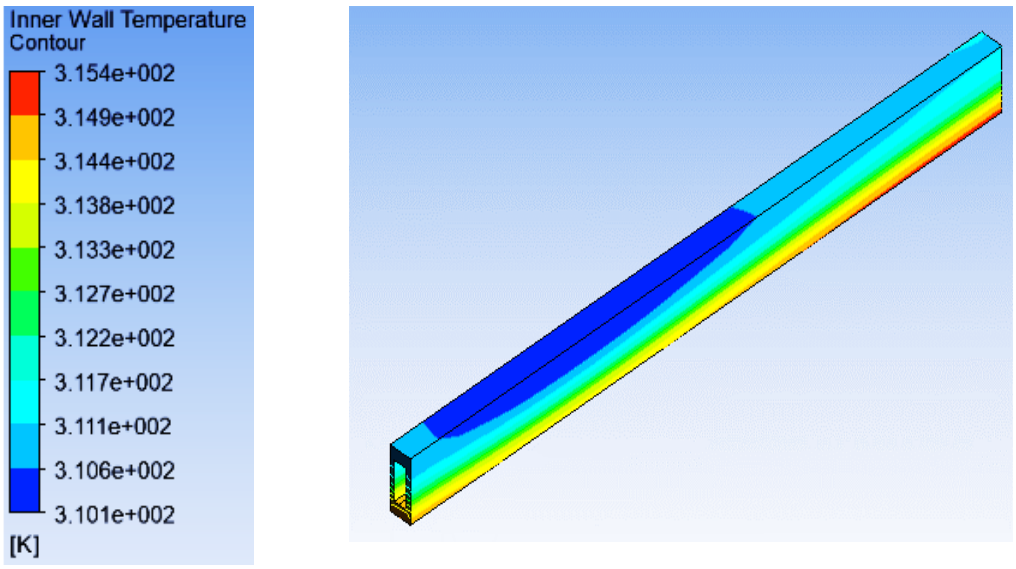

Figure 6.89. Inner wall temperature contour (base temperature = 315.488 K).

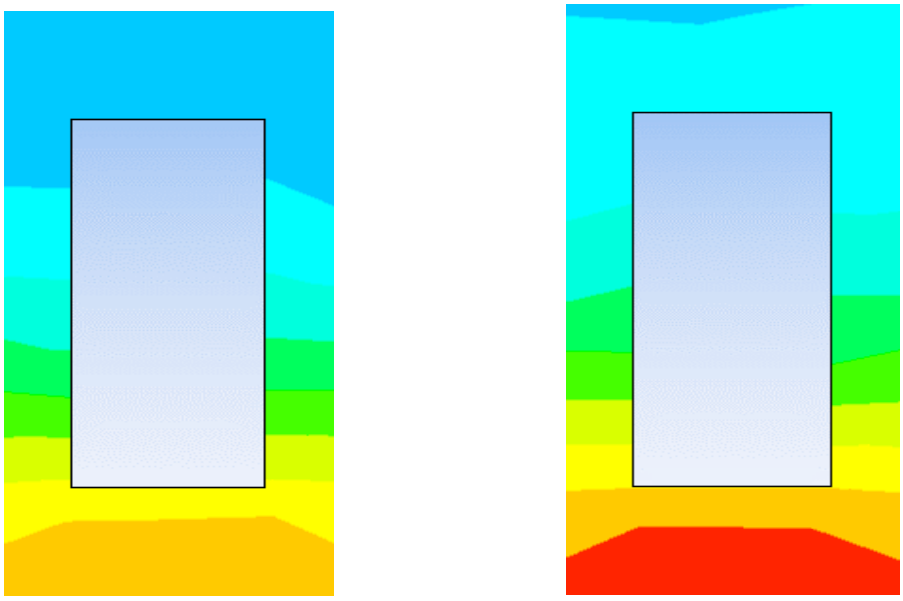

(a) Inlet wall temperature contour (b) Outlet wall temperature contour

Figure 6.90. Inlet and outlet wall temperature contours.

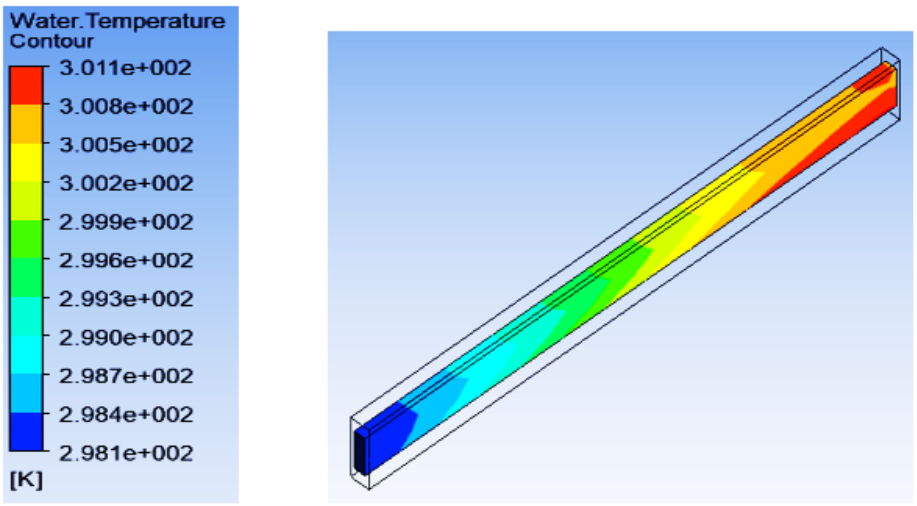

Figure 6.91. Water temperature contour.

(Outlet water temperature = 301.060 K, optimal velocity = 2.488 m/s)

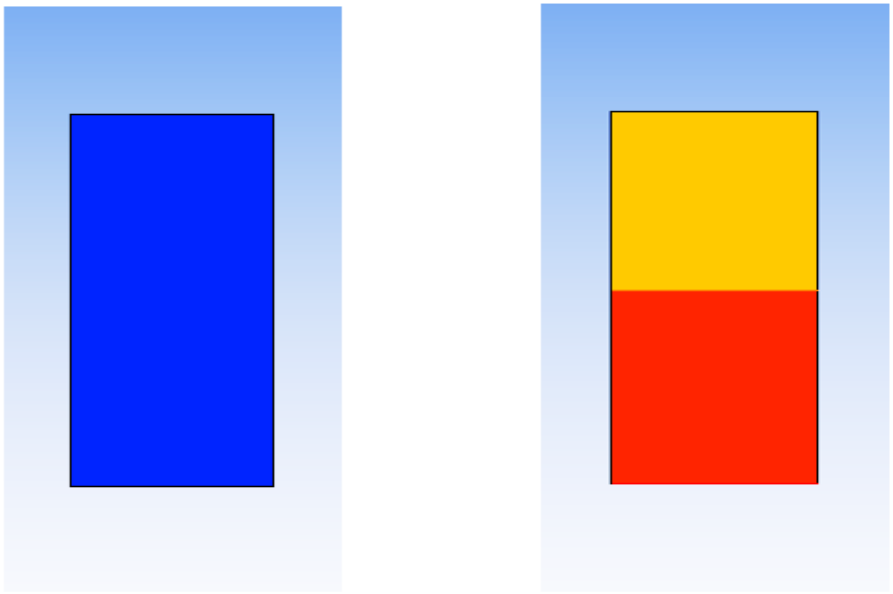

(a) Inlet water temperature contour (b) Outlet water temperature contour

Figure 6.92. Inlet and outlet water temperature contours.

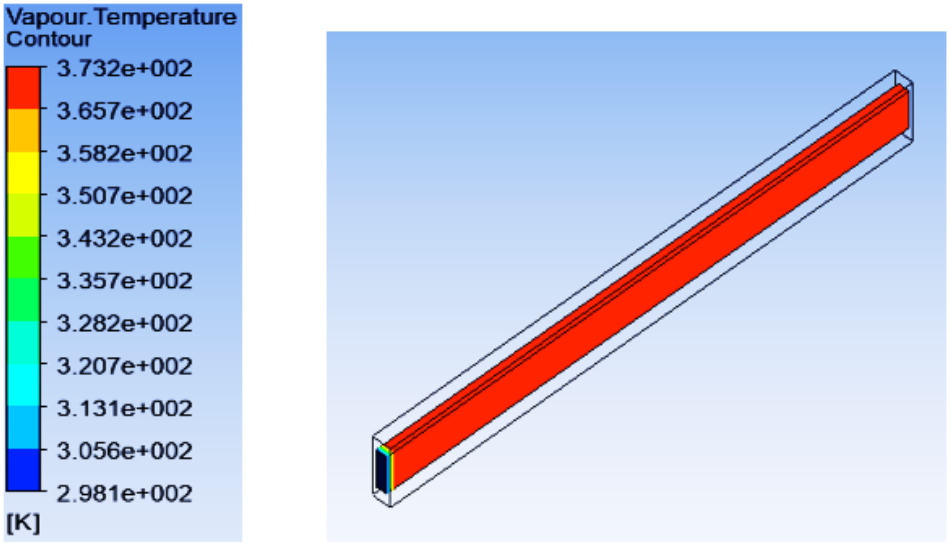

Figure 6.93. Vapour temperature contour.

6.2.3.2. Comparisons of single-phase and two-phase flow

Some of the advantages of two-phase cooling over single-phase cooling are: maintaining lower device temperatures for the same heat fluxes and velocity ranges and relatively small changes in device temperatures in response to large fluctuations in heat fluxes. Going from a lower to a

higher heat flux at the same velocity, temperature variation is small which is an advantage for two-phase cooling over single-phase cooling; this is in line with what is obtainable in the literature [7], [209].

Comparisons at 100 W/cm^2

Optimal microchannel heat sinks at 100 W/cm^2 have been compared as shown in Figure 6.94 to Figure 6.104. The thermal resistances of optimal microchannel heat sinks in relation to Reynolds number are shown in Figure 6.94 and the corresponding base temperatures are shown in Figure 6.95. The heat sinks are compared between 0.1-0.5 to 4.0-4.5 m/s in two-phase flow and 2.0-2.5 to 4.0-4.5 m/s in single-phase flow, and the base temperatures are below the maximum operating temperature of modern electronic devices. The thermal characteristics in two-phase flow are better than those of single-phase flow as expected and in line with Figure 6.16 and Figure 6.17, also Figure 6.61 and Figure 6.62.

The pumping power requirements for the optimal microchannel heat sinks are shown in Figure 6.96. Two-phase flow has higher pressure drops than single-phase flow and this reason explains why the pumping power requirements are higher especially at high Reynolds numbers as shown. The optimal aspect ratios are within a range and do not vary widely as Reynolds number and Bejan number increase (Figure 6.97 and Figure 6.98).

Optimal lengths in two-phase and single-phase flow vary with Reynolds number and Bejan number as shown in Figure 6.99 and Figure 6.100. The variations are expected just the same way they occurred in other microchannel configurations (Figure 6.19 and Figure 6.20, also Figure 6.64 and Figure 6.65). The relationships between hydraulic diameter, Reynolds number and Bejan number are shown in Figure 6.101 and Figure 6.102. The trend is in line with Figure 6.21 and Figure 6.22 and, Figure 6.66 and Figure 6.67.

In Figure 6.103 and Figure 6.104, pressure drop and Bejan number increase as Reynolds number increases. This phenomenon is comparable to Figure 6.23 and Figure 6.24, also Figure 6.68 and Figure 6.69.

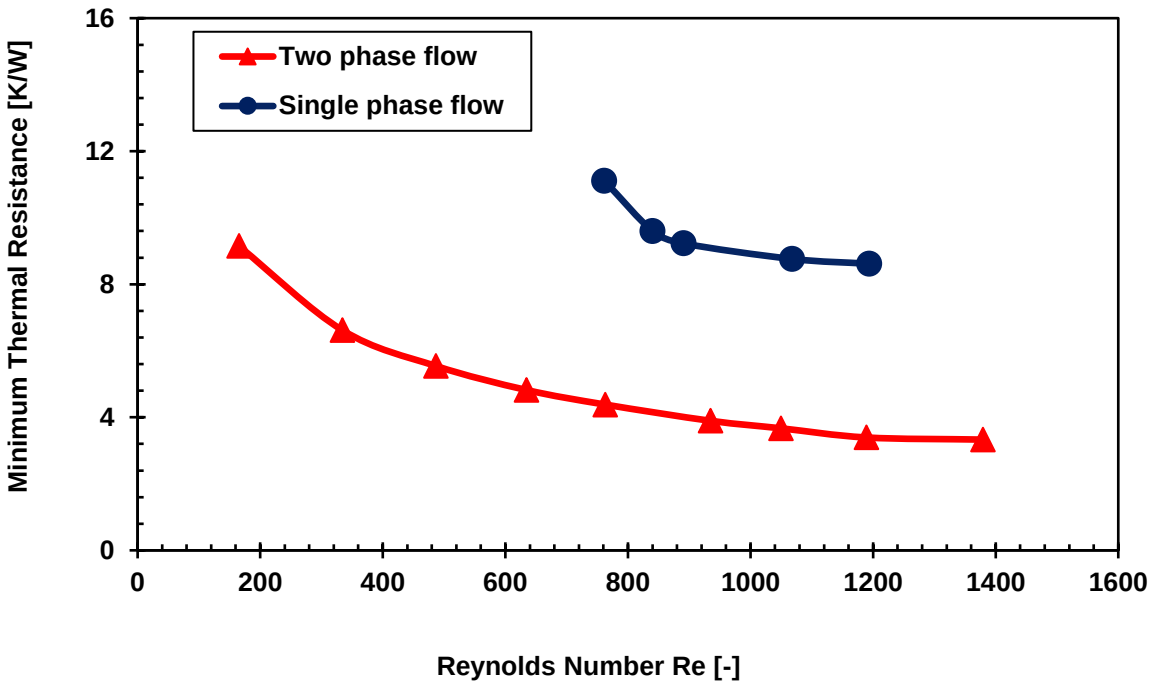

Figure 6.94. Thermal resistances of optimal microchannel heat sinks at 100 W/cm^2.

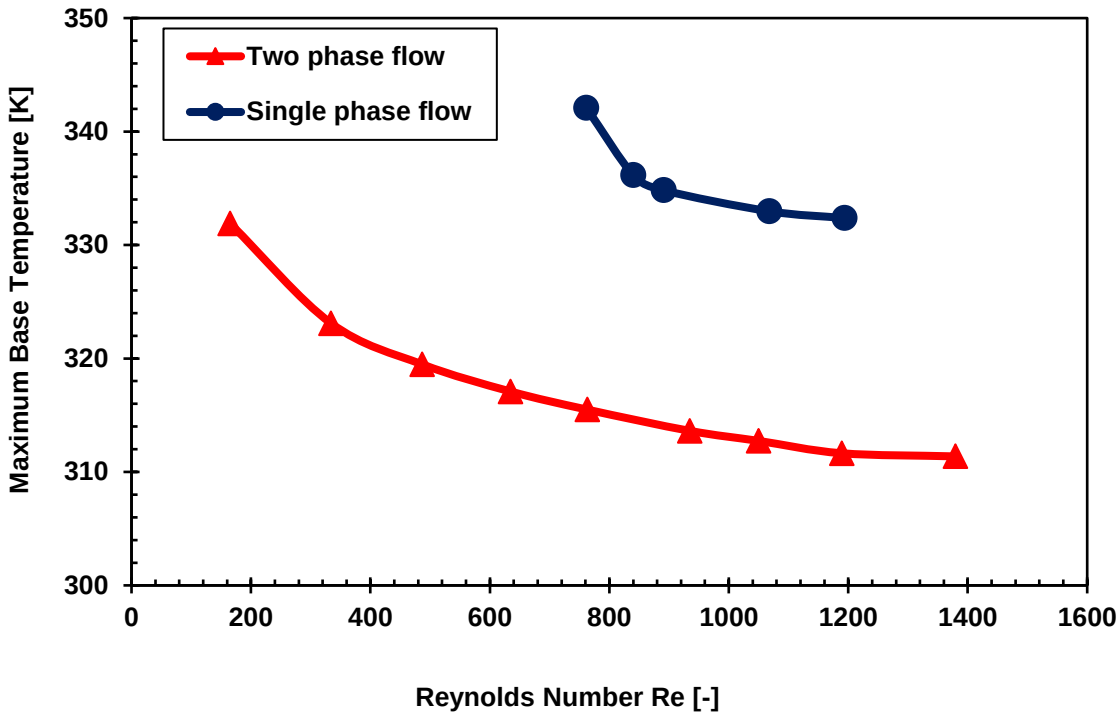

Figure 6.95. Maximum base temperatures of optimal microchannel heat sinks at 100 W/cm^2.

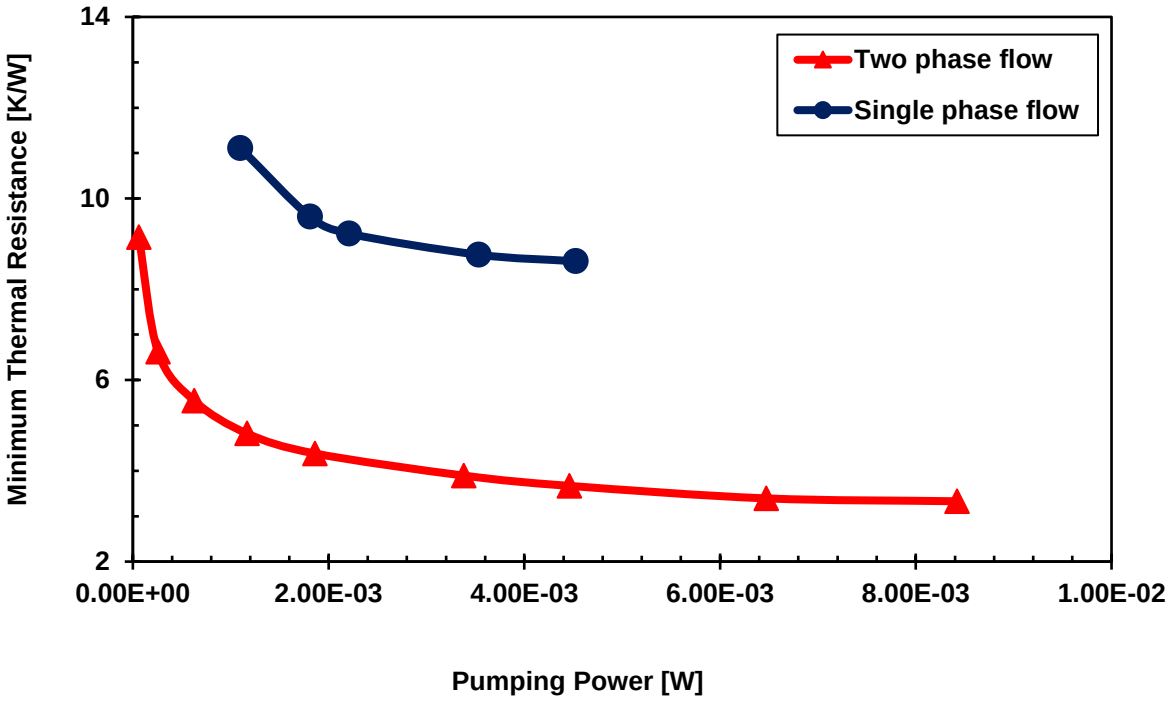

Figure 6.96. Pumping power of optimal microchannel heat sinks at 100 W/cm^2.

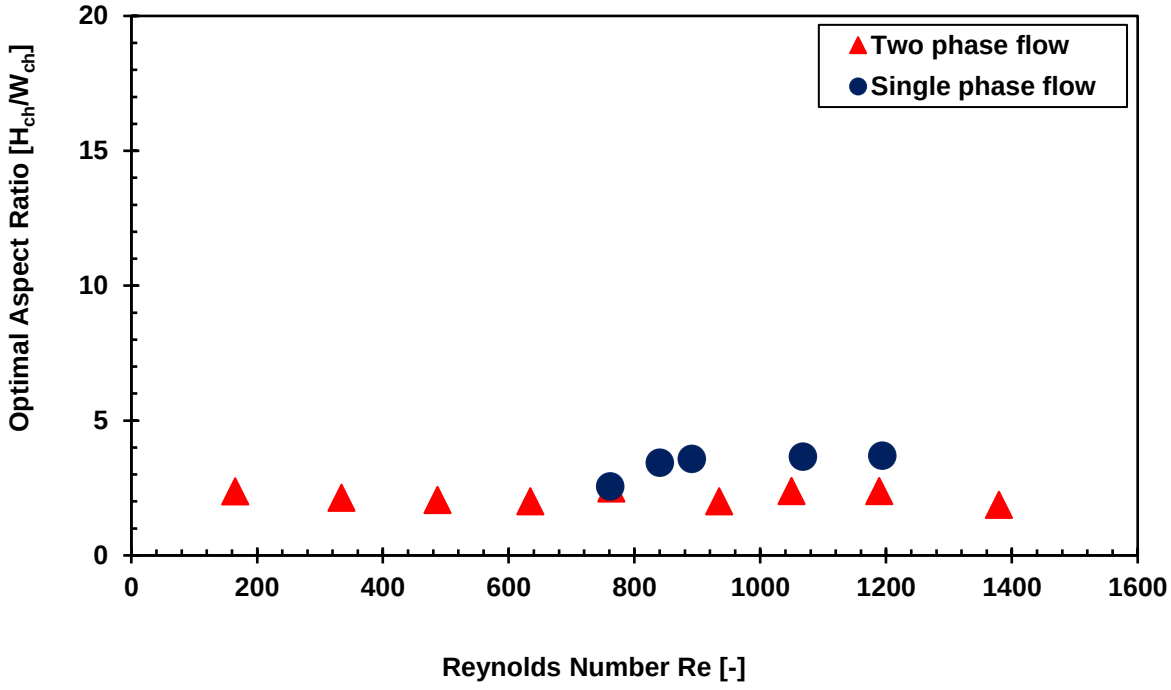

Figure 6.97. Effect of aspect ratio on optimal microchannel heat sinks at 100 W/cm^2.

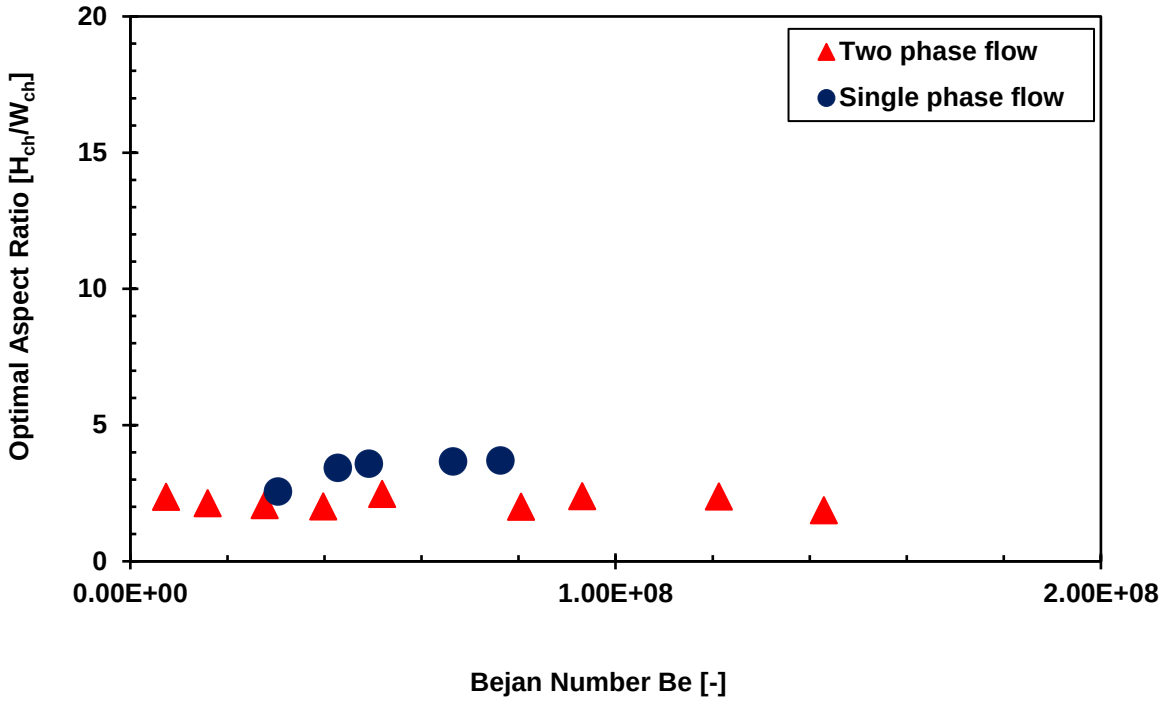

Figure 6.98. Effect of dimensionless pressure drop on optimal aspect ratio at 100 W/cm^2.

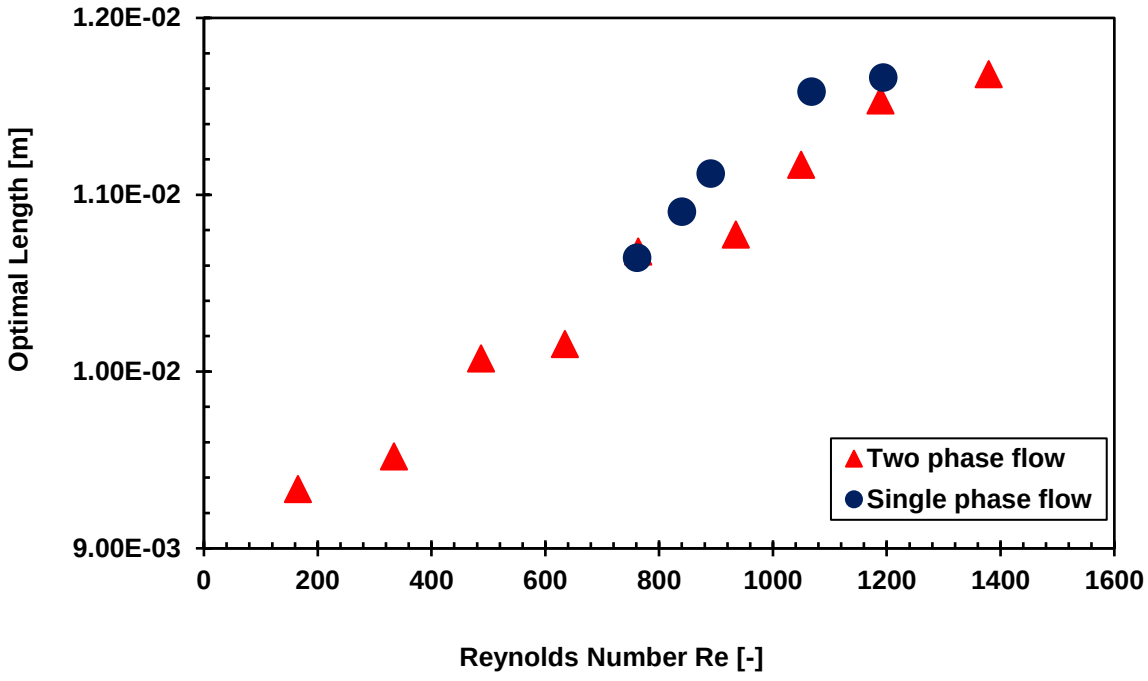

Figure 6.99. Effect of length on optimal microchannel heat sinks at 100 W/cm^2.

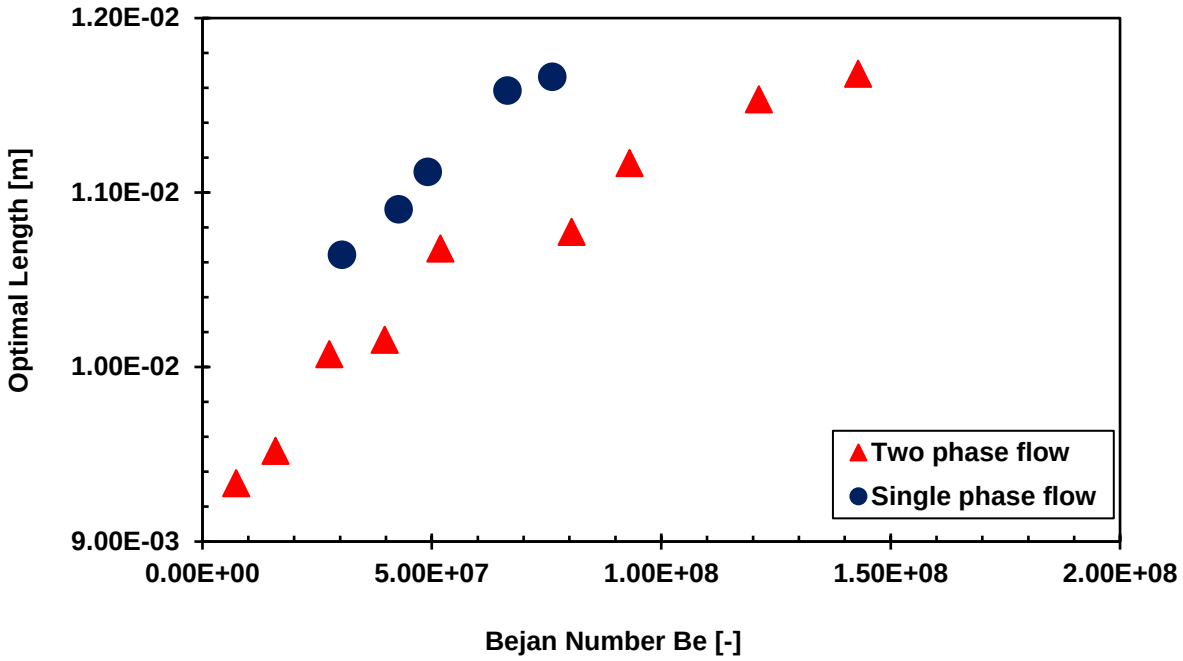

Figure 6.100. Effect of dimensionless pressure drop on optimal length at 100 W/cm^2.

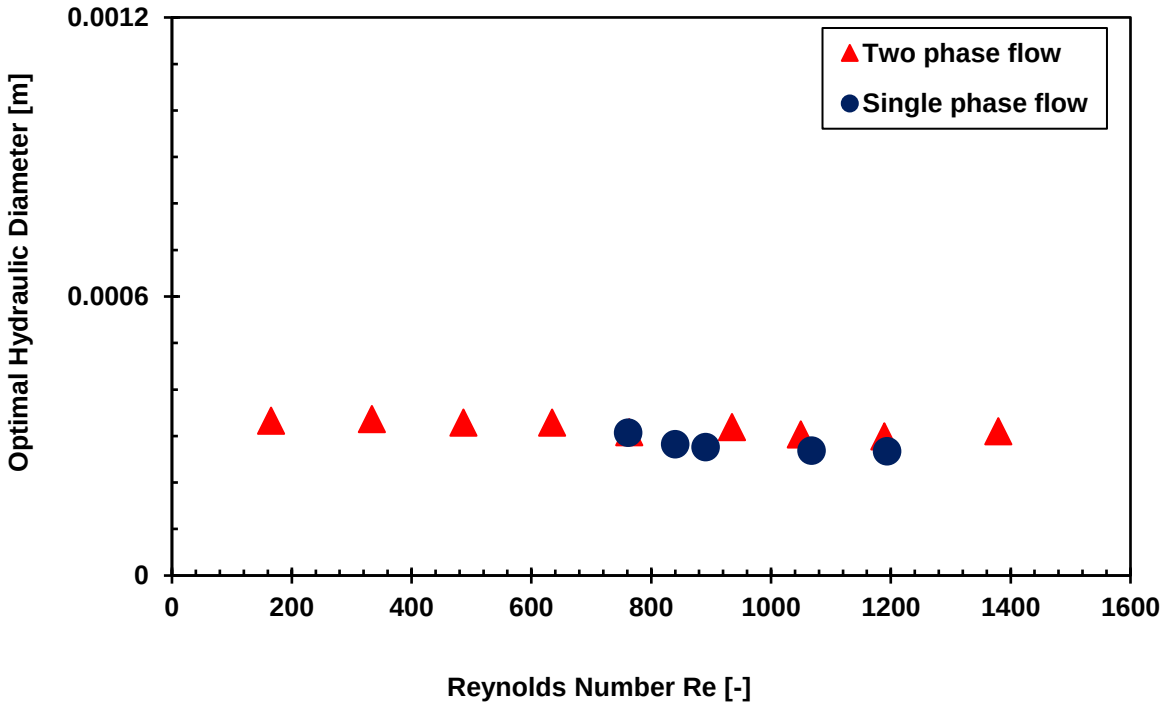

Figure 6.101. Effect of hydraulic diameter on optimal microchannel heat sinks at 100 W/cm^2.

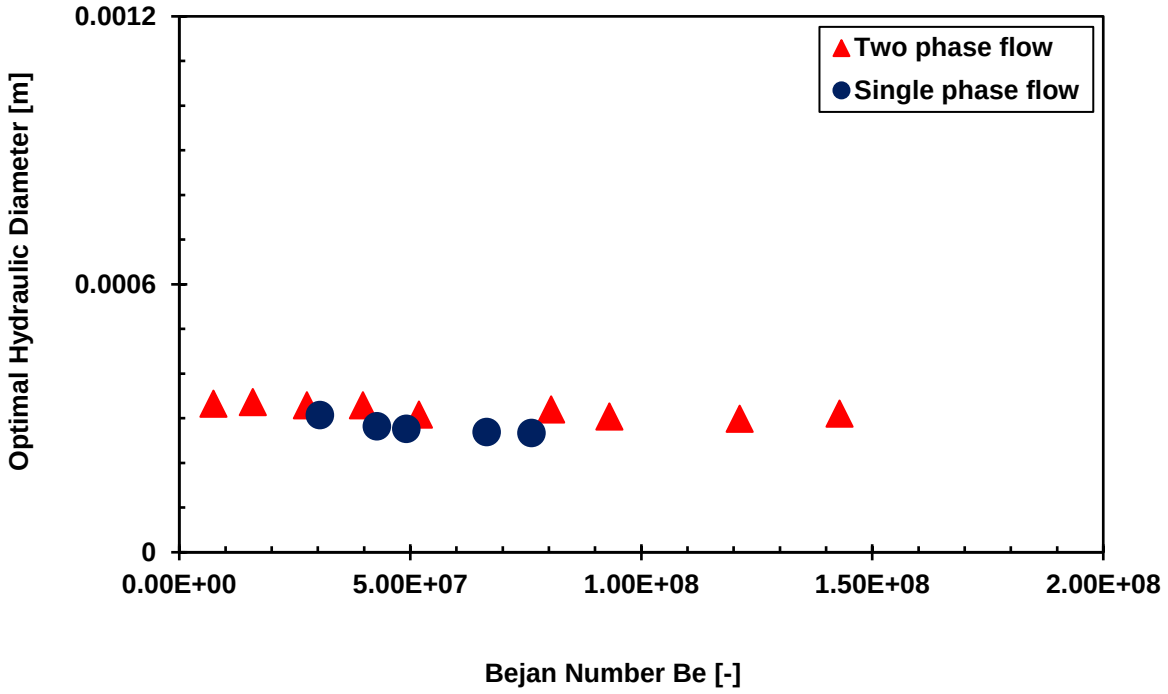

Figure 6.102. Effect of dimensionless pressure drop on optimal hydraulic diameter at 100 W/cm^2.

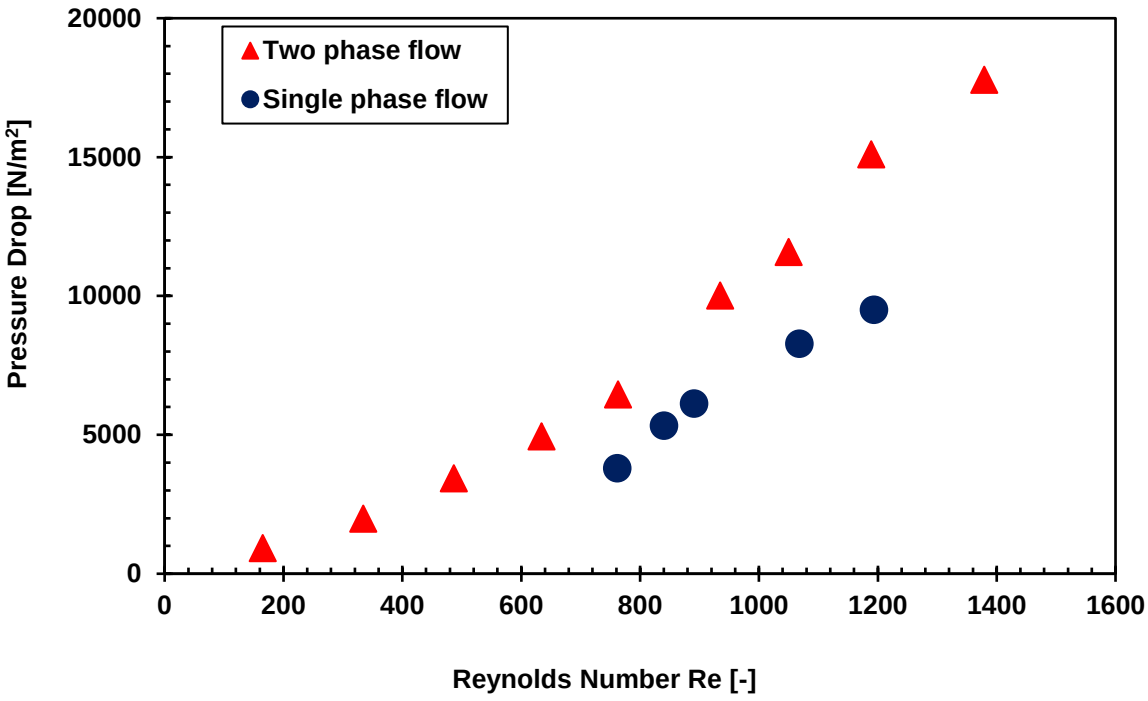

Figure 6.103. Effect of pressure drop on Reynolds number at 100 W/cm^2.

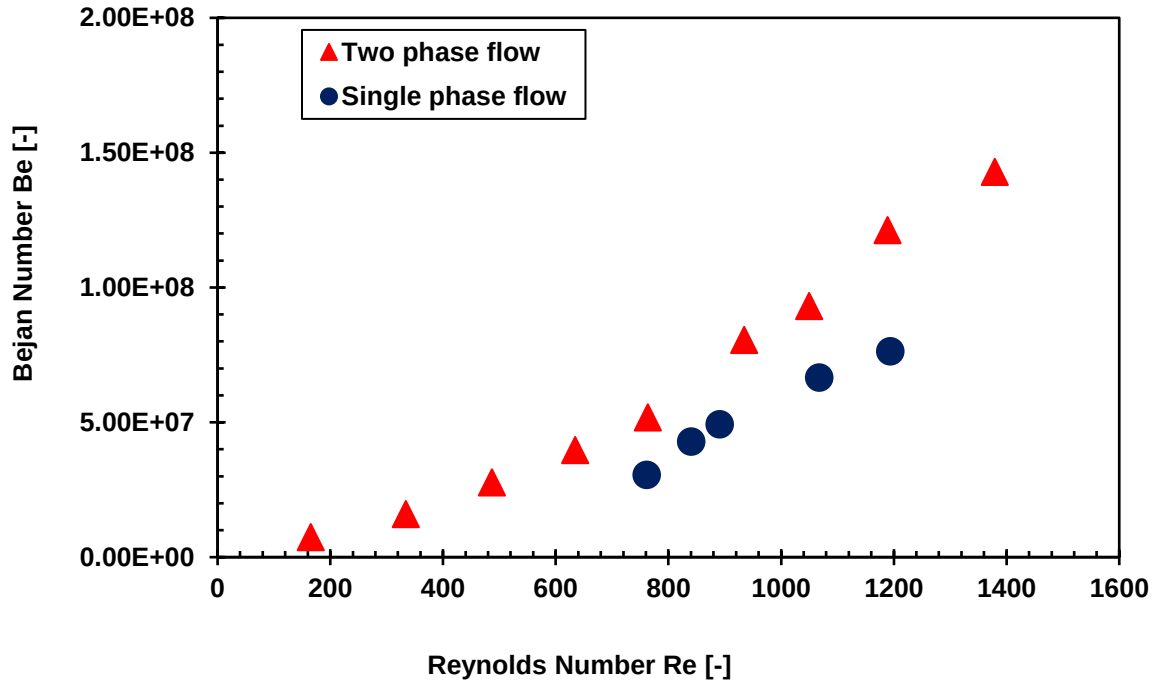

Figure 6.104. Effect of dimensionless pressure drop on Reynolds number at 100 W/cm^2.

Comparisons at 200 W/cm^2

The velocities for comparisons shown in Figure 6.105-Figure 6.115 are: 0.5-1.0 to 4.0-4.5 m/s in two-phase flow and 5.5-6.0 to 6.5-7.0 m/s in single-phase flow. Optimal parameters could not be obtained at velocities similar to two-phase flow in single-phase flow because of high base temperatures, hence the extension to 6.5-7.0 m/s. There was no basis for extending the velocities for two-phase flow because of the trend established already in Figure 6.94 and Figure 6.95 and the need to keep flow in the laminar range.

The thermal characteristics are shown in Figure 6.105 and Figure 6.106. Microchannel heat sinks operating in two-phase flow perform better with low thermal resistances and base temperatures even though the velocities are not similar to those of single-phase flow.

Figure 6.107 depicts the pumping power of the optimal microchannel heat sinks in both phases with better pumping power requirements for two-phase flow at low Reynolds numbers.

Optimal aspect ratios are higher in Figure 6.108 and Figure 6.109 for single-phase flow just as they were in Figure 6.97 and Figure 6.98. Optimal length and hydraulic diameter vary with Reynolds number and Bejan number for both two-phase and single-phase flow as expected, to obtain the desired microchannel heat sinks (Figure 6.110-Figure 6.113). The functional

relationships between pressure drop, Bejan number and Reynolds number are shown in Figure 6.114 and Figure 6.115.

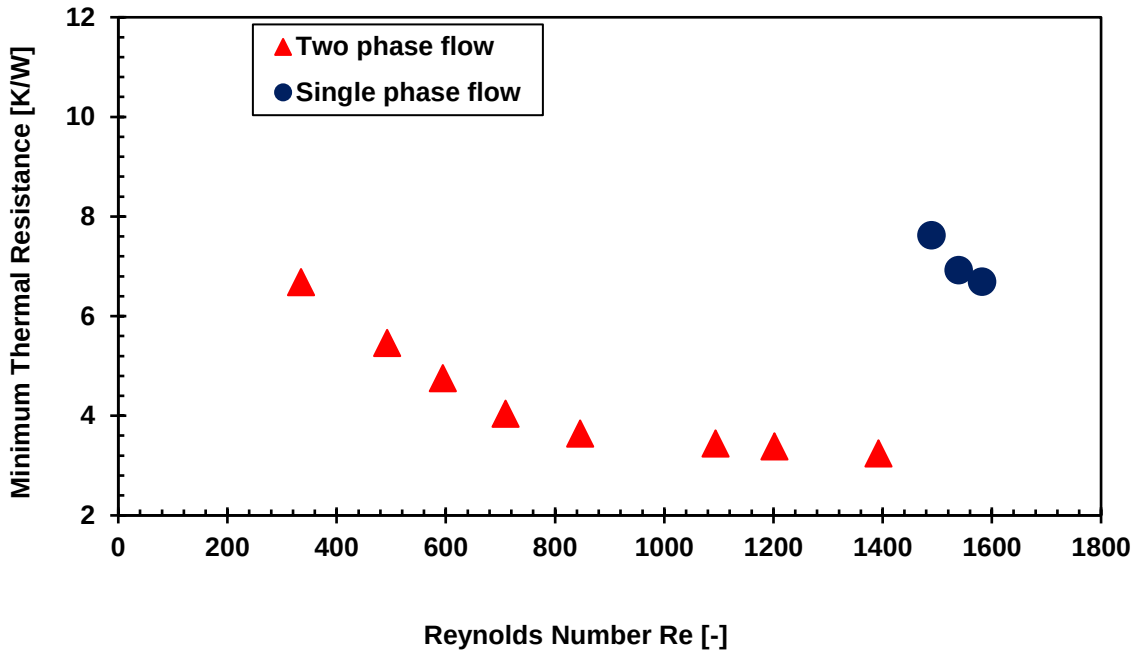

Figure 6.105. Thermal resistances of optimal microchannel heat sinks at 200 W/cm^2.

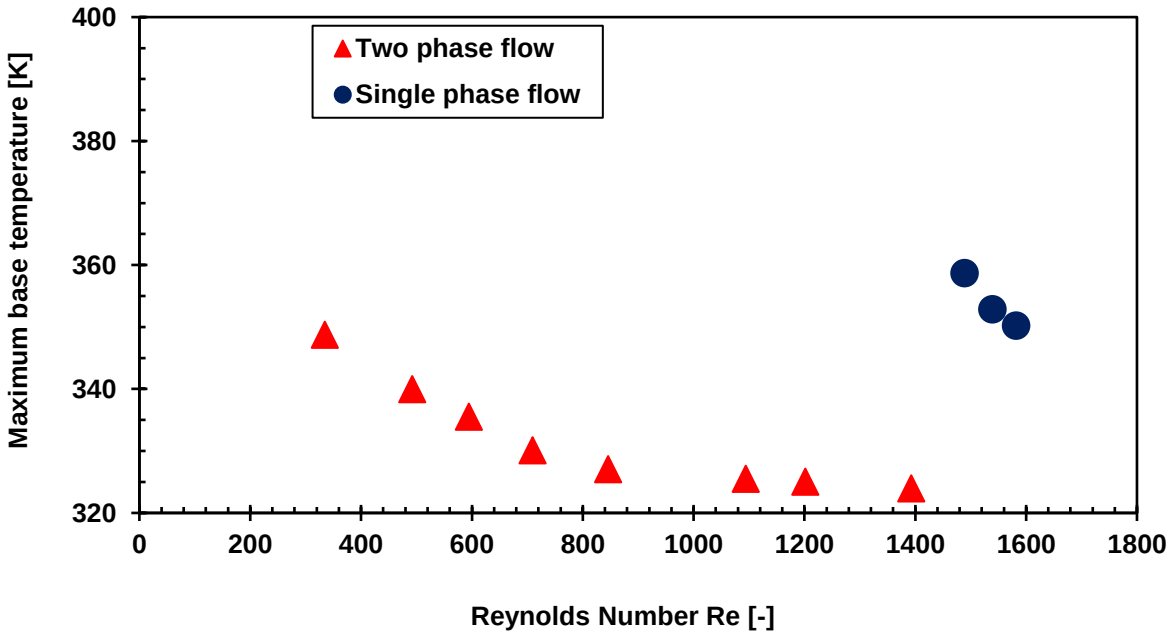

Figure 6.106. Maximum base temperatures of optimal microchannel heat sinks at 200 W/cm^2.

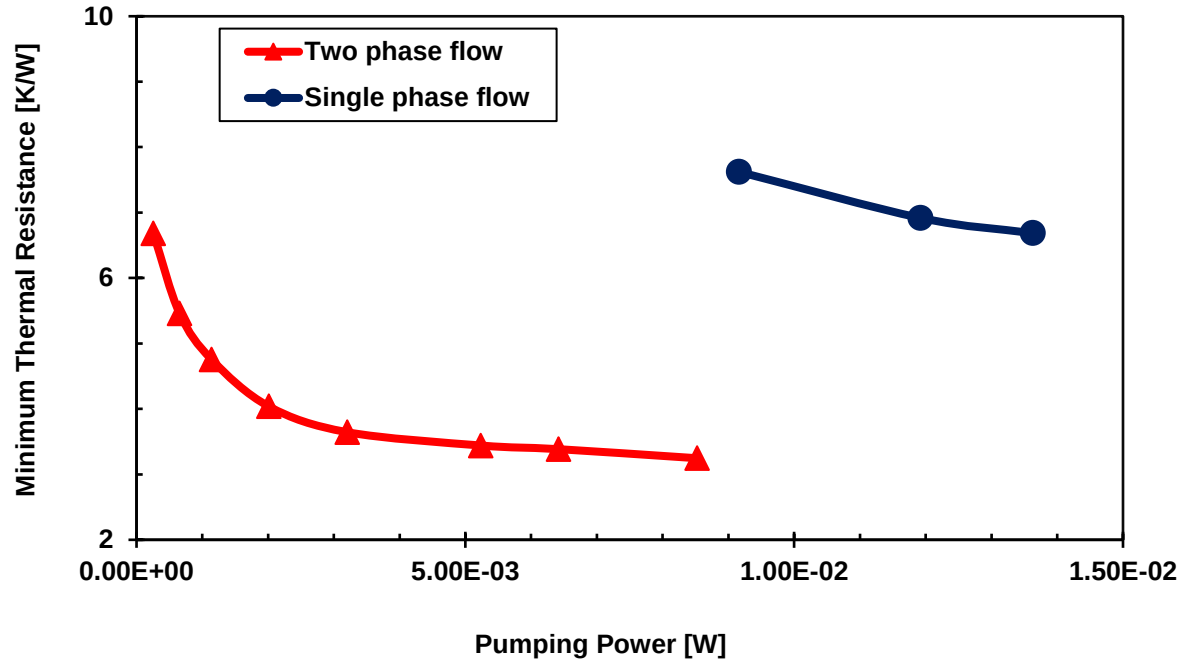

Figure 6.107. Pumping power of optimal microchannel heat sinks at 200 W/cm^2.

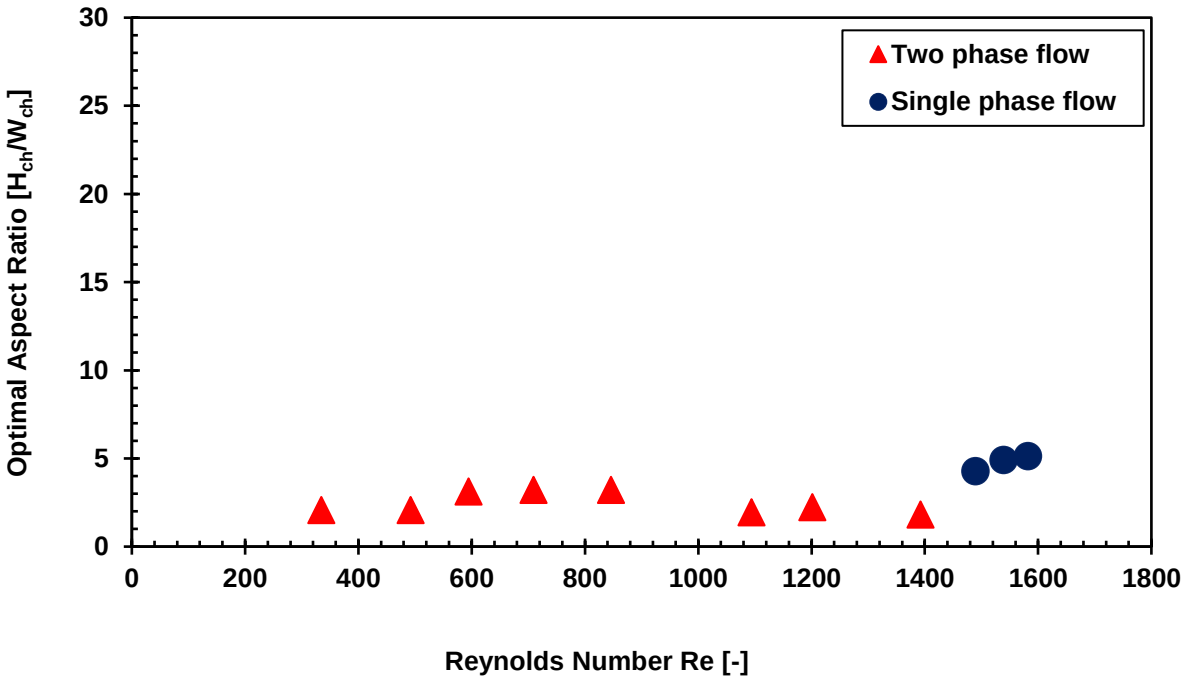

Figure 6.108. Effect of aspect ratio on optimal microchannel heat sinks at 200 W/cm^2.

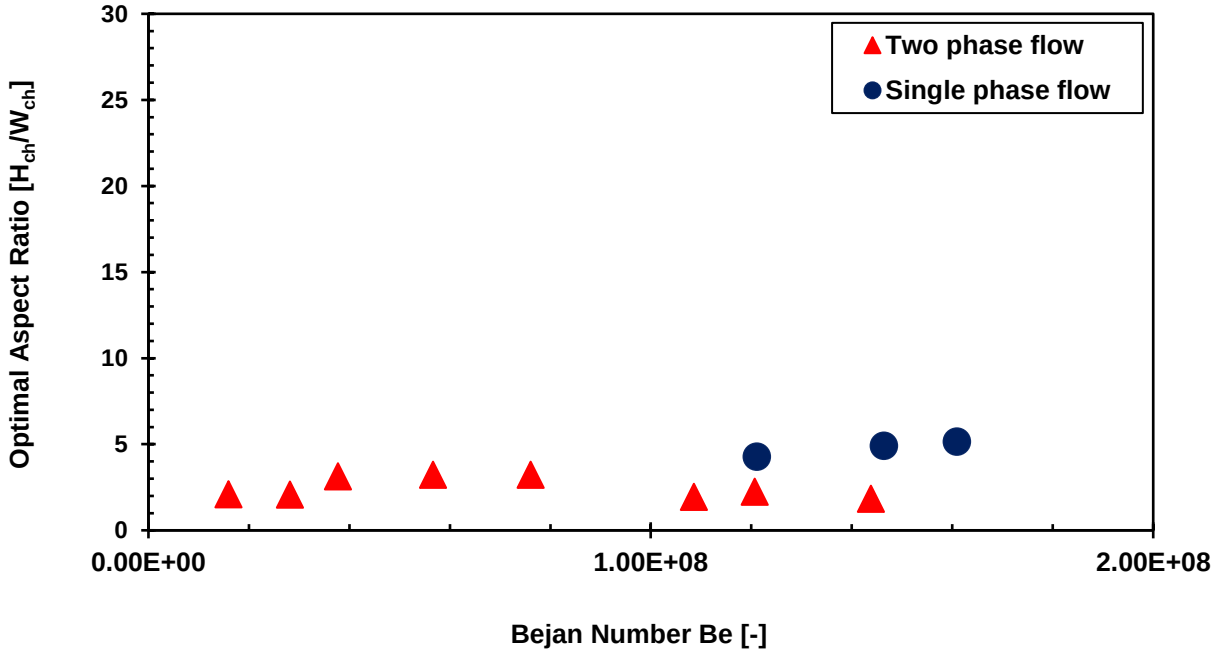

Figure 6.109. Effect of dimensionless pressure drop on optimal aspect ratio at 200 W/cm^2.

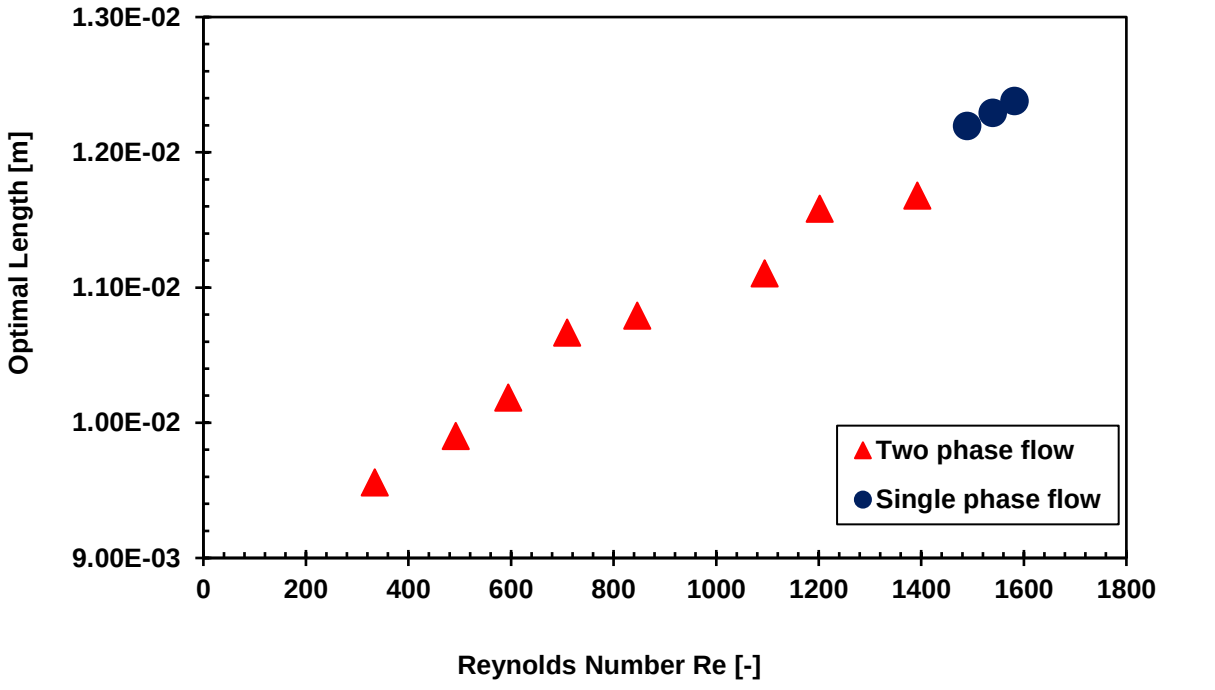

Figure 6.110. Effect of length on optimal microchannel heat sinks at 200 W/cm^2.

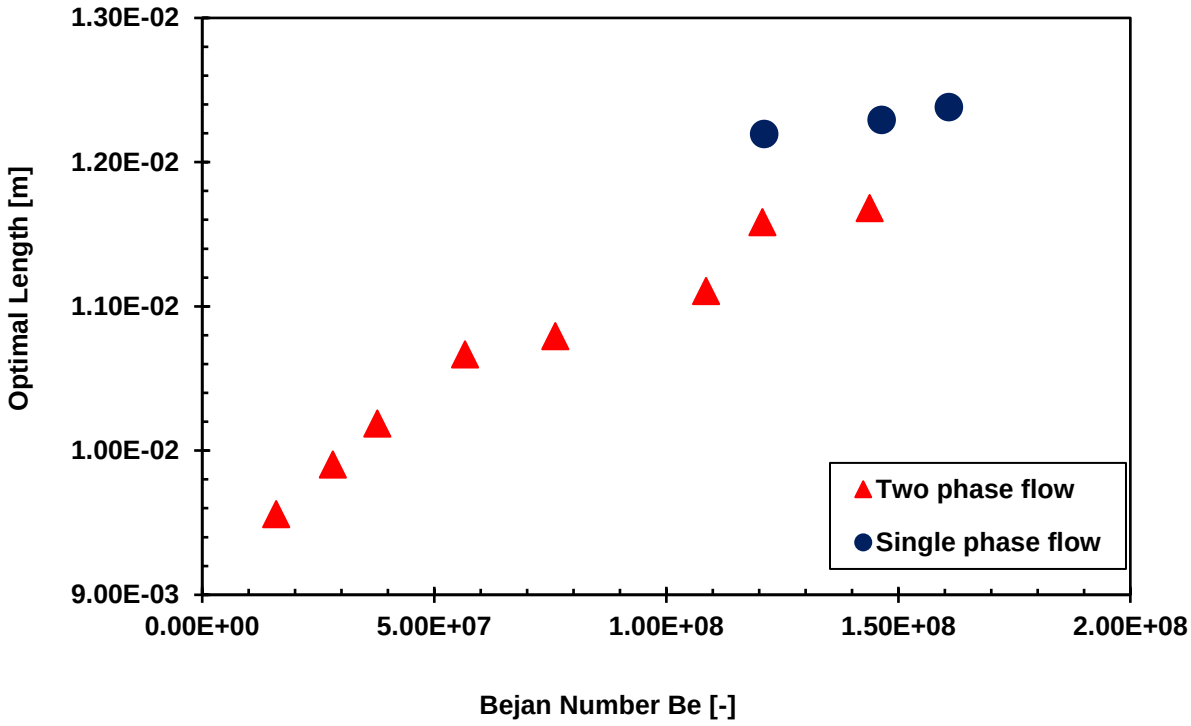

Figure 6.111. Effect of dimensionless pressure drop on optimal length at 200 W/cm^2.

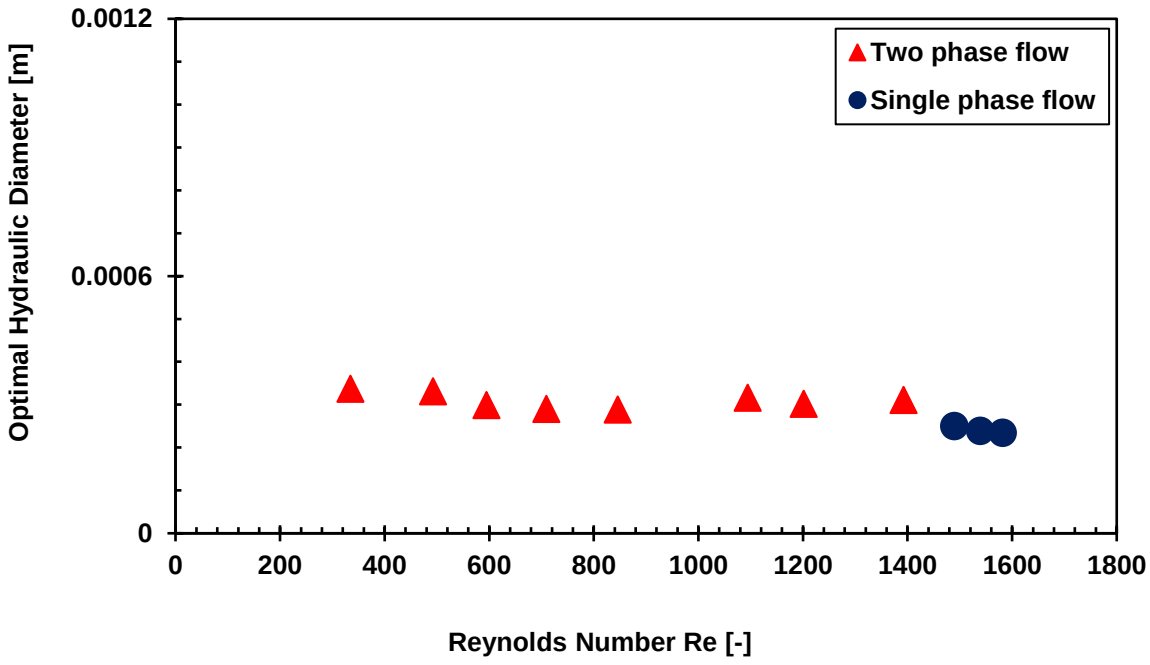

Figure 6.112. Effect of hydraulic diameter on optimal microchannel heat sinks at 200 W/cm^2.

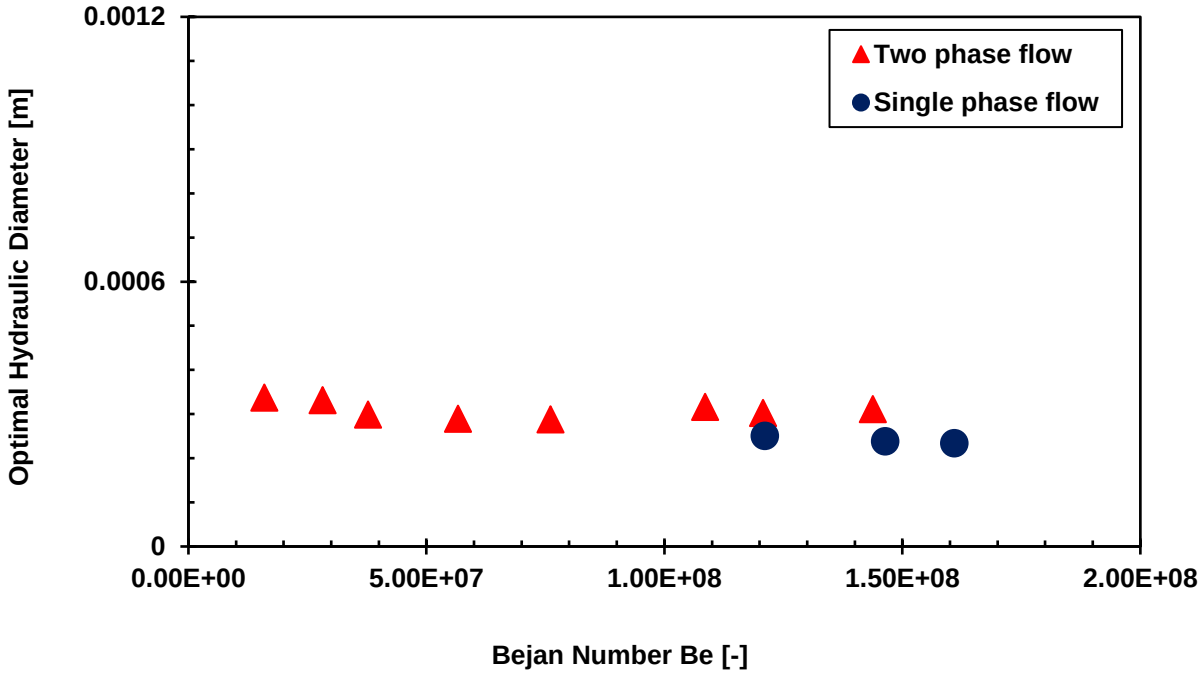

Figure 6.113. Effect of dimensionless pressure drop on optimal hydraulic diameter at 200 W/cm^2.

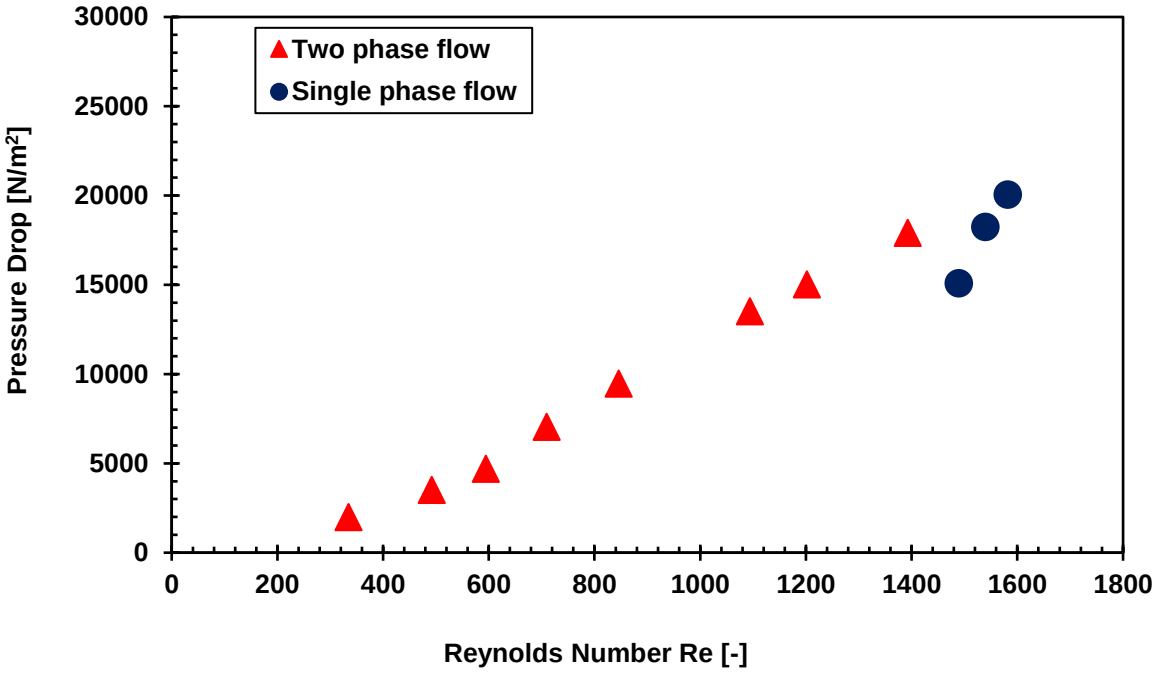

Figure 6.114. Effect of pressure drop on Reynolds number at 200 W/cm^2.

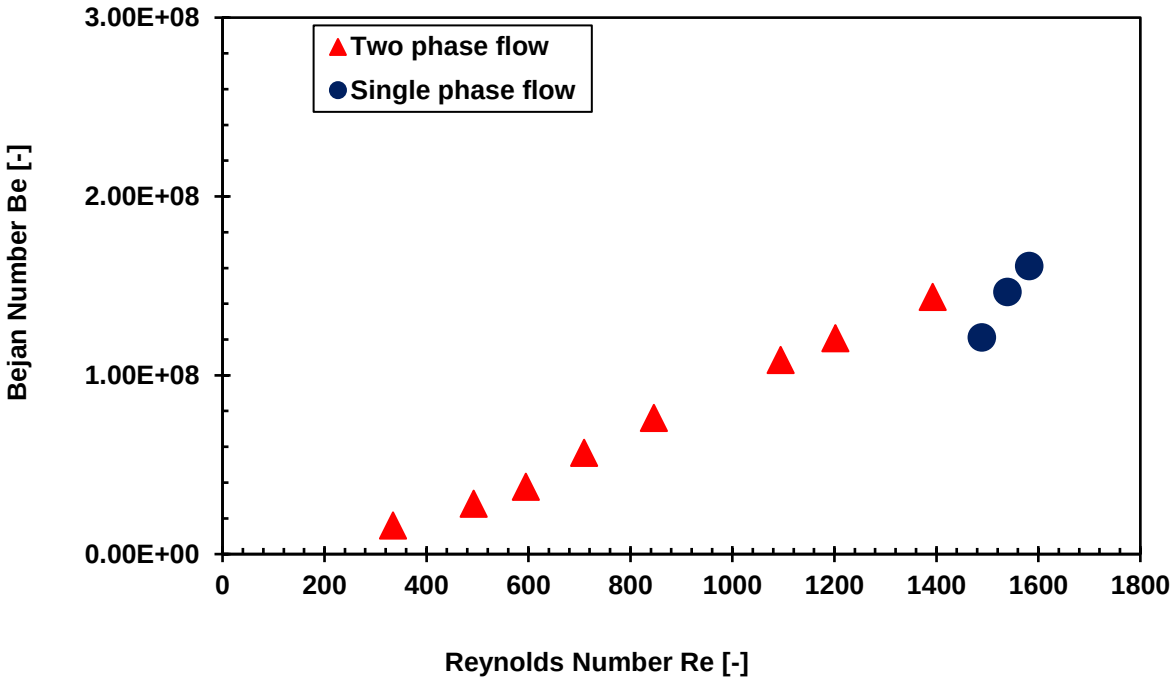

Figure 6.115. Effect of dimensionless pressure drop on Reynolds number at 200 W/cm^2.

6.2.3.3. Comparisons of single-phase flow at 100 and 200 W/cm^2

Optimal microchannel heat sinks are compared as shown in Figure 6.116- Figure 6.125. Figure 6.116 shows that optimal microchannel heat sinks performed well at their various velocities with the thermal resistances decreasing with increasing Reynolds number while base temperatures corresponding to optimal heat sinks are shown in Figure 6.117. The variations of aspect ratios, length and hydraulic diameter with Reynolds number in Figure 6.118 to Figure 6.123 provide the expected optimal microchannel heat sinks and velocities. In Figure 6.118 and Figure 6.119, aspect ratios are greater at high Reynolds numbers; the adjustment being the response to higher velocities. Figure 6.124 and Figure 6.125 provide information on the relationships between pressure drop, Bejan number and Reynolds number. For both heat fluxes, pressure drop and Bejan number increase as Reynolds number increases in line with Figure 6.41 and Figure 6.42.

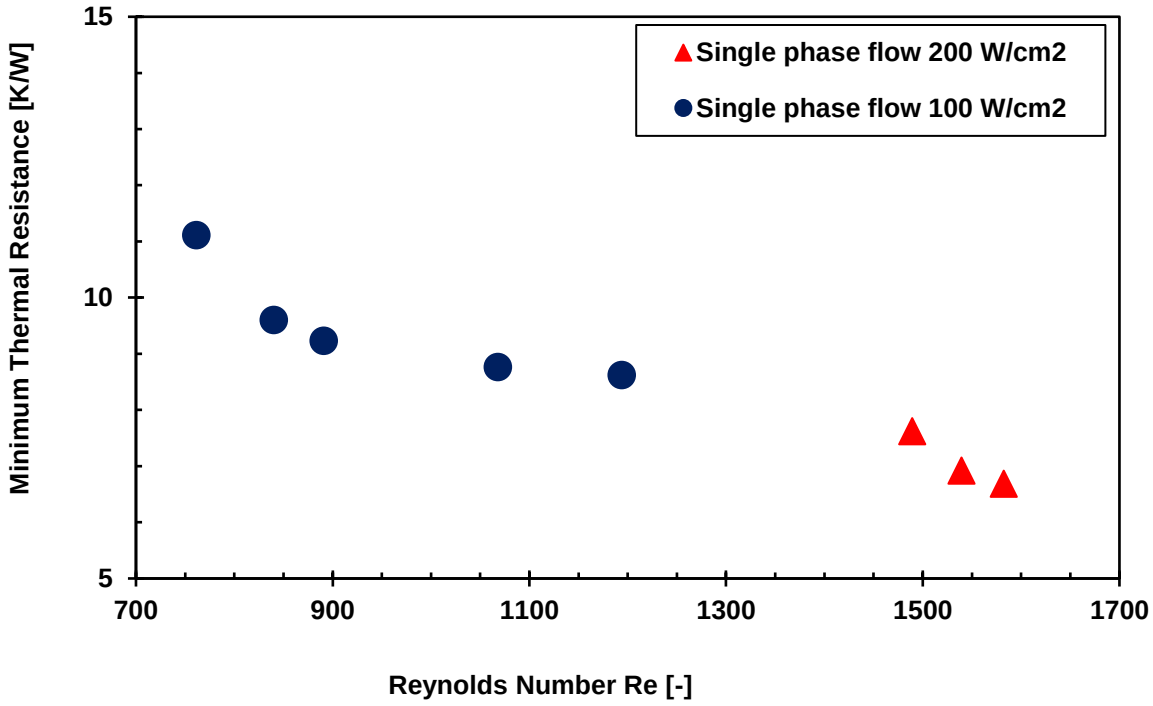

Figure 6.116. Thermal resistances of microchannel heat sinks at 100 and 200 W/cm^2.

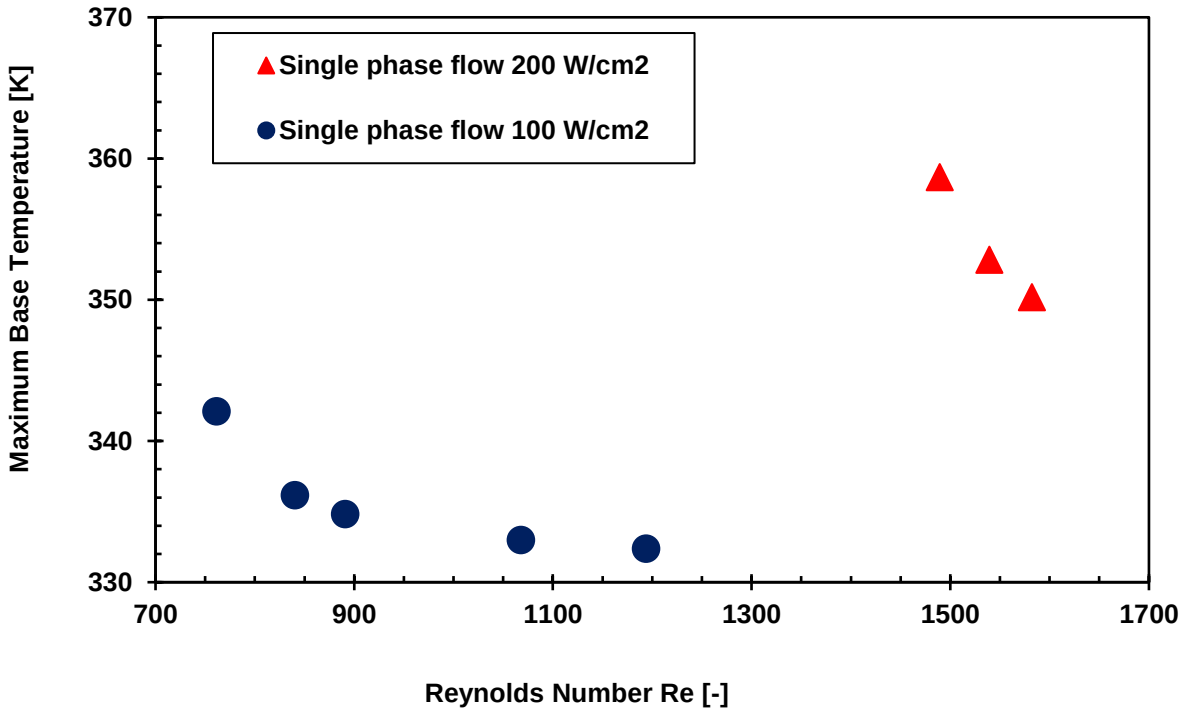

Figure 6.117. Maximum base temperatures of microchannel heat sinks at 100 and 200 W/cm^2.

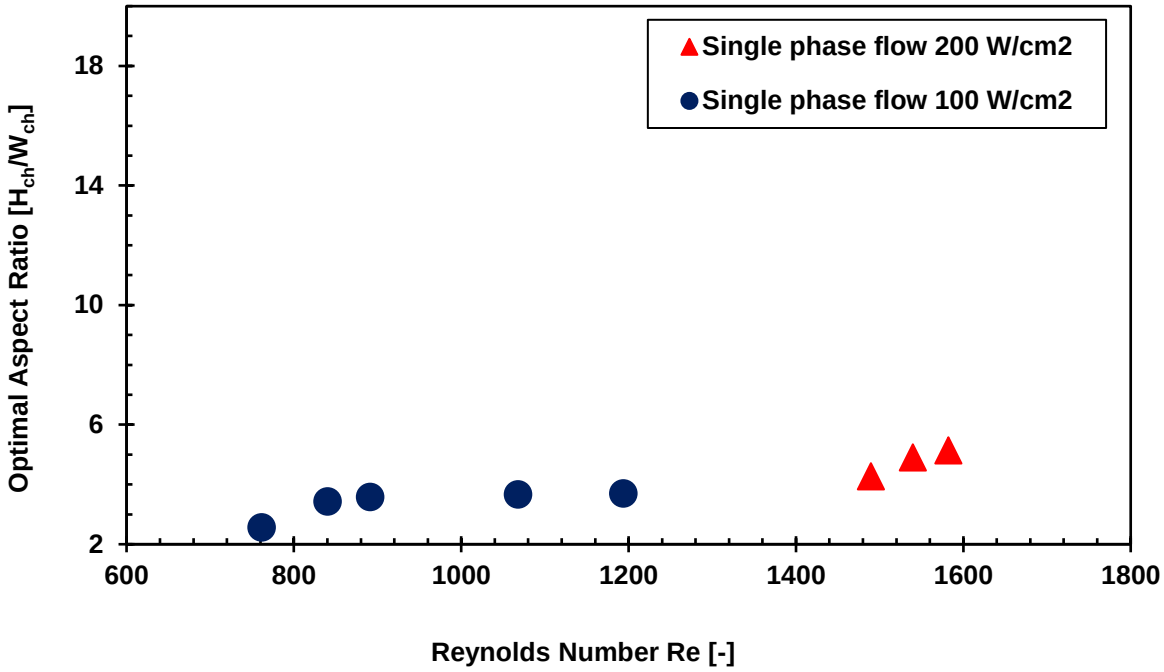

Figure 6.118. Effect of aspect ratio on optimal microchannel heat sinks at 100 and 200 W/cm^2.

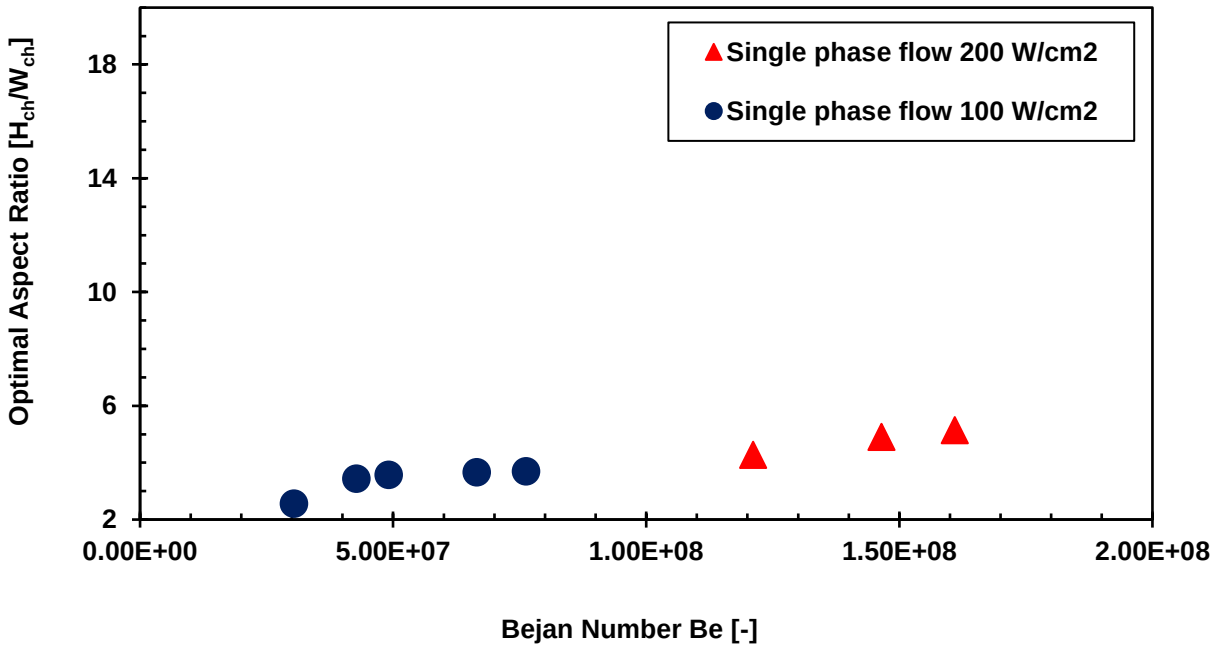

Figure 6.119. Effect of dimensionless pressure drop on optimal aspect ratio at 100 and 200 W/cm^2.

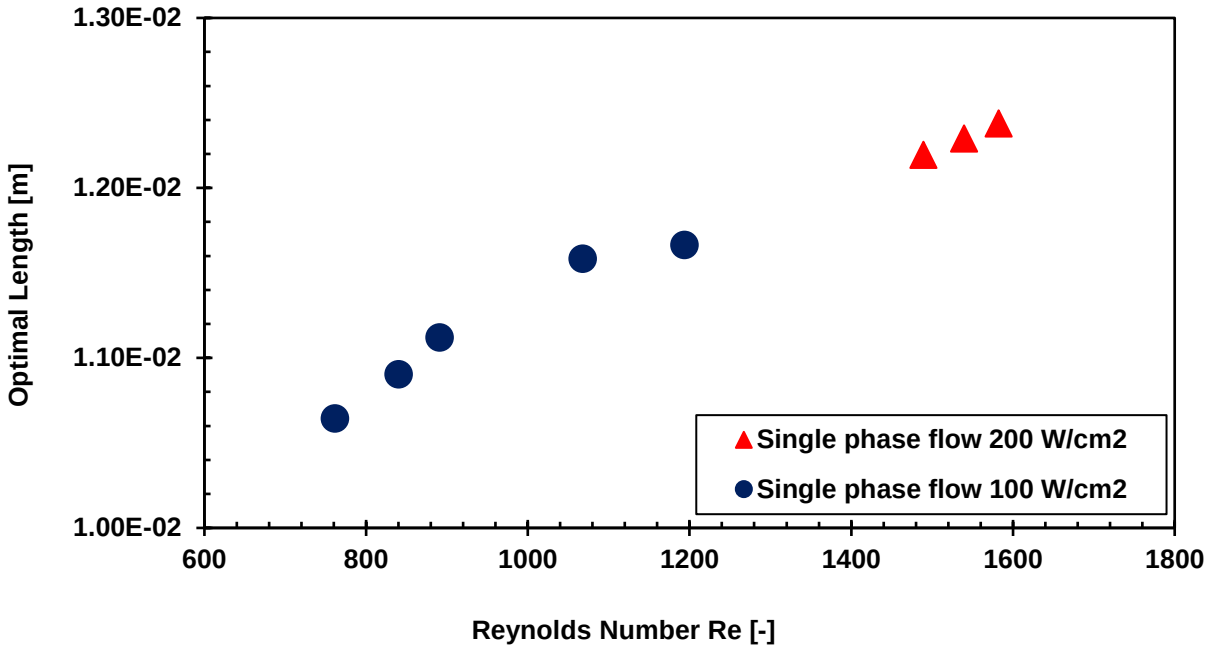

Figure 6.120. Effect of length on optimal microchannel heat sinks at 100 and 200 W/cm^2.

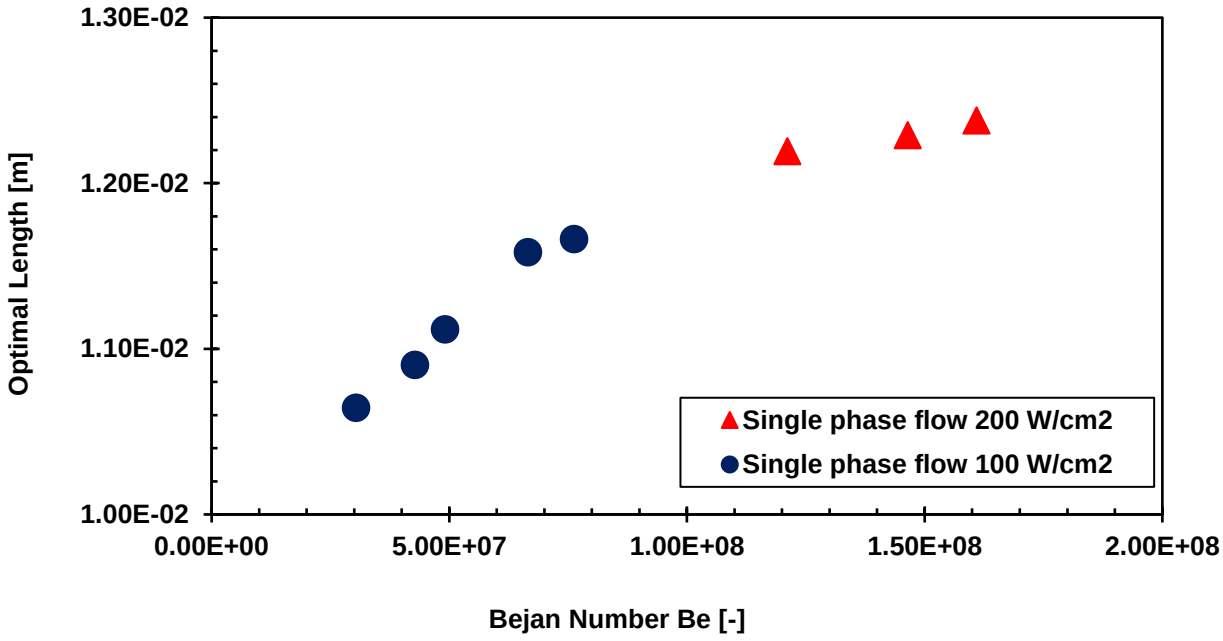

Figure 6.121. Effect of dimensionless pressure drop on optimal length at 100 and 200 W/cm^2.

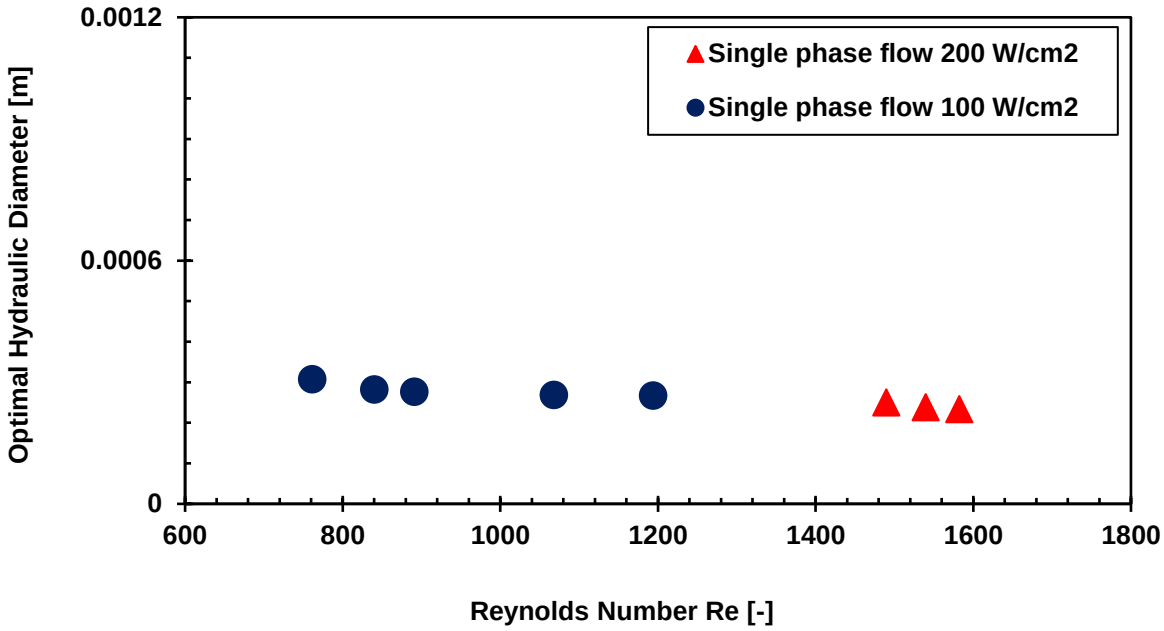

Figure 6.122. Effect of hydraulic diameter on optimal microchannel heat sinks at 100 and 200 W/cm^2.

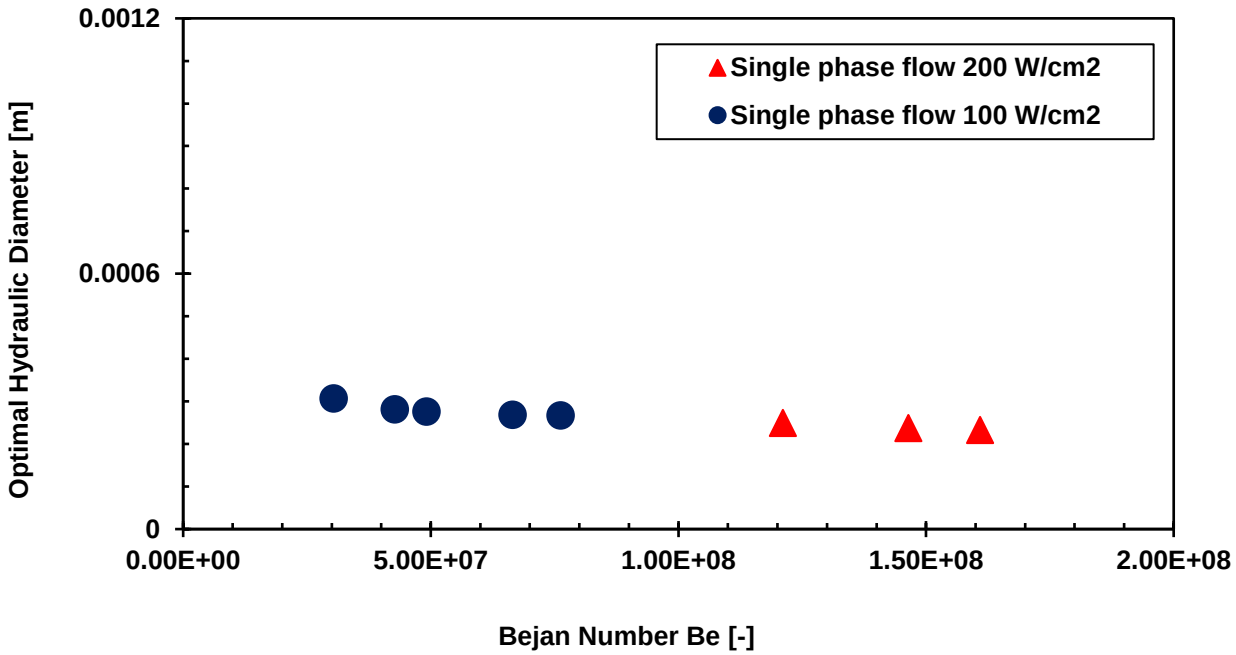

Figure 6.123. Effect of dimensionless pressure drop on optimal hydraulic diameter at 100 and 200 W/cm^2.

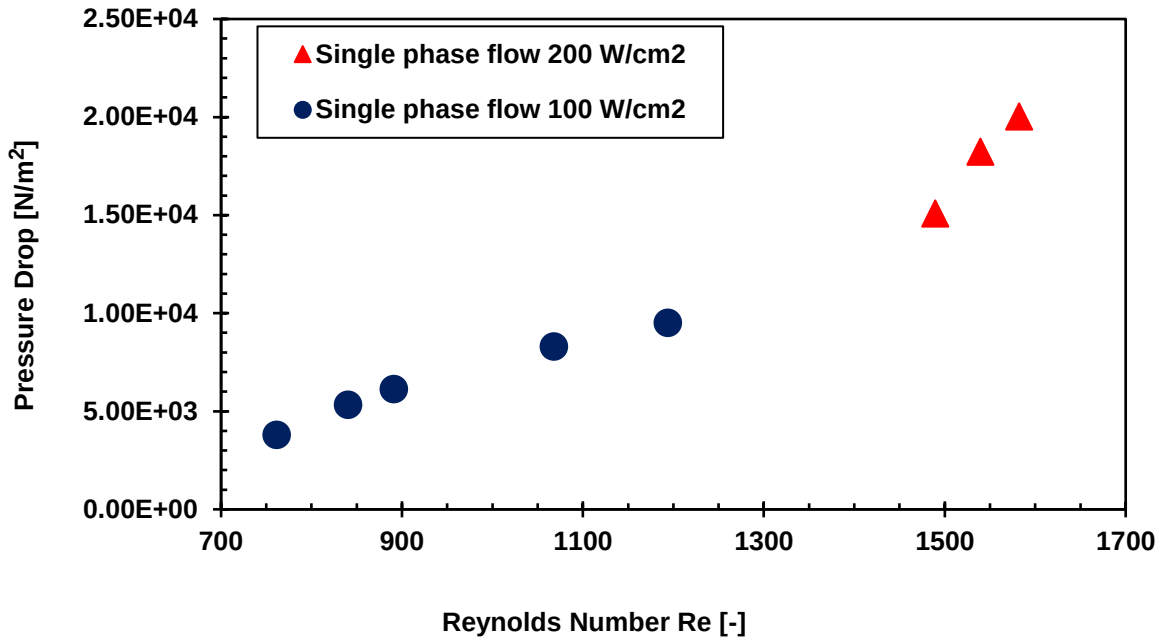

Figure 6.124. Effect of pressure drop on Reynolds number at 100 and 200 W/cm^2.

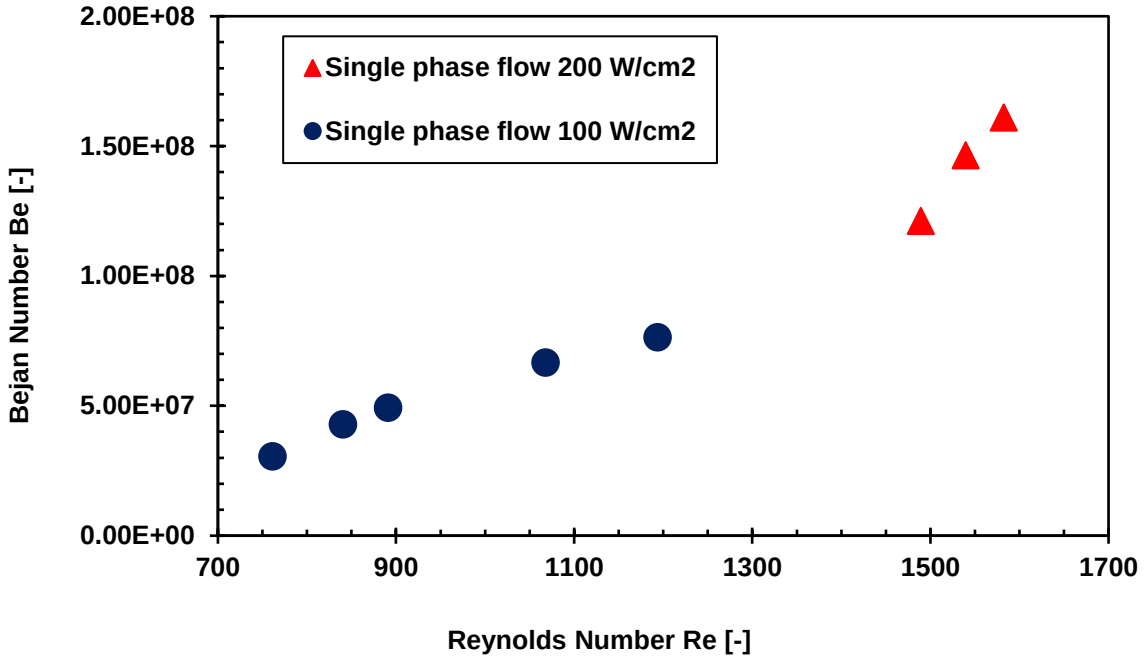

Figure 6.125. Effect of dimensionless pressure drop on Reynolds number at 100 and 200 W/cm^2.

Temperature contours

The contours in Figure 6.126-Figure 6.129 were obtained at 100 W/cm^2 in single-phase flow. The inner wall temperature range are: 310.1-315.4 K for two-phase flow (Figure 6.89) compared to 334.9 to 342 K (Figure 6.126) in single-phase flow. Inner wall, inlet and outlet wall temperature contours are shown in Figure 6.126 and Figure 6.127 respectively. Water temperature range for two-phase flow is 298.15-301.06 K (Figure 6.91) compared to 298.15-303.4 K in single-phase (Figure 6.128). Figure 6.128 provides information on the increase in water temperature across the microchannel while Figure 6.129 provides details of inlet and outlet water temperature distribution.

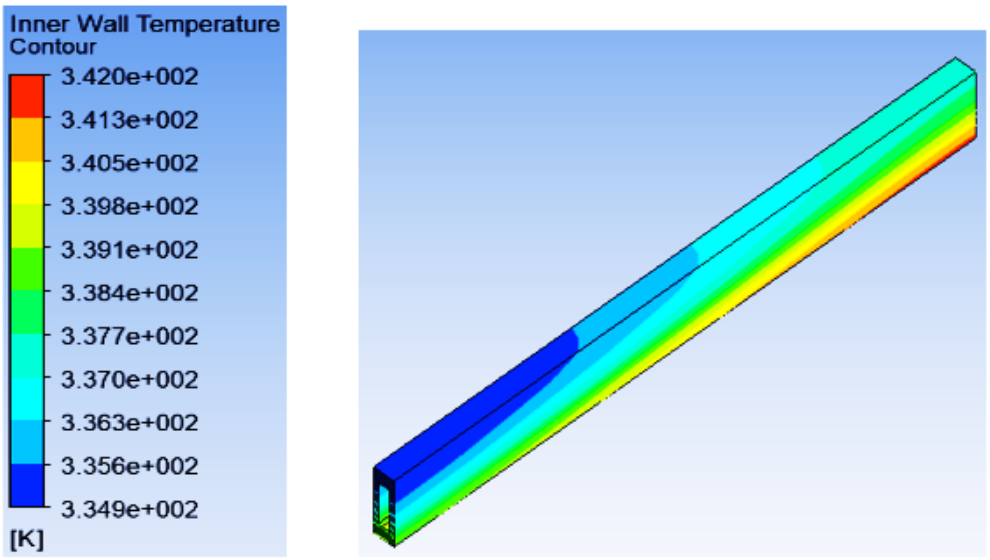

Figure 6.126. Inner wall temperature contour (base temperature = 342.08017 K).

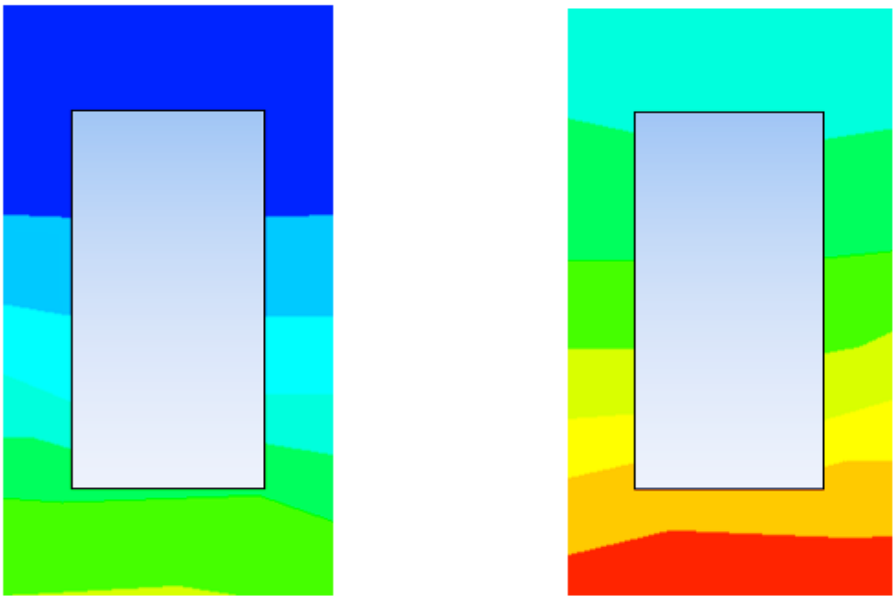

(a) Inlet wall temperature contour (b) Outlet wall temperature contour

Figure 6.127. Inlet and outlet wall temperature contours.

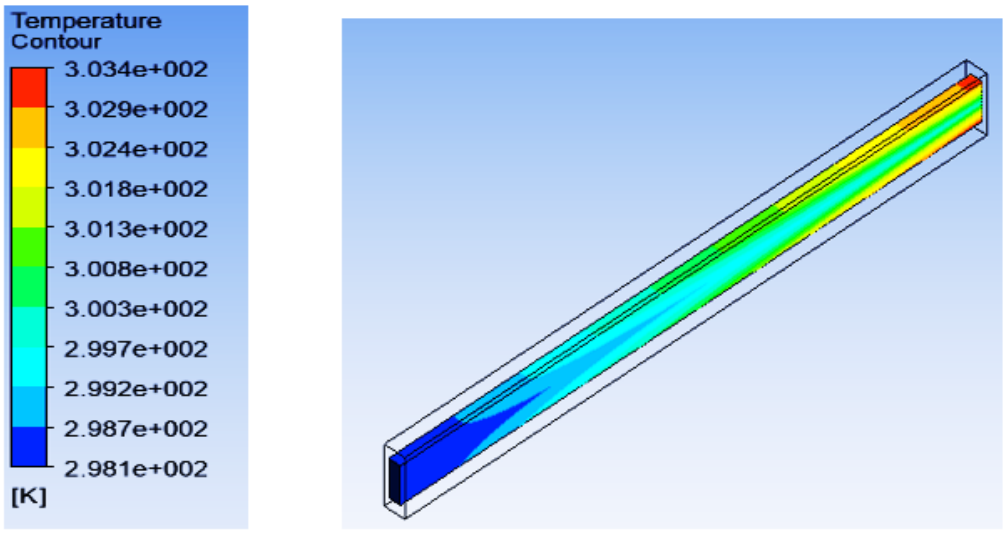

Figure 6.128. Water temperature contour.

(Outlet water temperature = 303.409 K, optimal velocity = 2.496 m/s)

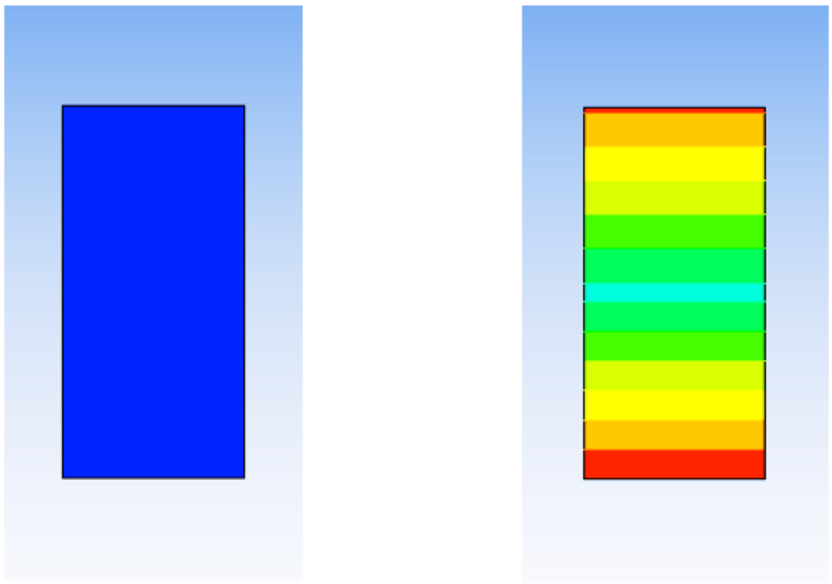

(a) Inlet water temperature contour (b) Outlet water temperature contour

Figure 6.129. Inlet and outlet water temperature contours.

6.2.4. Square microchannel heat sinks

6.2.4.1. Subcooled flow boiling (Two-phase flow)

Square microchannels have aspect ratio of 1, while the width of the heat sink is equal to the height (the same heat sink cross-section for circular and equilateral triangular configurations). The velocities for which optimal parameters were available for the computations and Figure 6.130-Figure 6.138 are: 0.1-0.5 to 4.0-4.5 m/s at 100 W/cm^2; 1.5-2.0 to 4.0-4.5 m/s at 200 W/cm^2; 3.0-3.5 to 6.5-7.0 m/s at 300 W/cm^2 and 4.5-5.0 to 6.5-7.0 m/s at 400 W/cm^2.

Figure 6.130 shows the variation of thermal resistance with Reynolds number. At 300 and 400 W/cm^2, the last optimal microchannel heat sinks are slightly in the turbulent flow region. Even though the thermal resistances are close (Figure 6.130), the base temperatures are not, as seen in Figure 6.131. This trend is the same with other configurations considered earlier (for example: Figure 6.2 and Figure 6.3).

High pumping power requirements are witnessed at 300 W/cm^2 because of increasing velocity resulting in high pressure drops as shown in Figure 6.132. The micro pumping trend is the same with what was obtained for other microchannel configurations. However, some optimal microchannel heat sinks at 300 W/cm^2 are operating at higher velocities in contrast to those of optimal rectangular microchannel heat sinks at the same heat flux (Figure 6.80).

Figure 6.133-Figure 6.136 show the relationships of length and hydraulic diameter with Reynolds number and Bejan number. As length and hydraulic diameter increase, Reynolds number and Bejan number increase which is in line with Figure 6.83-Figure 6.86 and other microchannel configurations. The slight decreases witnessed in optimal hydraulic diameters for optimal circular and triangular microchannels as Reynolds number increases (Figure 6.7 and Figure 6.8, also Figure 6.52 and Figure 6.53) are also observed for optimal square microchannels (Figure 6.135 and Figure 6.136) probably because of aspect ratio being 1 for circular and square microchannels and equal sides for equilateral microchannels as explained earlier.

Pressure drop and Bejan number vary with Reynolds number as shown in Figure 6.137 and Figure 6.138. This is in line with Figure 6.87, Figure 6.88 and other microchannel configurations.

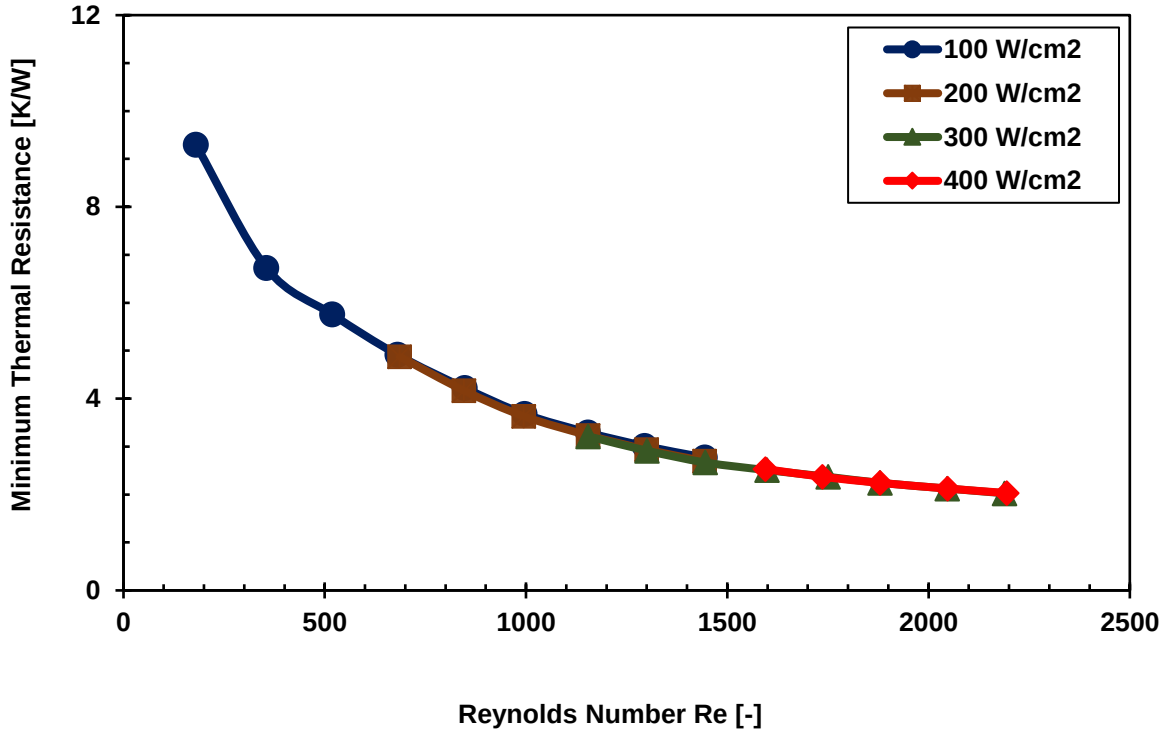

Figure 6.130. Thermal resistances of optimal microchannel heat sinks.

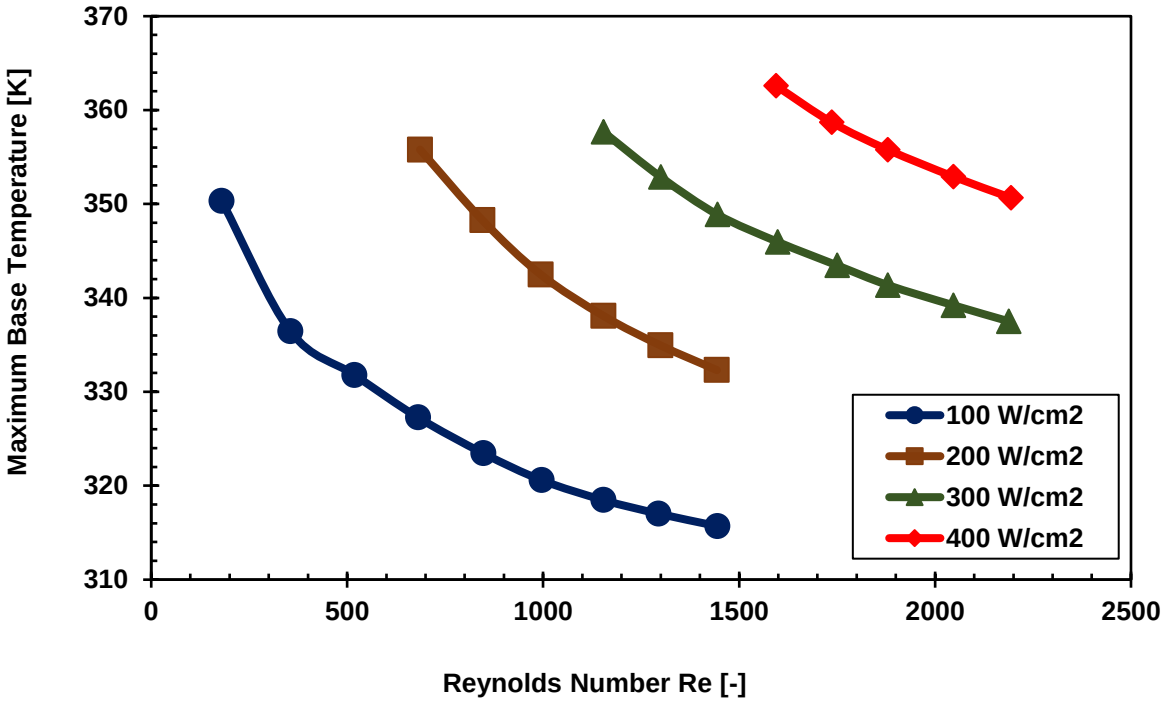

Figure 6.131. Maximum base temperatures of optimal microchannel heat sinks.

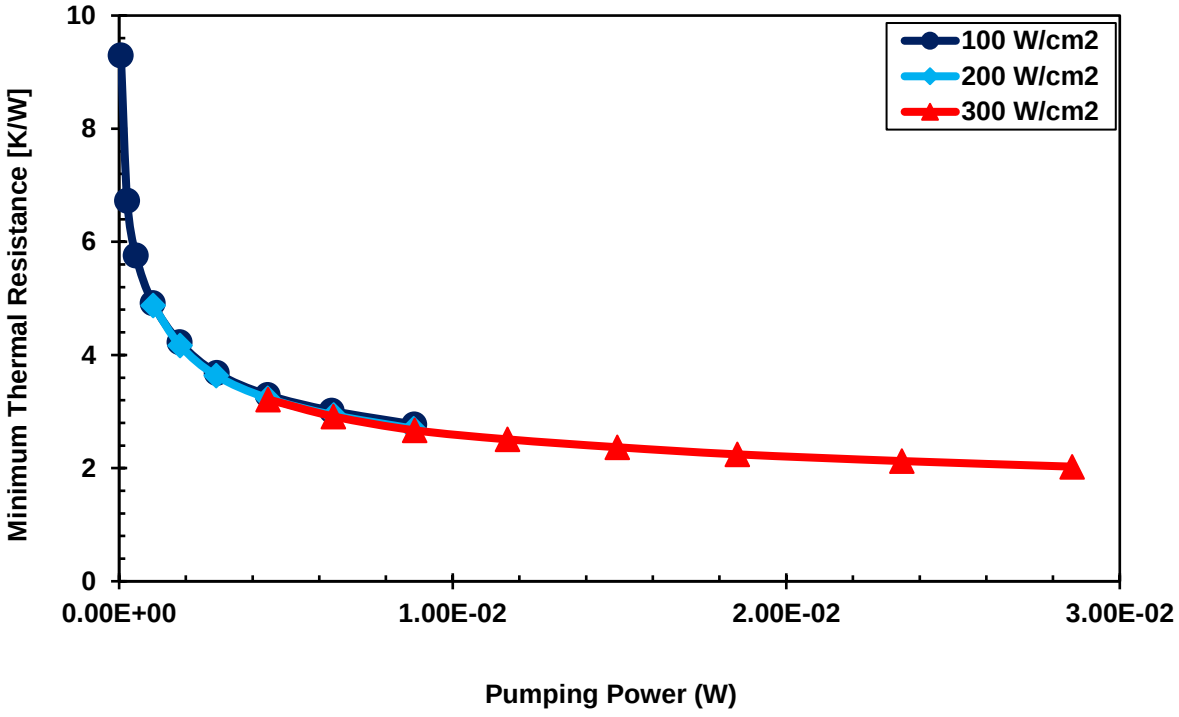

Figure 6.132. Pumping power of optimal microchannel heat sinks.

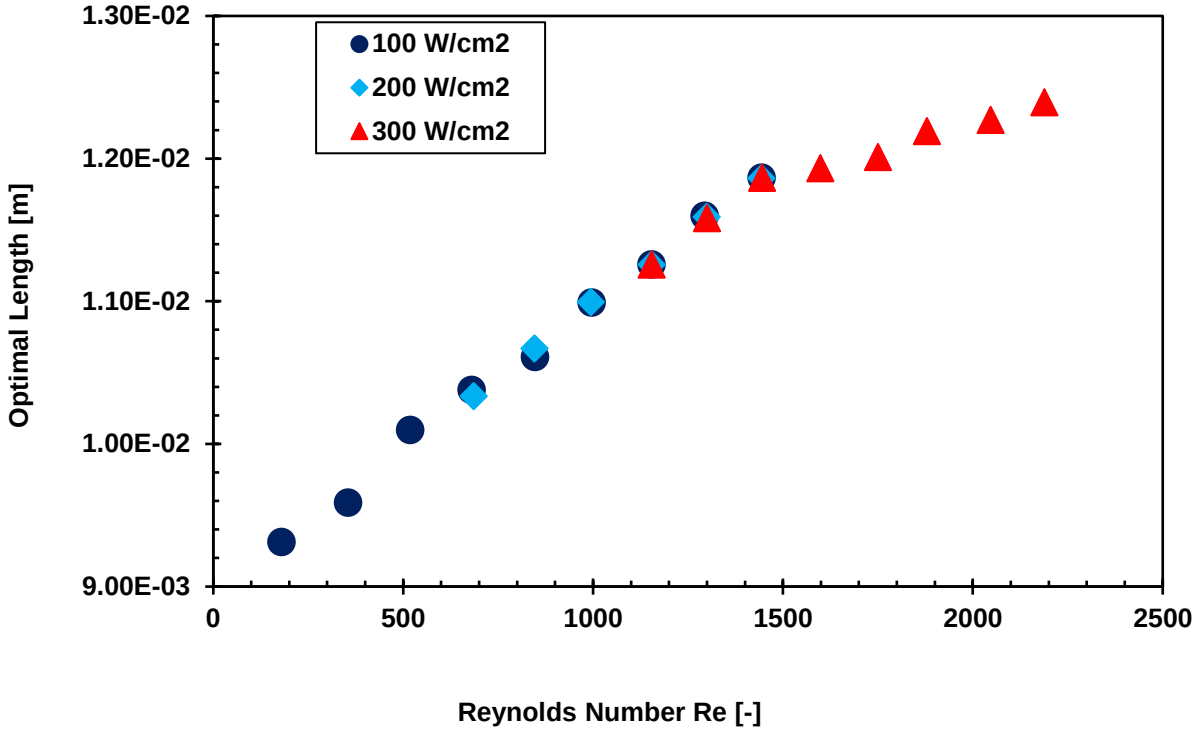

Figure 6.133. Effect of length on optimal microchannel heat sinks.

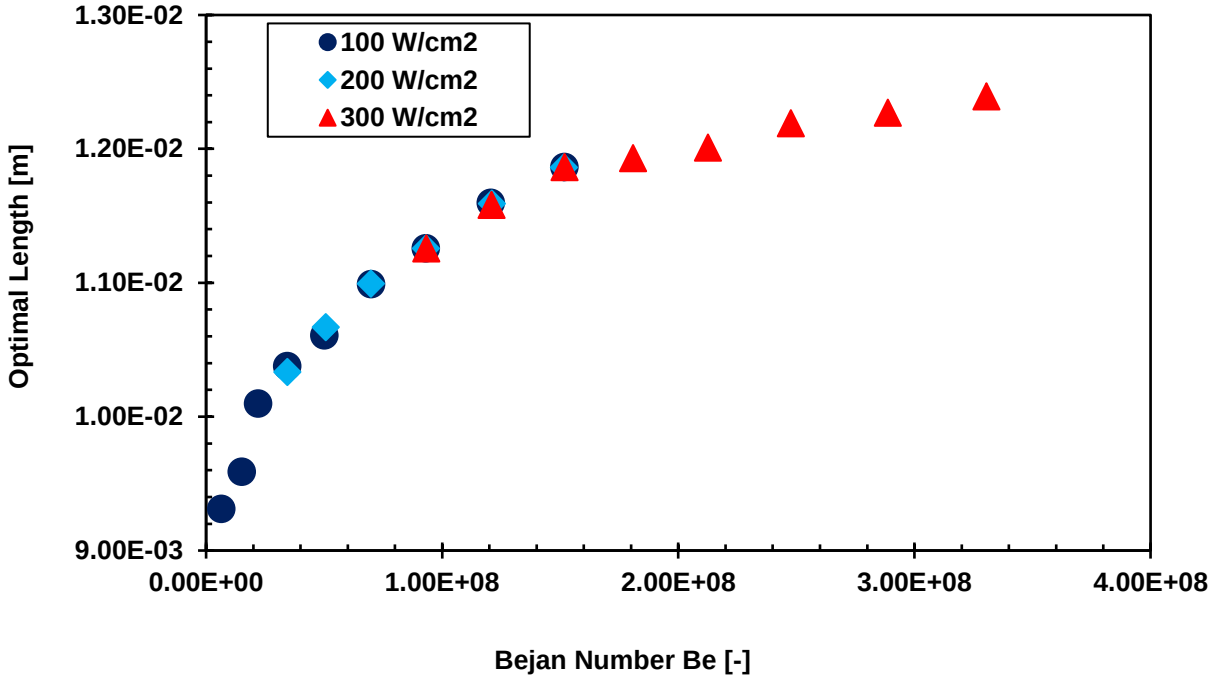

Figure 6.134. Effect of dimensionless pressure drop on optimal length.

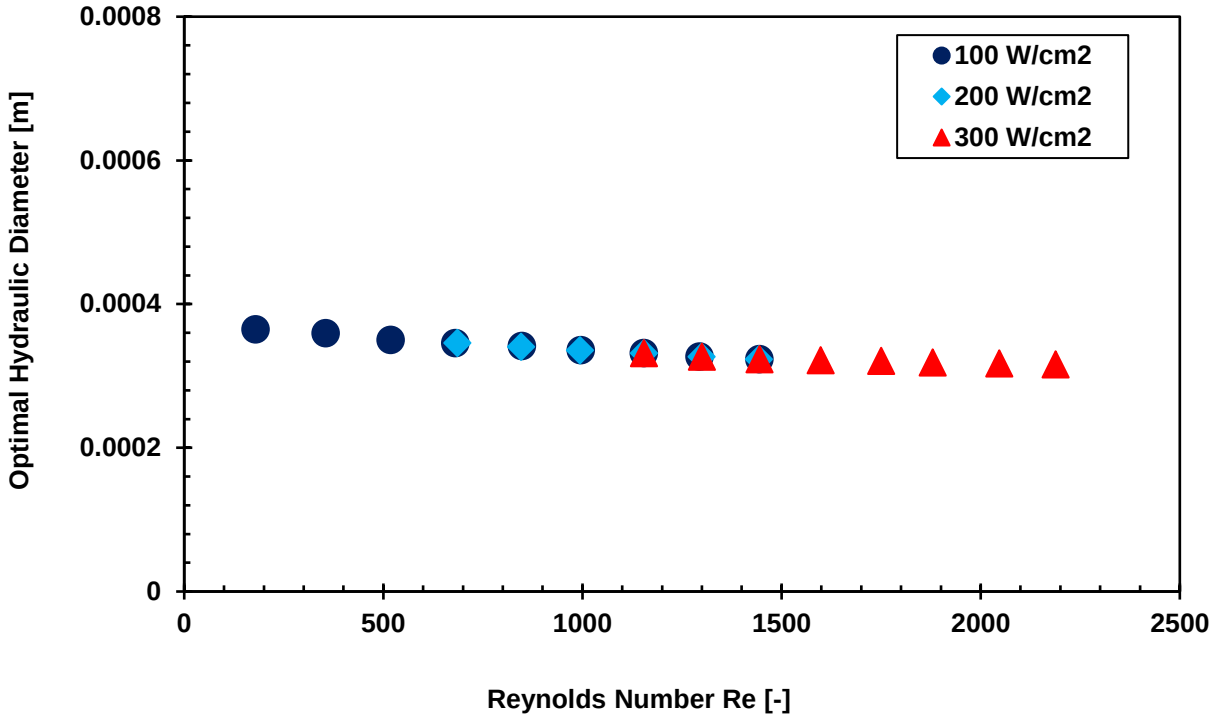

Figure 6.135. Effect of hydraulic diameter on optimal microchannel heat sinks.

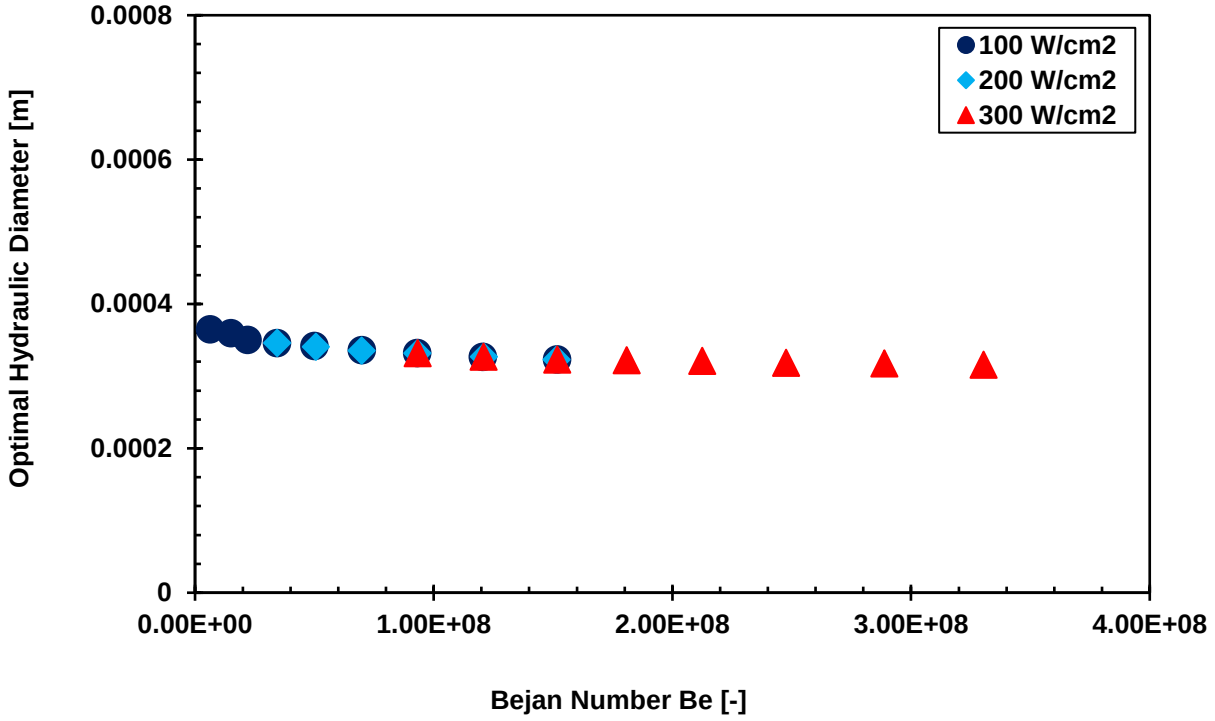

Figure 6.136. Effect of dimensionless pressure drop on optimal hydraulic diameter.

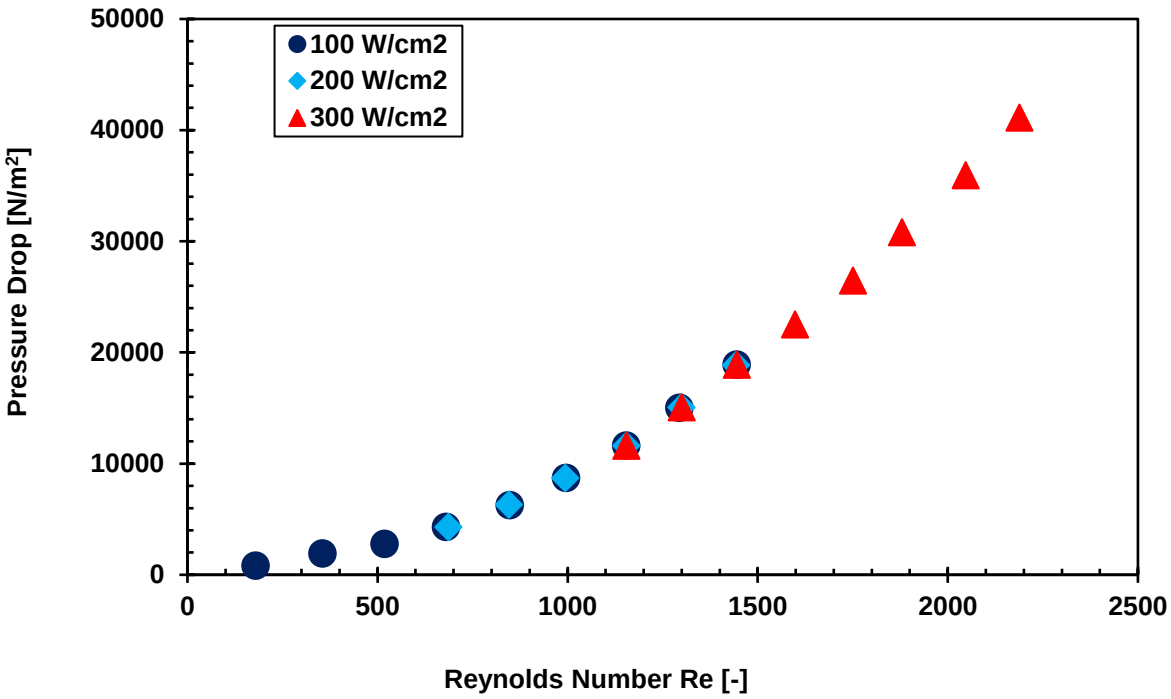

Figure 6.137. Effect of pressure drop on Reynolds number.

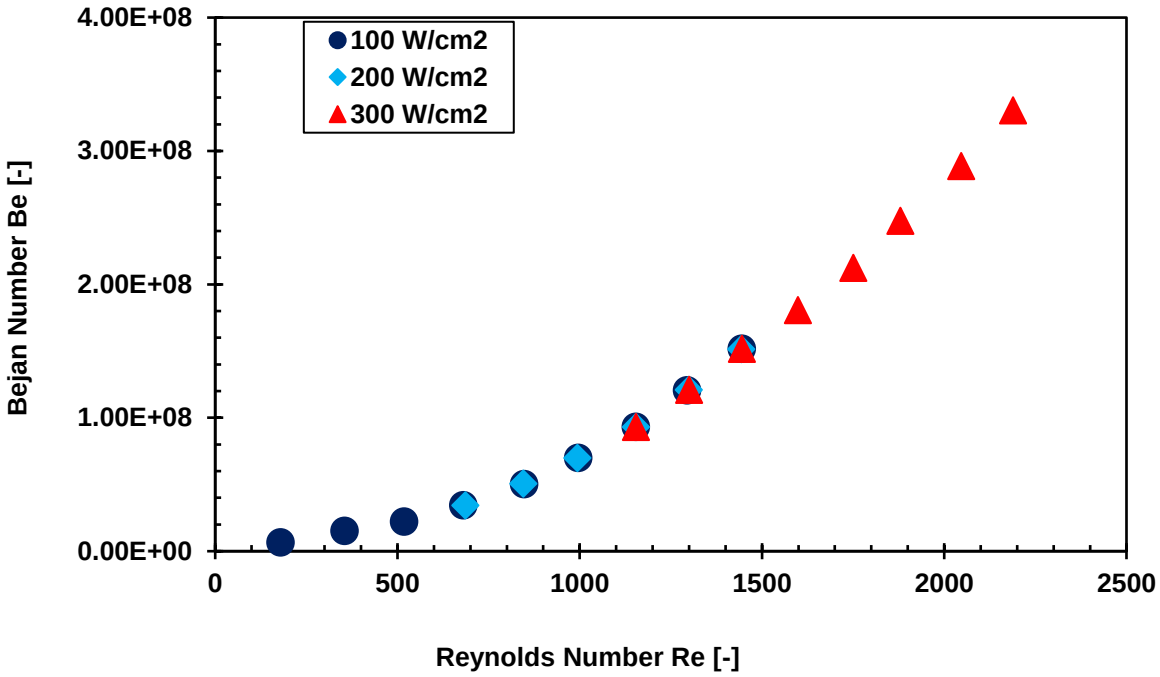

Figure 6.138. Effect of dimensionless pressure drop on Reynolds number.

Temperature contours

The contours in Figure 6.139-Figure 6.143 were obtained at 100 W/cm^2 in two-phase flow. Figure 6.139 shows inner wall temperature distribution across the optimal microchannel heat sink. In Figure 6.139, wall temperature increased from 317.5 K at the inlet to 323.4 K at the outlet compared to that of rectangular microchannel heat sink (Figure 6.89) ranging between 310.1 and 315.4 K. The corresponding inlet and outlet wall temperature distribution are shown in Figure 6.140(a) and Figure 6.140(b). The water temperature increased from 298.15 K at the inlet to 302.6 K (Figure 6.141) at the outlet of the microchannel compared to that of rectangular microchannel which increased from 298.15 K to 301.1 K (Figure 6.91). These differences are evidently as a result of different configurations of microchannel, hence the thermal characteristics of optimal rectangular microchannel heat sink at the same heat flux and velocity range are better than those of optimal square microchannel heat sink. The corresponding inlet and outlet water temperature contours are shown in Figure 6.142(a) and Figure 6.142(b). The vapour temperature contour in Figure 6.143 shows a range from 298.15 K where water entered the microchannel in single-phase to 373.15 K where there was nucleation of vapour bubbles at ONB to the exit of the microchannel.

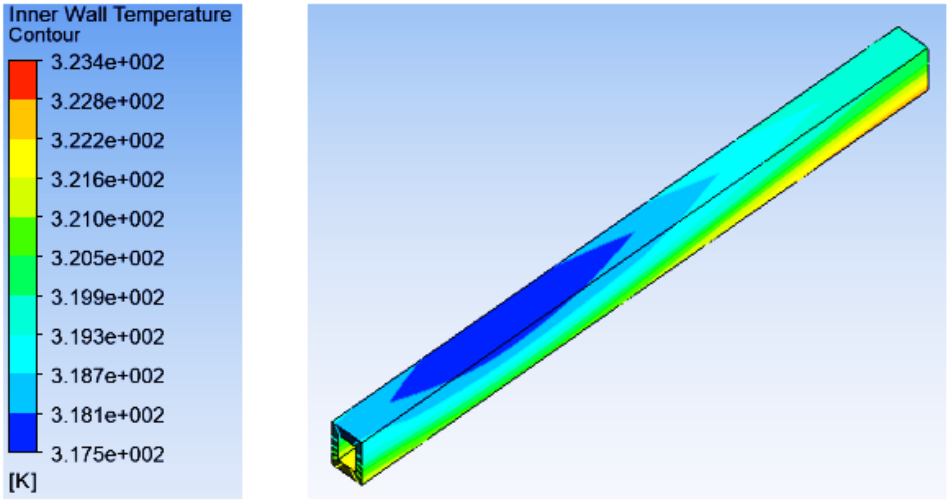

Figure 6.139. Inner wall temperature contour (base temperature = 323.444 K).

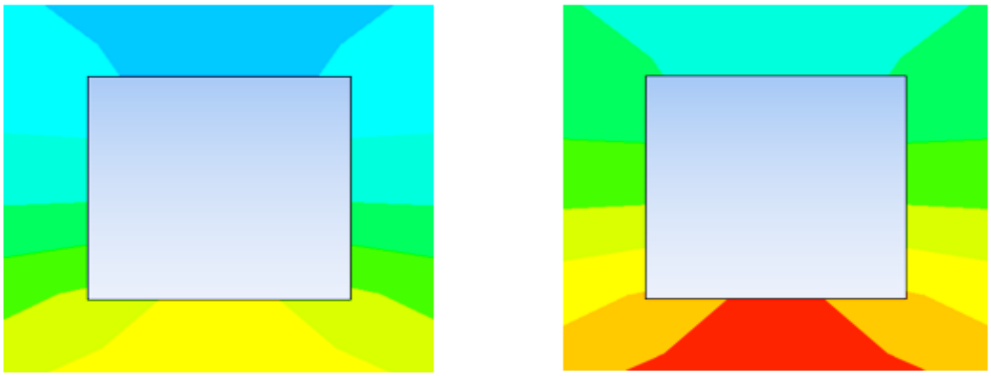

(a) Inlet wall temperature contour (b) Outlet wall temperature contour

Figure 6.140. Inlet and outlet wall temperature contours.

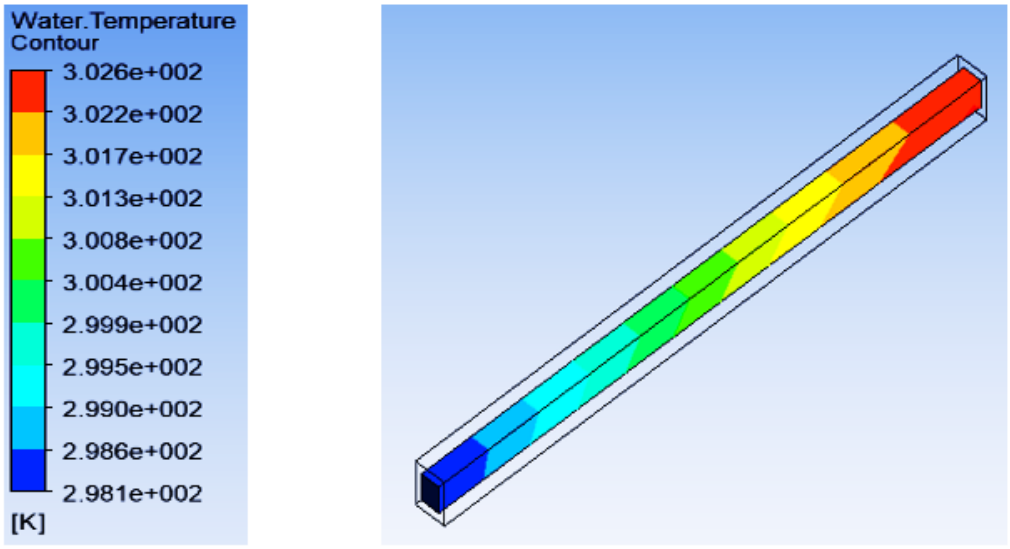

Figure 6.141. Water temperature contour.

(Outlet water temperature = 302.636 K, optimal velocity = 2.4946 m/s)

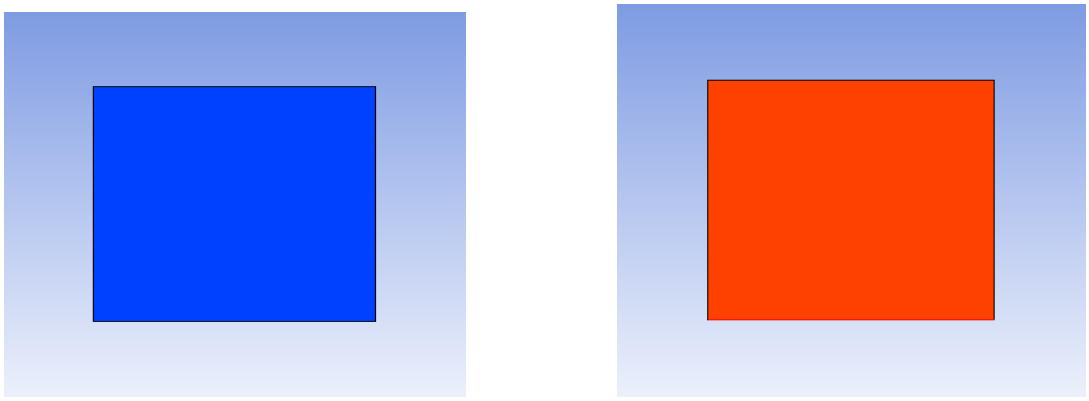

(a) Inlet water temperature contour (b) Outlet water temperature contour

Figure 6.142. Inlet and outlet water temperature contours.

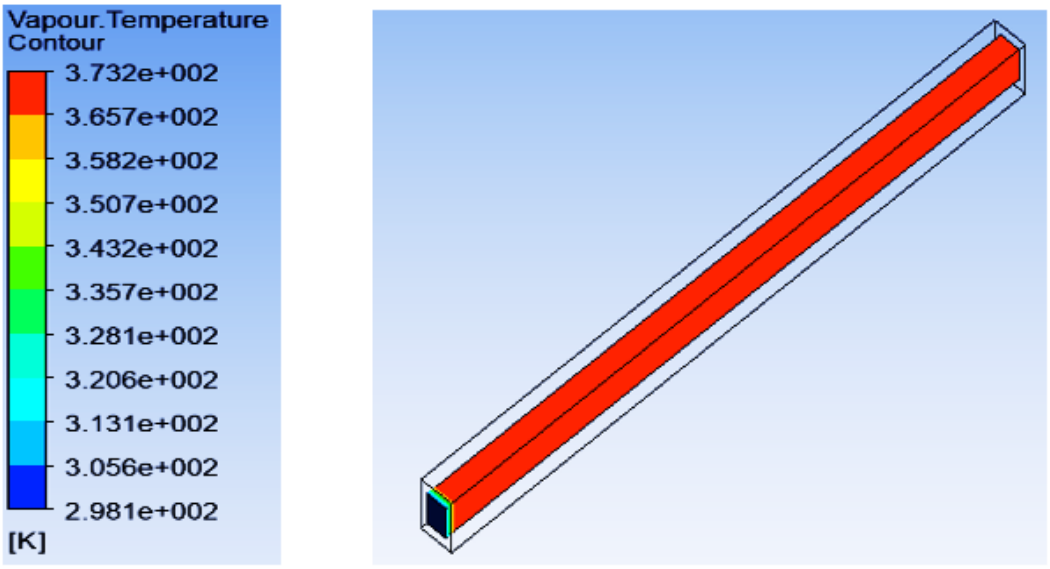

Figure 6.143. Vapour temperature contour.

6.2.4.2. Comparisons of two-phase and single-phase flow at 100 W/cm^2

The velocities for computations are: 0.1-0.5 to 4.0-4.5 m/s in two-phase flow and 2.0-2.5 to 4.0-4.5 m/s in single-phase flow. Figure 6.144 shows the thermal resistances of optimal microchannel heat sinks in two-phase and single-phase flow. The corresponding base temperatures are shown in Figure 6.145. The thermal characteristics of optimal microchannel heat sinks in two-phase flow are better than those in single-phase flow consistent with those of rectangular microchannel heat sinks (Figure 6.94 and Figure 6.95) and other heat sinks discussed earlier. The pumping power (Figure 6.146) also followed the trend of decreasing thermal resistance as pumping power increases (Figure 6.96). The increase in pumping power requirements in two-phase flow beyond those in single-phase flow is as a result of high pressure drops.

Optimal length varies with Reynolds number and Bejan number (Figure 6.147 and Figure 6.148) as anticipated to produce optimal microchannel heat sinks; this trend is in line with optimal rectangular microchannel heat sinks (Figure 6.99 and Figure 6.100) and other microchannel heat sinks discussed earlier. Optimal hydraulic diameters occurred in a narrow range (Figure 6.149 and Figure 6.150) consistent with Figure 6.101 and Figure 6.102.

Pressure drop and Bejan number increase as Reynolds number increases as shown in Figure 6.151 and Figure 6.152. The trend is similar to Figure 6.103 and Figure 6.104.

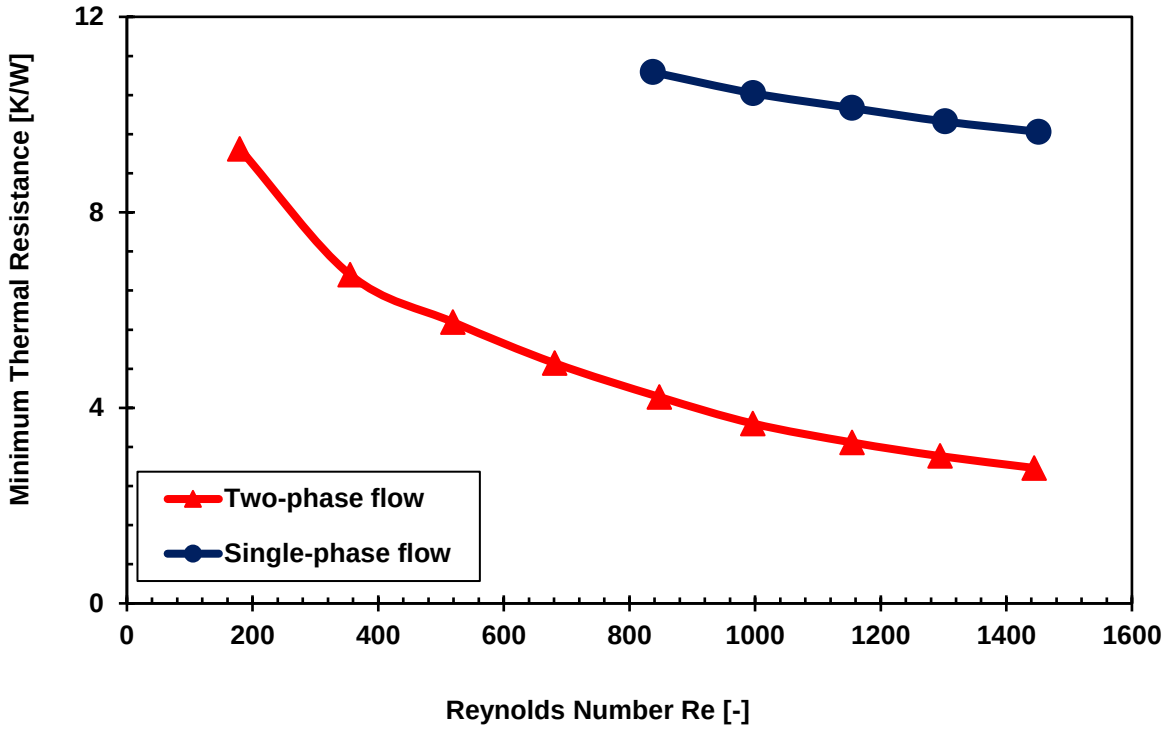

Figure 6.144. Thermal resistances of optimal microchannel heat sinks at 100 W/cm^2.

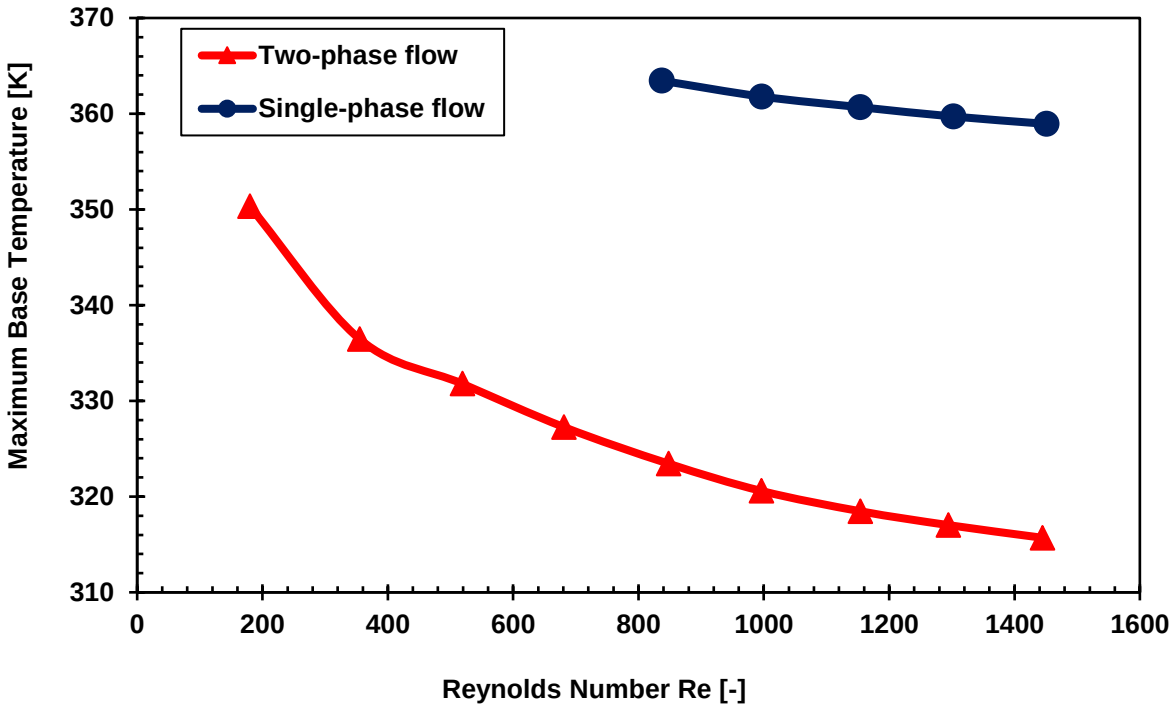

Figure 6.145. Maximum base temperatures of optimal microchannel heat sinks at 100 W/cm^2.

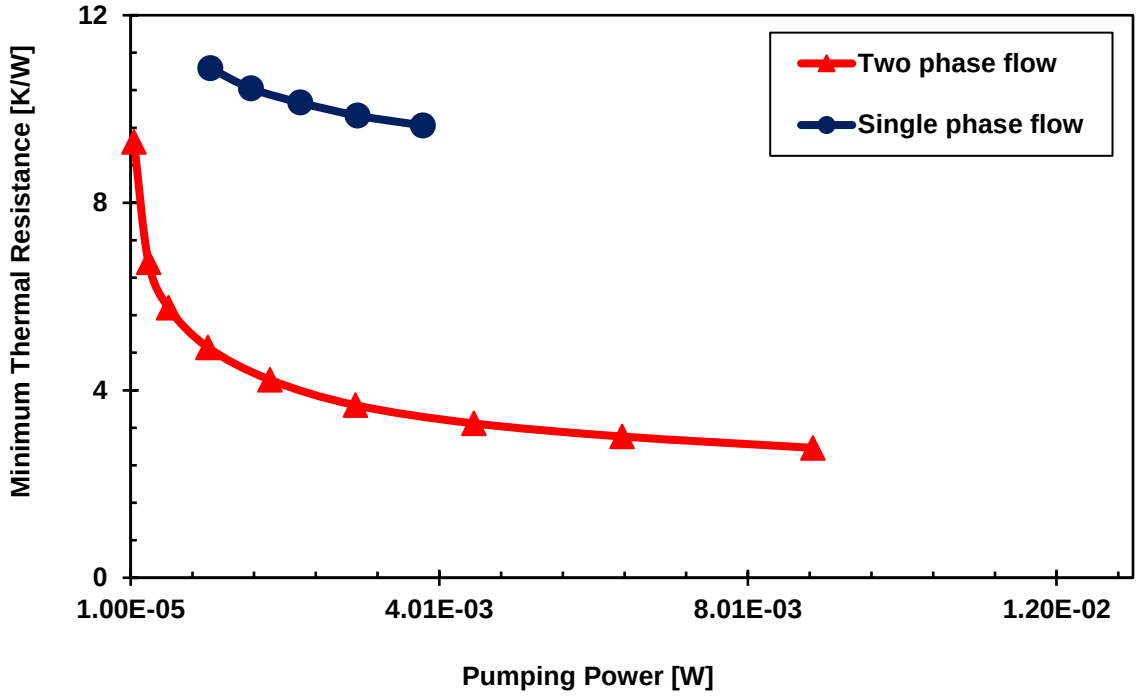

Figure 6.146. Pumping power of optimal microchannel heat sinks at 100 W/cm^2.

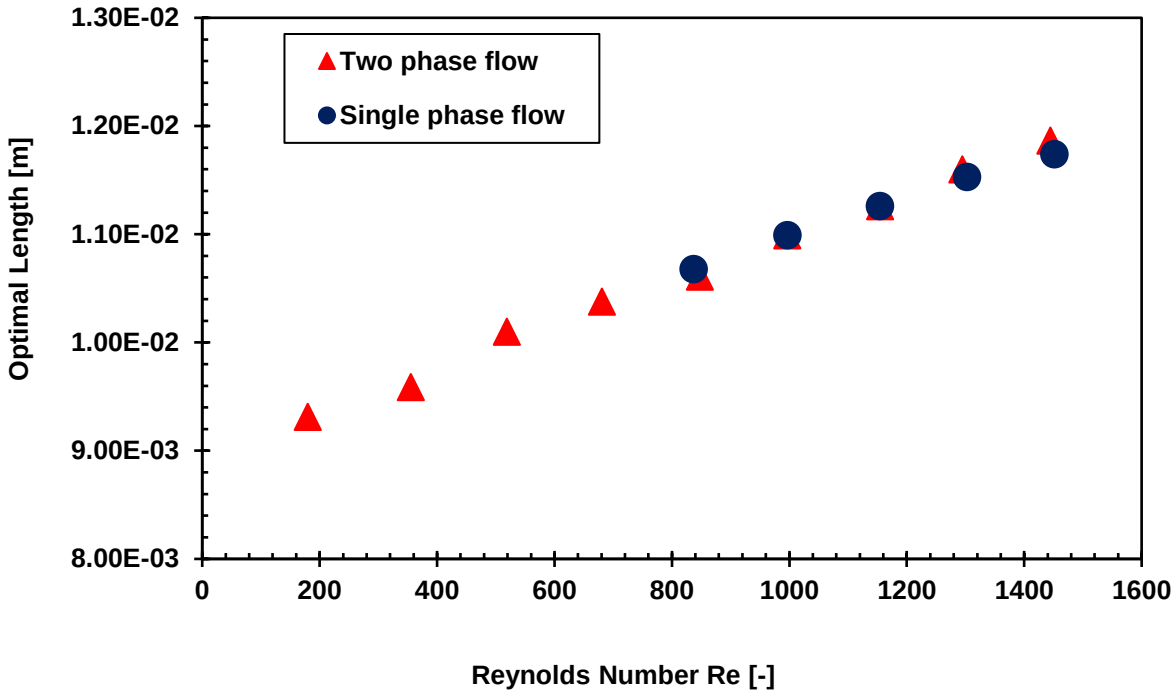

Figure 6.147. Effect of length on optimal microchannel heat sinks at 100 W/cm^2.

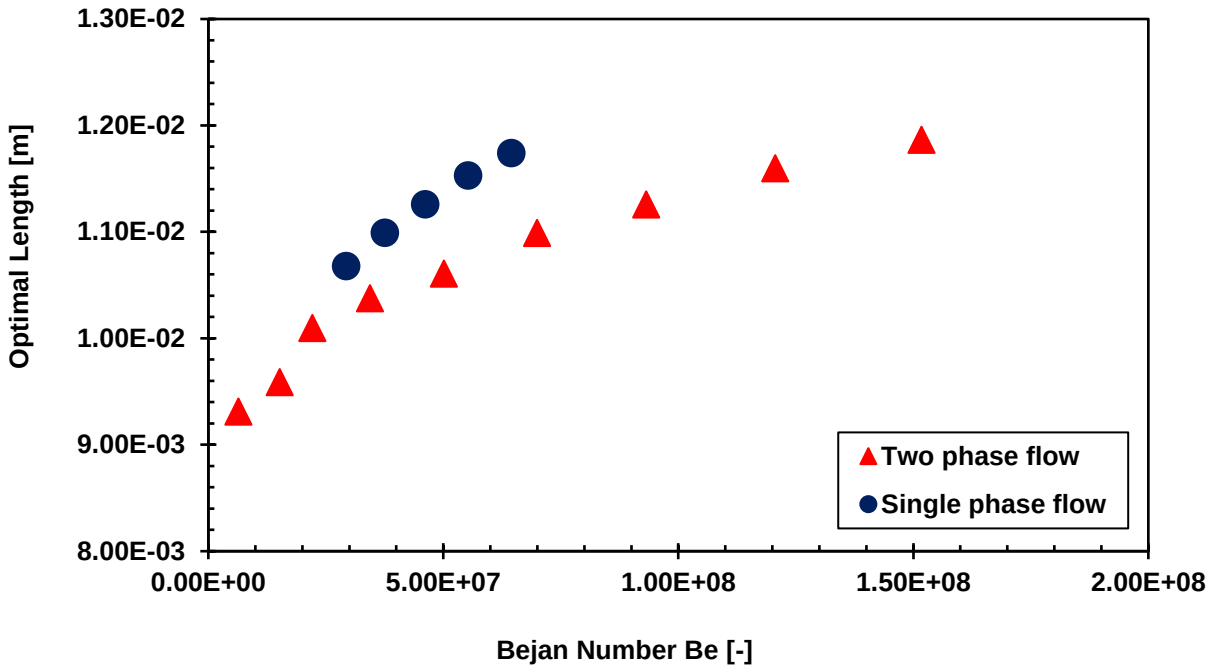

Figure 6.148. Effect of dimensionless pressure drop on optimal length at 100 W/cm^2.

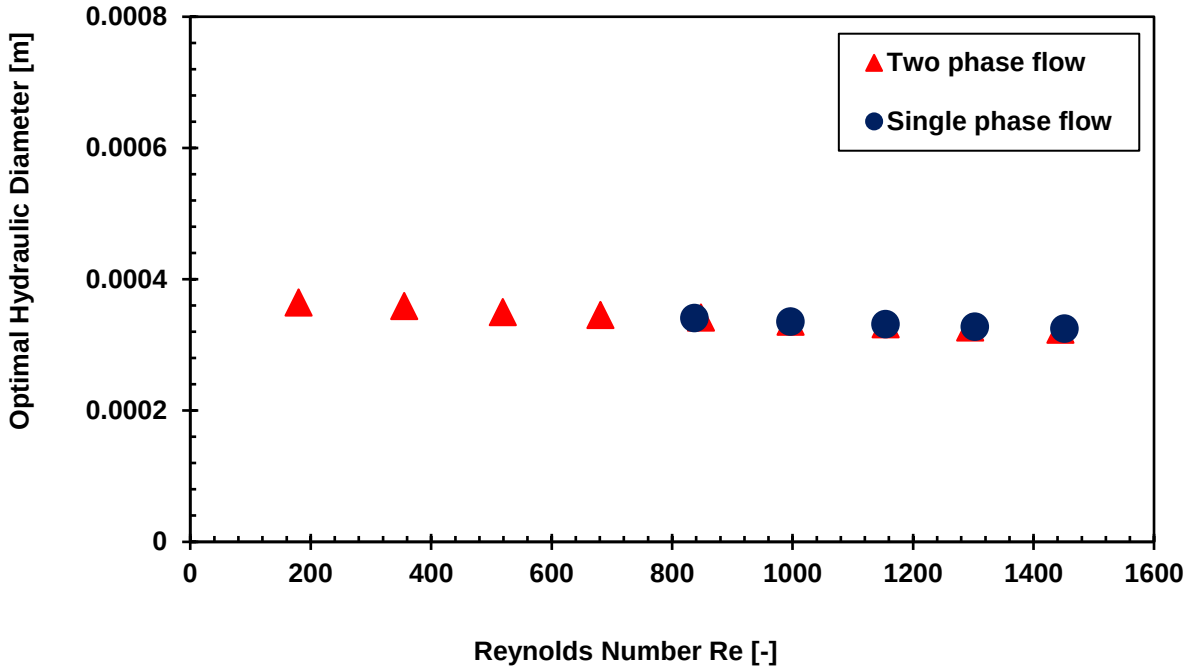

Figure 6.149. Effect of hydraulic diameter on optimal microchannel heat sinks at 100 W/cm^2.

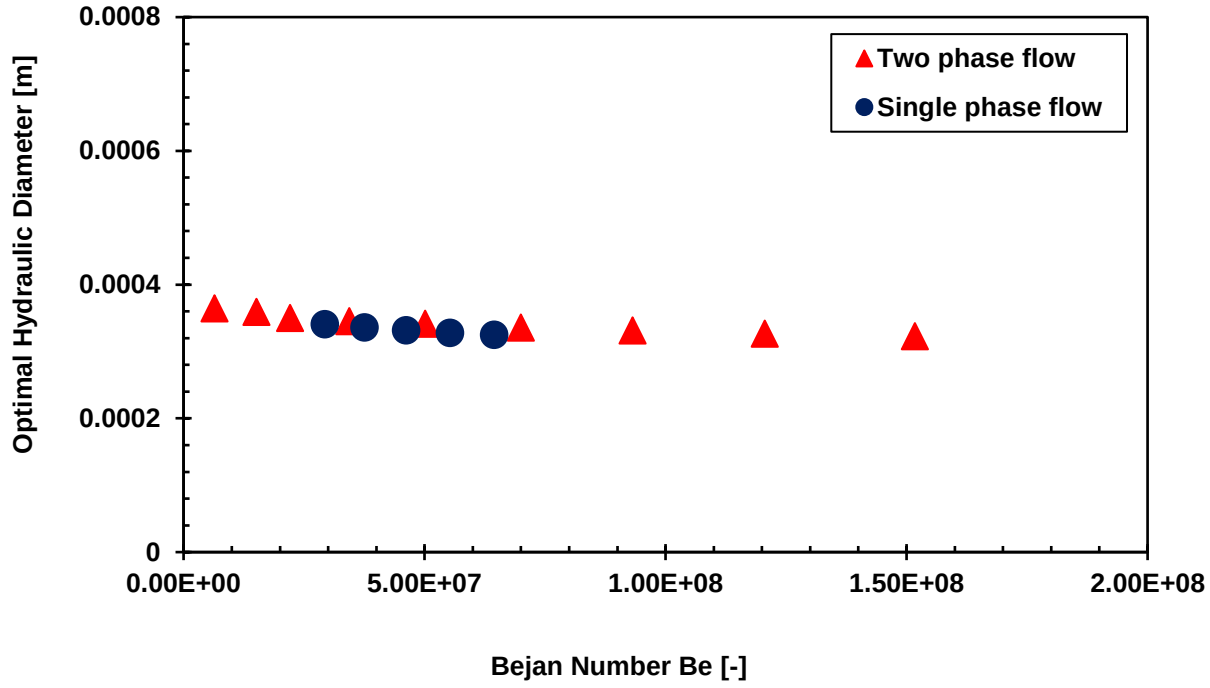

Figure 6.150. Effect of dimensionless pressure drop on optimal hydraulic diameter at 100 W/cm^2.

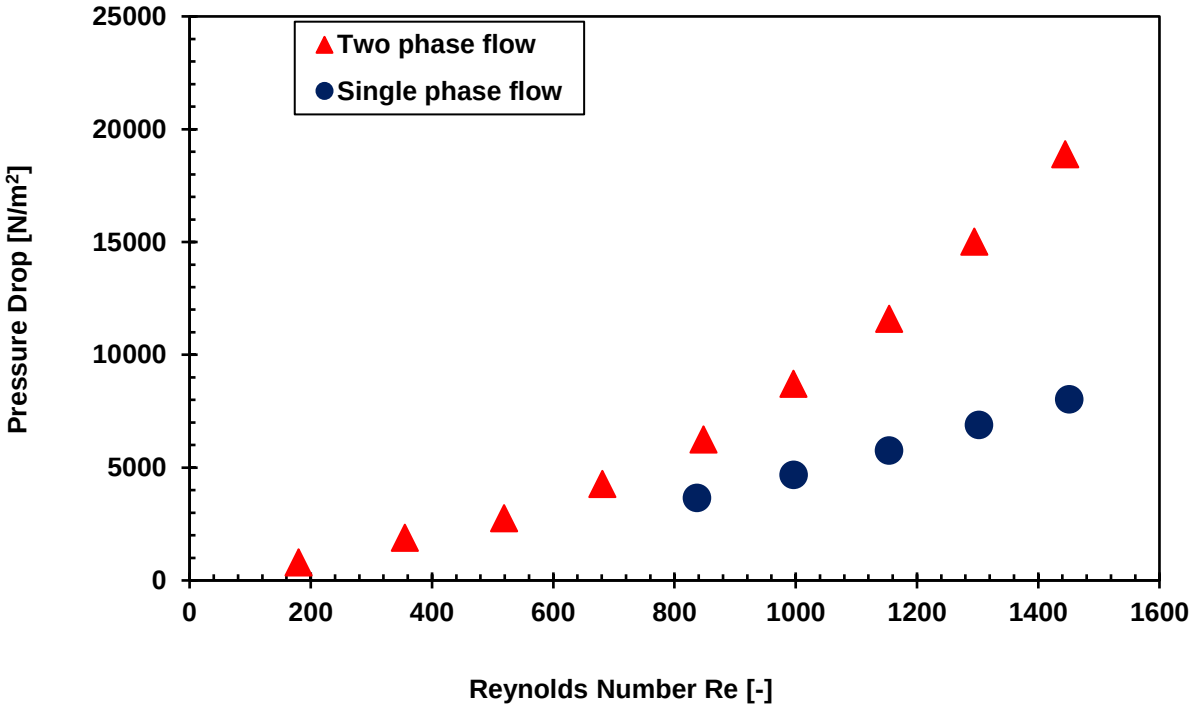

Figure 6.151. Effect of pressure drop on Reynolds number at 100 W/cm^2.

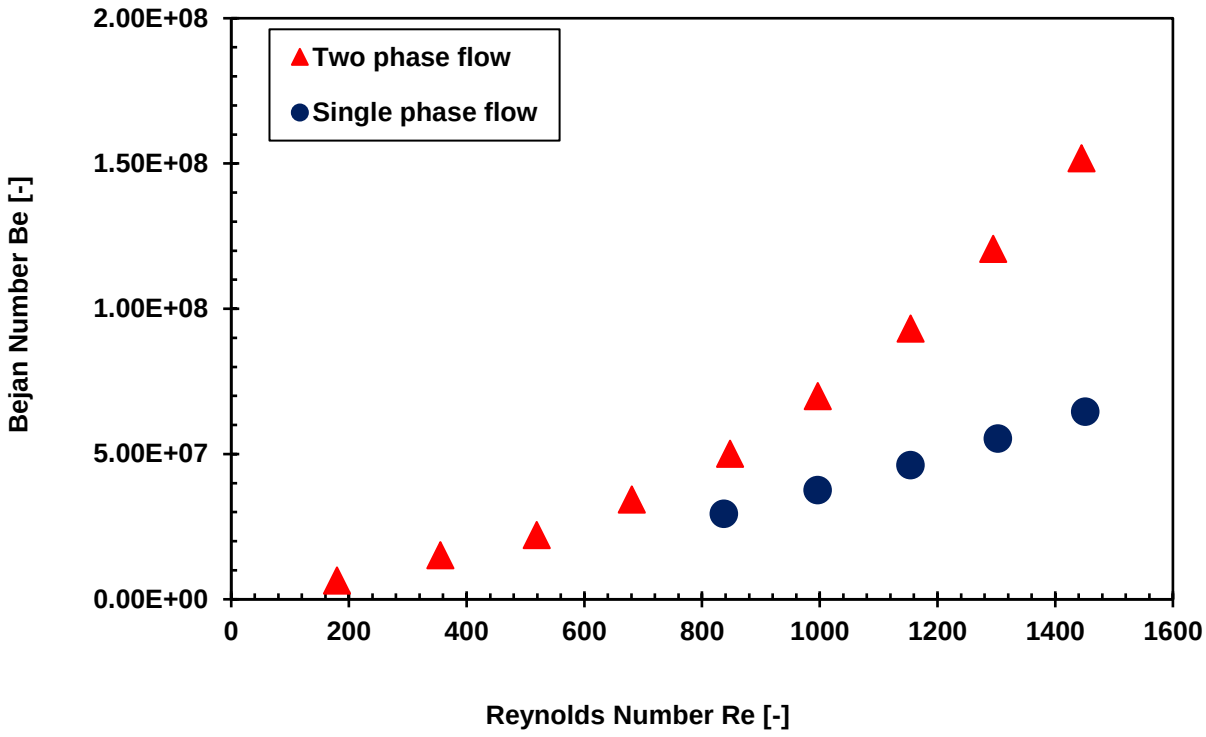

Figure 6.152. Effect of dimensionless pressure drop on Reynolds number at 100 W/cm^2.

Temperature contours

The contours in Figure 6.153-Figure 6.156 were obtained at 100 W/cm^2 in single-phase flow. Inner wall temperature varied from 356.3 K at inlet to 363.4 K at the outlet (Figure 6.153) compared to that of optimal rectangular heat sink which varied from 334.9 to 342 K (Figure 6.126). The corresponding inlet and outlet wall temperature contours are shown in Figure 6.154(a) and Figure 6.154(b). The temperature distribution for inner wall in two-phase flow increased from 317.5 to 323.4 K (Figure 6.139) which is better than single-phase flow.

Figure 6.155 shows water temperature distribution across the microchannel. Water temperature shows variation from 298.15 K at the inlet to 303.3 K at the outlet compared to that of optimal rectangular microchannel heat sink varying from 298.15 to 303.4 K (Figure 6.128). Water temperature distribution in two-phase flow in Figure 6.141 shows variation from 298.15 to 302.6 K. Figure 6.156(a) and Figure 6.156(b) depict water temperature distribution at inlet and outlet of the microchannel.

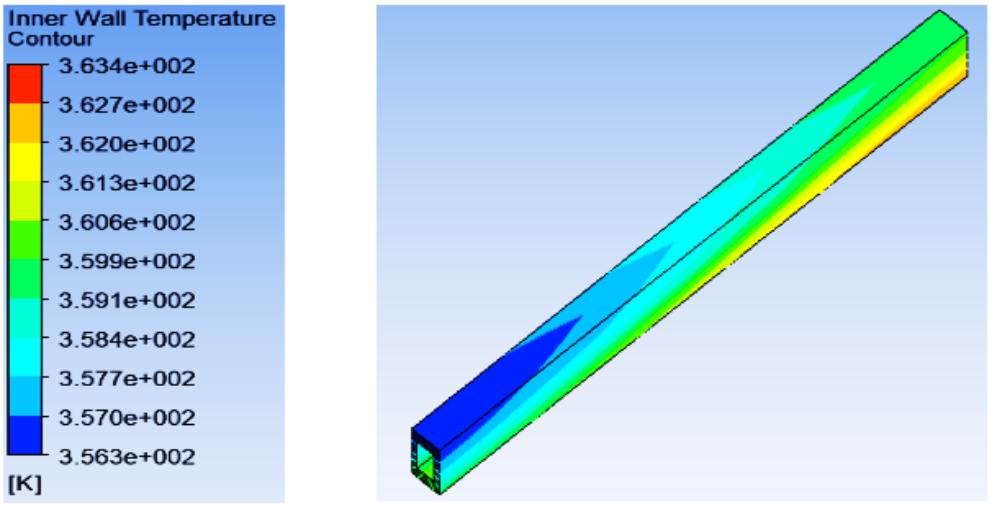

Figure 6.153. Inner wall temperature contour (base temperature = 363.447 K).

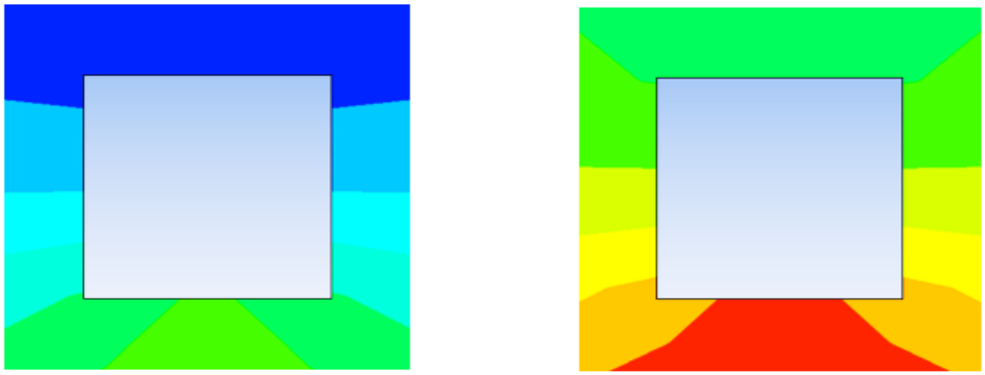

(a) Inlet wall temperature contour (b) Outlet wall temperature contour

Figure 6.154. Inlet and outlet wall temperature contours.

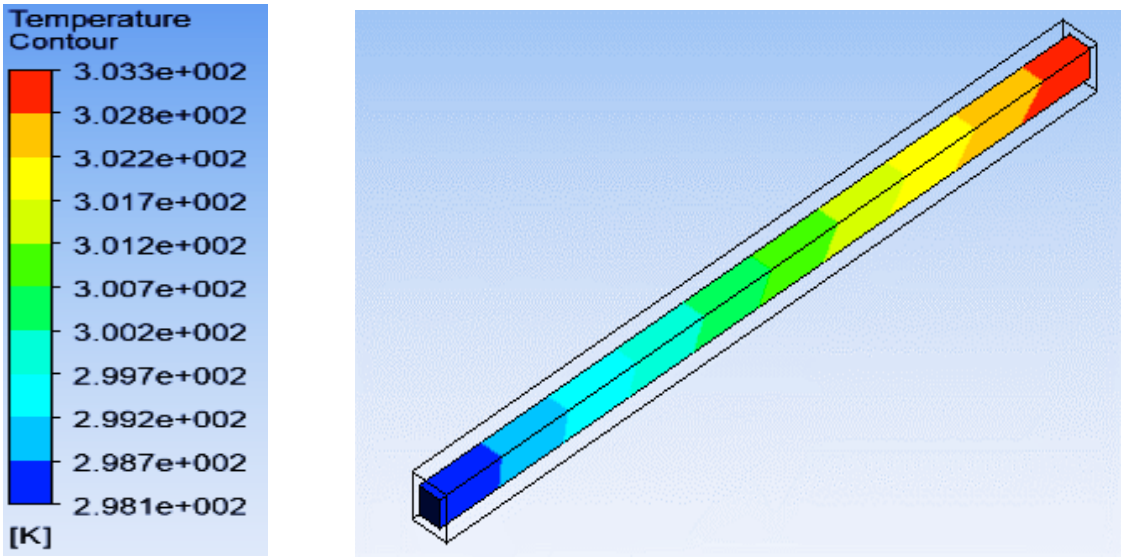

Figure 6.155. Water temperature contour.

(Outlet water temperature = 303.27 K, optimal velocity = 2.472 m/s)

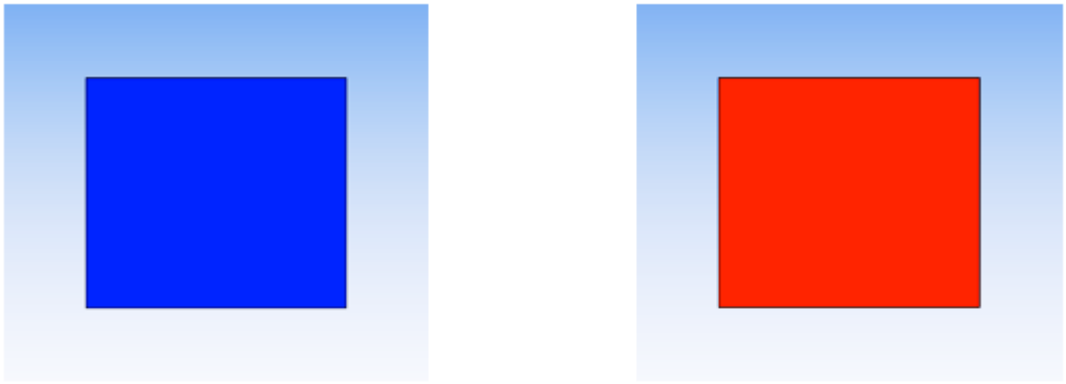

(a) Inlet water temperature contour (b) Outlet water temperature contour

Figure 6.156. Inlet and outlet water temperature contours.

6.3. Comparisons of microchannel configurations (multichannels)

6.3.1. Subcooled flow boiling (Two-phase flow)

The four microchannel configurations are compared here for possible practical applications, on a width of 1 cm which is common in electronic packaging. The heat sinks containing multichannels are analogous to Figure 5.1(a)-Figure 5.1(d). The number of optimal microchannel heat sinks that will fit into 1 cm width was calculated and that was the basis for computing the thermal resistances and pumping power of multichannels at optimal velocities. The thermal resistance for a heat sink with one microchannel is given as:

$R_{th} = \frac{T_{b,max} - T_{f,min}}{q.\ A_{b,s}}$ (Equation (3.38))

For a heat sink containing N microchannels, the thermal resistance can be written as:

$$R_{th} = \frac{T_{b,max} - T_{f,min}}{q.\ N.\ A_{b,s}} \quad (6.1)$$

where $N.\ A_{b,s}$ represents the base (bottom) area of the multichannel heat sink. Equation (6.1) shows that as the number of microchannel increases, thermal resistance decreases.

The pumping power for a heat sink containing one microchannel is written as:

$PP = u_{in}.A_{ch}.\Delta P$ (Equation ((3.40))

For a heat sink containing N microchannels, the pumping power can be expressed as:

$$PP = N\,.u_{in}.A_{ch}.\Delta P \quad (6.2)$$

Equation (6.2) shows that as the number of microchannel increases, the pumping power increases.

The number of microchannels on a 1 cm width was not the same in most cases for the microchannel configurations because optimal values for the width of microchannel heat sinks were different. For example, in two-phase flow at 100 W/cm^2 and 1.5-2.0 m/s, the approximate number of microchannels on 1 cm width for each configuration is given as:

Circular	18
Equilateral triangular	17
Rectangular	26
Square	18

The computations and comparisons were based on the number of optimal microchannels on 1 cm width for each configuration. The comparisons were made between 100 and 300 W/cm^2. Microchannel heat sinks that are operating in the turbulent flow region shown in Figure 6.159 and Figure 6.162 are retained for the purposes of comparison.

The thermal resistances of optimal microchannel heat sinks are shown in Figure 6.157-Figure 6.159. In all the three figures, rectangular microchannel heat sinks have the best performance followed by equilateral triangular microchannel heat sinks. As heat flux increases, thermal resistances of circular and square microchannel heat sinks are clearly shown to be different (Figure 6.158 and Figure 6.159).

Figure 6.160-Figure 6.162 provide the base temperatures of optimal microchannel heat sinks between 100 and 300 W/cm^2. The same trend of performance for thermal resistance is followed as rectangular microchannel heat sinks have the least base temperatures for the heat fluxes, followed by equilateral triangular microchannel heat sinks.

The pumping power requirements for the microchannel heat sinks are shown in Figure 6.163-Figure 6.165. All the microchannel heat sinks performed relatively well with low pumping power. The reason for having big differences in pumping power in Figure 6.165 is as a result of some optimal microchannel heat sinks operating at high velocities and consequently high pressure drops.

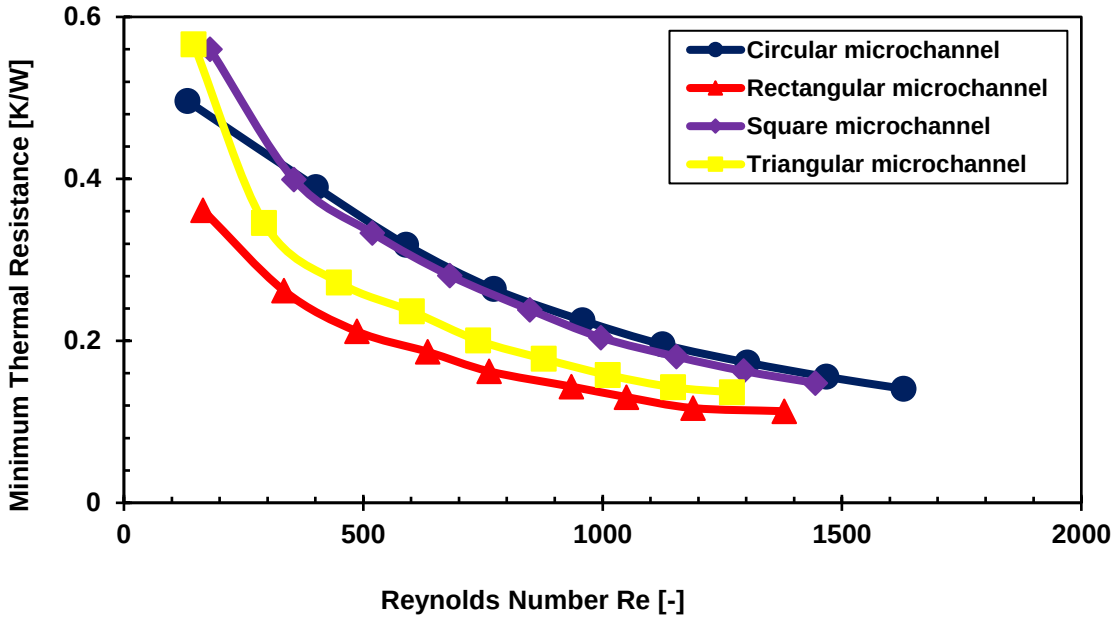

Figure 6.157. Thermal resistances of multichannel heat sinks at 100 W/cm^2.

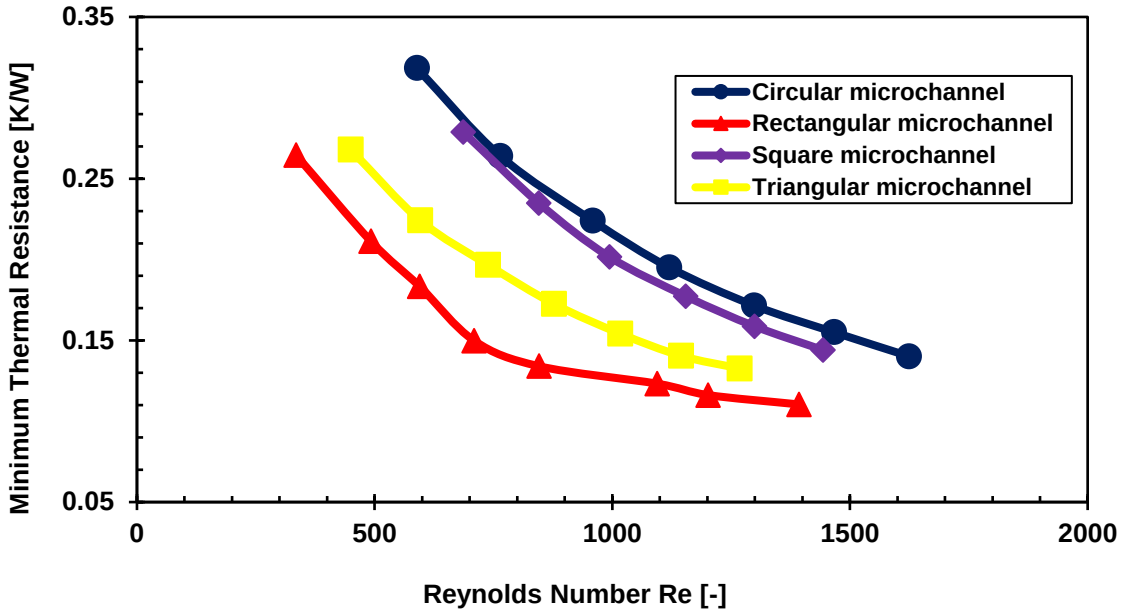

Figure 6.158. Thermal resistances of multichannel heat sinks at 200 W/cm^2.

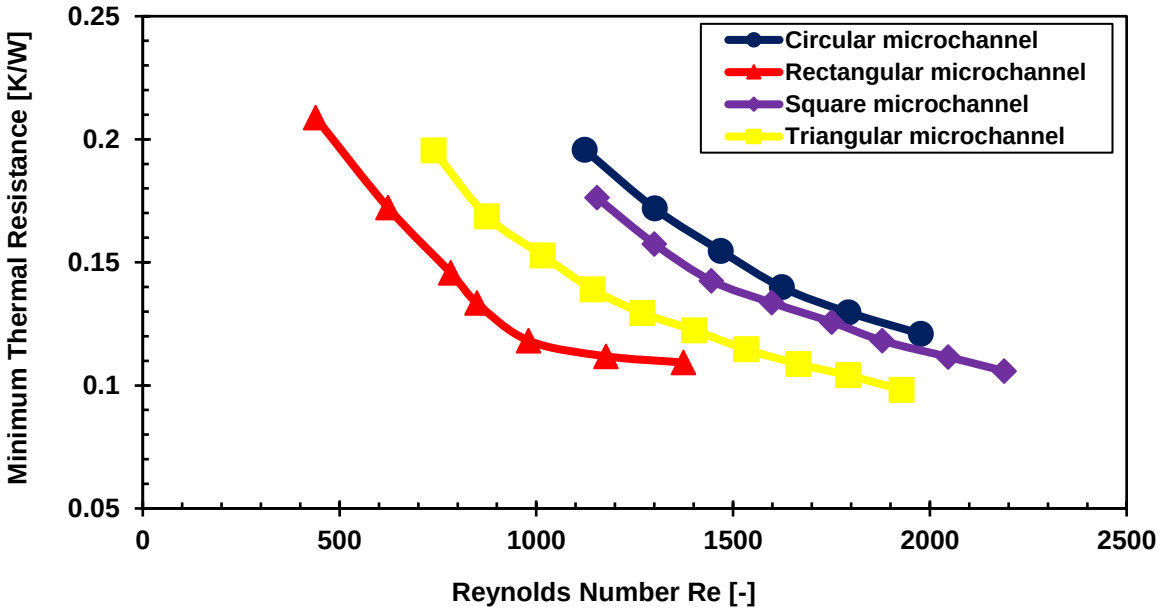

Figure 6.159. Thermal resistances of multichannel heat sinks at 300 W/cm^2.

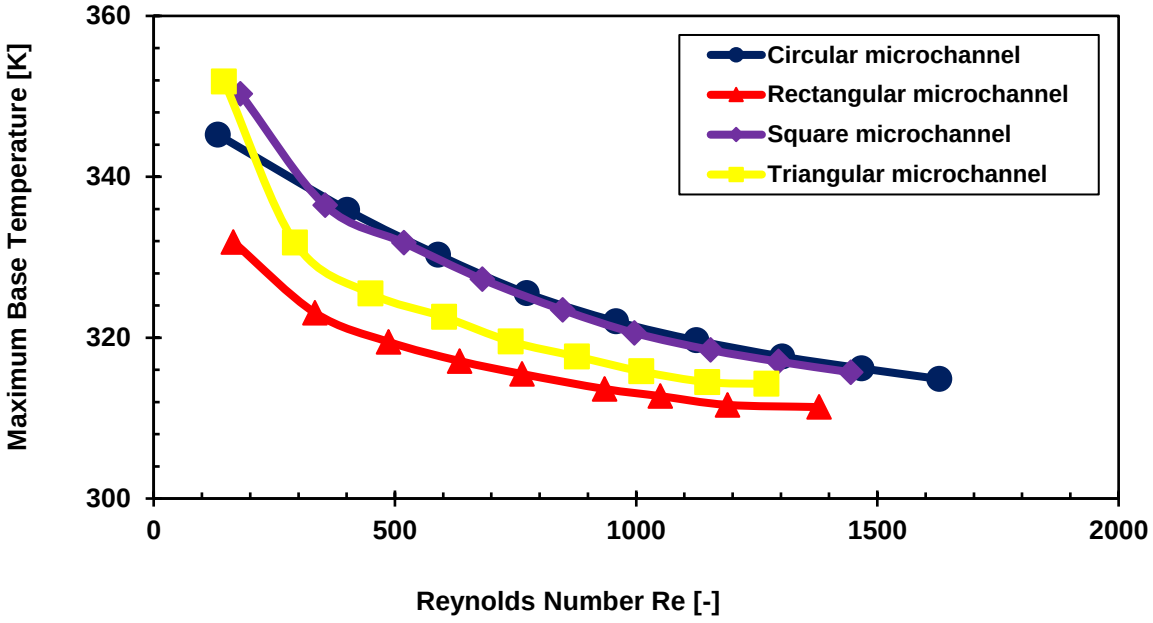

Figure 6.160. Maximum base temperatures of multichannel heat sinks at 100 W/cm^2.

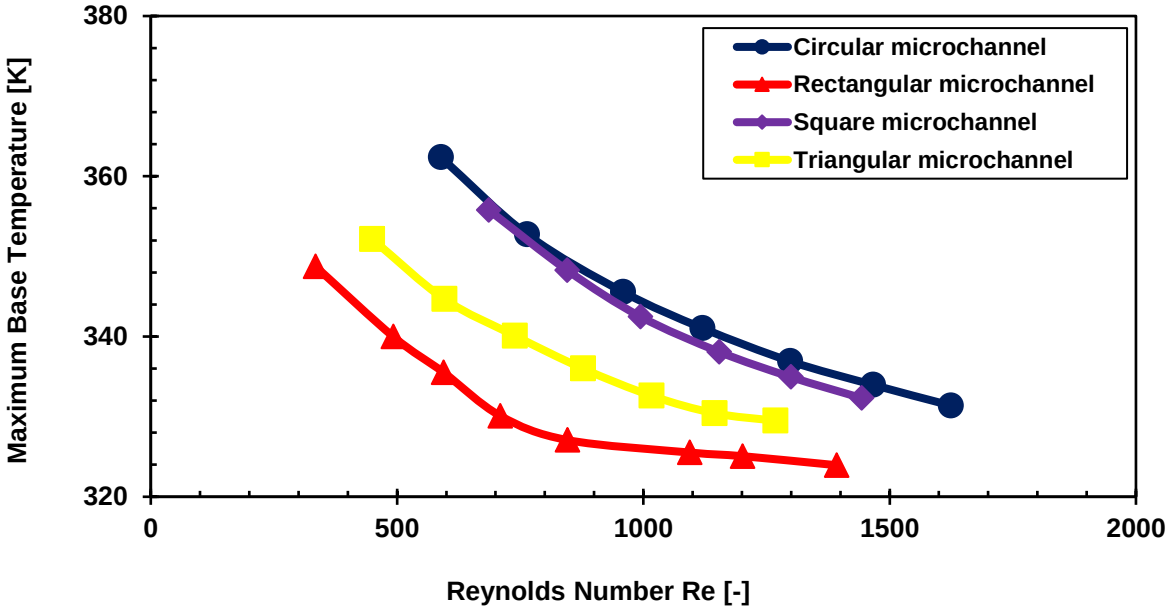

Figure 6.161. Maximum base temperatures of multichannel heat sinks at 200 W/cm^2.

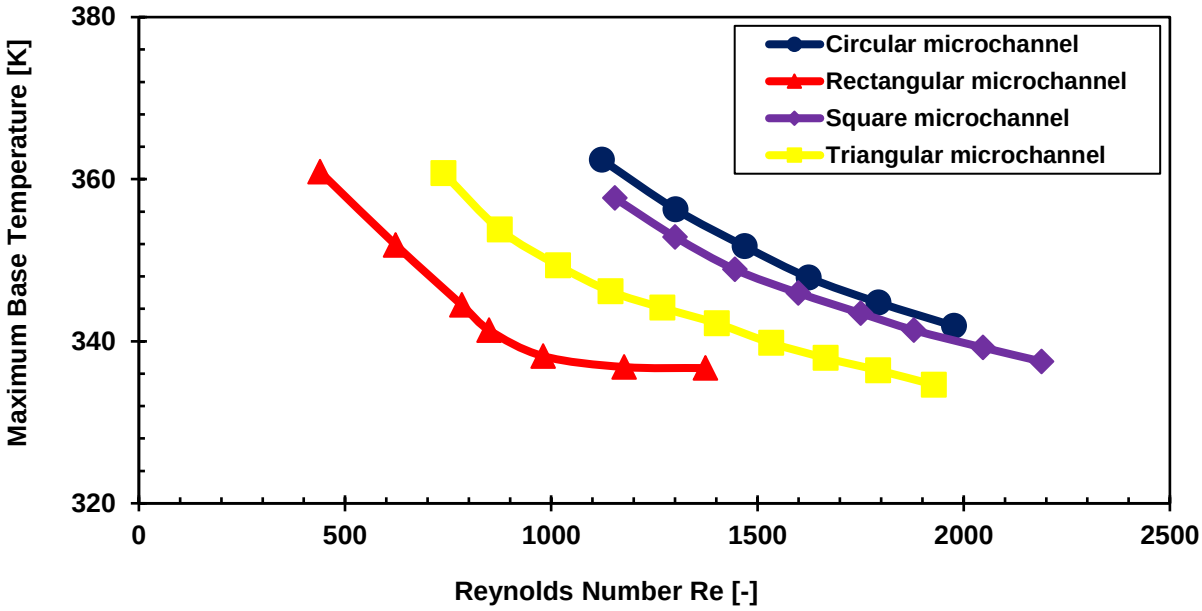

Figure 6.162. Maximum base temperatures of multichannel heat sinks at 300 W/cm^2.

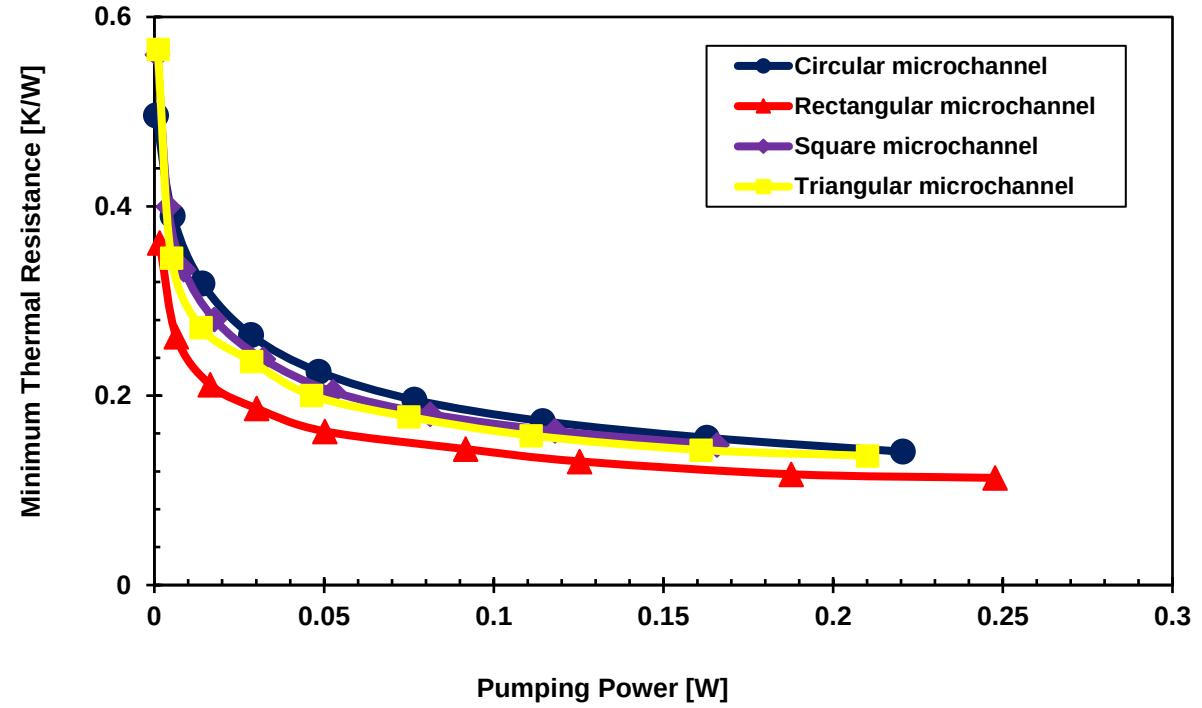

Figure 6.163. Pumping power of multichannel heat sinks at 100 W/cm^2.

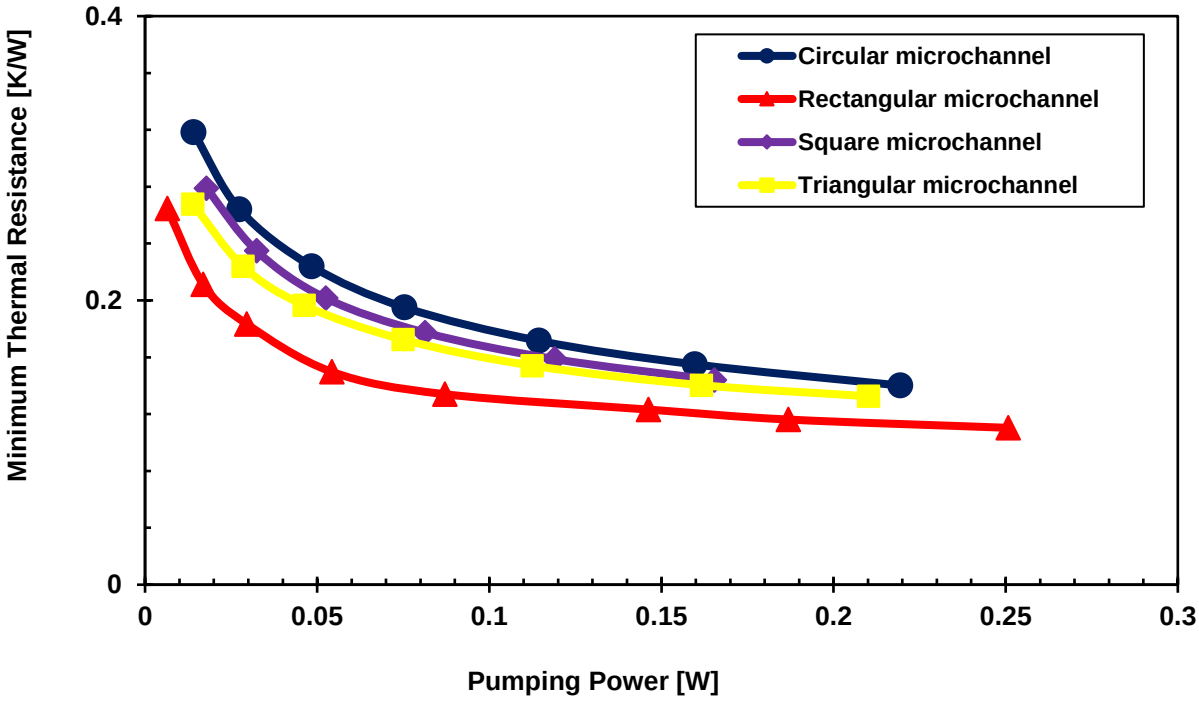

Figure 6.164. Pumping power of multichannel heat sinks at 200 W/cm^2.

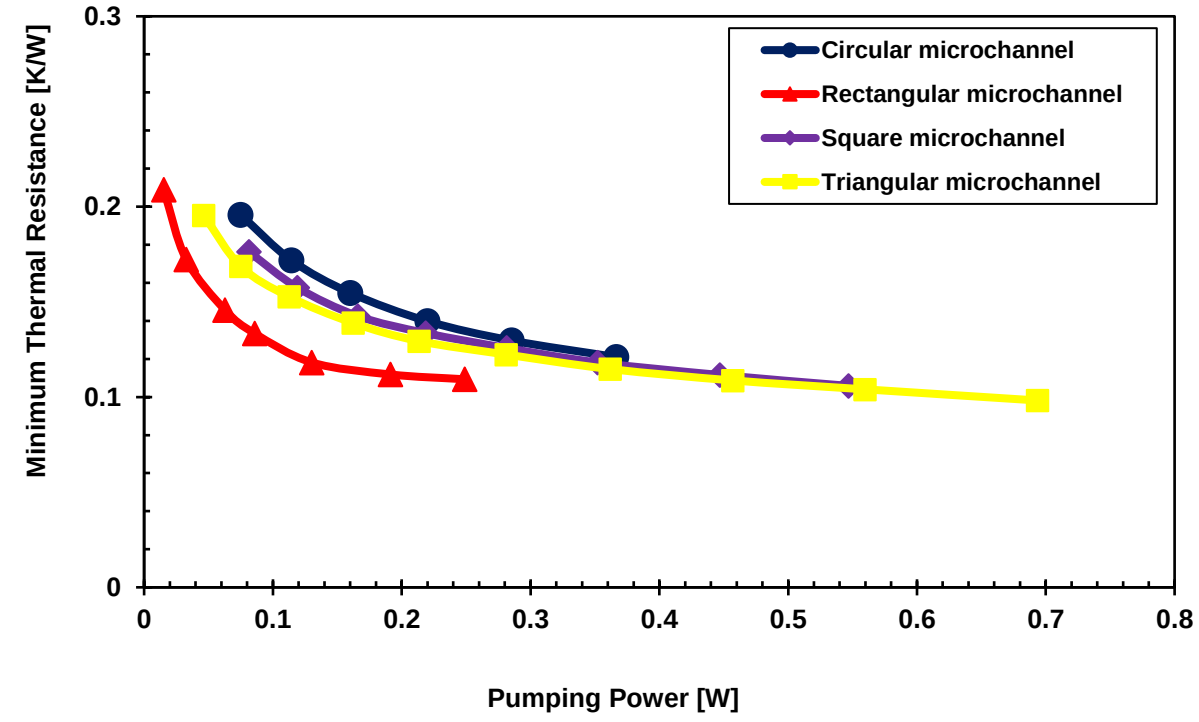

Figure 6.165. Pumping power of multichannel heat sinks at 300 W/cm^2.

6.3.2. Single-phase flow

Multichannel heat sinks were compared in single-phase flow at 100 W/cm^2 following the procedure for two-phase flow. The trend is a bit different because circular microchannel heat sinks performed better in single-phase flow than two-phase flow as shown in Figure 6.166-Figure 6.168. The thermal resistances for optimal microchannel heat sinks in two-phase flow (Figure 6.157) are better than those in single-phase flow (Figure 6.166). Similarly, the base temperatures in two-phase flow (Figure 6.160) are better than those in single-phase flow (Figure 6.167). Square microchannel heat sinks have the least thermal performance. The pumping power requirements (Figure 6.168) for these optimal microchannel heat sinks are low and comparable to those of two-phase flow (Figure 6.163).

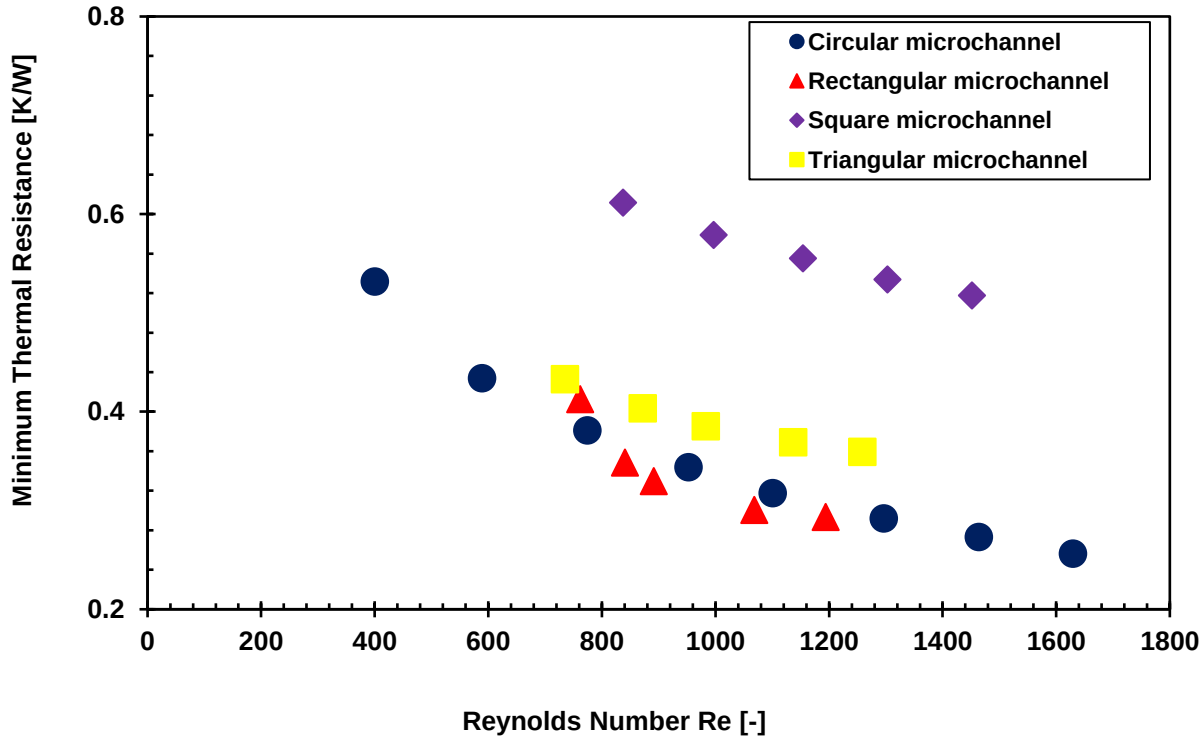

Figure 6.166. Thermal resistances of multichannel heat sinks at 100 W/cm^2.

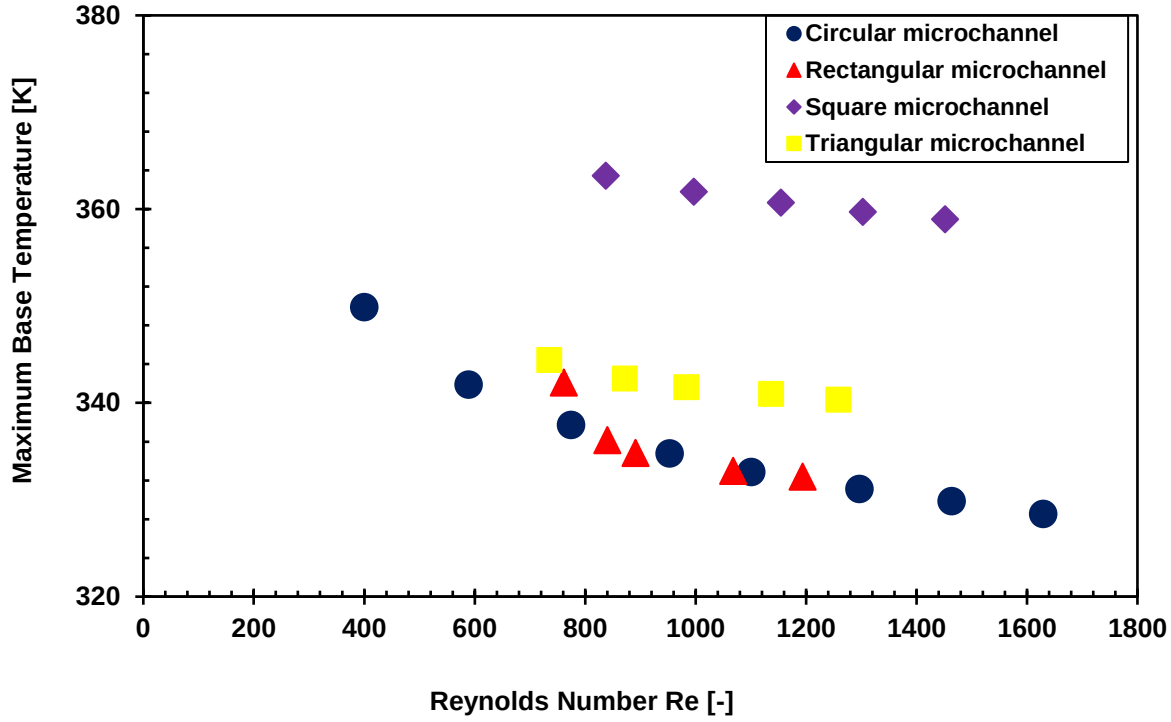

Figure 6.167. Maximum base temperatures of multichannel heat sinks at 100 W/cm^2.

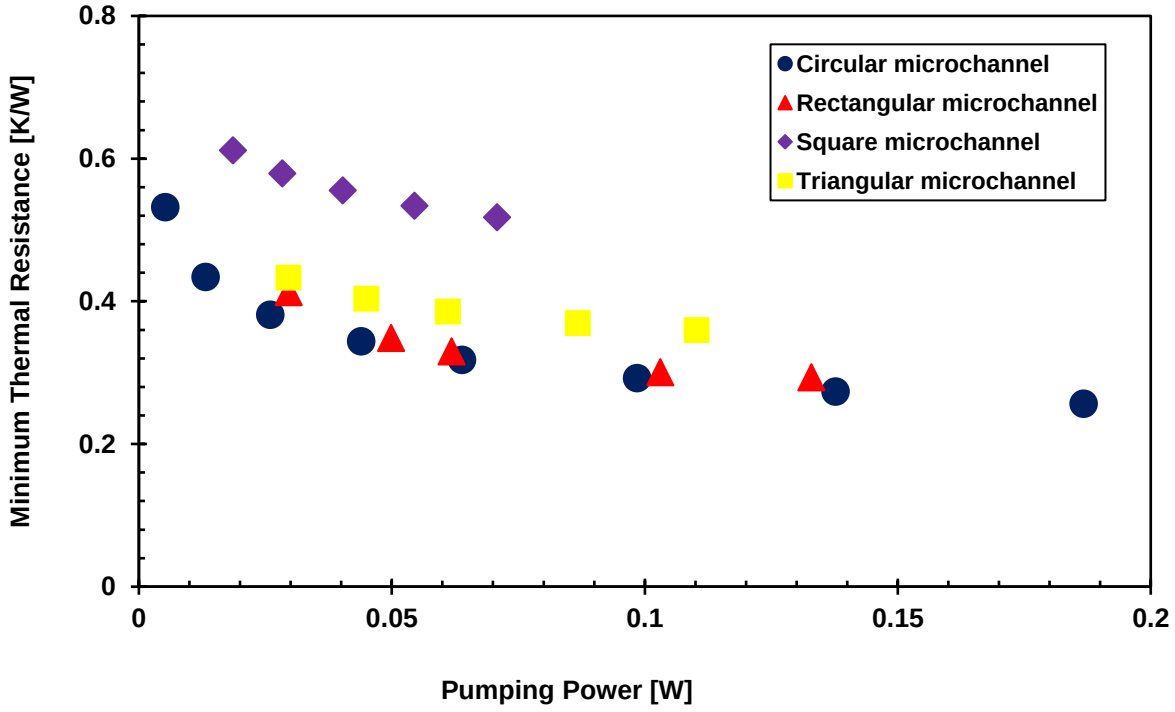

Figure 6.168. Pumping power of multichannel heat sinks at 100 W/cm^2.

6.4. High heat flux study in rectangular microchannel heat sinks (800-1200 W/cm^2)

High heat flux study was carried out in optimal rectangular microchannel heat sinks between 800 and 1200 W/cm^2. The reason for choosing rectangular microchannel heat sink being its best performance. Deionised water inlet temperature and heat sink material for Table 6.3-Table 6.8 are 283.15 K and copper respectively. An integral micro refrigeration system is inevitable because of low water inlet temperature; however, the cooling benefit could outweigh the extra cost. Apart from aluminium as heat sink material, silicon, copper and other materials had been used in the open literature. Aluminium is lightweight with lower cost and ease of manufacturing compared to copper. The thermal conductivity of silicon is less than those of aluminium and copper. Copper was used for high heat flux study because of its high thermal conductivity in order to reach the target of 1200 W/cm^2. The study was based on the number of microchannels that 1 cm width heat sink could accommodate. Table 6.3 provides optimal parameters of a unit cell heat sink at 800 W/cm^2. The multichannel heat sinks and computational domains are similar to Figure 5.1(c) and Figure 5.2(c). The number of microchannels, base temperature, thermal resistance and pumping power for the multichannel heat sink are also provided. The results are quite promising because the highest base temperature is below the maximum operating temperature of an electronic device. Table 6.4 gives information on an optimal heat sink operating at 900 W/cm^2. The thermal resistance, base temperature, pumping power and velocity are optimal just like in the case of 800 W/cm^2. Table 6.5 gives the parameters of optimal unit cell heat sink and information on multichannel heat sink at 1000 W/cm^2. The highest base temperature was 360.8008 K and this prompted the need for the innovation seen in Figure 6.169 and Figure 6.176 for 1100 and 1200 W/cm^2 because base temperatures were higher than 363.15 K.

Table 6.3. Optimal parameters of a unit cell rectangular microchannel heat sink (μm) at 800 W/cm^2.

Height of sink H_s	Width of sink W_s	Height of channel H_{ch}	Width of channel W_{ch}	Length of sink/channel L_s
852.25	321.28	587.63	170.43	12352

Note: No of microchannels = 31, $T_{b,\,max}$ = 347.1129 K, R_{th} = 0.0647, PP= 1.029 W, optimal velocity = 6.9786 m/s.

Table 6.4. Optimal parameters of a unit cell rectangular microchannel heat sink (μm) at 900 W/cm^2.

Height of sink H_s	Width of sink W_s	Height of channel H_{ch}	Width of channel W_{ch}	Length of sink/channel L_s
852.23	321.18	573.32	174.63	12356

Note: No of microchannels = 31, $T_{b,\,max}$ = 355.2238 K, R_{th} = 0.0648, PP= 1.0074 W, optimal velocity = 6.9751 m/s

Table 6.5. Optimal parameters of a unit cell rectangular microchannel heat sink (μm) at 1000 W/cm^2.

Height of sink H_s	Width of sink W_s	Height of channel H_{ch}	Width of channel W_{ch}	Length of sink/channel L_s
851.17	321.29	586.28	170.61	12367

Note: No of microchannels = 31, $T_{b,\,max}$ = 360.8008 K, R_{th} = 0.0628, PP= 1.014 W, optimal velocity = 6.9418 m/s

Counterflow and parallel flow arrangements

Figure 6.169(a) and Figure 6.169(b) give the details of counterflow and parallel flow arrangements to enhance heat removal from the electronic device attached to the bottom of the microchannels. Water enters at 283.15 K in the front of the lower microchannel and exits at the back, while water enters at 283.15 K in the upper microchannel at the back and exits in the front (Figure 6.169(a)). In the process, heat is exchanged between the lower and upper microchannel with the coolant in the lower microchannel loosing heat to the coolant in the upper microchannel. In Figure 6.169(b), the flow arrangement is parallel; water enters the lower and upper microchannels at 283.15 K in the front and exits at the back. The geometric parameters of the microchannel heat sinks are shown in Table 6.6 and Table 6.7 for 1100 and 1200 W/cm^2 respectively. Two-stacked microchannel heat sinks were obtained by stacking the single-stacked microchannel heat sinks in Table 6.6 and Table 6.7 respectively for counterflow and parallel flow analyses. Fixed volumes of microchannels and microchannel heat sinks were maintained for the two heat fluxes and flow arrangements. Figure 6.170 shows the thermal resistances of counterflow and parallel flow arrangements at 1100 W/cm^2 while Figure 6.171 and Figure 6.172 show the base temperatures and pumping power requirements also for the two arrangements. In all the comparisons, counterflow arrangement was better than parallel flow arrangement. Figure 6.173-Figure 6.175 also show similar comparisons at 1200 W/cm^2. In all the comparisons, counterflow arrangement performed better than parallel flow arrangement.

The thermal resistance for the multichannel counterflow and parallel flow arrangement is calculated the same way with Equation (3.38) for each two-stacked microchannel heat sink and N two-stacked microchannel heat sinks (Equation (6.1). Similar flow conditions were assumed in the lower and upper microchannels, hence the pumping power for a unit cell two-stacked microchannel heat sink can be expressed as:

$$PP = 2.u_{in}.A_{ch}.\Delta P \tag{6.3}$$

For N two-stacked microchannels,

$$PP = 2.N.u_{in}.A_{ch}.\Delta P \tag{6.4}$$

The ratio of two-stacked microchannel volume to total volume of heat sink is defined as

$$\frac{V_{ch,t}}{V_s} \tag{6.5}$$

where $V_{ch,t}$ and V_s are the volumes of two microchannels and heat sink respectively. This ratio is approximately 0.42 for both flow arrangements at 1100 and 1200 W/cm^2. The optimal values could change if this ratio is varied. The total height of heat sink was maintained at 1483 μm after stacking while other parameters remained unchanged. The volumes of microchannel and microchannel heat sink were fixed and the same for both flow arrangements.

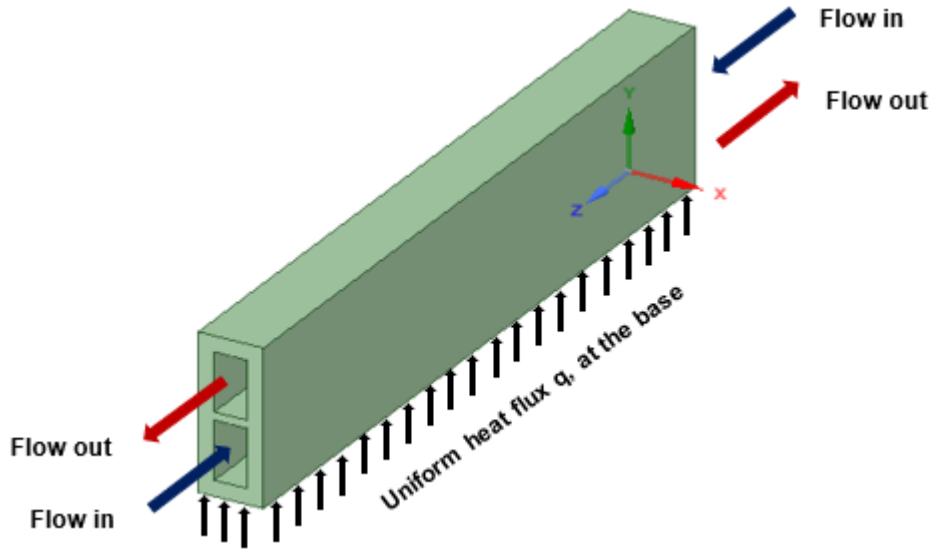

(a) Counterflow arrangement

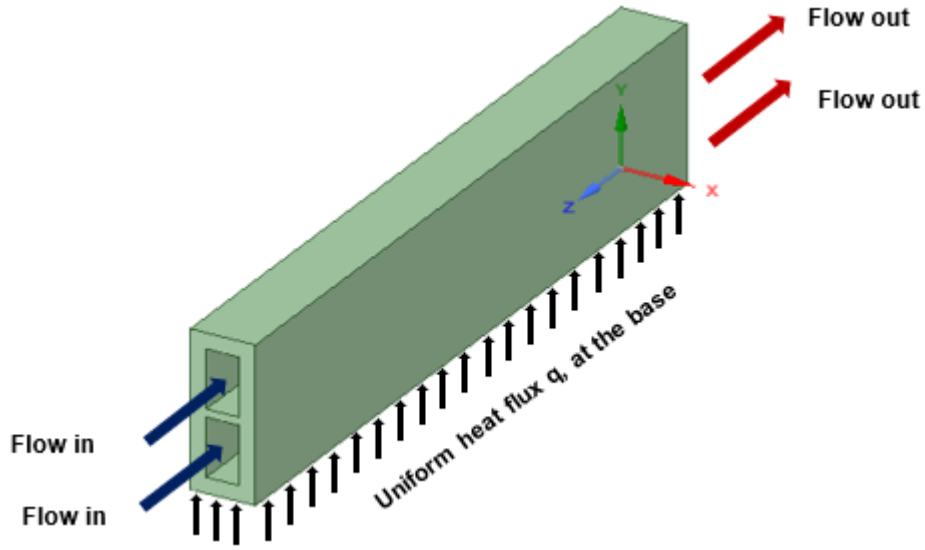

(b) Parallel flow arrangement

Figure 6.169. Two-stacked microchannel heat sinks.

Table 6.6. Optimal parameters of a unit cell rectangular microchannel heat sink (μm) at 1100 W/cm^2 (two-stacked counterflow and parallel flow arrangements).

Height of sink	Width of sink	Height of channel	Width of channel	Length of sink/channel
H_s	W_s	H_{ch}	W_{ch}	L_s
852.13	321.17	586.62	170.64	12358

Note: No of two-stacked microchannels = 31

Table 6.7. Optimal parameters of a unit cell rectangular microchannel heat sink (μm) at 1200 W/cm^2 (two-stacked counterflow and parallel flow arrangements).

Height of sink	Width of sink	Height of channel	Width of channel	Length of sink/channel
H_s	W_s	H_{ch}	W_{ch}	L_s
852.23	321.18	586.1	170.82	12356

Note: No of two-stacked microchannels = 31

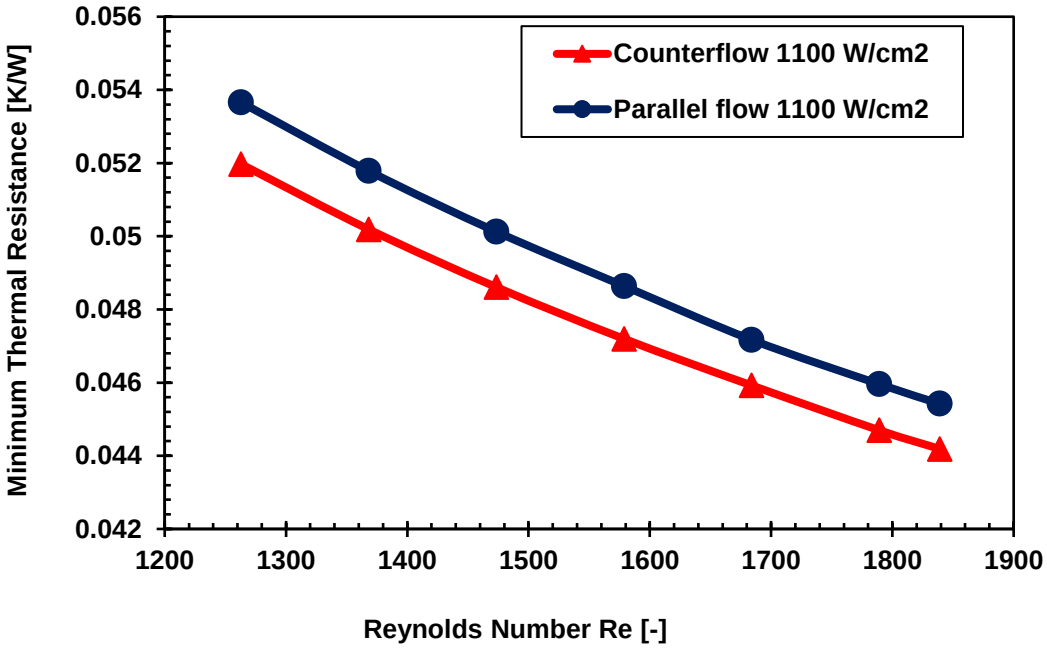

Figure 6.170. Thermal resistances of two-stacked multichannel heat sinks at 1100 W/cm^2.

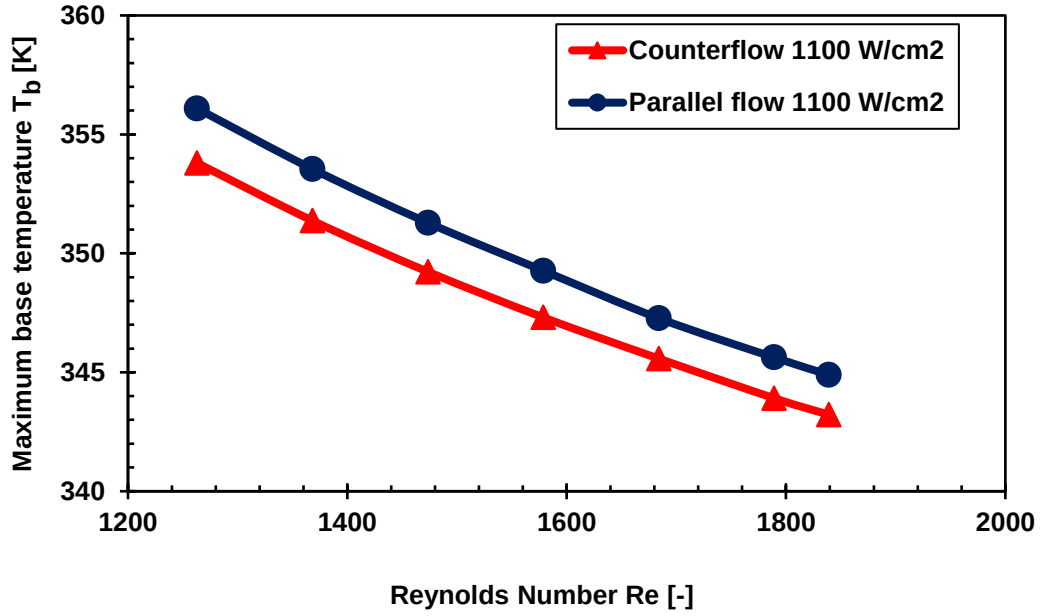

Figure 6.171. Maximum base temperatures of two-stacked multichannel heat sinks at 1100 W/cm^2.

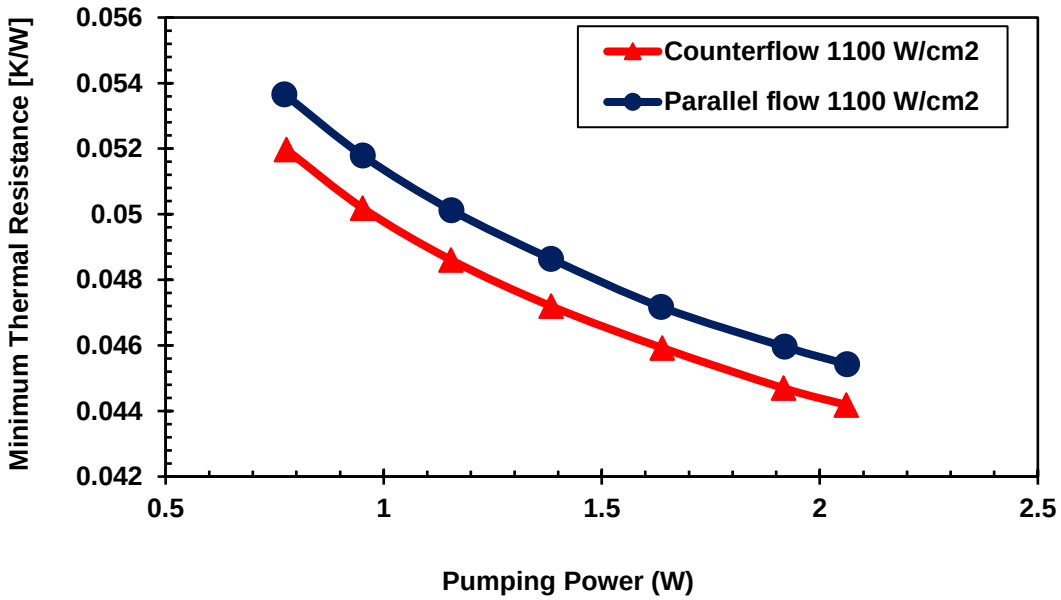

Figure 6.172. Pumping power of two-stacked multichannel heat sinks at 1100 W/cm^2.

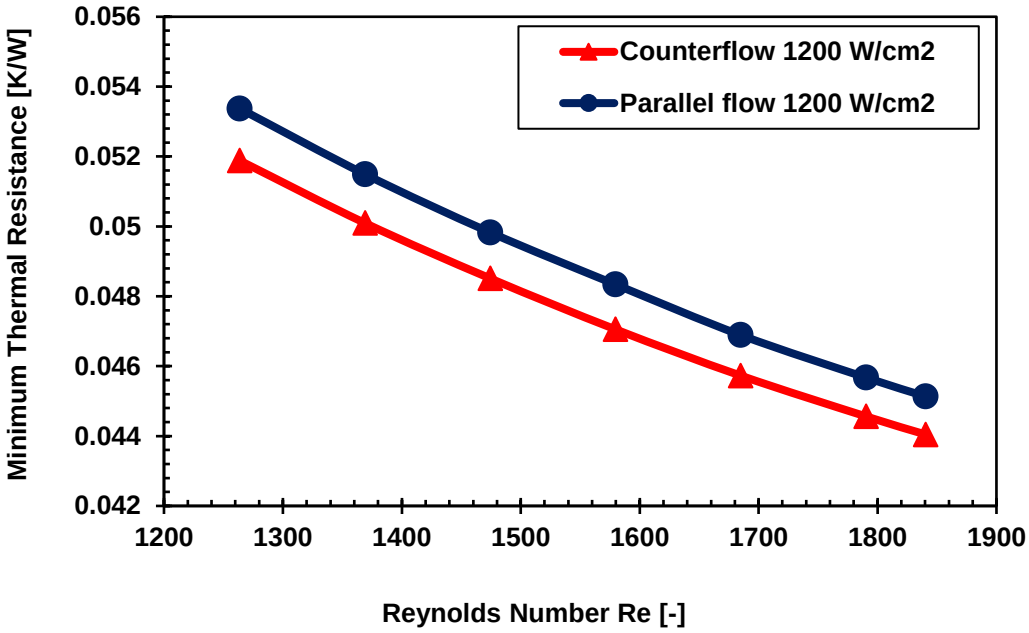

Figure 6.173. Thermal resistances of two-stacked multichannel heat sinks at 1200 W/cm^2.

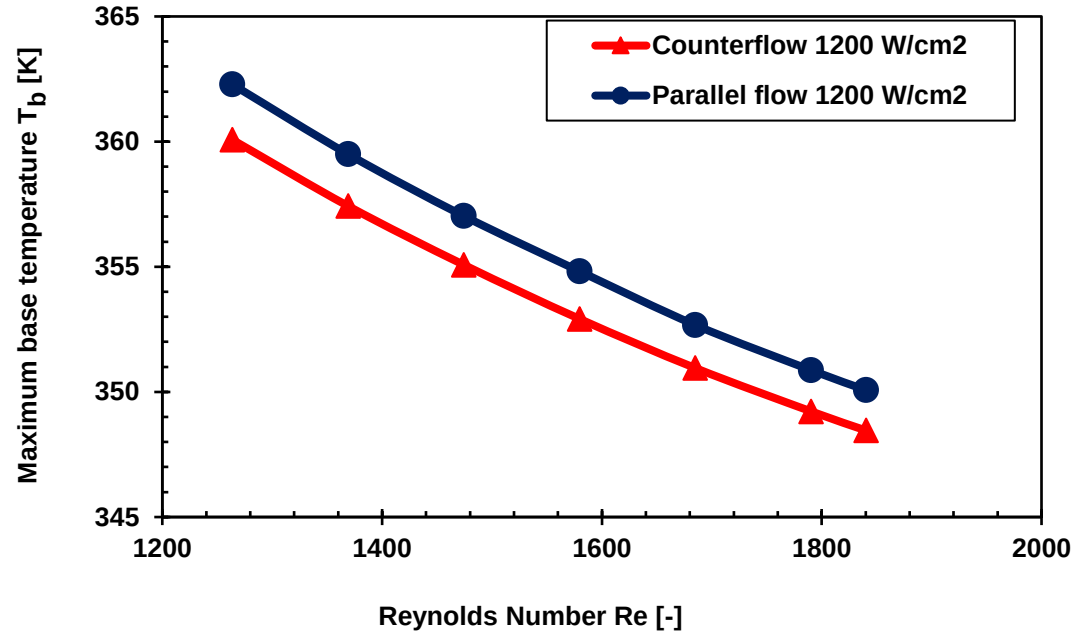

Figure 6.174. Maximum base temperatures of two-stacked multichannel heat sinks at 1200 W/cm^2.

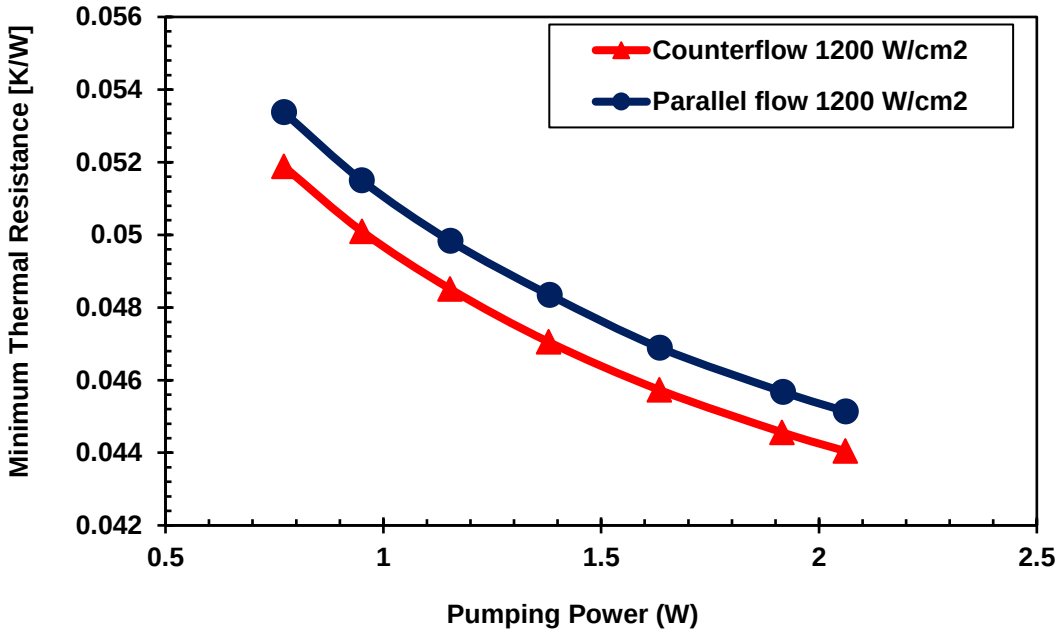

Figure 6.175. Pumping power of two-stacked multichannel heat sinks at 1200 W/cm^2.

Another innovation to the study was the use of single row v-grooved microchannel for 1200 W/cm^2. Three and two gooves were tried initially, the base temperaures were more than when one groove was used. Therefore one groove which spanned the whole length of the microchannel was used as shown in Figure 6.176(a). Coolant flow-in and flow-out with the source of heat from the elctronic device at the base of the heat sink are shown in the figure. Figure 6.176(b) shows the front view of the heat sink with v-groove in the microchannel. Table 6.8 provides the results for v-grooved and plain microchannels of the same dimensions. The base temperature recorded for the v-grooved microchannel was 365.2728 K which is slightly above the maximum expected for an electronic device. However, there is room for improvement because the groove angle and width can be varied. The plain microchannel recorded a base temperature of 373.941 K which is indicative of the fact that v-grooved microchannel could be an area of research.

The ratio of v-grooved microchannel to plain microchannel is calculated as

$$\frac{V_{ch}+V_{vg}}{V_{ch}} \tag{6.6}$$

where V_{ch} and V_{vg} are volumes of microchannel and v-groove respectively. The ratio for this particular design is 1.00079. This ratio could be varied to obtain different results.

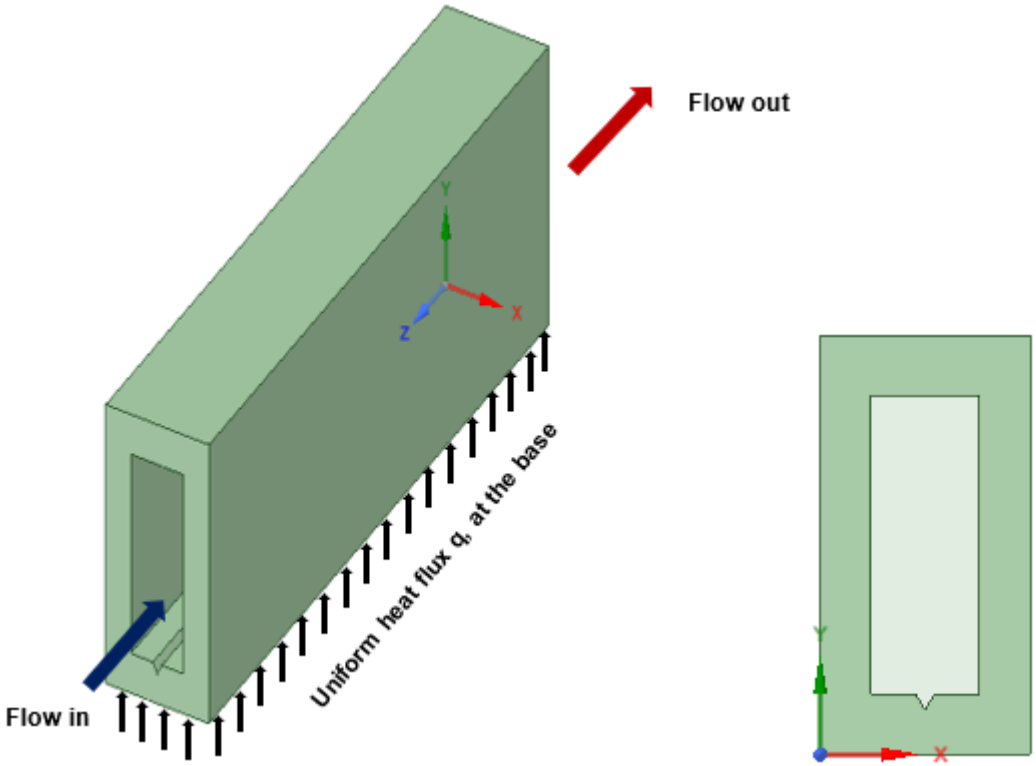

(a) unit cell v-grooved microchannel heat sink (b) Front view

Figure 6.176. V-grooved microchannel heat sink.

Table 6.8. Optimal parameters of a unit cell rectangular microchannel heat sink (μm) at 1200 W/cm^2 (Single-row v-grooved microchannel, groove angle = 60°, sides = 15 μm).

Height of sink H_s	Width of sink W_s	Height of channel H_{ch}	Width of channel W_{ch}	Length of sink/channel L_s
897.23	376.93	675.02	183.26	10000

Note: No of microchannels = 27

V-grooved microchannel: $T_{b,\,max}$ = 365.2728 K, R_{th} = 0.0684, PP= 1.0255 W,

optimal velocity = 6.9935 m/s

Plain microchannel: $T_{b,\,max}$ = 373.941 K, R_{th} = 0.0757, PP= 0.8101 W, optimal velocity = 6.9935 m/s

6.5. Critical heat flux study in optimal microchannel configurations

Critical heat flux (CHF) is the highest heat flux for the safe operation of microchannel heat sinks. It is a situation where liquid in contact with the inner wall of the microchannel heat sink is replaced by a vapour blanket, which is a phenomenon similar to that of macroscale critical heat flux. Occurrence of CHF may be witnessed in subcooled and saturated flow boiling situations [147]. Heat transfer rate is reduced because the thermal conductivity of vapour is considerably low compared to that of liquid. This leads to a drastic reduction in surface heat transfer coefficient which culminates in instantaneous increase of the surface temperature and probability of destroying the device being cooled. The bulk liquid temperature is subcooled and the thermodynamic equilibrium vapour quality at the exit of the microchannel is less than zero in subcooled CHF while in saturated flow boiling CHF, the thermodynamic equilibrium vapour quality at the exit of the microchannel is greater or equal to zero [108].

Optimal microchannel heat sinks at 100 W/cm^2 and velocities from 2.0-2.5 to 3.5-4.0 m/s were used for the critical heat flux study. Critical heat flux study in two-phase flow is important because it is the upper thermal limit of operation of a microchannel heat sink. Beyond critical heat flux, temperature rises sharply leading to the destruction of the microchannel heat sink and the device being cooled. It is important to operate the heat sink below CHF to protect it and the device being cooled. Maximum wall temperatures at the exits of optimal microchannel heat sinks were used in the computations.

Figure 6.177 shows critical heat fluxes for the heat sinks with different microchannel configurations operating in the velocity range of 2.0-2.5 m/s. The CHF for the optimal rectangular heat sink is shown in the figure as 1000 W/cm^2 approximately. Critical heat fluxes for other microchannel heat sinks can also be located at or close to their turning points. Circular and square microchannel heat sinks had the least critical heat flux performance which is also shown in the figure.

Microchannel heat sinks operating in the velocity range of 2.5-3.0 m/s and with different critical heat fluxes are shown in Figure 6.178 with rectangular microchannel heat sink having the highest critical heat flux performance followed by equilateral triangular microchannel heat sink. The trend is the same in Figure 6.179 and Figure 6.180. In all the figures, it can be observed that as the velocity increases, CHF increases.

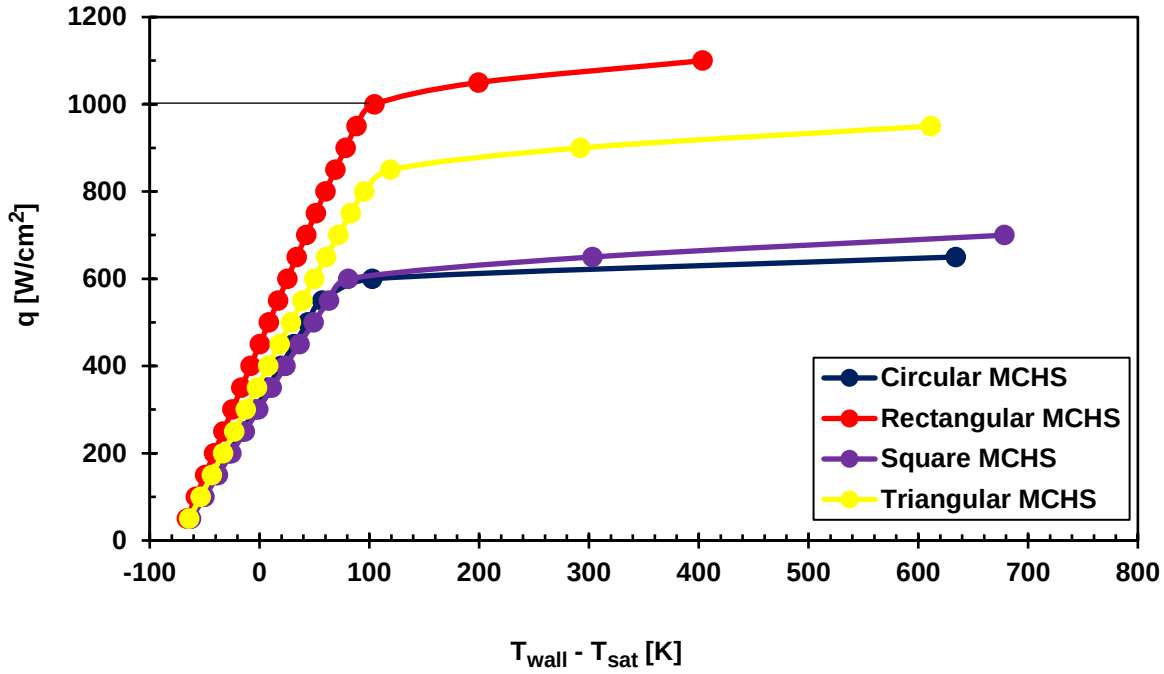

Figure 6.177. Critical heat flux at optimal velocity range of 2.0-2.5 m/s.

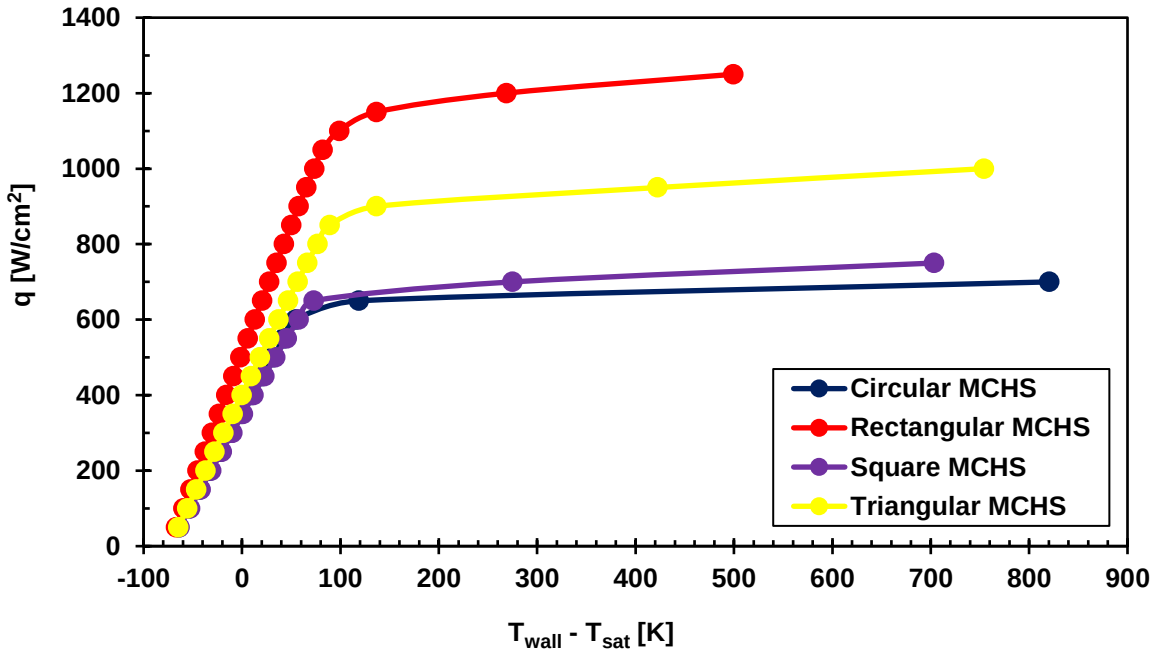

Figure 6.178. Critical heat flux at optimal velocity range of 2.5-3.0 m/s.

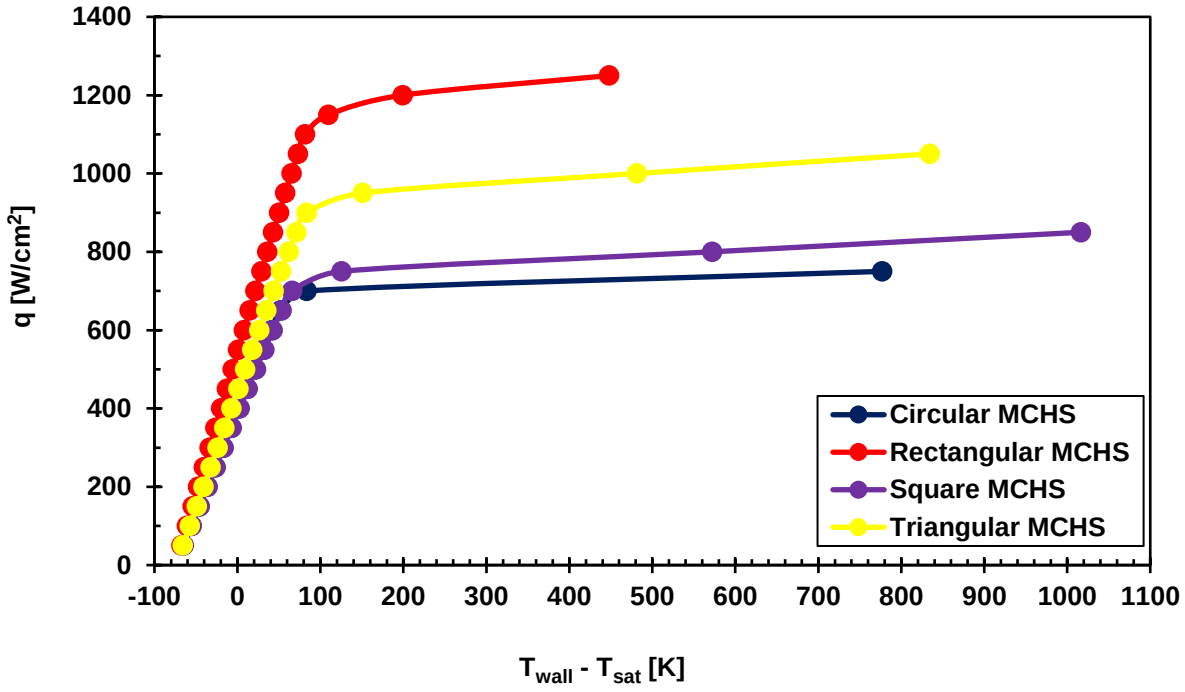

Figure 6.179. Critical heat flux at optimal velocity range of 3.0-3.5 m/s.

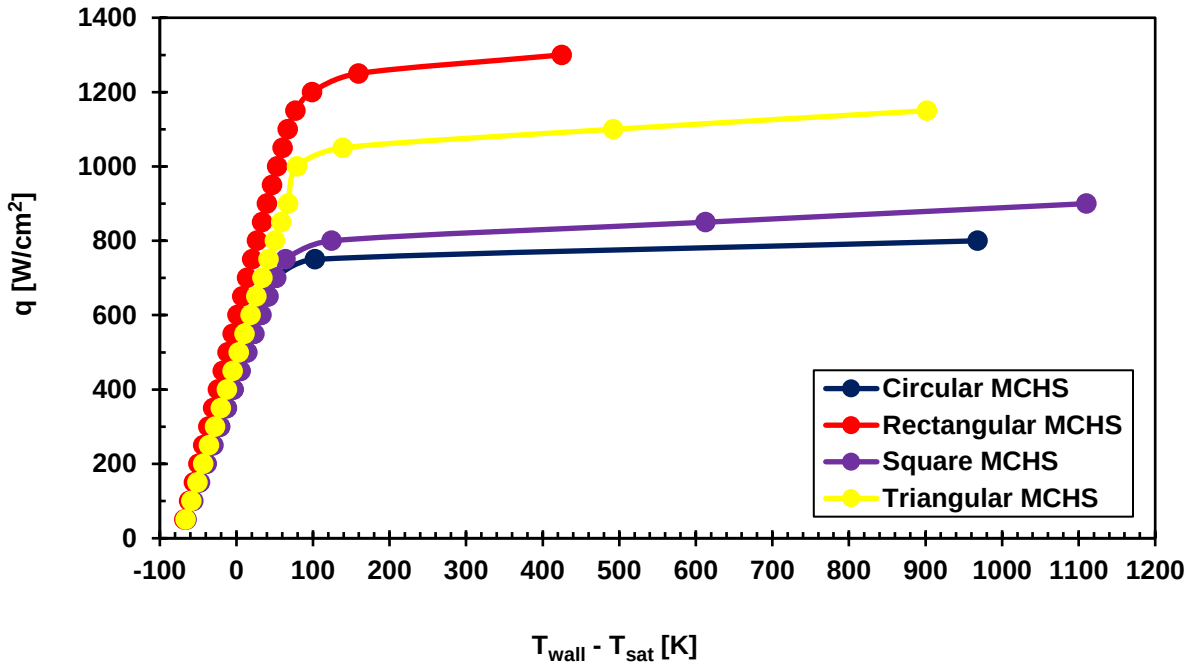

Figure 6.180. Critical heat flux at optimal velocity range of 3.5-4.0 m/s.

CHAPTER 7
CONTRIBUTIONS OF THE STUDY, CONCLUSIONS AND RECOMMENDATIONS

7.1. Contributions of the study

1. Numerical analyses and optimisations were done to obtain microchannel heat sinks that performed optimally at high heat fluxes not familiarly reported for similar geometric parameters in the open literature. The study shows the effects of optimal geometric and flow parameters on thermal performances of optimal microchannel heat sinks in subcooled flow boiling and single-phase flow. The optimal designs were reliable for all the heat fluxes considered because due attention was paid to simulation and optimisation procedures for each of the microchannel configurations. The geometric and flow parameters had their optimal values for each velocity range and heat flux.

2. optimal multichannel heat sink analysis provided in this study gives the opportunity for possible practical applications in electronic cooling and other areas.

3. Simulations and optimisations were carried out for two-phase flow up to 1000 W/cm^2 in one-stacked (single-layered) plain rectangular microchannel heat sinks (no heat transfer enhancements) while for 1100 and 1200 W/cm^2, two-stacked (double-layered) microchannel heat sinks were used and additionally a new concept of v-grooved microchannel heat sink was introduced and used at 1200 W/cm^2. Optimal microchannel heat sinks were obtained for one-stacked plain circular, equilateral triangular and square microchannel heat sinks up to 400, 500 and 400 W/cm^2 respectively without heat transfer enhancements. In Single-phase flow, optimal one-stacked plain microchannel heat sinks were obtained for circular, equilateral, rectangular and square microchannel heat sinks up to 200, 100, 200 and 100 W/cm^2 respectively.

4. Wall heat flux partitioning (RPI) model was used for the optimisations, and the results were used in the extension of the model (non-equilibrium subcooled model) to predict the critical heat fluxes when optimal microchannel heat sinks were operated beyond the heat flux (100 W/cm^2 used in the study) for which they had been optimised.

7.2. Conclusions

The optimal geometric parameters were obtained from the simulations and optimisations for the four microchannel heat sink configurations. Wall heat flux partitioning (RPI) model was used to predict the experimental data of Qu and Mudawar [154] and the numerical results were in good agreement with the experimental data. The extension of wall heat partitioning model (non-equilibrium subcooled boiling model) was used for the critical heat flux study to determine the maximum operating limits of optimal microchannel heat sink configurations. Single-phase flow validation was done and the agreement between the numerical and experimental data of Tuckerman and Pease [8] was good.

The optimal thermal resistance and base temperature curves together with the temperature contours provided in this study showed that the thermal characteristics of optimal microchannel heat sinks were good in single-phase flow and better in subcooled flow boiling even at high heat fluxes. Thermal resistances, base temperatures, pumping power, geometric and flow parameters of optimal microchannel heat sinks were compared in two-phase flow (subcooled flow boiling) and single-phase flow. The performances in two-phase flow outweighed those in single-phase flow. Two-phase cooling was superior to single-phase cooling in the optimal microchannel heat sinks and higher pressure drops in two-phase flow cannot be compared with the cooling advantage achieved. This is consistent with the experimental data of Qu and Mudawar [154].

Rectangular microchannel heat sinks had the best overall performance and this study was able to obtain good performances up to 1200 W/cm^2 not reported before in the open literature, for optimal rectangular microchannel heat sinks with similar parameters. The v-grooved microchannel heat sink could be a promising area of study; hence due attention is required to explore its heat transfer enhancement potential. Instabilities are a big problem in two-phase flow, the effects that two-stacked (double-layered) microchannel could have to alleviate static and dynamic instabilities were not studied, therefore these could be given the deserved attention.

Eulerian multiphase model in conjunction with wall heat flux partitioning model (RPI) was used for the simulations without exceeding bubbly flow. Response surface method, a goal driven optimisation was used to obtain optimal geometric and flow parameters. The simulation and optimisation procedures were carried out for circular, equilateral triangular, rectangular

and square microchannel heat sinks; the same procedures can be repeated for other microchannel configurations.

The microchannel heat sinks are deemed stable because their geometric and flow parameters are optimal. The thermal resistances, pumping power requirements and base temperatures for the optimal microchannels in two-phase and single-phase flow are considered adequate and could be useful in practical applications.

Critical heat flux simulations were carried out to obtain critical heat fluxes corresponding to wall superheats (Figure 6.177-Figure 6.180). The temperature contours provide information on the temperature distribution at selected locations in the microchannels. The highest wall temperatures of the microchannel heat sinks which occurred at their outlets were used in the computations of CHF and this approach makes the results more reliable. Simulations were done up to CHF for the selected microchannel heat sinks to distinguish between optimal performance and maximum limit of operation. It is advisable to use the microchannel heat sinks at their optimal values for best performance. They could be used off their optimal values as long as their base temperatures do not exceed the maximum for modern electronic devices.

Different global optimal geometric and flow parameters were produced from the optimisations; hence these could affect the response of optimal microchannel heat sinks to critical heat fluxes when used in the critical heat flux simulations. It is worth mentioning that different optimal velocities were obtained for the velocity ranges considered and these were used correspondingly for the CHF simulations. Sharp temperature rise occurred after critical heat flux; this is consistent with the literature.

7.3 Recommendations for future studies

The simulations and optimisations were done to obtain optimal horizontal microchannel heat sinks of circular, equilateral triangular, rectangular and square configurations; the same method could be employed to other microchannel heat sink configurations.

All the geometric parameters were allowed to vary while the volumes of microchannels and heat sinks were kept constant in this study. Future studies could fix most of the parameters and allow one or two parameters to vary at a time while maintaining fix volume constraints for the

microchannels and heat sinks over a wide range of heat fluxes and velocities to obtain optimal values for the parameters being varied and consequently optimal microchannel heat sinks.

V-grooved and two-stacked microchannels are recommended for future studies especially in two-phase flow to explore the possibility of using them to solve the problems of static and dynamic instabilities especially when microchannels are operating off the optimal values. Improvements in other areas of microchannel heat sink study with the aforementioned microchannel heat sinks can also be looked into.

REFERENCES

[1] J. F. Tullius, R. Vajtai, Y. Bayazitoglu, A Review of Cooling in Microchannels, Heat Transfer Engineering 32(7-8) (2011) 527-541 DOI: 10.1080/01457632.2010.506390.

[2] S.M.S. Murshed, C.A. Nieto de Castro, A critical review of traditional and emerging techniques and fluids for electronics cooling, Renewable and Sustainable Energy Reviews 78 (2017) 821-833 https://doi.org/10.1016/j.rser.2017.04.112.

[3] M. Pedram, S. Nazarian, Thermal modelling, analysis, and management in VLSI Circuits: principles and methods, Proceedings of the IEEE 94(8) (2006)1487-1501 DOI**:** 10.1109/JPROC.2006.879797.

[4] S. S. Anandan, V. Ramalingam, Thermal management of electronics: A Review of literature, Thermal Science 12(2) (2008) 5-26 DOI: 10.2298/TSCI0802005A.

[5] C.S. Sharma, S. Zimmermann, M.K. Tiwaria, B. Michel, D. Poulikakos, Optimal thermal operation of liquid-cooled electronic chips, International Journal of Heat and Mass Transfer 55 (2012) 1957-1969 doi:10.1016/j.ijheatmasstransfer.2011.11.052.

[6] J.R. Thome, E. Costa-Patry, Two-phase flow boiling in microchannels for cooling of microelectronics, 8th International Conference on Heat Transfer, Fluid Mechanics and Thermodynamics (HEFAT 2011) 11-13 July 2011, Pointe Aux Piments, Mauritius http://hdl.handle.net/2263/40510.

[7] T.G. Karayiannis, M.M. Mahmoud, Flow boiling in microchannels: Fundamentals and applications, Applied Thermal Engineering 115 (2017) 1372–1397 https://doi.org/10.1016/j.applthermaleng.2016.08.063.

[8] D.B. Tuckerman, R.F.W. Pease, High-performance heat sink for VLSI, IEEE Electron Device Letters 2 (5) (1981) 126-129 DOI: 10.1109/EDL.1981.25367.

[9] S.G. Kandlikar, High flux heat removal with microchannels-A roadmap of challenges and opportunities, Heat Transfer Engineering 26(8) (2005) 5-14 DOI:10.1080/01457630591003655.

[10] C. Gilliot, C. Schaffer, A. Bricard, Integrated micro heat sink for power multichip module, IEEE Transactions of Industrial Applications 36(1) (2000) 217-221 DOI: 10.1109/28.821819.

[11] R.J. Philips, Microchannel heat sink, Lincoln Laboratory Journal 1(1) (1988) 31-48.

[12] M. Avelino, S. Kakaç, Convective heat transfer in microchannels, A Review, Proceedings of the 10th Brazilian Congress of Thermal Sciences and Engineering,

Brazillian Society of Mechanical Sciences and Engineering, ABCM, Rio de Janeiro, Brazil, ENCIT 2004, (Nov. 29-Dec. 03, 2004).

[13] C. Nonino, S. Savino, S. Del Giudice, L. Mansutti, Conjugate forced convection and heat conduction in circular microchannels, International Journal of Heat and Fluid Flow 30 (5) (2009) 823-830 https://doi.org/10.1016/j.ijheatfluidflow.2009.03.009.

[14] W. Owhaib, B Palm, Experimental investigation of single-phase convective heat transfer in circular microchannels, Experimental Thermal and Fluid Science 28 (2004) 105-110 https://doi.org/10.1016/S0894-1777(03)00028-1.

[15] T. M. Bandhauer, A. Agarwal, S. Garimella, Measurement and modelling of condensation heat transfer coefficients in circular microchannels, Journal of Heat Transfer 128 (10) (2006) 1050-1059 https://doi.org/10.1115/1.2345427.

[16] D. C. Knupp, F.S. Mascouto, L.A.S. Abreu, C.P. Naveira-Cotta, R.M. Cotta, Conjugated heat transfer in circular microchannels with slip flow and axial diffusion effects, International Communications in Heat and Mass Transfer 91 (2018) 225-233 https://doi.org/10.1016/j.icheatmasstransfer.2017.12.003.

[17] S. Khodaparast, N. Borhani, J. R. Thome, Sudden expansions in circular microchannels: flow dynamics and pressure drop, Microfluid Nanofluid 17 (2014) 561-572 DOI 10.1007/s10404-013-1321-7.

[18] J. Yan, Q. Bi, L. Cai, G. Zhu, Q. Yuan, Subcooled flow boiling heat transfer of water in circular tubes with twisted-tape inserts under high heat fluxes, Experimental Thermal and Fluid Science 68 (2015) 11-21.

[19] J. Judy, D. Maynes, B.W. Webb, Characterization of frictional pressure drop for liquid flows through microchannels, International Journal of Heat and Mass Transfer 45 (2002) 3477-3489 https://doi.org/10.1016/S0017-9310(02)00076-5.

[20] V. Talimi, Y.S. Muzychka, S. Kocabiyik, Slug flow heat transfer in square microchannels, International Journal of Heat and Mass Transfer 62 (2013) 752-760 https://doi.org/10.1016/j.ijheatmasstransfer.2013.03.035.

[21] A. Ferrari, M. Magnini, J. R. Thome, Numerical analysis of slug flow boiling in square microchannels, International Journal of Heat and Mass Transfer 123 (2018) 928-944 https://doi.org/10.1016/j.ijheatmasstransfer.2018.03.012.

[22] J. Guo, M. Xu, J. Cai, X. Huai, Viscous dissipation effect on entropy generation in curved square microchannels, Energy 36 (8) (2011) 5416-5423 https://doi.org/10.1016/j.energy.2011.06.060.

[23] A. Bordbar, R. Kamali, A. Taassob, Thermal performance analysis of slug flow in square microchannels, Heat Transfer Engineering 41(1) (2020) 84-100 DOI:10.1080/01457632.2018.1513630.

[24] H.A. Mohammed, P. Gunnasegaran, N.H. Shuaib, The impact of various nanofluid types on triangular microchannels heat sink cooling performance, International Communications in Heat and Mass Transfer 38 (6) (2011) 767-773 https://doi.org/10.1016/j.icheatmasstransfer.2011.03.024.

[25] O. Rezaei, O. A. Akbari, A. Marzban, D. Toghraie, F. Pourfattah, R. Mashayekhi, The numerical investigation of heat transfer and pressure drop of turbulent flow in a triangular microchannel, Physica E 93 (2017) 179-189 https://doi.org/10.1016/j.physe.2017.06.013.

[26] M. Niklas, M. Favre-Marinet, An Experimental study and numerical modelling of the flow in a network of triangular microchannels, Heat Transfer Engineering 26(8) (2005) 15-23 DOI: 10.1080/01457630591003673.

[27] M. Mardani, M. R. Salimpour, Optimization of triangular microchannel heat sinks using constructal theory, Journal of Mechanical Science and Technology 30 (10) (2016) 4757-4764 DOI:10.1007/s12206-016-0947-2.

[28] J. P. McHale, S. V. Garimella, Heat transfer in trapezoidal microchannels of various aspect ratios, International Journal of Heat and Mass Transfer 53 (2010) 365-375 https://doi.org/10.1016/j.ijheatmasstransfer.2009.09.020.

[29] L. Chai, G. Xia, J. Qi, Experimental and numerical study of flow and heat transfer in trapezoidal microchannels, Heat Transfer Engineering 33(11) (2012) 972-981 DOI: 10.1080/01457632.2012.654731.

[30] H. Wang, Z. Chen, J. Gao, Influence of geometric parameters on flow and heat transfer performance of micro-channel heat sinks, Applied Thermal Engineering 107 (2016) 870-879 https://doi.org/10.1016/j.applthermaleng.2016.07.039.

[31] G.E. Moore, Cramming more components onto integrated circuits, Electronics 38(8) (1965) 114-117 DOI: S 0018-9219(98)00753-1(Reprinted).

[32] B. Agostini, J. R. Thome, M. Fabbri, B. Michel, D. Calmi, U. Kloter, High heat flux flow boiling in silicon multi-microchannels-Part I: Heat transfer characteristics of refrigerant R236fa, International Journal of Heat and Mass Transfer 51(21-22) (2008) 5400-5414 https://doi.org/10.1016/j.ijheatmasstransfer.2008.03.006.

[33] J.R. Thome, State-of-the-art overview of boiling and two-phase flows in microchannels, Heat Transfer Engineering 27(9) (2006) 4-19 DOI: 10.1080/01457630600845481.

[34] G. Xu, B. Guenin, M. Vogel, Extension of air cooling for high power processors**,** IEEE Inter Society Conference on Thermal Phenomena 1 (2004) 186-193 DOI:10.1109/ITHERM.2004.1319172.

[35] M. Saini, R.L. Webb, Heat rejection limits of air-cooled plane fin heat sinks for computer cooling, IEEE Transaction Component Package Technology 26(1) (2003) 71-79.

[36] L. Zhang, Phase change phenomena in silicon microchannel heat sink for IC chip cooling, PhD thesis in the Department of Mechanical Engineering (2002) Stanford University.

[37] T. Saenen, Modelling a two-phase microchannel electronics cooling system, PhD Thesis, Faculty of Engineering Celestijnenlaan, Katholieke Universiteit (2013), Heverlee, Belgium.

[38] M.J. Ellsworth Jr., High powered chip cooling-air and beyond, Electronics Cooling 11(3) (2005) 1-5.

[39] G. Lin, R. Ponnappan, Heat transfer characteristics of spray cooling in a closed loop, International Journal of Heat and Mass Transfer 46 (2003) 3737-3746 https://doi.org/10.1016/S0017-9310(03)00217-5.

[40] G. Pautsch, A. Bar-Cohen, Thermal management of multichip modules with evaporative spray cooling, Advances in Electronic Packaging ASME EEP 26(2) (1999) 1453-1462.

[41] C. Lasance, R. Simons, Advances in high performance cooling for electronics, Electronics Cooling 11(4) (2005) 22-39.

[42] Zalman Tech Co., Ltd., ZM-WB4 Gold. www.zalman.com. Last visit: 07.09.2020.

[43] A. Faghri, Heat pipes: review, opportunities and challenges. Frontiers in heat pipe (FHP) 5(1) (2014) 1-48 DOI: 10.5098/fhp.5.1.

[44] R. Hopkins, A. Faghri, D. Khrustalev, Flat miniature heat pipes with micro capillary grooves, Journal of Heat Transfer 121(1) (1999) 102-109 http://dx.doi.org/10.1115/1.2825922.

[45] W. Seifert, V. Pluschke, N.F. Hinsche, Thermoelectric cooler concepts and the limit for maximum cooling, Journal of Physics: Condensed Matter 26(25) (2014) 1-8. DOI: 10.1088/0953-984/26/25/255803.

[46] R.E. Simons, R.C. Chu, Application of thermoelectric cooling to electronic equipment: a review and analysis, Proceedings of the 16th Annual IEEE semiconductor thermal

measurement and management symposium San Jose, CA, USA, (2000) 1-9 DOI: 10.1109/STHERM.2000.837055.

[47] Y.W. Chang, C.C. Chang, M.T. Ke, S.L. Chen, Thermoelectric air-cooling module for electronic devices, Applied Thermal Engineering 29(13) (2009) 2731-2737 https://doi.org/10.1016/j.applthermaleng.2009.01.004.

[48] G.F. Snyder, M. Soto, R. Alley, D. Koester, B. Conner, Hot spot cooling using embedded thermoelectric coolers, 22nd IEEE SEMI-THERM Symposium (2006) 135-143.

[49] V. Semenyuk, Thermoelectric micro modules for spot cooling of high-density heat sources, International Conference on Thermoelectrics (Cat. No.01TH8589) (2001) 391-396.

[50] J. Darabi, M.M. Ohadi, D. DeVoe, An electrohydrodynamic polarization micropump for electronic cooling, Journal of Microelectromechanical Systems 10 (1) (2001) 98-106 DOI: 10.1109/84.911097.

[51] Y. Wei, Y.K. Joshi, Stacked microchannel heat sinks for liquid cooling of microelectronic components, Journal of Electronic Packaging 126 (1) (2004) 60-66 https://doi.org/10.1115/1.1647124.

[52] S.V. Garimella, V. Singhal, D. Liu, On-chip thermal management with microchannel heat sinks and integrated micropumps, Proceedings of the IEEE 94(8) (2006) 1534-1548 DOI: 10.1109/JPROC.2006.879801.

[53] H.Y. Zhang, D. Pinjala, T.N. Wong, K.C. Toh, Y.K. Joshi, Single-phase liquid cooled microchannel heat sink for electronic packages, Applied Thermal Engineering 25(10) (2005) 1472-1487 https://doi.org/10.1016/j.applthermaleng.2004.09.014.

[54] Colgan, et al., A practical implementation of silicon microchannel coolers for high power chips, IEEE Transactions on Components and Packaging Technologies 30(2) (2007) 218-225 DOI: 10.1109/TCAPT.2007.897977.

[55] S. Kandlikar, H. Upadhye, Extending the heat flux limit with enhanced microchannels in direct single-phase cooling of computer chips, Proceedings of 21st semitherm symposium, USA 15-17 March (2005) DOI: 10.1109/STHERM.2005.1412152.

[56] J. Dix, A. Jokar, R. Martinsen, A microchannel heat exchanger for electronics cooling applications, Proceedings of 6th International conference on nanochannels, microchannels and minichannels, Darmstadt, Germany June 23-25 (2008) https://doi.org/10.1115/ICNMM2008-62351.

[57] A. Abdoli, G.S. Dulikravich, G. Vasquez, S. Rastkar, Thermo-fluid-stress-deformation analysis of two-layer microchannels for cooling chips with hot spots, Journal of Electronic Packaging, 137(3) (2015) 031003-1-8 https://doi.org/10.1115/1.4030005.

[58] T-C. Hung, W-M. Yan, W-P. Li, Analysis of heat transfer characteristics of double-layered microchannel heat sink, International Journal of Heat and Mass Transfer 55 (2012) 3090-3099 https://doi.org/10.1016/j.ijheatmasstransfer.2012.02.038.

[59] S.G. Kandlikar, S. Colin, Y. Peles, S. Garimella, R.F. Pease, J.J. Brandner, D.B. Tuckerman, Heat transfer in microchannels-2012 status and research needs, Journal of Heat Transfer 135 (2013) 091001-1-18 https://doi.org/10.1115/1.4024354.

[60] R. A. Krishnan, K.R. Balasubramanian, S. Suresh, The effect of heating area orientation on flow boiling performance in microchannels heat sink under subcooled condition, International Journal of Heat and Mass Transfer 110 (2017) 276-293 https://doi.org/10.1016/j.ijheatmasstransfer.2017.03.030.

[61] A.M. Adham, N. Mohd-Ghazali, R. Ahmad, Thermal and hydrodynamic analysis of microchannel heat sinks: A review, Renewable and Sustainable Energy Reviews 21 (2013) 614-622 https://doi.org/10.1016/j.rser.2013.01.022.

[62] ANSYS FLUENT 18.1, Theory Guide (2017). www.fluent.com

[63] ANSYS FLUENT 18.1, User's Guide (2017). www.fluent.com

[64] I. Dinçer, C. Zamfirescu, Drying Phenomena: Theory and Applications, First Edition (2016) John Wiley & Sons, Ltd, UK.

[65] M.A. Arie, A.H. Shooshtari, S.V. Dessiatoun, E. Al-Hajri, M.M. Ohadi, Numerical modelling and thermal optimization of a single-phase flow manifold-microchannel plate heat exchanger, International Journal of Heat and Mass Transfer 81 (2015) 478-489 https://doi.org/10.1016/j.ijheatmasstransfer.2014.10.022.

[66] T. Dixit, I. Ghosh, Review of micro- and mini-channel heat sinks and heat exchangers for single phase fluids, Renewable and Sustainable Energy Reviews 41(C) (2015) 1298-1311 https://doi.org/10.1016/j.rser.2014.09.024.

[67] Z. Wu, B. Sunden, On further enhancement of single-phase and flow boiling heat transfer in micro/minichannels, Renewable and Sustainable Energy Reviews 40 (2014) 11-27 https://doi.org/10.1016/j.rser.2014.07.171.

[68] G.L. Morini, Single-phase convective heat transfer in microchannels: a review of experimental results, International Journal of Thermal Sciences 43(7) (2004) 631-651 DOI:10.1016/j.ijthermalsci.2004.01.003.

[69] K.C. Toh, X.Y. Chen, J.C. Chai, Numerical computation of fluid flow and heat transfer in microchannels, International Journal of Heat and Mass Transfer 45 (26) (2002) 5133-5141 https://doi.org/10.1016/S0017-9310(02)00223-5.

[70] J. Li, G.P. Peterson, P. Cheng, Three-dimensional analysis of heat transfer in a micro-heat sink with single phase flow, International Journal of Heat and Mass Transfer 47 (2004) 4215-4231 https://doi.org/10.1016/j.ijheatmasstransfer.2004.04.018.

[71] T. Bello-Ochende, L. Liebenberg, J.P. Meyer, Constructal cooling channels for micro-channel heat sinks, International Journal of Heat and Mass Transfer 50 (2007) 4141-4150 https://doi.org/10.1016/j.ijheatmasstransfer.2007.02.019.

[72] T. Bello-Ochende, J.P. Meyer, Combined microchannel heat sink optimisation for cooled electronics, Proceedings of HT2007 (2007) ASME-JSME Thermal Engineering Summer Heat Transfer Conference July 8-12, 2007, Vancouver, British Columbia, Canada DOI: 10.1115/HT2007-32049.

[73] A.M. Sahar, M.R. Ozdemir, E.M. Fayyadh, J. Wissink, M.M. Mahmoud, T.G. Karayiannis, Single phase flow pressure drop and heat transfer in rectangular metallic microchannels, Applied Thermal Engineering 93 (2016) 1324-1336 https://doi.org/10.1016/j.applthermaleng.2015.08.087.

[74] V.L. Vinodhan, K.S. Rajan, Fine-tuning width and aspect ratio of an improved microchannel heat sink for energy-efficient thermal management, Energy Conversion and Management 105 (2015) 986-994 https://doi.org/10.1016/j.enconman.2015.08.068.

[75] A.J. Shkarah, M.Y.B. Sulaiman, M.R.B. Hj Ayoba, H. Togun, A 3D numerical study of heat transfer in a single-phase micro-channel heat sink using graphene, aluminium and silicon as substrates, International Communications in Heat and Mass Transfer 48 (2013) 108-115 https://doi.org/10.1016/j.icheatmasstransfer.2013.08.006.

[76] M. Ohadi, K. Choo, S. Dessiatoun, E. Cetegen, Next generation microchannel heat exchangers, Springer Briefs in Applied Sciences and Technology (Thermal Engineering and Applied Science) Springer New York (2013) 10-12, 44 DOI 10.1007/978-1-4614-0779-9.

[77] V. Leela Vinodhan, K.S. Rajan, Computational analysis of new microchannel heat sink configurations, Energy Conversion and Management 86 (2014) 595-604 https://doi.org/10.1016/j.enconman.2014.06.038.

[78] R. Chein, J. Chen, Numerical study of the inlet/outlet arrangement effect on microchannel heat sink performance, International Journal of Thermal Sciences 48(8) (2009) 1627-1638 https://doi.org/10.1016/j.ijthermalsci.2008.12.019.

[79] D. Liu, S.V. Garimella, Investigation of liquid flow in microchannels, AIAA Journal of Thermophysics and Heat Transfer 18(1) (2004) 65-72 https://doi.org/10.2514/1.9124.

[80] H.R. Upadhye, S.G Kandlikar, Optimization of microchannel geometry for direct chip cooling using single phase heat transfer, International Conference on Microchannels and Minichannels (2004) (June 17-19, 2004), Rochester, New York, USA. 679-685 https://doi.org/10.1115/ICMM2004-2398.

[81] A. Bejan, S. Lorente, Constructal theory of generation and configuration in nature and engineering, Journal of Applied Physics 100 (2006) 041301-27 DOI: 10.1063/1.2221896.

[82] A. Bejan, Shape and structure from engineering to nature, Cambridge University Press (2000) Cambridge, UK.

[83] R.W. Knight, D.J. Hall, J.S. Goodling, R.C. Jaeger, Heat sink optimization with application to microchannels, IEEE Transactions on components, hybrids, and manufacturing technology 15 (5) (1992) 832-842 DOI: 10.1109/33.180049.

[84] P. Lee, S.V. Garimella, D. Liu, Investigation of heat transfer in rectangular microchannels, International Journal of Heat and Mass Transfer 48(9) (2005) 1688-1704 https://doi.org/10.1016/j.ijheatmasstransfer.2004.11.019.

[85] C. Chen, Forced convection heat transfer in microchannel heat sinks, International Journal of Heat and Mass Transfer 50 (2007) 2182-2189 https://doi.org/10.1016/j.ijheatmasstransfer.2006.11.001.

[86] D.J. Laser, J.G. Santiago, A review of micropumps, Journal of Micromechanics and Microengineering 14 (2004) R35-R64 DOI: 10.1088/0960-1317/14/6/R01.

[87] M. Asadi, G. Xie, B. Sunden, A review of heat transfer and pressure drop characteristics of single and two-phase microchannels, International Journal of Heat and Mass Transfer 79 (2014) 34-53 https://doi.org/10.1016/j.ijheatmasstransfer.2014.07.090.

[88] B. Dai, M. Li, C. Dang, Y. Ma, Q. Chen, Investigation on convective heat transfer characteristics of single-phase liquid flow in multi-port micro-channel tubes, International Journal of Heat and Mass Transfer 70 (2014) 114-118 https://doi.org/10.1016/j.ijheatmasstransfer.2013.10.048.

[89] S. Lee, W. Qu, Thermal design methodology for low flow rate single-phase and two-phase micro-channel heat sinks, IEEE Transactions on Components and Packaging 30(4) (2007) 830-841 DOI: 10.1109/TCAPT.2007.910157.

[90] I. Mudawar, Two-phase microchannel heat sinks: theory, applications and limitations, Journal of Electronic Packaging- Transactions of ASME 133 (2011) 041002-1-31 https://doi.org/10.1115/1.4005300.

[91] I. Mudawar, Recent advances in high-flux, two-phase thermal management, Journal of Thermal Science and Engineering Applications-Transactions of ASME 5(2) (2013) 021012- 1-15 DOI: 10.1115/1.4023599.

[92] C.R. Kharangate, I. Mudawar, Review of computational studies on boiling and condensation, International Journal of Heat and Mass Transfer 108 (A) (2017) 1164-1196 https://doi.org/10.1016/j.ijheatmasstransfer.2016.12.065.

[93] A. Mukherjee, S.G. Kandlikar, Numerical simulation of growth of a vapour bubble during flow boiling of water in a microchannel, Microfluids and Nanofluids 1 (2005) 137-145 DOI 10.1007/s10404-004-0021-8.

[94] G.R. Warrier, C.J. Kim, Y.S. Ju, Microchannel cooling device with perforated side walls: design and modelling, International Journal of Heat and Mass Transfer 68 (2014) 174-183 https://doi.org/10.1016/j.ijheatmasstransfer.2013.09.022.

[95] X. Wang, A.S. Mujumdar, C. Yap, Thermal characteristics of tree shaped microchannel nets for cooling of a rectangular heat sink, International Journal of Thermal Sciences 45(11) (2006) 1103-1112 https://doi.org/10.1016/j.ijthermalsci.2006.01.010.

[96] S.M. Senn, D. Poulikakos, Laminar mixing, heat transfer and pressure drop in tree-like microchannel nets their application for thermal management in polymer electrolyte fuel cells, Journal of Power Sources 130 (1-2) (2004) 178-191 https://doi.org/10.1016/j.jpowsour.2003.12.025.

[97] R. Revellin, J.R. Thome, A. Bejan, J. Bonjour, Constructal tree shaped microchannel networks for maximizing the saturated critical heat flux, International Journal of Thermal Sciences 48 (2) (2009) 342-352 https://doi.org/10.1016/j.ijthermalsci.2008.06.009.

[98] X. Yu, C. Zhang, J. Teng, S. Huang, S. Jin, Y. Lian, C. Cheng, T. Xu, J. Chu, Y. Chang, T. Dang, R. Greif, A study on the hydraulic and thermal characteristics in fractal tree-like microchannels by numerical and experimental methods, International Journal of Heat and Mass Transfer 5 (25-26) (2012) 7499-7507 DOI: https://doi.org/10.1016/j.ijheatmasstransfer.2012.07.050.

[99] L. Wang, W. Wu, X. Li, Numerical and experimental investigation of mixing characteristics in the constructal tree-shaped microchannel, International Journal of Heat and Mass Transfer 67 (2013) 1014-1023 https://doi.org/10.1016/j.ijheatmasstransfer.2013.08.077.

[100] V. Dupont, J.R. Thome, Evaporation in microchannels: influence of the channel diameter on heat transfer, Microfluid Nanofluid 1 (2005) 119-127.

[101] C. Vlasie, H. Macchi, J. Guilpart, B. Agostini, Flow boiling in small diameter channels, International Journal of Refrigeration 27(2) (2004) 191-201 https://doi.org/10.1016/S0140-7007(02)00035-X.

[102] S.V. Garimella, C.B. Sobhan, Transport in microchannels-a critical review, Annual Reviews of Heat Transfer- Begell House, Inc. 13 (2003) 1-50.

[103] S.S Bertsch, E.A. Groll, S.V. Garimella, Review and comparative analysis of studies on saturated flow boiling in small channels, Nanoscale Microscale Thermophysical Engineering 12(3) (2008) 187-227. DOI:10.1080/15567260802317357.

[104] L. Cheng, D. Mewes, Review of two-phase flow and flow boiling of mixtures in small and minichannels, International Journal of Multiphase Flow 32(2) (2006) 183-207 https://doi.org/10.1016/j.ijmultiphaseflow.2005.10.001.

[105] J.R. Thome, Boiling in microchannels: a review of experiment and theory, International Journal of Heat and Fluid Flow 25(2) (2004) 128-139 https://doi.org/10.1016/j.ijheatfluidflow.2003.11.005.

[106] S.S. Bertsch, E.A. Groll, S.V. Garimella, A composite heat transfer correlation for saturated flow boiling in small channels, International Journal of Heat and Mass Transfer 52 (2009) 2110-2118 https://doi.org/10.1016/j.ijheatmasstransfer.2008.10.022.

[107] S. Lee, V.S. Devahdhanush, I. Mudawar, Investigation of subcooled and saturated boiling heat transfer mechanisms, instabilities, and transient flow regime maps for large length-to-diameter ratio micro-channel heat sinks, International Journal of Heat and Mass Transfer 123 (2018) 172-191 https://doi.org/10.1016/j.ijheatmasstransfer.2018.02.020.

[108] J. Lee, I. Mudawar, Critical heat flux for subcooled flow boiling in microchannel heat sinks, International Journal of Heat and Mass Transfer 52 (2009) 3341-3352 https://doi.org/10.1016/j.ijheatmasstransfer.2008.12.019.

[109] G. Wang, P. Cheng, Subcooled flow boiling and microbubble emission boiling phenomena in a partially heated microchannel, International Journal of Heat and Mass Transfer 52 (2009) 79-91 https://doi.org/10.1016/j.ijheatmasstransfer.2008.06.031.

[110] R. Zhuan, W. Wang, Simulation of subcooled flow boiling in a microchannel, International Journal of Refrigeration 34(3) (2011) 781-795 https://doi.org/10.1016/j.ijrefrig.2010.12.004.

[111] J.S. Murallidharan, B.V.S.S.S. Prasad, B.S.V. Patnaik, G.F. Hewitt, V. Badalassi, CFD investigation and assessment of wall heat flux partitioning model for the prediction of high-pressure subcooled flow boiling, International Journal of Heat and Mass Transfer 103 (2016) 211-230 https://doi.org/10.1016/j.ijheatmasstransfer.2016.06.050.

[112] J. Lee, I. Mudawar, Fluid flow and heat transfer characteristics of low temperature two-phase microchannel heat sinks-Part 2: Subcooled boiling pressure drop and heat transfer, International Journal of Heat and Mass Transfer 51 (2008) 4327-4341 https://doi.org/10.1016/j.ijheatmasstransfer.2008.02.013.

[113] T. Harirchian, S.V. Garimella, Effects of channel dimension, heat flux, and mass flux on flow boiling regimes in microchannels, International Journal of Multiphase Flow 35(4) (2009) 349-362 https://doi.org/10.1016/j.ijmultiphaseflow.2009.01.003.

[114] R. Zhuan, W. Wang, Flow pattern of boiling in microchannel by numerical simulation, International Journal of Heat and Mass Transfer 55 (2012) 1741-1753 https://doi.org/10.1016/j.ijheatmasstransfer.2011.11.029.

[115] A. Mukherjee, S.G. Kandlikar, Z.J. Edel, Numerical study of bubble growth and wall heat transfer during flow boiling in a microchannel, International Journal of Heat and Mass Transfer 54 (2011) 3702-3718 https://doi.org/10.1016/j.ijheatmasstransfer.2011.01.030.

[116] A.K. Sadaghiani, A. Kosar, Numerical and experimental investigation on the effects of diameter and length on high mass flux subcooled flow boiling in horizontal microtubes, International Journal of Heat and Mass Transfer 92 (2016) 824-837 https://doi.org/10.1016/j.ijheatmasstransfer.2015.09.004.

[117] K. Fukuda, O. Iqbal, R.M. Barron, R. Balachandar, Numerical investigation of internal flows with subcooled nucleate boiling, 12th International Conference on Heat Transfer, Fluid Mechanics and Thermodynamics, Costa de Sol, Spain, 11-13 July (2016) 24-29.

[118] R. Zhang, T. Cong, W. Tian, S. Qiu, G. Su, Effects of turbulence models on forced convection subcooled boiling in vertical pipes, Annals of Nuclear Energy 80 (2015) 293-302 https://doi.org/10.1016/j.anucene.2015.01.039.

[119] M. Colombo, M. Fairweather, Accuracy of Eulerian-Eulerian two-fluid CFD boiling models of subcooled boiling flows, International Journal of Heat and Mass Transfer 103 (2016) 28-44 https://doi.org/10.1016/j.ijheatmasstransfer.2016.06.098.

[120] C. Lifante, Th. Frank, A. Burns, Wall boiling modelling extension towards critical heat flux, The 15th International Topical Meeting on Nuclear Reactor Thermalhydraulics, NURETH-15, Pisa, Italy, May 12-15, (2013).

[121] S. Kakac, B. Bon, A Review of two-phase flow dynamic instabilities in tube boiling systems, International Journal of Heat and Mass Transfer 51(3-4) (2008) 399-433 https://doi.org/10.1016/j.ijheatmasstransfer.2007.09.026.

[122] J.A. Boure, A.E. Bergles, L.S. Tong, Review of two-phase flow instability, Nuclear Engineering and Design 25(2) (1973) 165-192 https://doi.org/10.1016/0029-5493(73)90043-5.

[123] H. Grzybowski, R. Mosdor, Modelling of pressure-drop instability in single and multi microchannels, Acta Mechanica et Automatica 6(3) (2012) 45-51.

[124] L. Tadrist, Review on two-phase flow instabilities in narrow spaces, International Journal of Heat and Fluid Flow 28 (2007) 54-62 https://doi.org/10.1016/j.ijheatfluidflow.2006.06.004.

[125] C.J. Kuo, Y. Peles, Pressure effects on flow boiling instabilities in parallel microchannels, International Journal of Heat and Mass Transfer 52 (2009) 271-280 https://doi.org/10.1016/j.ijheatmasstransfer.2008.06.015.

[126] G. Hetsroni, A. Mosyak, Z. Segal, E. Pogrebnyak, Two-phase flow patterns in parallel micro-channels, International Journal of Multiphase Flow 29(3) (2003) 341-360 https://doi.org/10.1016/S0301-9322(03)00002-8.

[127] G. Hetsroni, D. Klein, A. Mosyak, Z. Segal, and E. Pogrebnyak, Convective boiling in parallel microchannels, Microscale Thermophysical Engineering 8 (2004) 403-421 https://doi.org/10.1080/10893950490516965.

[128] W. Qu, I. Mudawar, Transport phenomena in two-phase micro-channel heat sinks, Journal of Electronic Packaging 126(2) (2004) 213-224 https://doi.org/10.1115/1.1756145.

[129] K.M. Kelkar, S.V. Patankar, S. Kang, Computational method for characterization of a microchannel heat sink involving two-phase flow, ASME 2005 Heat Transfer Summer Conference: Advances in electronic packaging, Parts A, B, and C, San Francisco,

California, USA, July 17-22, (2005) 151-160 https://doi.org/10.1115/IPACK2005-73119.

[130] A.M. Jacobi, J.R. Thome, Heat transfer model for evaporation of elongated bubble flows in microchannels, Journal of Heat Transfer 124(6) (2002) 1131-1136 https://doi.org/10.1115/1.1517274.

[131] X.F. Peng, H.Y. Hu, B.X. Wang, Boiling nucleation during liquid flow in microchannels, International Journal of Heat and Mass Transfer 41(1) (1998) 101-106 https://doi.org/10.1016/S0017-9310(97)00096-3.

[132] M. B. Bowers, I. Mudawar, High flux boiling in low flow rate, low pressure drop mini-channel and micro-channel heat sinks, International Journal of Heat and Mass Transfer 37(2) (1994) 321-332 https://doi.org/10.1016/0017-9310(94)90103-1.

[133] M. B. Bowers, I. Mudawar, Two-phase electronic cooling using mini-channel and micro-channel heat sinks: part 1-Design criteria and heat diffusion constraints, ASME Journal of Electronic Packaging 116 (1994a) 290-297.

[134] M. B. Bowers, I. Mudawar, Two-phase electronic cooling using mini-channel and micro-channel heat sinks: Part 2-Flow rate and pressure drop constraints, ASME Journal of Electronic Packaging116 (1994b) 298-305.

[135] A. E. Bergles, T. Dormer Jr., Subcooled boiling pressure drop with water at low pressure, International Journal of Heat and Mass Transfer 12(4) (1969) 459-470 https://doi.org/10.1016/0017-9310(69)90141-0.

[136] T. Harirchian, S.V. Garimella, Flow regime-based modelling of heat transfer and pressure drop in microchannel flow boiling, International Journal of Heat and Mass Transfer 55(4) (2012) 1246-1260 https://doi.org/10.1016/j.ijheatmasstransfer.2011.09.024.

[137] R.K. Sarangi, A. Bhattacharya, R.S. Prasher, Numerical modelling of boiling heat transfer in microchannels, Applied Thermal Engineering 29(2-3) (2009) 300-309 https://doi.org/10.1016/j.applthermaleng.2008.02.039.

[138] J. Lee, I. Mudawar, Two-phase flow in high heat flux microchannel heat sink for refrigeration cooling applications: Part I-pressure drop characteristics, International Journal of Heat and Mass Transfer 48(5) (2005) 928-940 https://doi.org/10.1016/j.ijheatmasstransfer.2004.09.018.

[139] E. Galvis , R. Culham, Measurements and flow pattern visualizations of two-phase flow boiling in single channel microevaporators, International Journal of Multiphase Flow 42 (2012) 52-61 https://doi.org/10.1016/j.ijmultiphaseflow.2012.01.009.

[140] M. Bruder, G. Bloch, T. Sattelmayer, Critical heat flux in flow boiling-Review of the current understanding and experimental approaches, Heat Transfer Engineering 38(3) (2017) 347-360 https://doi.org/10.1080/01457632.2016.1189274.

[141] A.P. Roday, M.K. Jensen, A review of the critical heat flux condition in mini-and microchannels, Journal of Mechanical Science and Technology 23 (2009) 2529-2547.

[142] A.E. Bergles, S.G. Kandlikar, On the nature of critical heat flux in microchannels, ASME Journal of Heat Transfer 127(1) (2005) 101-107 https://doi.org/10.1115/1.1839587.

[143] M.C. Vlachou, J.S. Lioumbas, K. David, D. Chasapis, T.D. Karapantsios, Effect of channel height and mass flux on highly subcooled horizontal flow boiling, Experimental Thermal and Fluid Science 83 (2017) 157-168 https://doi.org/10.1016/j.expthermflusci.2017.01.001.

[144] R. Maurus, T. Sattelmayer, Bubble and boundary layer behaviour in subcooled flow boiling, International Journal of Thermal Sciences 45(3) (2006) 257-268 https://doi.org/10.1016/j.ijthermalsci.2004.05.006.

[145] H. Steiner, A. Kobor, L. Gebhard, A wall heat transfer model for subcooled boiling flow, International Journal of Heat and Mass Transfer 48 (2005) 4161-4173 https://doi.org/10.1016/j.ijheatmasstransfer.2005.03.032.

[146] L. Cheng, 2013, Fundamental issues of critical heat flux phenomena during flow boiling in microscale-channels and nucleate pool boiling in confined spaces, Heat Transfer Engineering 34(13) (2013) 1016-1043 DOI: 10.1080/01457632.2013.763538.

[147] R. Revellin, J. R. Thome, A theoretical model for the prediction of the critical heat flux in heated microchannels, International Journal of Heat and Mass Transfer 51 (2008) 1216-1225 https://doi.org/10.1016/j.ijheatmasstransfer.2007.03.002.

[148] A. Kosar, A model to predict saturated critical heat flux in minichannels and microchannels, International Journal of Thermal Sciences 48(2) (2009) 261-270 https://doi.org/10.1016/j.ijthermalsci.2008.08.008.

[149] S.S. Mehendale, A.M. Jacobi, R.K. Ahah, Fluid flow and heat transfer at micro- and meso-scales with application to heat exchanger design, Applied Mechanics Reviews 53(7) (2000) 175-193 https://doi.org/10.1115/1.3097347.

[150] S.G. Kandlikar, Fundamental issues related to flow boiling in minichannels and microchannels, Experimental Thermal and Fluid Science 26 (2002) 389-407 https://doi.org/10.1016/S0894-1777(02)00150-4.

[151] S.G. Kandlikar, W.J. Grande, Evolution of microchannel flow passages-Thermohydraulic performance and fabrication technology, Heat Transfer Engineering 24(1) (2003) 3-17 DOI: 10.1080/01457630304040.

[152] P.A. Kew, K. Cornwell, Correlations for the prediction of boiling heat transfer in small-diameter channels, Applied Thermal Engineering 17(8-10) (1997) 705-715 https://doi.org/10.1016/S1359-4311(96)00071-3.

[153] M. Kawaji, P. M.-Y. Chung, Adiabatic gas-liquid flow in microchannels, Microscale Thermophysical Engineering, 8(3) (2004) 239-257, DOI:10.1080/10893950490477518.

[154] W. Qu, I. Mudawar, Prediction and measurement of incipient boiling heat flux in microchannel heat sinks, International Journal of Heat and Mass Transfer 45(19) (2002) 3933-3945 https://doi.org/10.1016/S0017-9310(02)00106-0.

[155] D. Liu, S.V. Garimella, Flow Boiling Heat Transfer in Microchannels, Journal of Heat Transfer 129(10) (2007) 1321-1332 https://doi.org/10.1115/1.2754944.

[156] ANSYS 18.1 DesignXplorer, User's Guide (2017). www.fluent.com

[157] A. Brucato, F. Grisafi, G. Montante, Particle drag coefficients in turbulent fluids, Chemical Engineering Science 53(18) (1998) 3295-3314.

[158] C. O. Popiel, J. Wojtkowiak, Simple formulas for thermophysical properties of liquid water for heat transfer calculations (from 0°C to 150°C), Heat Transfer Engineering 19(3) (1998) 87-101 DOI: 10.1080/01457639808939929.

[159] Z.H. Wang, X.D. Wang, W.M. Yan, Y.Y. Duan, D.J. Lee, J.L. Xu, Multi-parameters optimization for microchannel heat sink using inverse problem method, International Journal of Heat and Mass Transfer 54 (2011) 2811-2819 https://doi.org/10.1016/j.ijheatmasstransfer.2011.01.029.

[160] C.W. Chen, J.J. Lee, H.S. Kou, Optimal thermal design of microchannel heat sinks by the simulated annealing method, International Communications in Heat and Mass Transfer 35(8) (2008) 980-984 https://doi.org/10.1016/j.icheatmasstransfer.2008.04.006.

[161] H.S. Kou, J.J. Lee, C.W. Chen, Optimum thermal performance of microchannel heat sink by adjusting channel width and height, International Communications in Heat and Mass Transfer 35(5) (2008) 577-582 https://doi.org/10.1016/j.icheatmasstransfer.2007.12.002.

[162] T-C. Hung, W-M. Yan, X-D. Wang, Y-X. Huang, Optimal design of geometric parameters of double-layered microchannel heat sinks, International Journal of Heat and Mass Transfer 55(11-12) (2012) 3262-3272 https://doi.org/10.1016/j.ijheatmasstransfer.2012.02.059.

[163] J.H. Ryu, D.H. Choi, S.J. Kim, Numerical optimization of the thermal performance of a microchannel heat sink, International Journal of Heat and Mass Transfer 45(13) (2002) 2823-2827 https://doi.org/10.1016/S0017-9310(02)00006-6.

[164] A. A. Koga, E. C. C. Lopes, H. F. V. Nova, Cícero R. de Lima, Emílio Carlos Nelli Silva, Development of heat sink device by using topology optimization, International Journal of Heat and Mass Transfer 64 (2013) 759-772 https://doi.org/10.1016/j.ijheatmasstransfer.2013.05.007.

[165] T. Dbouk, A review about the engineering design of optimal heat transfer systems using topology optimization, Applied Thermal Engineering 112 (2017) 841-854 https://doi.org/10.1016/j.applthermaleng.2016.10.134.

[166] N. Amanifard, N. Nariman-Zadeh, M. Borji, A. Khalkhali, A. Habibdoust, Modelling and Pareto optimization of heat transfer and flow coefficients in microchannels using GMDH type neural networks and genetic algorithms, Energy Conversion and Management 49(2) (2008) 311-325 https://doi.org/10.1016/j.enconman.2007.06.002.

[167] H. Shen, X. Jin, F. Zhang, G. Xie, B. Sunden, H. Yan, Computational optimization of counter-flow double-layered microchannel heat sinks subjected to thermal resistance and pumping power, Applied Thermal Engineering 121 (2017) 180-189 https://doi.org/10.1016/j.applthermaleng.2017.04.058.

[168] A. Husain, K-Y. Kim, Multi objective optimization of a microchannel heat sink using evolutionary algorithm, Journal of Heat Transfer 130(11) (2008) 114505-1-3 DOI: 10.1115/1.2969261.

[169] A. Husain, K-Y, Kim, Shape optimization of microchannel heat sink for micro-electronic cooling, IEEE Transactions on Components and Packaging Technologies 31(2) (2008) 322-330 DOI: 10.1109/TCAPT.2008.916791.

[170] T. Bello-Ochende, L. Liebenberg, J.P. Meyer**,** Constructal design: geometric optimisation of micro-channel heat sinks, South African Journal of Science 103 (2007) 483-489.

[171] T. Bello-Ochende, L. Liebenberg, A. Bejan, J. P. Meyer, Optimal geometry for conjugate heat transfer in a cooling channel, International Heat Transfer Conference, January 2006, DOI: 10.1615/IHTC13.p17.20.

[172] T. Bello-Ochende, J.P. Meyer, F.U. Ighalo, Combined numerical optimization and constructal theory for the design of microchannel heat sinks, Numerical Heat Transfer Part A: Applications 58(11) (2010) 882-899 DOI:10.1080/10407782.2010.529036.

[173] T-C Hung, T-S. Sheu, W-M. Yan, Optimal thermal design of microchannel heat sinks with different geometric configurations, International Communications in Heat and Mass Transfer 39 (2012) 1572-1577 https://doi.org/10.1016/j.icheatmasstransfer.2012.10.008.

[174] B. Shao, Z. Sun, L. Wang, Optimization design of microchannel cooling heat sink, International Journal of Numerical Methods for Heat and Fluid Flow 17 (6) (2007) 628-637 DOI: 10.1108/09615530710761243.

[175] O. O. Adewumi, T. Bello-Ochende, J. P. Meyer, Numerical investigation into the thermal performance of single microchannels with varying axial length and different shapes of micro pin-fin inserts, Heat Transfer Engineering 38(13) (2017) 1157-1170 DOI: 10.1080/01457632.2016.1239927.

[176] O.O. Adewumi, T. Bello-Ochende, J.P. Meyer, Geometric optimisation of multi-layered microchannel heat sink with different flow arrangements, Proceedings of the 15th Heat Transfer Conference IHTC-15, August 10-15 (2014), Kyoto, Japan.

[177] M. R. Salimpour, M. Sharifhasan, E. Shirani, Constructal optimization of the geometry of an array of micro-channels, International Communications in Heat and Mass Transfer 38(1) (2011) 93-99 https://doi.org/10.1016/j.icheatmasstransfer.2010.10.008.

[178] J. Cruz, I. Amaya, R. Correa, Optimal rectangular microchannel design, using simulated annealing, unified particle swarm and spiral algorithms, in the presence of spreading resistance, Applied Thermal Engineering 84 (2015) 126-137 https://doi.org/10.1016/j.applthermaleng.2015.03.049.

[179] F. U. Ighalo, T. Bello-Ochende, J. P. Meyer, Mathematical optimization: application to the design of optimal micro-channel heat sinks, Engenharia Térmica (Thermal Engineering) 8(58) (2009) 58-64 http://dx.doi.org/10.5380/reterm.v8i1.61883.

[180] S.J. Kim, Methods for thermal optimization of microchannel heat sinks, Heat Transfer Engineering 25(1) (2004) 37-49 DOI: 10.1080/01457630490248359.

[181] D.D. Ma, G.D. Xia, Y.T. Jia, Y.F. Li, J. Wang, Multi-parameter optimization for micro-channel heat sink under different constraint conditions, Applied Thermal Engineering 120 (2017) 247-256 https://doi.org/10.1016/j.applthermaleng.2017.03.123.

[182] T-C. Hung, W-M. Yan, Optimization of a microchannel heat sink with varying channel heights and widths, Numerical Heat Transfer Part A: Applications 62(9) (2012) 722-741 DOI: 10.1080/10407782.2012.709437.

[183] W. A. Khan, M. B. Kadri, Q. Ali, Optimization of microchannel heat sinks using genetic algorithm, Heat Transfer Engineering 34(4) (2013) 279-287, DOI: 10.1080/01457632.2013.694758.

[184] J. Li, G.P. Peterson, 3-Dimensional numerical optimization of silicon-based high performance parallel microchannel heat sink with liquid flow, International Journal of Heat and Mass Transfer 50 (2007) 2895-2904. https://doi.org/10.1016/j.ijheatmasstransfer.2007.01.019.

[185] S. Ndao, Y. Peles, M. K. Jensen, Multi-objective thermal design optimization and comparative analysis of electronics cooling technologies, International Journal of Heat and Mass Transfer 52 (2009) 4317-4326. https://doi.org/10.1016/j.ijheatmasstransfer.2009.03.069.

[186] S.V. Patankar, Numerical Heat Transfer and Fluid Flow (1980), McGraw-Hill, New York.

[187] N. Kurul, M. Podowski, On the modelling of multidimensional effects in boiling channels, Proceedings of the 27th National Heat Transfer Conference, Minneapolis, Minnesota, USA, July (1991).

[188] V. I. Tolubinsky, D.M. Kostanchuk, Vapour bubbles growth rate and heat transfer intensity at subcooled water boiling, 4th International Heat transfer Conference, Paris, France (1970).

[189] V.H. Del Valle, D.B.R. Kenning, Subcooled flow boiling at high heat flux, International Journal of Heat and Mass Transfer 28(10) (1985) 1907-1920 https://doi.org/10.1016/0017-9310(85)90213-3.

[190] M. Lemmert, J.M. Chawla, Influence of flow velocity on surface boiling heat transfer coefficient in Heat Transfer in Boiling, E. Hahne and U. Grigull, Eds., Academic Press and Hemisphere, New York, NY, USA (1977) 237-247.

[191] R. Cole, A photographic study of pool boiling in the region of the critical heat flux, AIChE Journal 6 (1960) 533-542 https://doi.org/10.1002/aic.690060405.

[192] J. Lavieville, E. Quemerais, S. Mimouni, M. Boucker, N. Mechitoua, NEPTUNE CFD V1.0 Theory Manual, EDF. (2005).

[193] T. Hibiki, M. Ishii, One-group interfacial area transport of bubbly flows in vertical round tubes, International Journal of Heat and Mass Transfer 43(15) (2000) 2711-2726 https://doi.org/10.1016/S0017-9310(99)00325-7.

[194] W. Yao, C. Morel, Volumetric interfacial area prediction in upward bubbly two-phase flow, International Journal of Heat and Mass Transfer 47(2) (2004) 307-328 https://doi.org/10.1016/j.ijheatmasstransfer.2003.06.004.

[195] M. Ishii, Two-fluid model for two-phase flow, 2nd International workshop on two-phase flow fundamentals, RPI, Troy, NY. (1979).

[196] A. Tomiyama, Struggle with computational bubble dynamics, Third International Conference on Multiphase Flow, Lyon, France, June 8-12, (1998) in ANSYS Theory Guide 2017.

[197] S. P. Antal, R. T. Lahey, J.E. Flaherty, Analysis of phase distribution in fully developed laminar bubbly two-phase flow, International Journal of Multiphase Flow 17(5) (1991) 635-652 https://doi.org/10.1016/0301-9322(91)90029-3.

[198] M. Lopez de Bertodano, Turbulent Bubbly Flow in a Triangular Duct, Ph.D. Thesis, Rensselaer Polytechnic Institute, Troy, New York. (1991).

[199] D. A. Drew, R. T. Lahey, Particulate two-phase flow, Butterworth-Heinemann, Boston, MA (1993) 509-566.

[200] W. E. Ranz, W. R. Marshall, Jr., Evaporation from drops, Part I, Chemical Engineering Progress 48(3) (March 1952) 141-146.

[201] W. E. Ranz, W. R. Marshall, Jr., Evaporation from drops, Part I and Part II, Chemical Engineering Progress 48(4) (April 1952) 173-180.

[202] A. A. Troshko, Y. A. Hassan, A two-equation turbulence model of turbulent bubbly flow, International Journal of Multiphase Flow 27(11) (2001) 1965-2000 https://doi.org/10.1016/S0301-9322(01)00043-X.

[203] Z. Guo, D.F. Fletcher, B.S. Haynes, A review of computational modelling of flow boiling in microchannels, Journal of Computational Multiphase Flows 6(2) (2014) 79-110 https://doi.org/10.1260/1757-482X.6.2.79.

[204] W. Qu, I. Mudawar, Thermal design methodology for high heat flux single-phase and two-phase microchannel heat sinks, IEEE Transactions on Components and Packaging Technologies 26(3) (2003) 598-609 DOI: 10.1109/ TCAPT.2003.817652.

[205] C.J. Ho, L.C. Wei, Z.W. Li, An experimental investigation of forced convective cooling performance of a microchannel heat sink with Al2O3/water nanofluid, Applied Thermal Engineering 30 (2010) 96–103 https://doi.org/10.1016/j.applthermaleng.2009.07.003.

[206] S-M. Kim, I. Mudawar, Thermal design and operational limits of two-phase microchannel heat sinks, International Journal of Heat and Mass Transfer 106 (2017) 861-876 https://doi.org/10.1016/j.ijheatmasstransfer.2016.10.020.

[207] A. Bejan, S. Lorente, The Constructal law of design and evolution in nature, Philosophical Transactions of the Royal Society B 365 (2010) 1335-1347 https://doi.org/10.1098/rstb.2009.0302.

[208] A.H. Reis, Book review, International Journal of Heat and Mass Transfer 49 (2006) 445 doi:10.1016/j.ijheatmasstransfer.2005.07.031.

[209] C.R. Kharangate, L.E. O'Neill, I. Mudawar, Effects of two-phase inlet quality, mass velocity, flow orientation, and heating perimeter on flow boiling in a rectangular channel: Part 2-CHF experimental results and model, International Journal of Heat and Mass Transfer 103 (2016) 1280-1296 https://doi.org/10.1016/j.ijheatmasstransfer.2016.05.059.